

Nr. 389

Xia Zhuge

Characterizing slope instability kinematics by integrating  
multi-sensor satellite remote sensing observations

HANNOVER 2023

---





Nr. 389

Characterizing slope instability kinematics by integrating multi-sensor  
satellite remote sensing observations

Von der Fakultät für Bauingenieurwesen und Geodäsie  
der Gottfried Wilhelm Leibniz Universität Hannover  
zur Erlangung des Grades

**DOKTOR-INGENIEUR (Dr.-Ing.)**

genehmigte Dissertation  
von

Zhuge Xia, M.Sc.

HANNOVER 2023

---

Diese Arbeit ist gleichzeitig veröffentlicht in:  
Ausschuss Geodäsie der Bayerischen Akademie der Wissenschaften (DGK)  
Reihe C, Nr. 907, München 2023, ISBN 978-3-7696-5319-9, ISSN 0065-5325, [www.dgk.badw.de](http://www.dgk.badw.de)

Prüfungskommission

Vorsitzender: Prof. Dr.-Ing. habil. Monika Sester

Referent: Prof. Dr. Mahdi Motagh

Korreferenten: Prof. Dr.-Ing. Ingo Neumann

Prof. Dr. Roberto Tomás Jover (University of Alicante)

Tag der mündlichen Prüfung: 06.07.2023

# Abstract

Over the past few decades, the occurrence and intensity of geological hazards, such as landslides, have substantially risen due to various factors, including global climate change, seismic events, rapid urbanization and other anthropogenic activities. Landslide disasters pose a significant risk in both urban and rural areas, resulting in fatalities, infrastructure damages, and economic losses. Nevertheless, conventional ground-based monitoring techniques are often costly, time-consuming, and require considerable resources. Moreover, some landslide incidents occur in remote or hazardous locations, making ground-based observation and field investigation challenging or even impossible.

Fortunately, the advancements in spaceborne remote sensing technology have led to the availability of large-scale and high-quality imagery, which can be utilized for various landslide-related applications, including identification, monitoring, analysis, and prediction. This efficient and cost-effective technology allows for remote monitoring and assessment of landslide risks and can significantly contribute to disaster management and mitigation efforts. Consequently, spaceborne remote sensing techniques have become vital for geohazard management in many countries, benefiting society by providing reliable downstream services. However, substantial effort is required to ensure that such benefits are provided.

For establishing long-term data archives and reliable analyses, it is essential to maintain consistent and continued use of multi-sensor spaceborne remote sensing techniques. This will enable a more thorough understanding of the physical mechanisms responsible for slope instabilities, leading to better decision-making and development of effective mitigation strategies. Ultimately, this can reduce the impact of landslide hazards on the general public. The present dissertation contributes to this effort from the following perspectives:

- To obtain a comprehensive understanding of spaceborne remote sensing techniques for landslide monitoring, we integrated multi-sensor methods to monitor the entire life cycle of landslide dynamics. We aimed to comprehend the landslide evolution under complex cascading events by utilizing various spaceborne remote sensing techniques, e.g., the precursory deformation before catastrophic failure, co-failure procedures, and post-failure evolution of slope instability.
- To address the discrepancies between spaceborne optical and radar imagery, we present a methodology that models four-dimensional (4D) post-failure landslide kinematics using a decaying mathematical model. This approach enables us to represent the stress relaxation for the landslide body dynamics after failure. By employing this methodology, we can overcome the weaknesses of the individual sensor in spaceborne optical and radar imaging.
- We assessed the effectiveness of a newly designed small dihedral corner reflector for landslide monitoring. The reflector is compatible with both ascending and descending satellite orbits, while it is also suitable for applications with both high-resolution and medium-resolution satellite imagery. Furthermore, although its echoes are not

as strong as those of conventional reflectors, the cost of the newly designed reflectors is reduced, with more manageable installation and maintenance. To overcome this limitation, we propose a specific selection strategy based on a probability model to identify the reflectors in satellite images.

# Zusammenfassung

In den letzten Jahrzehnten hat das Auftreten und die Intensität geologischer Gefahren wie Erdbeben aufgrund verschiedener Faktoren erheblich zugenommen. Dazu zählen unter anderem der globale Klimawandel, seismische Ereignisse, die schnelle Urbanisierung und andere menschliche Aktivitäten. Erdbeben stellen sowohl in städtischen als auch in ländlichen Gebieten ein erhebliches Risiko dar, da sie zu Todesfällen, Schäden an der Infrastruktur und wirtschaftlichen Verlusten führen können. Herkömmliche bodengestützte Überwachungsverfahren sind oft kostspielig, zeitaufwändig und erfordern beträchtliche Ressourcen. Darüber hinaus treten einige Erdbeben an abgelegenen oder gefährlichen Orten auf, wo eine bodengestützte Überwachung und Untersuchung vor Ort schwierig oder sogar unmöglich ist.

Glücklicherweise haben Fortschritte in der weltraumgestützten Fernerkundungstechnologie dazu geführt, dass großflächige und qualitativ hochwertige Bilder zur Verfügung stehen, die für verschiedene Anwendungen im Zusammenhang mit Erdbeben genutzt werden können, wie z.B. Identifizierung, Überwachung, Analyse und Vorhersage. Diese effiziente und kostengünstige Technologie ermöglicht die Fernüberwachung und -bewertung des Erdbebenrisikos und kann einen wichtigen Beitrag zum Katastrophenmanagement und zur Schadensbegrenzung leisten. Weltraumgestützte Fernerkundungstechniken sind daher in vielen Ländern unerlässlich geworden, um das Risiko von Erdbeben zu managen und durch Bereitstellung von zuverlässigen nachgelagerten Diensten der Gesellschaft zugute zu kommen. Allerdings erfordert die Erbringung dieser Dienste erhebliche Anstrengungen, um sicherzustellen, dass sie zuverlässig sind.

Für die Einrichtung von langfristigen Datenarchiven und zuverlässigen Analysen sind konsequente und kontinuierliche Multisensor-Fernerkundungstechniken unerlässlich. Dies wird zu einem besseren Verständnis der physikalischen Mechanismen führen, die zur Hanginstabilität beitragen und zu besseren Entscheidungen und effektiven Sanierungsrichtlinien führen. Letztendlich könnte dies die Auswirkungen von Erdbeben auf die Öffentlichkeit verringern. Die vorliegende Dissertation trägt in folgender Weise zu diesen Arbeiten bei:

- Um ein umfassendes Verständnis der weltraumgestützten Fernerkundungstechniken zur Überwachung von Erdbeben zu erlangen, haben wir Multisensormethoden integriert, um den gesamten Prozess der Erdbebedynamik zu überwachen. Unser Ziel war es, die Entwicklung von Erdbeben bei komplexen Kaskadenereignissen durch den Einsatz verschiedener weltraumgestützter Fernerkundungstechniken zu verstehen, zum Beispiel die Vorverformung vor dem katastrophalen Ausfall, die Vorgänge bei einem Mitausfall und die Entwicklung der Hanginstabilität nach einem Ausfall.
- Um die Diskrepanzen zwischen optischen und radarbasierten Fernerkundungstechniken im Weltraum zu überwinden, stellen wir eine Methode vor, die die vierdimensionale (4D) Kinematik von Erdbeben nach dem Ausfall mithilfe eines abklingenden mathematischen Modells beschreibt. Dieser Ansatz ermöglicht es uns, die Spannungsrelaxation für die Dynamik des Erdbebenkörpers nach dem Bruch darzustellen.

Durch den Einsatz dieser Methode können wir die Schwächen der einzelnen Sensoren bei der optischen und radargestützten Bildgebung im Weltraum überwinden.

- Wir bewerteten die Wirksamkeit eines neu entwickelten kleinen dihedralen Eckreflektors für die Überwachung von Erdrutschen. Der Reflektor ist mit auf- und absteigenden Satellitenumlaufbahnen kompatibel und eignet sich für Anwendungen mit hoch- und mittelauflösenden Satellitenbildern. Außerdem sind seine Echos zwar nicht so stark wie die herkömmlicher Reflektoren, aber die Kosten für die neu entwickelten Reflektoren sind geringer und ihre Installation und Wartung ist einfacher. Um diese Einschränkung zu überwinden, schlagen wir eine spezielle Auswahlstrategie vor, die auf einem Wahrscheinlichkeitsmodell zur Identifizierung der Reflektoren in Satellitenbildern basiert.

# Acknowledgements

As I come to the end of my long and memorable Ph.D. journey, I am grateful to many people who have accompanied and supported me physically and mentally. Through this journey, I have encountered various individuals who have joined and left me on this path, while I have experienced countless moments of joy and sadness, success and failure. The landscapes I have witnessed along this road are beautiful and incredible. Meanwhile, the challenges and obstacles I have encountered throughout this journey have pushed me to my limits and beyond, testing my resilience, perseverance, and determination. As I prepare to take my final bow, I am committed to expressing my appreciation to all the individuals who have played a role along my trip.

I am enormously grateful to my supervisor, Professor Mahdi Motagh, for allowing me to pursue my doctoral degree, as well as for his unwavering support throughout my research journey. As an accomplished professor and group leader, he has provided me with invaluable professional insights, widened my horizons, and demonstrated practical team management skills that have made me a proficient researcher and a responsible person. Behind the scenes, he always provides insightful suggestions and critical feedback that can help me to improve my work. Whenever I encounter any questions or issues, he is consistently addressed them in a prompt and efficient manner. I can still remember his encouragement for my first paper and his comments on my latest work. In academic lives, he generously offers his group members opportunities to attend various international conferences and present their researches to the scientific community. In daily lives, he is friendly to organize outdoor activities, gatherings, and social events that help to alleviate the pressure of our research work.

I really appreciate Professor Ingo Neumann and Professor Roberto Tomás Jover for their kindness and for squeezing out their time to be the committee members of my thesis. I want to acknowledge Professor Heipke Christian for organizing the retreat of the Institute of Photography and Information at Leibniz University Hannover, which has provided me with an excellent opportunity to carefully consider and meticulously organize my Ph.D. plans and studies.

I thank all my collaborators, coauthors, and anonymous reviewers for my work. I am profoundly grateful to Professor Tao Li for his invaluable contribution to our collaborative works, as well as for offering excellent satellite data. His comments and insights have greatly improved the quality of our research. Furthermore, his unwavering support for fieldwork has given me great opportunities to conduct my experiments. I sincerely thank Dr. Sigrid Roessner for her invaluable contribution to my research. Her critical and constructive feedback, coupled with her unwavering motivation, has significantly enhanced the quality of my manuscripts and enriched my knowledge. Additionally, I would like to thank Associate Professor Mimi Peng, Associate Professor Chao Zhou, Magdalena Stefanova Vassileva, and Wandu Wang for their kindness, cooperation, valuable scientific guidance, and contributions to my work and the cooperation works. Their assistance allowed me to gain a comprehensive understanding of various fields and aspects related to my research.

I also would like to thank those who offered assistance, suggestions, and kindness, Dr. Mahmud Haghshenas Haghighi, Dr. Jiyuan Hu, Dr. Deying Ma, Binayak Ghosh, and Andreas Piter, for their kind help and instructions, especially at the beginning of my Ph.D. studies. They generously shared their rich knowledge, and offered professional assistance and informative discussions, allowing me to expand my understanding of my research field rapidly.

I want to give special thanks to Sylvia Magnussen for managing IT and computer-related issues that ensure and ease my research life. She is always friendly in helping me overcome my difficulties when using Linux and other technical stuff, which greatly saved my time.

Besides, I am also grateful to the colleagues who shared the same office room with me at GFZ, Shanyu Zhou and Mimi Peng, who supported each other with me in struggling for the doctoral degree. Truly thanks to all friends and new colleagues I met here along the journey: Zhiyuan Wang, Carolina Cañizares, Zelong Guo, Dibakar Kamalini Ritushree, Xiaohang Wang, Shagun Garg, Yufang He, Juanjuan Yu, Haonan Jiang, Dr. Alina Shevchenko. I cherish the time spent with them, whether meeting, discussing, cycling, traveling, hiking, wandering, sharing meals and drinks, or having game nights. Those memories together still serve as a source of inspiration for me when faced with all kinds of challenges.

Most importantly, to conclude, I want to express my sincere gratitude to my family. They had always respected my various decisions, especially when I was in my early 20th and decided to come to Germany for a long period of study. I am grateful to them for always trusting me, keeping in contact with me, and giving me all kinds of help and support, particularly during the challenging pandemic. The shift to a home office brought plenty of difficulties, and I found myself struggling, uncomfortable and depressed at that hard moment. Without their unwavering support, I could barely have completed my Ph.D. studies.



# Contents

<b>List of Abbreviations</b>	<b>xv</b>
<b>1 Introduction</b>	<b>1</b>
1.1 Research Objectives . . . . .	2
1.2 Outline and Structure of Thesis . . . . .	4
<b>2 Theoretical Background</b>	<b>7</b>
2.1 Introduction . . . . .	7
2.2 Glance at Landslide Hazards . . . . .	7
2.2.1 Overview . . . . .	7
2.2.2 Landslide Types . . . . .	8
2.2.2.1 Type of Movement . . . . .	8
2.2.2.2 Material Classification . . . . .	10
2.2.2.3 Landslide Depth . . . . .	11
2.2.3 Landslide Distribution . . . . .	11
2.2.4 Landslide Implications and Measurements . . . . .	11
2.2.5 Slow-moving Landslide . . . . .	13
2.3 Landslide Remote Sensing . . . . .	14
2.3.1 Overview . . . . .	14
2.3.2 Airborne Remote Sensing . . . . .	15
2.3.3 Spaceborne Remote Sensing . . . . .	16
2.4 Spaceborne Optical Imagery . . . . .	17
2.4.1 Overview . . . . .	17
2.4.2 Pixel Offset Tracking (POT) . . . . .	18
2.5 Spaceborne Radar Imagery . . . . .	20
2.5.1 Synthetic Aperture Radar (SAR) Basic . . . . .	20
2.5.1.1 SAR Geometry . . . . .	20
2.5.1.2 SAR Acquisition Mode . . . . .	21
2.5.1.3 SAR Distortion . . . . .	22
2.5.1.4 SAR Mission . . . . .	22
2.5.2 Interferometric SAR (InSAR) . . . . .	23
2.5.2.1 Workflow of InSAR Processing . . . . .	24
2.5.2.2 Coherence and Decorrelation . . . . .	27
2.5.2.3 Topographic and Orbital Errors . . . . .	28
2.5.2.4 Atmospheric Artifacts . . . . .	29
2.5.2.5 Sensitivity of Line-of-sight (LOS) to Slope Motion . . . . .	29
2.5.3 Advanced Multi-temporal InSAR (MT-InSAR) . . . . .	31
2.5.3.1 Scattering Mechanism . . . . .	32
2.5.3.2 Interferogram Stacking . . . . .	33
2.5.3.3 Persistent Scatterer Interferometry (PSI) . . . . .	33
2.5.3.4 Small Baseline Subsets (SBAS) . . . . .	34

2.5.4	Corner Reflector InSAR (CR-InSAR)	35
2.5.4.1	Overview	35
2.5.4.2	Conventional Designs	35
2.5.4.3	Our Experimental Designs	36
2.5.4.4	CR-InSAR Processing	37
<b>3</b>	<b>Methodological Contribution</b>	<b>39</b>
3.1	Challenges in Landslide Monitoring Using Spaceborne Remote Sensing	39
3.2	Proposed Methodology	40
3.2.1	Analytically-based Modeling for Inverse Velocity	40
3.2.2	Identification of Small-scale CR-like Objectives	41
3.2.3	Modeling 4D Slope Instability Dynamics	41
<b>4</b>	<b>Pre- and Co-failure: Slope Instability Monitoring Using Spaceborne Remote Sensing</b>	<b>45</b>
4.1	Abstract	46
4.2	Introduction	46
4.3	Environmental and Geomorphological Settings	48
4.4	Data and Methodology	51
4.4.1	Remote Sensing Optical Images	51
4.4.2	MT-InSAR Analysis Using Sentinel-1 SAR Data	51
4.4.3	Auxiliary Data	52
4.4.4	Inverse-velocity Theory for Anticipating the Time of Failure	53
4.5	Results	54
4.5.1	Horizontal Displacement Based on High-resolution Optical Images	54
4.5.2	MT-InSAR Analysis	55
4.5.3	Influence of Precipitation on the Kinematics of the Landslide	57
4.5.4	INV Results for Anticipating the Time of Failure	60
4.5.5	Comparison of NDVI and Coherence Values	61
4.6	Discussion	62
4.7	Conclusion	66
4.8	Acknowledgements	67
4.9	Supplementary Materials	67
4.9.1	Comparison of River Courses	67
4.9.2	Detailed Parameters of Exploited SAR Data	68
4.9.3	Comparison of Baseline Graphs	69
<b>5</b>	<b>Post-failure: Slope Instability Monitoring Using Artificial Corner Reflectors</b>	<b>71</b>
5.1	Abstract	72
5.2	Introduction	72
5.3	Experiments and Methodology	73
5.3.1	Experimental Design	73
5.3.2	Selection Strategy for CRs	73
5.3.3	Radar Cross-section (RCS)	75
5.3.4	Signal-to-clutter Ratio (SCR)	75
5.3.5	CR-InSAR Processing	76
5.4	Results and Discussion	76

5.5	Conclusion . . . . .	79
5.6	Acknowledgments . . . . .	79
5.7	Supplementary Materials . . . . .	80
5.7.1	Calculation of SCR . . . . .	80
5.7.2	Selection Strategy . . . . .	80
5.7.3	Radar Intensity Map . . . . .	81
5.7.4	Site Photo of Interference Reflector . . . . .	82
<b>6</b>	<b>Post-failure: Characterizing 4D Slope Instability Dynamics</b>	<b>85</b>
6.1	Abstract . . . . .	86
6.2	Introduction . . . . .	86
6.3	Geographical Setting of the Study Area . . . . .	88
6.4	Methodology . . . . .	89
6.4.1	Optical Images Processing . . . . .	89
6.4.2	Multi-temporal InSAR Processing . . . . .	90
6.4.3	Spatiotemporal Independent Component Analysis (ICA) of Dis- placement . . . . .	92
6.4.4	Multi-sensor Integration Modeling . . . . .	93
6.5	Results . . . . .	94
6.5.1	Horizontal Deformation Based on Planet Images . . . . .	94
6.5.2	MT-InSAR Results . . . . .	96
6.5.3	Feature Extraction Using ICA . . . . .	98
6.5.4	4D Deformation Modeling . . . . .	99
6.6	Discussion . . . . .	102
6.6.1	Early Post-failure Deformation from Planet . . . . .	102
6.6.2	Post-failure Kinematics from MT-InSAR . . . . .	103
6.6.3	ICA-based Spatiotemporal Features of Deformation . . . . .	104
6.6.4	Resolving 4D Post-failure Kinematics . . . . .	104
6.7	Conclusion . . . . .	106
6.8	Acknowledgments . . . . .	106
<b>7</b>	<b>Summary and Future Perspectives</b>	<b>107</b>
7.1	Summary . . . . .	107
7.2	Future Perspectives . . . . .	110
	<b>List of Figures</b>	<b>113</b>
	<b>List of Tables</b>	<b>119</b>
	<b>Bibliography</b>	<b>121</b>



# List of Abbreviations

Abbreviation	Description
3D	Three-dimensional.
4D	Four-dimensional.
a.s.l.	Above Sea Level.
ALOS	Advanced Land Observing Satellite.
BRDF	Bidirectional Reflectance Distribution Function.
CHIRPS	Climate Hazards Group InfraRed Precipitation with Station.
CR	Corner Reflector.
CR-InSAR	Corner Reflector Interferometric Synthetic Aperture Radar.
CSK	COSMO-Skymed.
DCR	Dihedral Corner Reflector.
DEM	Digital Elevation Model.
DInSAR	Differential InSAR.
DLR	German Space Agency.
DRR	Disaster Risk Reduction.
DS	Distributed Scatterer.
E-W	East-west.
EHV	Extra High Voltage.
Envisat	Environmental Satellite.
ERS	European Remote Sensing Satellite.
ESA	European Space Agency.
EWS	Early Warning System.
FastICA	Fixed-point Algorithms for Independent Component Analysis.
GACOS	Generic Atmospheric Correction Online Service.
GEE	Google Earth Engine.
GNSS	Global Navigation Satellite System.
GPS	Global Positioning System.
HS	High-resolution Spotlight.

*List of Abbreviations*

<b>Abbreviation</b>	<b>Description</b>
IC	Independent Component.
ICA	Independent Component Analysis.
IGN	French National Institute of Geographic and Forest Information.
InSAR	Interferometric Synthetic Aperture Radar.
INV	Inverse Velocity.
IPC	Identical Point Collection.
ISRO	Indian Space Research Organisation.
IW	Interferometric Wide Swath.
LAMBDA	Least Squares Ambiguity Decorrelation Adjustment.
LIDAR	Light Detection and Ranging.
LOS	Line-of-sight.
MODIS	Moderate-resolution Imaging Spectroradiometer.
MT-InSAR	Multi-temporal InSAR.
N-S	North-south.
N-W	North-west.
NASA	National Aeronautics and Space Administration.
NCC	Normalized Cross-correlation.
NDVI	Normalized Difference Vegetation Index.
NISAR	NASA-ISRO Synthetic Aperture Radar.
PCA	Principal Component Analysis.
POT	Pixel Offset Tracking.
PS	Persistent Scatterer.
PSI	Persistent Scatterer Interferometry.
RCS	Radar Cross-section.
RMSE	Root-mean-square Error.
ROI	Area of Interest.
S1	Sentinel-1.
S2	Sentinel-2.
SAR	Synthetic Aperture Radar.
SBAS	Small Baseline Subset.
SCR	Signal-to-clutter Ratio.
SNR	Signal-to-noise Ratio.
SRTM	Shuttle Radar Topography Mission.
TCR	Trihedral Corner Reflector.

<b>Abbreviation</b>	<b>Description</b>
TEC	Total Electron Content.
TOPS	Terrain Observation with Progressive Scan.
TSX	TerraSAR-X.
U-D	Up-down.
UAV	Unmanned Aerial Vehicle.
WGS84	World Geodetic System 1984.
WLS	Weighted Least Squares.





# 1 Introduction

Landslides represent one of the most prevalent forms of geological disasters all over the world. They often manifest as sudden failures that cause the rapid downslope movement of soil, rocks, and fluids (Lacroix et al., 2020). Unstable slopes can pose a grave threat when they lose their stability, resulting in widespread destruction and catastrophic consequences such as fatalities, damage to critical infrastructure, disruption of agriculture, and significant economic losses.

Therefore, it is essential to monitor the evolution of slope instabilities, which can sometimes be challenging since their mechanism is often complicated, e.g., some of them move rapidly, while others can start with creeping motions, but experience sudden acceleration triggered by heavy precipitation, floods, or seismic activity, culminating in catastrophic failure or avalanche (Lacroix et al., 2020; Debella-Gilo and Kääb, 2011). Just taking China as an example, thousands of landslide disasters occur every year, causing hundreds of fatalities and billions of RMB in direct economic losses (NBSC, 2018). The recent ones, such as the 2017 Mao Xian landslide, the 2018 Baige landslide, and the 2020 Aniangzhai landslide, have caused significant damages and losses, receiving widespread attention from worldwide scholars (Habumugisha et al., 2022; Zhao et al., 2021; Zhang et al., 2019a,b; Intrieri et al., 2018; Fan et al., 2017). Moreover, increased urbanization and anthropogenic activities have made landslides occur more frequently. Especially when landslides coincide or are in close proximity to other catastrophic events, such as dam failure, the impact of slope failure would be significantly magnified. An example is that in 1963, a massive mass slid into the newly built Vajont reservoir in northern Italy, creating a huge wave that broke through the dam and killed approximately 2,000 people (Genevois and Ghirotti, 2005).

We need to improve our understanding for monitoring of landslide hazards regarding cascading events in order to establish effective early warning systems (EWSs) and achieve an overall reduction and mitigation of their inherent risks. Moreover, analyzing the potential impact of anthropogenic activities on the local geological environment and susceptibility to natural hazards, as well as the cascading events and their triggers, are particularly useful for controlling or predicting such events. Therefore, the methods of landslide monitoring should meet at least the following requirements: adequate area coverage and temporal sampling capability, adequate measurement accuracy concerning the speed of various processes, and cost-effective (Xia et al., 2022b).

In this regard, ground-based methods with field measurements are essential for detecting, studying and understanding complex processes of landslides, such as leveling, extensometry, and continuous Global Navigation Satellite System (GNSS). However, for landslide monitoring, such methods are time-consuming, expensive, and challenging to establish and implement in mountainous and remote areas. In contrast, spaceborne optical and radar remote sensing techniques have the potential to significantly enhance landslide monitoring by fulfilling the mentioned requirements. Over the past few decades, satellite remote sensing has been exploited extensively and effectively in monitoring and assessing ground instabilities, providing accurate displacement measurements over large regions, and

can be comprehensively integrated into a multidisciplinary disaster risk reduction (DRR) framework and the investigation of cascading events.

In optical remote sensing, pixel offset tracking (POT) techniques utilizing the normalized cross-correlation (NCC) algorithms have been widely implemented due to their simplicity and reliability in assessing slope instabilities. Optical satellite imagery has become increasingly accessible in recent years and is easily understood and managed by non-experts. However, several factors, such as measurement precision, alignment error between relevant image pairs, and different interpolation factors, can significantly impact the accuracy of the deformation maps derived through the NCC. It is also challenging to acquire cloud-free images during catastrophic failures as sliding occurs more frequently in mountainous regions and during the rainy seasons. Hence, optical remote sensing has both strengths and weaknesses when monitoring landslides.

Alternatively, synthetic aperture radar (SAR) and interferometric SAR (InSAR) offer new opportunities to systematically identify and monitor landslide disasters on a regional or even continental scale, which can be implemented regardless of sunlight or weather conditions. The growing accessibility of SAR data and the advanced Multi-temporal InSAR (MT-InSAR) techniques have been exploited and developed to address the limitations of traditional InSAR techniques. MT-InSAR approaches, e.g., persistent scatterer interferometry (PSI) and small baseline subset (SBAS) techniques, involve searching a stack of SAR data to locate persistent scatterers (PSs) or distributed scatterers (DSs) and connecting their interferometric phase over time to track the displacement history of each pixel (Hooper et al., 2007, 2004; Ferretti et al., 2001). In order to minimize errors and extract accurate displacement time series, MT-InSAR methods also exploited temporal and spatial filtering or external information as supplement (Hooper et al., 2012). Over the past few decades, a significantly growing number of spaceborne SAR missions have already been implemented with sensors of various wavelengths, orbits and repeat cycles, and different temporal and spatial resolutions. However, SAR sensors still have some limitations when monitoring slope instability, e.g., they are more sensitive to displacement in line-of-sight (LOS) directions. Therefore, new methods are needed to efficiently deal with the various processes of ground motion and extract essential information from multivariate time series analysis.

### 1.1 Research Objectives

This thesis comprehensively exploits spaceborne remote sensing geodetic measurements to improve the understanding of landslide hazards. The research is conducted from three main perspectives. The first perspective is monitoring, which involves precise measurements of landslide deformation at a specific location, providing insights into the slope kinematics and the evolution of the entire life cycle of landslide process. The second perspective is the experiment, which involves examining ground auxiliaries for remote sensing measurements, i.e., newly designed artificial corner reflectors (CRs) are evaluated for their efficacy in remote sensing measurements. The third perspective is modeling, which integrates multi-sensor spaceborne remote sensing imagery to characterize landslide's four-dimensional (4D) deformation dynamics. For the three perspectives, the 2020 catastrophic failure of a deep-seated Aniangzhai landslide in Danba County, Southwest China, is comprehensively exploited and analyzed.

The first perspective of this study involves monitoring and measuring the precursory and co-failure displacements of the Aniangzhai landslide. The studies employ optical and SAR remote sensing techniques to derive slope displacement from various remote sensing datasets and further establish the relationship between landslides and the underlying driving mechanisms.

The second perspective of this study involves the experimentation and examination of the newly designed dihedral corner reflectors (DCRs) in SAR remote sensing. First of all, a general selection strategy is proposed to identify the new DCRs in different SAR images based on the various properties and power variations in pixels that arise from their installation. Then, the performance and efficacy of these reflectors are evaluated and compared using both high-resolution and medium-resolution satellite imagery to measure slope instability.

The third perspective of this study involves integrating and modeling satellite optical and SAR remote sensing techniques using the time series decomposition method and a mathematical relaxation model. We propose a framework that allows for the assessment of complete 4D spatiotemporal patterns of post-failure slope evolution. This framework leverages the advantages of both optical and SAR sensors to overcome and mitigate their unique limitations. Specifically, the feature extraction technique identifies relevant features from optical and SAR images, while the relaxation model facilitates the spatiotemporal modeling of slope instability.

This thesis discusses several challenges in landslide monitoring using spaceborne remote sensing techniques and the solutions to tackle them. One major challenge is the various types of landslides and observation restrictions from satellite remote sensing sensors. The methodology for combining and integrating different sensors for monitoring complicated processes is assessed in this thesis. Furthermore, the effectiveness and performances of auxiliary for spaceborne remote sensing are investigated to be suitable for densely vegetated slopes. Other significant challenges are interpreting the InSAR time series, particularly with different time series of triggering factors. The time series decomposition analysis can contribute to a better understanding and systematic analyze landslide kinematics and the related triggering factors during cascading events. In summary, this thesis addresses the main research question as follows:

1. Question: What is the most important role of spaceborne remote sensing technology in identifying, monitoring, predicting and managing landslide hazards? What are the advantages of spaceborne remote sensing compared to other geodetic methodologies?
2. Question: What is the performance of spaceborne remote sensing techniques in monitoring slope instability caused by different triggering factors and procedures? How can these triggers be integrated into landslide analysis for the causality, mechanism and anticipation during the complex cascading event?
3. Question: What is the difference between spaceborne optical and SAR remote sensing sensors in monitoring local and regional scale slope instability? What are their advantages and limitations? To what extent can they be integrated to address and highlight the deformation at different scales?
4. Question: How and to what extent can landslide monitoring be improved using auxiliaries like artificial corner reflectors? What is the better strategy for designing the reflectors and selection in imagery?

### 1.2 Outline and Structure of Thesis

Chapter 1 gives a short introduction to this thesis, including the research objectives, research perspectives, and research questions; the outline and structure of this thesis are also introduced.

Chapter 2 presents a brief overview of the landslide hazards, including landslide types, distributions, implications and measurements, as well as slow-moving landslide. This chapter also explicates landslide remote sensing and various landslide remote sensing techniques, including the fundamental principles of optical remote sensing utilizing the NCC method, SAR imaging geometry, and InSAR processing flow. It also provides insight into the various phase components and errors associated with InSAR. This chapter further outlines the advanced MT-InSAR and Corner Reflector InSAR (CR-InSAR) approaches employed in this thesis.

Chapter 3 provides the methodological contribution of this thesis in landslide remote sensing using satellite imagery, including the challenges and motivations in landslide monitoring, mapping and prediction. Our proposed methodologies and frameworks involve analytically-based modeling to improve the interpretation of time series of remote sensing observations, the identification strategy of small-scale CR-like objectives using a probability model, and a framework to model 4D post-failure instability dynamics integrating spaceborne optical and SAR imagery.

In Chapter 4, cm-scale precursory displacement of a localized catastrophic failure in Aniangzhai, Southwest China, is estimated using different MT-InSAR analyses. This study indicates that the landslide was active long before the catastrophic failure in June 2020. Furthermore, this study demonstrates the potential of spaceborne optical and SAR remote sensing data for a comprehensive analysis of an ancient landslide that has been destabilized and reactivated as a result of a series of complex cascading events. This chapter has been published in *Landslides* (Xia et al., 2022b).

In Chapter 5, the performance of a newly designed small DCR for monitoring post-failure creep has been investigated and evaluated. Both high-resolution TerraSAR-X (TSX) data and medium-resolution Sentinel-1 (S1) SAR images are exploited and compared. At the same time, we propose a strategy aiming to identify new DCRs in various SAR images through a probability test by taking different properties and power variations present in pixels resulting from their installation. This strategy can be adopted as a general selection approach for detecting artificial CRs and similar CR-like objects. This chapter has been published in *IEEE Geoscience and Remote Sensing Letters* (Xia et al., 2022a).

Chapter 6 introduces a proposed framework integrating satellite optical and SAR remote sensing techniques. Feature extraction methods using independent component analysis (ICA) and a mathematical relaxation model can help to find common deformation components and to assess the complete 4D spatiotemporal patterns of post-failure slope evolution. With our proposed methodology, the constraints of individual remote sensing sensors are mitigated and overcome in monitoring complicated landslide dynamics. This chapter has been published in *ISPRS Journal of Photogrammetry and Remote Sensing* (Xia et al., 2023).

In the end, Chapter 7 serves as the conclusion of this dissertation and provides insight into potential future research directions about satellite-based landslide remote sensing based on this thesis.

The presented thesis is a cumulative dissertation, wherein Chapters 4–6 comprise individual research studies previously published in peer-reviewed scientific journals in their original form, with adjustments made for formatting and referencing. It should be noted that Chapters 4–6 are based on research studies that were led by the author of this thesis. The references for these studies are compiled at the end of the thesis.



## 2 Theoretical Background

### 2.1 Introduction

This chapter outlines the basics of landslide hazards, landslide remote sensing, spaceborne optical and SAR imagery.

- Section 2.2 introduces the landslide hazard, landslide glossary, various landslide types, landslide distribution worldwide, landslide implication, the conventional measurement to mitigate the landslide hazard, and slow-moving landslide.
- Section 2.3 explains the landslide remote sensing, application categories, and various remote sensing techniques for landslide monitoring, especially the airborne and spaceborne remote sensing techniques for landslide monitoring and mapping. Some applications are introduced as well, such as detecting and mapping landslides for early warning or deriving landslide inventories.
- Section 2.4 begins with an overview of the evolution of satellite-based optical remote sensing techniques, followed by a detailed explanation of the POT method, which utilizes NCC algorithms to detect and measure land surface deformation accurately.
- Section 2.5 introduces spaceborne SAR imaging, including different acquisition modes, potential image distortions, and a summary of the various SAR satellite missions historically and currently in operation. Then the workflow of conventional differential InSAR (DInSAR) is explained to measure surface displacement. The potential errors, sensitivity of InSAR measurements, and advanced MT-InSAR techniques are also explained. Lastly, numerous applications of SAR remote sensing techniques in landslide monitoring are introduced.

### 2.2 Glance at Landslide Hazards

#### 2.2.1 Overview

As concentrations of greenhouse gases continue to rise, the effects of climate change, specifically global warming, will intensify and increase the frequency and magnitude of geological hazards, such as landslide hazards (Gariano and Guzzetti, 2016). Furthermore, as the world's population grows, non-renewable resources are depleted, the environment experiences degradation, and human expansion encroaches on more habitats, people will be increasingly exposed to geological hazards (Petley, 2012).

Among these geological hazards, landslides have a profound impact on various regions and populations as they are one of the most common and most destructive hazards. The term “landslide” is commonly used in geological hazard investigations to describe the downward and outward movement of materials, such as rock, earth, artificial fill, or a

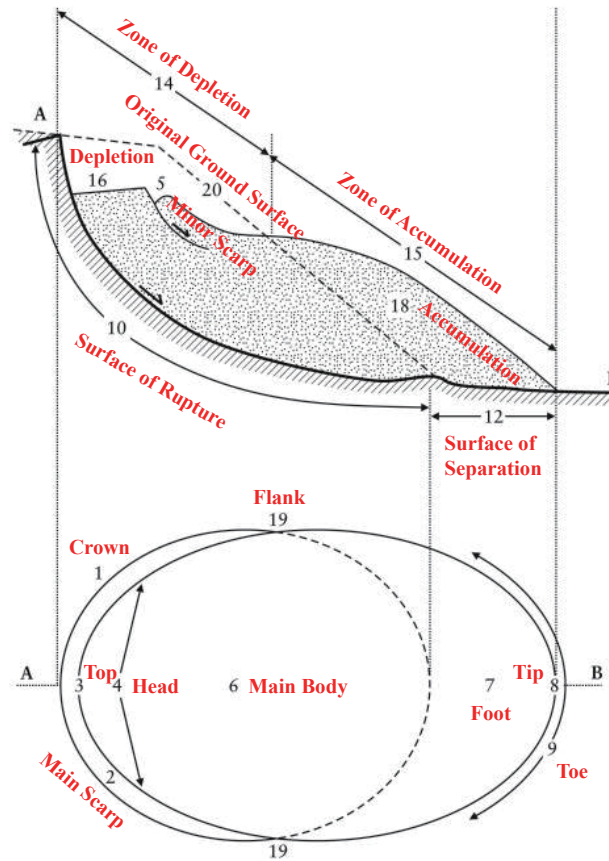


**Figure 2.1:** Terminology of landslide glossary (Source: adapted by Cooper et al. (2007)).

combination of these (Guzzetti et al., 2012). Various factors can trigger landslides, including heavy precipitation, earthquakes, snowmelt, volcanic eruptions, disturbances in vegetation cover (e.g., wildfires and logging), terrain damage (e.g., reservoir storage and road construction), ground shaking, and human activities such as deforestation and construction. Figure 2.1 demonstrates the terminology often used for landslides.

### 2.2.2 Landslide Types

Landslides encompass a range of complexities and diverse types, spanning from creeping movements that progress at a rate of millimeters per year, to catastrophic failures that occur at speeds of several meters per second (Lacroix et al., 2020). Consequently, there are different ways to classify landslide hazards. As revealed by analysis conducted by Reichenbach et al. (2018) of approximately 400 landslide-related articles, landslides could be grouped into three general classes, as demonstrated in Figure 2.2.

#### 2.2.2.1 Type of Movement

Based on landslide movements, landslides could be categorized into the following basic types (Highland et al., 2008), which are revealed in Figure 2.3 and Figure 2.4:

- **Fall:** The falling process is initiated by separating soil, rock, or both, from a steep slope where minimal or no shear displacement occurs. Subsequently, the loose ma-



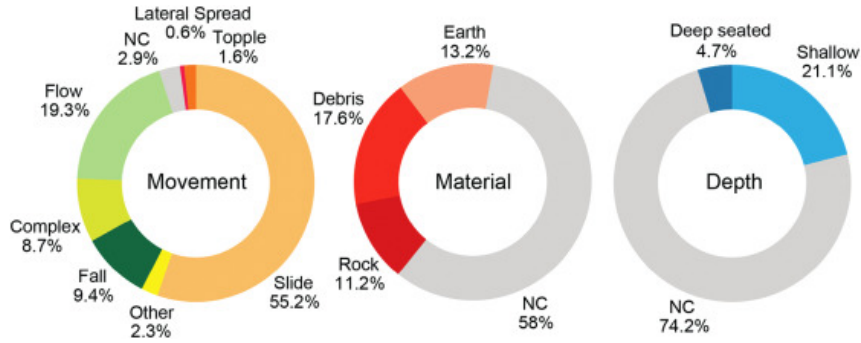


**Figure 2.2:** The diagram features three rings, each representing different types of landslides, which comes from statistical analysis of 383 landslide-related articles (Source: Reichenbach et al. (2018)). The left ring depicts eight classes of landslide movements, while the center ring displays four classes of landslide materials. The right ring shows two classes of estimated landslide depth, as described in the studied literature database. In all three rings, NC denotes non-classified.

terial descends primarily by either falling, bouncing, or rolling. A typical example is rockfall.

- **Topple:** The process of a topple occurs when a mass rotates out of a slope around an axis or point below the center of gravity of the displaced mass. The force driving the topple is sometimes the weight of the material uphill from the displaced mass, while other times, it is due to water or ice present in the cracks of the mass. Topples can involve either rock debris or earth materials. They can also be complex and composite.
- **Slide:** The process of a slide refers to the downward movement of soil or mass on surfaces of rupture or relatively thin zones of intense shear strain. The initial movement does not occur uniformly over the entire rupture surface. Instead, it starts in a localized area of failure and then expands to displace a larger volume of material. Typical examples are rotational landslide (the mass rotates parallel to the slope contour axis) and translational landslide (the mass moves outward/downward on a flat surface with minimal rotation or backward tilt).
- **Spread:** The cohesive soil or rock mass spread process can occur due to its extension and subsequent subsidence into the softer underlying material. The flow and extrusion of the softer material may cause this. Liquefaction can also contribute to the spread. Typical examples are block spreads, liquefaction spreads, or lateral spreads.
- **Flow:** The flow process refers to a continuous movement throughout space. It is characterized by short-lived shear surfaces, which are closely spaced and typically not preserved over time. The component velocities within the displacing mass of a flow are similar to those observed in a viscous liquid. The transition from sliding to flowing is often gradual and depends on water content, mobility, and movement evolution. Examples are debris flows, lahars (volcanic debris flows), and earth flows.

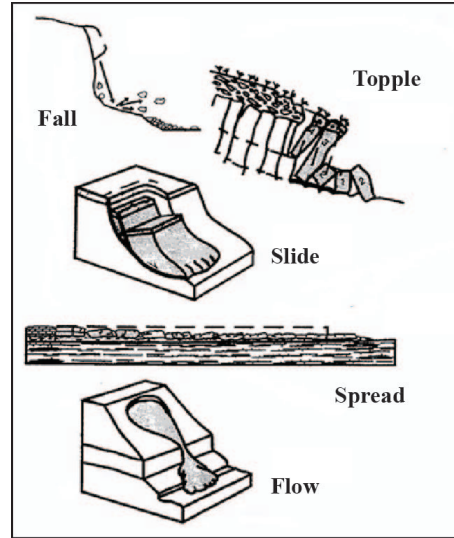


**Figure 2.3:** Landslide types according to different movements (Source: adapted by Hungr et al. (2014) and Cruden and Varnes (1996)).

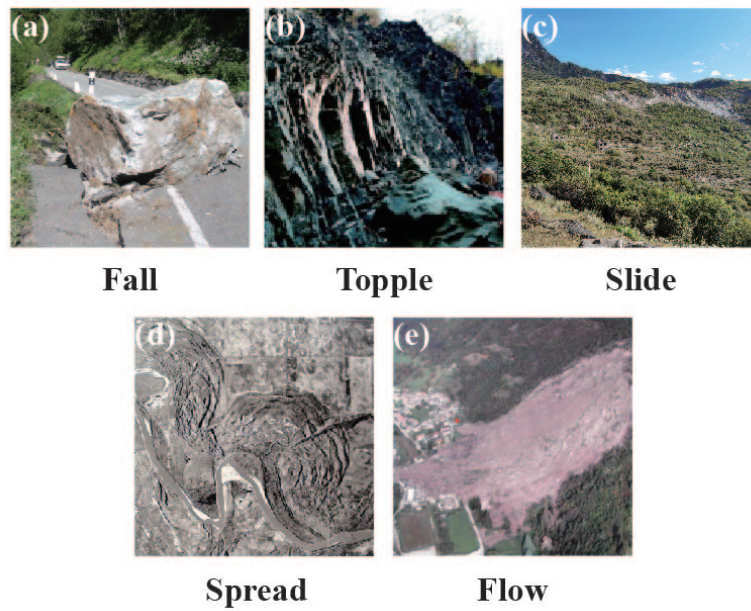


**Figure 2.4:** Examples of landslide types revealed by photos according to different movements, i.e., (a) fall, (b) topple, (c) slide, (d) spread, and (e) flow (Source: adapted by Regmi et al. (2014), Hungr et al. (2014), and Michoud et al. (2012)).

#### 2.2.2.2 Material Classification

Based on landslide materials, landslides could be categorized into the following classes (Causes, 2001):

- **Rock:** Rock refers to any type of consolidated geological material, such as solid bedrock or large boulders.

- **Earth:** Earth refers to any unconsolidated soil or regolith. This can include sand, silt, clay, and gravel.
- **Debris:** Debris refers to a mixture of rock and earth materials and any other materials present in the landslide, such as vegetation, buildings, or other debris.

Regarding landslide classification, the distinction between rock, earth, and debris is important because it can help determine the cause of the landslide, the potential impact on infrastructure and communities, and the appropriate mitigation strategies. For example, rock falls may be more common in mountainous regions with steep slopes, while earth slides may be more common in areas with softer, more easily erodible soils. Debris flows, on the other hand, are typically associated with heavy rainfall or other forms of intense precipitation, and can be particularly destructive due to the high volume of material involved.

### 2.2.2.3 Landslide Depth

Based on landslide depth, landslides could be categorized into the following classes (Duman et al., 2005):

- **Shallow:** A shallow landslide (depth < 5m) is a sort of landslide that appears in the upper layer of the soil or weathered rock. It is generally triggered by rainfall or other external factors and is typically characterized by a small movement area. The slope failure occurs at a depth less than or equal to the soil layer's thickness or the weathered rock's depth.
- **Deep-seated:** A deep-seated landslide (depth > 5m) involves a much larger volume of soil or rock and extends to much greater depths. It typically occurs in areas with complex geology, such as distinct rock layers or fault zones. Deep-seated landslides are generally triggered by internal factors such as changes in groundwater levels or the weathering and erosion of the underlying rock. These landslides can be slow-moving, persistent, and may continue for years or even decades.

### 2.2.3 Landslide Distribution

The occurrence of landslides exhibits a distinct spatial variability (Figure 2.5), with regions of heightened incidence observed in Asia, Turkey, Iran, the European Alps, Central America, the Caribbean islands, South America, and East Africa (Froude and Petley, 2018). Notably, the highest number of landslides are concentrated in Asia, accounting for 75% of the actual events. Remarkably, the Himalayan Arc, states across southeastern China, India, and neighboring countries such as Laos, Bangladesh, Myanmar, and southwards on islands comprising Indonesia and the Philippines, report substantial landslides (Froude and Petley, 2018).

### 2.2.4 Landslide Implications and Measurements

Landslides have severe implications for human life, property, and infrastructure. In areas where landslides are prevalent, there are increased risks of injuries, fatalities, and property loss. In 1963, a striking illustration of the devastating force of landslides was witnessed as an enormous mass, comprising 270 million cubic meters, plunged into the newly built

## 2 Theoretical Background

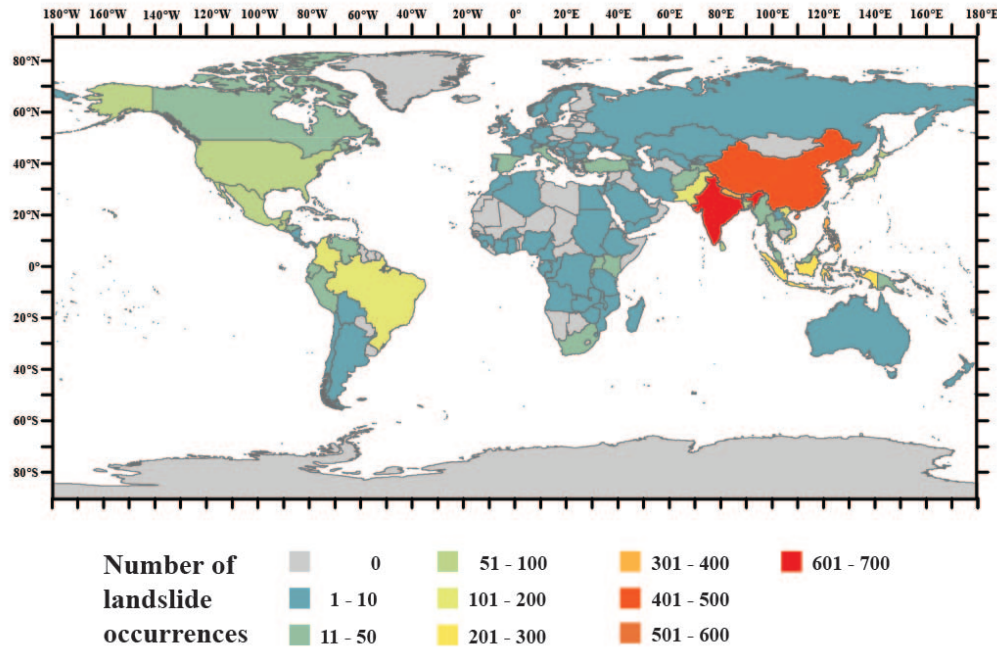


**Figure 2.5:** The count and distribution of fatal landslides that were not triggered by seismic activity between 2004 and 2016, categorized by different countries (Source: adapted by Froude and Petley (2018)).

Vajont Reservoir in northern Italy. This incident produced an immense wave that breached the dam, causing the loss of approximately 2,000 lives (Genevois and Ghirotti, 2005). As another example, the recent landslide that occurred in the province of Guizhou, China, resulted in the death of 14 people and the relocation of over 1000 residents (Chen et al., 2022). Numerous landslide disasters, amounting to thousands, transpire each year, leading to hundreds of fatalities and direct economic losses in the billions of RMB within China (NBSC, 2018). Similarly, in the United States, landslides cause billions of dollars in damages yearly, with California reporting the highest number of landslides in the country (Causess, 2001).

The impacts of landslides are not limited to human life and property. They also have environmental implications, such as soil erosion, degradation of ecosystems, and alteration of natural drainage systems (Montanarella, 2007). Landslides can lead to the loss of vegetation cover and soil nutrients, affecting the productivity of land and causing a decline in agricultural yields (Zuazo and Pleguezuelo, 2009; Smyth and Royle, 2000). Moreover, landslides can lead to the contamination of water resources, as debris and sediments can clog rivers, streams, and other water bodies, disrupting aquatic ecosystems, and contaminating drinking water (Hancock, 2002).

To mitigate the impacts of landslides, it is essential to understand the underlying causes and risk factors associated with landslides. Researchers have identified several factors that contribute to the occurrence of landslides, such as the geological and physical characteristics of slopes, land-use changes, and climatic conditions. Therefore, managing landslides involves a combination of preventive and response measures. Preventive measures include land-use planning, slope stabilization, and the implementation of EWSs to alert residents of imminent landslides (Lacasse et al., 2009). Response measures include search and rescue

operations, emergency shelter, and providing relief supplies and medical assistance (Twigg and Mosel, 2017).

In addition, technological advancements have been instrumental in predicting and assessing the risks of landslides. The technical means must meet specific requirements for effective EWSs and monitoring of landslide disasters. These include adequate regional coverage and temporal sampling capacity, precise measuring accuracy related to the speed of the monitored processes, and cost-effectiveness (Xia et al., 2022b). However, implementing ground-based methods, like continuous GNSS, for landslide monitoring in mountainous and remote areas can sometimes be challenging (Akbarimehr et al., 2013). Instead, space-borne remote sensing holds great promise for driving innovation in the detection, monitoring, and assessment of landslide hazards on a large scale. Integrating these techniques into a multidisciplinary DRR framework can be immensely valuable.

### 2.2.5 Slow-moving Landslide

The term “slow-moving landslide” describes various landslides, at velocities ranging from several mm/year to 100 m/year (from very slow to intermediate rates), including those that flow, creep, topple, and slide (Lacroix et al., 2020; Hungr et al., 2014). Slow-moving landslides occur worldwide, often in areas with weak mechanical properties, clay and rock formations, and high seasonal precipitation. These landslides exhibit non-uniform spatial and temporal movement and are often deep-seated with complex subsurface hydrological systems (Krzeminska et al., 2013; Simoni et al., 2013; Coe et al., 2009).

The roles of slow-moving landslides are listed as follows:

- Slow-moving landslides play an essential role in controlling the evolution of mountain landscapes, causing significant erosion (Simoni et al., 2013; Mackey and Roering, 2011).
- While these slow-moving landslides rarely claim lives (Mansour et al., 2011), they can cause significant damage to the lives of local communities by damaging human infrastructure and agriculture, as shown in Figure 2.6. Therefore, local communities must adapt to coexist with landslides or relocate to new areas.
- Sometimes slow-moving landslides can result in catastrophic failure, accelerating rapidly, and transforming into fast-moving landslides, with rocks, soil, and liquids moving at speeds approaching tens of meters per second, causing numerous casualties and property losses.

Although it is difficult to monitor catastrophic landslides in real-time, non-catastrophic slow-moving landslides, provide an excellent opportunity to study landslide processes, which can move downhill for several months or even longer for decades (Palmer, 2017). The continuous and long-term movement of slow-moving landslides provides a unique opportunity to study the process and mechanism of landslides. However, constraining the mechanisms that control slope failure remains challenging.

Lacroix et al. (2020) believes that utilizing remote sensing data for retrospective analysis of numerous case studies can provide a more reasonable understanding of the physical aspects of landslide damage processes. Moreover, creeping ground movement is often identified as a precursor deformation signal before catastrophic landslides (Carlà et al., 2019; Handwerger et al., 2019; Federico et al., 2012; Hendron Jr and Patton, 1985).





**Figure 2.6:** (a) Example for one of the largest slow-moving landslides in China, i.e., the Huangtupo landslide, with annual displacement rates of around 10–20 mm/year. (b) Examples of the potential damages for the slow-moving Huangtupo landslides. Note that north arrows approximately indicate the downhill direction. (Source: adapted by Wang et al. (2018) and Tomás et al. (2014).)

## 2.3 Landslide Remote Sensing

### 2.3.1 Overview

Landslide remote sensing refers to detecting, monitoring and assessing landslides and their associated environmental factors using remote sensing techniques (Mantovani et al., 1996), such as spaceborne and airborne remote sensing. Through remote sensing, large-scale, high-resolution surface information and various datasets, such as topography and landforms, can be obtained, providing essential support for landslide research and response.

Remote sensing techniques offer a robust approach for investigating landslides, with applications typically classified into three categories (Scaioni et al., 2014). While the distinctions between them may be unclear at times, their boundaries can often be ambiguous:

- The first category involves techniques for identifying landslides, such as mapping past or present slope failures.
- The second category involves techniques for landslide monitoring, encompassing ground deformation measurements and analyzing changes over time, such as variations in land use or vegetation cover.
- The third category encompasses methods for analyzing and predicting landslide hazards.

There are various techniques to identify landslides, including ground-based and remote sensing techniques, e.g., leveling, GNSS, photogrammetry, three-dimensional (3D) laser scanners, radar, and so on. Various sensors can be installed on spaceborne or airborne platforms, such as satellites, drones, helicopters, or stationary installations before the landslide. Moreover, landslide remote sensing have significantly advanced in recent years, enabling the estimation of surface displacements.

On the other hand, monitoring landslide movement helps people better understand evolution process of unstable slopes, the evolution of their morphological features over time, and how external forces such as precipitation and groundwater level changes control landslide movement (Hu et al., 2019), which play a crucial role in landslide hazards prevention and control. Moreover, precisely measuring a landslide’s geometry and mechanical characteristics relies on accurately determining the surface displacement field parameter (Delacourt et al., 2007). Displacement time series of landslides can also provide vital information for early landslide warning (Intrieri et al., 2018).

Scholars must select the appropriate combination of techniques and data to achieve the study’s objectives and account for the landslide’s distinctive characteristics. These techniques vary in resolution, accuracy, coverage surface, and revisit times. Unmanned aerial vehicles (UAVs), cameras, and light detection and ranging (LIDAR) are examples of adaptable platforms and sensors that provide highly accurate 3D data with a high resolution, suitable for accurate scientific and operational applications (Delacourt et al., 2007). However, they are unsuitable for large-scale monitoring and mapping in mountainous areas. In mountainous areas, scientific investigations typically employ radar satellite data processed via differential interferometry or advanced interferometry methods due to application constraints (Wasowski and Bovenga, 2014). Alternatively, optical satellite and aerial imagery can provide high-resolution data with detailed features for scientific research, although it is susceptible to atmospheric conditions. In general, landslide remote sensing methodologies have considerably improved the ability to quantify surface displacement fields of landslides, which has enhanced our comprehension of their geometry and mechanical properties.

### 2.3.2 Airborne Remote Sensing

Airborne imagery captured by cameras can be employed for scientific and hazard assessment of landslides, although the quality of the image archive depends on the specific landslide cases (Lissak et al., 2020). Furthermore, processing such images requires suitable

## 2 Theoretical Background

atmospheric and lighting conditions. Data acquired under poor conditions can only be used for qualitative analysis if a digital elevation model (DEM) is available. In contrast, photogrammetry laser scanning is a highly versatile technique that allows for observing landslide velocities over varying ranges (Kenner et al., 2014). However, due to the limited viewing angle, mosaicking of data is necessary to cover a significant surface area (Kenner et al., 2014). In addition, global interpretation of mass movement data is difficult due to the high spatial resolution of the technique, which necessitates further development in data processing (Delacourt et al., 2007).

Aerial imagery offers a highly advantageous data archive with a resolution of close to one meter (Fritz et al., 2013; Delacourt et al., 2007). For instance, the French territory has an aerial photograph archive from successive surveys dating back to 1937 under the responsibility of the French National Institute of Geographic and Forest Information (IGN) (Delacourt et al., 2007). In such cases, even with images characterized by low radiometric dynamics, georeferenced DEMs can be created with a resolution of one meter and relative accuracy better than one meter. The corresponding orthophoto is also constructed with a resolution of one meter, enabling the estimation of a 3D displacement field with accuracy at the meter level, even in the worst-case scenario. Besides, numerous prior studies have utilized POT techniques to obtain the horizontal ground displacement of landslides (Lucieer et al., 2014; Delacourt et al., 2004; Kääb, 2002). However, the main limitation of this method is its low temporal resolution, with specialized missions being an expensive solution to improve it.

### 2.3.3 Spaceborne Remote Sensing

Spaceborne optical remote sensing has emerged as a valuable tool for landslide monitoring, offering a means of capturing detailed imagery and data regularly and over large areas. Studies have investigated spaceborne optical remote sensing for landslide monitoring, demonstrating its effectiveness in detecting and mapping landslide occurrences, characterizing the features of landslide events, and monitoring the evolution of landslides over time (Casagli et al., 2017; Frodella et al., 2017). Such imagery can detect changes in land surface features, such as slope, vegetation cover, and topography, that may indicate the occurrence of landslides. In addition, scholars have used spaceborne optical remote sensing to assess the susceptibility of different regions to landslides based on factors such as terrain characteristics, geology, and rainfall patterns (Shahabi and Hashim, 2015; Pradhan, 2010). This approach can provide valuable information for land-use planning and hazard mitigation efforts, such as identifying areas that require slope stabilization measures or evacuation plans.

Over the past few decades, scholars have used spaceborne optical imagery to map landslides in remote and inaccessible areas, where traditional ground-based monitoring methods are challenging to implement (Ji et al., 2020; Amatya et al., 2019; Casagli et al., 2017; Lissak et al., 2020; Casagli et al., 2017; Frodella et al., 2017; Scaioni et al., 2014). Due to the simplicity and reliability, an increasing number of studies have adopted the POT techniques to monitor landslide disasters, exploiting the spaceborne optical imagery. For instance, horizontal deformation can be obtained using the NCC to evaluate the kinematic properties of landslides (Provost et al., 2022; Dille et al., 2021; Xiong et al., 2020; Stumpf et al., 2017; Debella-Gilo and Kääb, 2011; Delacourt et al., 2009; Leprince et al., 2008; Delacourt et al., 2004; Kääb, 2002). Moreover, automated and semi-automated approaches utilizing time series of multi-sensor spaceborne optical images have already been developed



to create multi-temporal inventories by identifying landslide areas based on variation in vegetation cover (Yang et al., 2019; Behling et al., 2016). Besides, the applicability of the NCC method has been extensively examined by researchers such as Debella-Gilo and Kääb (2011) and Delacourt et al. (2004). Their studies have assessed the method’s sensitivities to various factors, including inherent image noise, errors induced by rotation and shear between image pairs, and inaccuracies in image orthorectification. Despite these challenges, optical imagery can still effectively monitor substantial movements.

On the other hand, SAR and InSAR techniques, a microwave remote sensing technique that offers another opportunity to monitor subtle deformations at a large scale, have played an increasingly important role in landslide identification. InSAR can provide a unique perspective for landslide research by its ability to acquire spatial and temporal surface deformation with high accuracy and derive historical deformation using archived data (Liu et al., 2020). In addition, the interpretation and modeling of landslide mechanisms can provide insight into the landslide damage process and essential references for preventing and controlling similar landslide cases (Hu et al., 2020; Handwerger et al., 2019).

Over the past few decades, InSAR techniques have been widely applied to support the systematic identifying and monitoring of unstable slopes over extensive and regional-scale regions, as well as the exploitation of early warning of landslide hazards (Festa et al., 2022; Garg et al., 2022; Hu et al., 2022; Zhou et al., 2022b; Tomás et al., 2019; Motagh et al., 2017, 2013; Bianchini et al., 2013; Herrera et al., 2013; Colesanti and Wasowski, 2006). The C-band S1 satellite has provided a substantial increase in the number of available images since its launch in 2014, which has led to a growing interest among academics in utilizing InSAR for monitoring slope instability dynamics (Festa et al., 2022; Dai et al., 2020; Dini et al., 2020; Tomás et al., 2019; Intrieri et al., 2018; Dai et al., 2016; Barra et al., 2016; Feng et al., 2015). Meanwhile, the development of the high-resolution X-band TSX mission and COSMO-SkyMed (CSK) mission have made InSAR techniques even more reliable and promising in low coherence areas (Xia et al., 2022a; Di Martire et al., 2018; Singleton et al., 2014; Bovenga et al., 2014; Motagh et al., 2013). Moreover, L-band SAR sensors contain better penetration capability and reveal improved performance in monitoring the landslides over densely vegetated regions (Schlögel et al., 2015; Zhao et al., 2012). Besides, advanced MT-InSAR methods offer new opportunities to better evaluate subtle changes in landslide creep rates with centimeter to millimeter level precision in response to external triggering factors (Zhou et al., 2022a; Hu et al., 2020; Teshebaeva et al., 2015; Tomás et al., 2016, 2014; Motagh et al., 2013).

## 2.4 Spaceborne Optical Imagery

### 2.4.1 Overview

Satellite-based optical remote sensing has significantly developed since the first Earth observation satellite, Landsat-1, was launched in 1972 (Maul and Gordon, 1975). Initially, remote sensing was limited to data collection in visible and near-infrared bands. However, technological advancements in sensor design and calibration have led to the development of sensors that can collect data in multiple spectral bands, including the electromagnetic spectrum’s thermal infrared and microwave.

The development of satellite optical remote sensing techniques has resulted in improved spatial and spectral resolution and increased temporal coverage of the available data. The

launch of high-resolution optical sensors such as QuickBird, WorldView, PlanetScope and Pleiades has enabled the capture of fine-scale details on the Earth's surface. In addition, the development of multi-spectral and hyper-spectral sensors has enabled the identification of materials and features based on spectral signatures.

With the development of big data and cloud computing, spaceborne optical remote sensing data can now be processed and analyzed more efficiently. This has led to a wide range of applications, including determining land use and mapping land cover, crop monitoring, pollution detection, disaster management, and urban planning (Zhou et al., 2022c, 2021; Mahdianpari et al., 2018; Joshi et al., 2016; Inglada et al., 2015; Hall et al., 2002). The evolution of spaceborne optical remote sensing techniques has generally renewed our understanding of the Earth's surface and its processes.

### 2.4.2 Pixel Offset Tracking (POT)

POT technique utilizing the NCC algorithm has gained widespread use in the field of optical remote sensing for monitoring horizontal displacement due to its simplicity and reliability (Paul et al., 2015; Debella-Gilo and Kääb, 2011; Delacourt et al., 2004). In addition, correlation methods are popular for determining offsets because they can achieve sub-pixel accuracy, particularly when the displacement field can be locally estimated by a smoothly varying translation spanning multiple pixels (Hu et al., 2014; Yoo and Han, 2009; Michel et al., 1999). The NCC algorithm is customized to calculate both the line and column offsets, considering any disparities in brightness and contrast between two images through its normalization component (Yoo and Han, 2009).

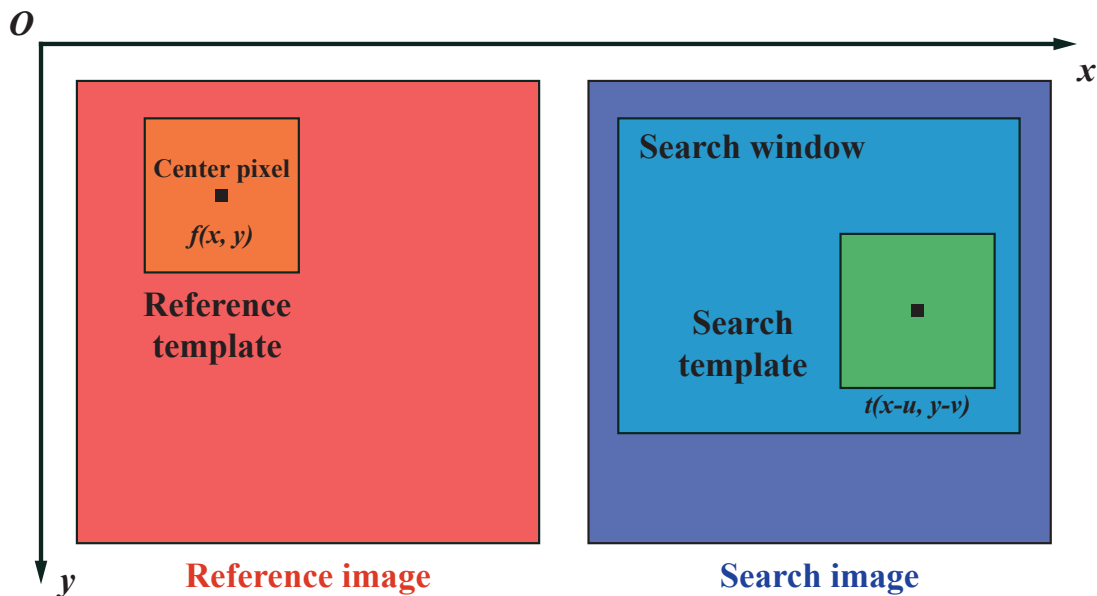


**Figure 2.7:** Schematic of pixel offset tracking techniques using the normalized cross-correlation algorithms showing the investigated pixel for the reference and search images (Source: adapted by Debella-Gilo and Kääb (2011)). The corresponding coordinate system is pixel coordinate.

For NCC processing, the spaceborne optical images are acquired before and after the event, i.e., the reference and search images, as revealed in Figure 2.7. In order to find the reference template  $f(x,y)$  within the search image, the maximum NCC coefficient  $\rho$  is searched between the reference template and all possible values within the search window as follows:

$$\rho(x,y) = \frac{\Sigma_{x,y}(f(x,y) - \bar{f})(t(x-u, y-v) - \bar{t})}{\sqrt{\Sigma_{x,y}(f(x,y) - \bar{f})^2 \Sigma_{x,y}(t(x-u, y-v) - \bar{t})^2}} \quad (2.1)$$

where variables  $u$  and  $v$  indicate the offsets in the  $x$  and  $y$  directions, respectively. The intensity values of a subset area from the reference image are denoted by  $f(x,y)$  with the corresponding area of the same size in the search image represented by  $t(x-u, y-v)$ . The mean values of intensity for the reference template and search window are represented by  $\bar{f}$  and  $\bar{t}$ , respectively.

The horizontal displacement between the center pixel in the reference image and the highest correlated matching point in the search image is determined by the Euclidean distance and given by the magnitude  $d(x,y)$ . Therefore, we can express the standard deviation  $\sigma$  of POT as the error in estimating pixel offset, measured in pixel units. This can be demonstrated through the following equation (Hu et al., 2014):

$$\sigma = \frac{1}{\sqrt{2}} \sqrt{\frac{3}{2N} \frac{\sqrt{1-\rho^2}}{\pi\rho}} \quad (2.2)$$

where  $N$  is the number of samples in the estimation window,  $\rho$  is the maximum NCC coefficient.

The selection of parameters for NCC window size and sampling frequency requires careful consideration concerning the scale of deformation features and pixel size of optical images:

- The search template must be sufficient to maximize the signal-to-noise ratio (SNR) while minimizing the spatial velocity gradient, while the search window should be large enough to include the farthest moving distance while minimizing processing time (Singleton et al., 2014).
- Increasing the number of samples in the reference template and achieving a high cross-correlation value close to one can improve the accuracy of NCC, with precision in the offset fields approaching one-tenth of a pixel size (Hu et al., 2013; Hanssen, 2005).
- Limitations in the accuracy of NCC have been investigated, with sensitivity to noise in images and displacement greater than the mean registration error being significant factors (De Blasio, 2011; Delacourt et al., 2004).
- It is essential to maintain surface properties of the reference template unchanged, except for positional shifts, to ensure accurate cross-correlation and minimize potential limitations that could result in spurious offset measurements and reduced precision (Singleton et al., 2014).

Finally, it is worth noting that the POT method can only determine the horizontal deformation, specifically the displacements in the east-west (E-W) and north-south (N-S) directions, while exploiting spaceborne optical imagery is unable to produce information regarding vertical displacements.

## 2.5 Spaceborne Radar Imagery

### 2.5.1 Synthetic Aperture Radar (SAR) Basic

#### 2.5.1.1 SAR Geometry

SAR is an imaging system that utilizes electromagnetic waves in the microwave range. SAR sensor functions by emitting microwave signals from its antenna towards the Earth's surface at an off-nadir angle called the slant range. These signals interact with the surface, and a proportion of them are reflected towards the satellite, where the onboard sensor records them. As the satellite progresses along its flight path, it continues illuminating and capturing new areas of the Earth's surface, ultimately creating a comprehensive SAR image (Figure 2.8). As illustrated in the schematic, the SAR system utilizes a side-looking configuration to prevent any ambiguity from echoes that may return from the opposite side of the satellite's flight path. The timing of the echoes that return from the surface is directly related to the range distance between the sensor and the target.

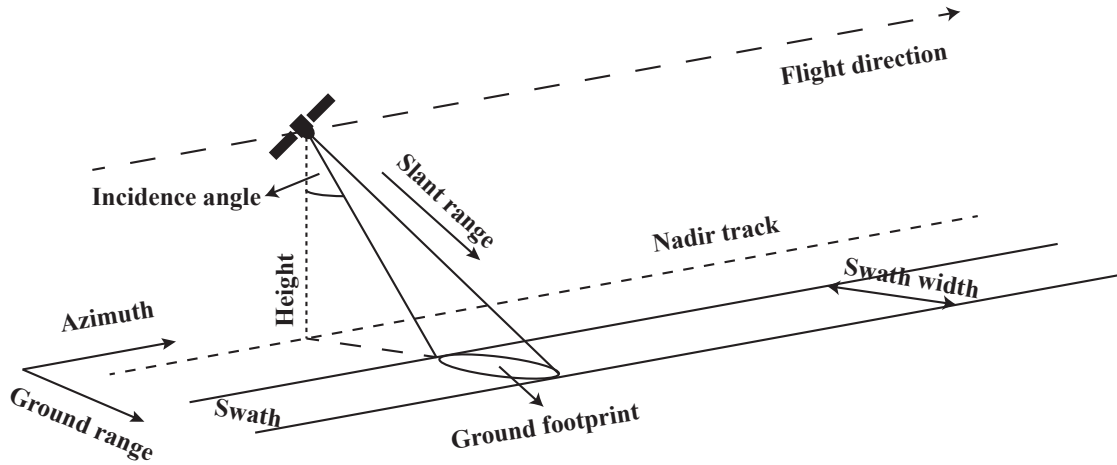


**Figure 2.8:** Schematic of spaceborne SAR imagery.

The SAR sensor can measure two critical parameters, i.e., the amplitude and phase difference of the received echoes. The amplitude value indicates the degree of interaction between the signal and the illuminated surface. A higher amplitude value denotes a more substantial reflection, while a lower value suggests a weaker reflection. The amplitude of the target in SAR images is determined by the image resolution, target size and wavelength of the SAR sensor. On the other hand, the phase difference can be used to determine the distance between the sensor and the ground pixel, enabling accurate estimations of the surface's topography or displacement (Bürgmann et al., 2000). Generally, when using natural terrain as a target, such as grass or forest trees, these targets tend to be smaller than the resolution cell. As a result, the echoes received from one pixel can be a combination of several individual echoes, and the phase values can vary randomly. Additionally, the amplitude may fluctuate significantly, resulting in speckle error (Singleton et al., 2014), which can be addressed through multi-looking processing.

### 2.5.1.2 SAR Acquisition Mode

Satellite SAR sensors employ different acquisition modes, as illustrated in Figure 2.9, i.e., the StripMap mode, the Spotlight mode, and the Interferometric Wide Swath (IW) or Terrain Observation with Progressive Scan (TOPS):

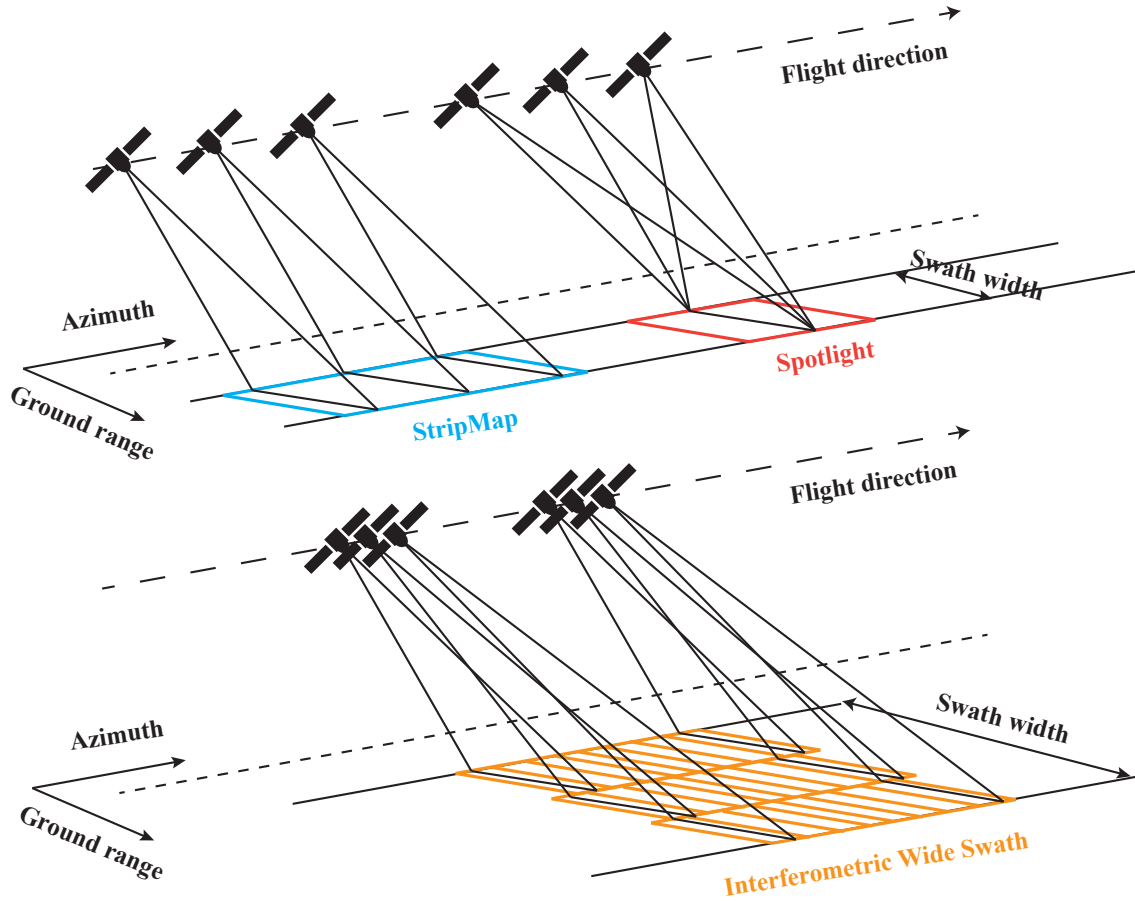


**Figure 2.9:** Different modes of spaceborne SAR missions for image acquisition.

- StripMap mode, utilized by various SAR satellites, including European Remote Sensing Satellite (ERS), Environmental Satellite (Envisat), Advanced Land Observing Satellite (ALOS), and TSX, is the standard mode. In this mode, the sensor's pointing direction is fixed, and it records lines of the image as it moves along its orbit (Lanari et al., 2001).
- Spotlight mode, is designed to obtain high-resolution SAR imaging at the expense of spatial coverage. This mode steers the antenna in the azimuth direction, which prolongs the illumination time for each image element, resulting in higher spatial resolution. However, the scene size is smaller than that of the StripMap mode (Eineder et al., 2009).
- IW or TOPS mode was developed. This mode is the default acquisition mode for Sentinel-1 over land. An IW image is formed from three sub-swaths containing

several bursts that overlap slightly. The image is not continuously acquired, but after recording a burst from a sub-swath, the antenna is steered to measure a burst from the next sub-swath. This method results in an image with extensive spatial coverage and moderate resolution (Torres et al., 2012).

### 2.5.1.3 SAR Distortion

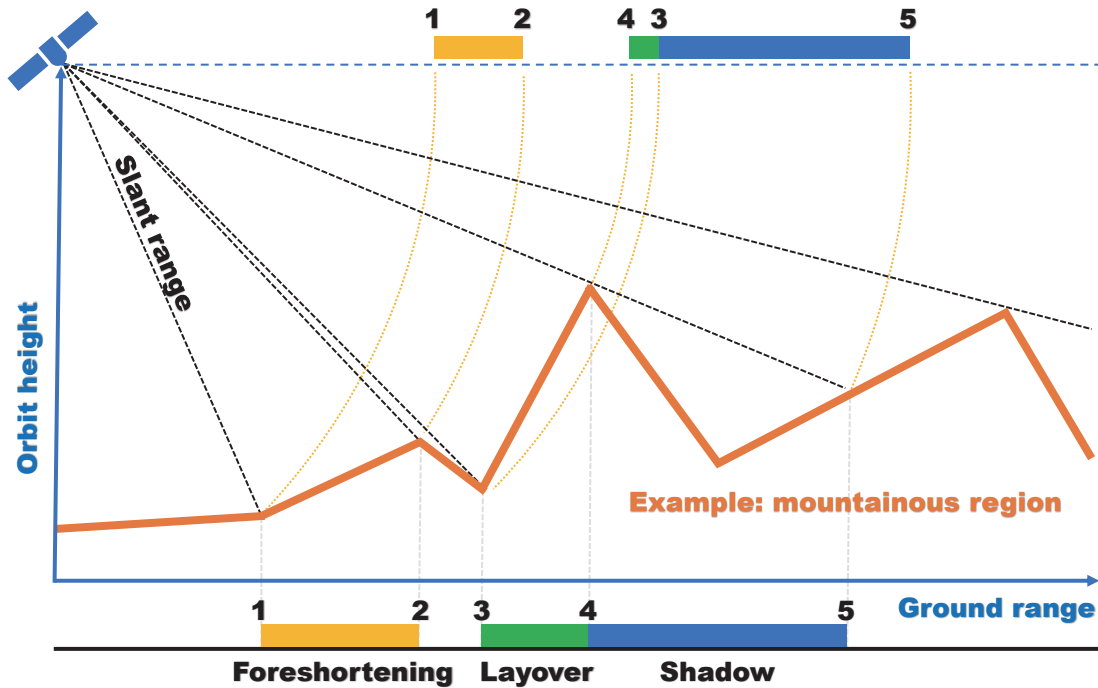


**Figure 2.10:** Simplified example of distortions in satellite SAR imagery.

For all imagery modes, the side-looking configuration has implications for SAR distortions since SAR sensors are used to map objectives on the ground in the slant-range coordinate, which can result in three different types of distortions in the acquired SAR image as revealed in Figure 2.10, i.e., foreshortening, layover and shadow effects (Rosen et al., 2000):

- Foreshortening occurs when a slope is mapped in the slant range and appears shorter than it would while the surface is flat.
- Layover effects occur on specific slopes where the location of pixels is inverted after being mapped on the slant range.
- Shadow is a phenomenon that occurs when the SAR sensor does not illuminate an object on the ground because other elements that are closer to the sensor are located at a higher elevation and obstruct the radar signal from reaching the object.

### 2.5.1.4 SAR Mission

An overview of the important SAR satellite missions since the 1990s is demonstrated in Figure 2.11, including their timeline, frequency band, and repeat cycle. In recent decades,

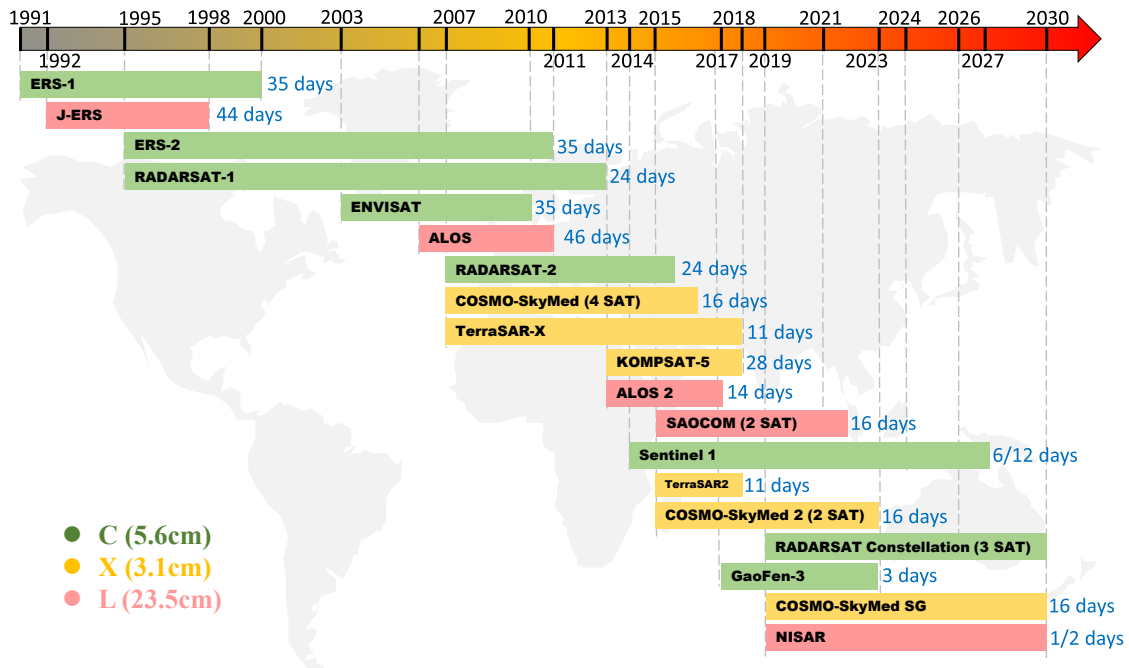


**Figure 2.11:** Overview of the major spaceborne SAR missions, the duration at the end of each mission (unit: days) indicates the repeat cycle of the satellites.

a wealth of SAR data has been available for the Earth's surface analysis, proving extremely valuable. Launching the ERS-1, ERS-2, and Envisat satellites by European Space Agency (ESA) significantly improved InSAR techniques and time series analysis, enabling it to be widely utilized (Berardino et al., 2002; Ferretti et al., 2001).

The start of the S1 mission in 2014 marked a significant milestone in the availability of SAR data. It was the first mission designed explicitly for SAR imaging, making it suitable for InSAR applications. It acquires medium-resolution data worldwide regularly, providing a reliable source of SAR data for at least twenty years (Torres et al., 2012). However, it has been challenging to apply InSAR to specific regions and objectives due to the temporal sparsity and limited coverage of the SAR data provided by these satellites. On the other hand, the launch of high-resolution sensors such as TSX and CSK has further broadened the applications of InSAR, particularly in urban and infrastructure monitoring, as well as in vegetate and semi-vegetated areas, due to their high spatial and temporal resolutions, making them suitable for detailed displacement mapping (Cigna et al., 2014; Berardino et al., 2002). However, their archive of data is sporadic in some areas.

### 2.5.2 Interferometric SAR (InSAR)

It is possible to generate an interferogram by subtracting the phases of two SAR images obtained from slightly different spatial positions, as illustrated in Figure 2.12. This method can be applied for two significant applications: topographic mapping, which has been discussed in prior research (Rossi et al., 2012; Rufino et al., 1998; Zebker and Goldstein, 1986), as well as displacement monitoring (Amelung et al., 1999; Gabriel et al., 1989).

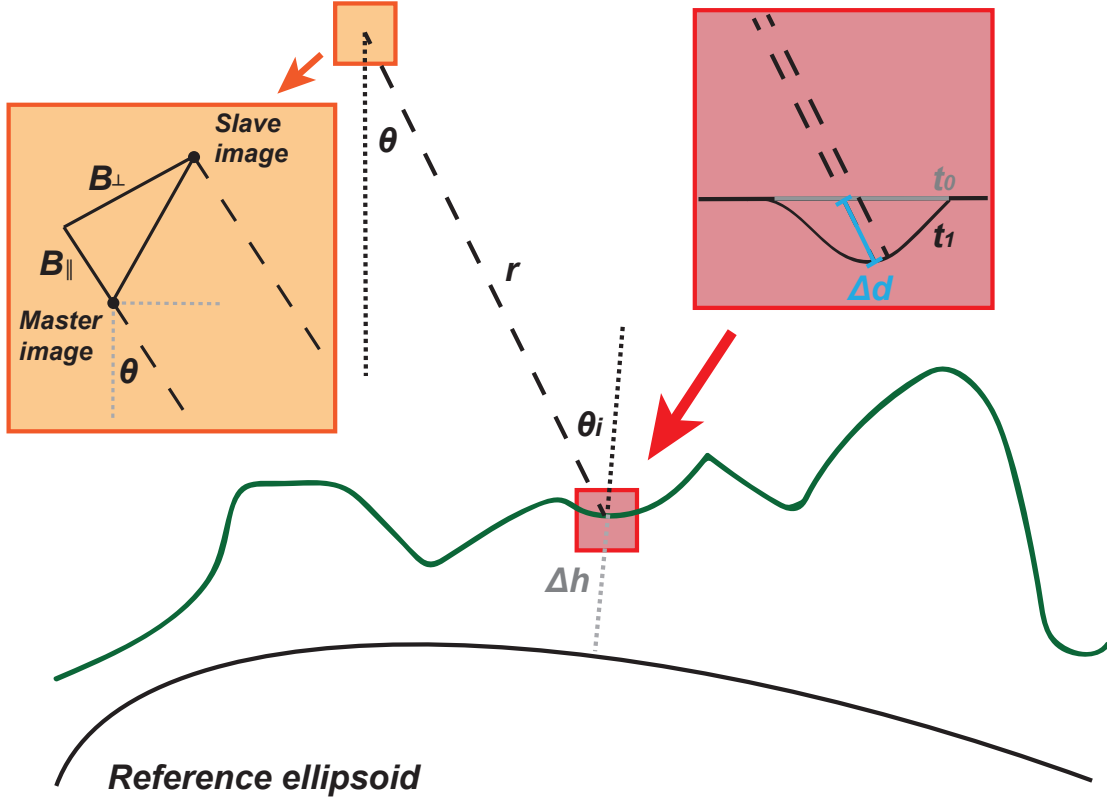


**Figure 2.12:** Displacement of InSAR geometry in the plane normal to the flight.  $B_{\perp}$  and  $B_{\parallel}$  are the perpendicular and parallel baselines, respectively.  $\theta$  and  $\theta_i$  represent the look and incidence angles, respectively.  $r$  is the distance between the SAR sensor and the Earth's surface.  $\Delta d$  denotes the Earth surface deformation between the two times of image acquisitions  $t_0$  and  $t_1$ .

### 2.5.2.1 Workflow of InSAR Processing

The simplified workflow of DInSAR, illustrating the process from the original SAR images to the final displacement map, is demonstrated in Figure 2.13. This workflow comprises a series of essential steps, including coregistration, resampling, interferogram generation, differential interferogram filtering, phase unwrapping and geocoding to obtain the displacement map, which is elaborated in detail as follows:

1. In order to mitigate the impact of noise components, the interferogram is frequently processed by exploiting a multi-looking process whereby neighboring pixels are spatially averaged. This technique improves the SNR but at the cost of spatial resolution (Hanssen, 2001).
2. Coregistration refers to the mathematical alignment of the slave image with the master image using a transformation model based on a low-order polynomial. To calculate the parameters for transformation, we need to estimate shifts at various locations across the amplitude images using a least squares fit method. The coregistration accuracy can be enhanced using an external DEM (Nitti et al., 2010), as



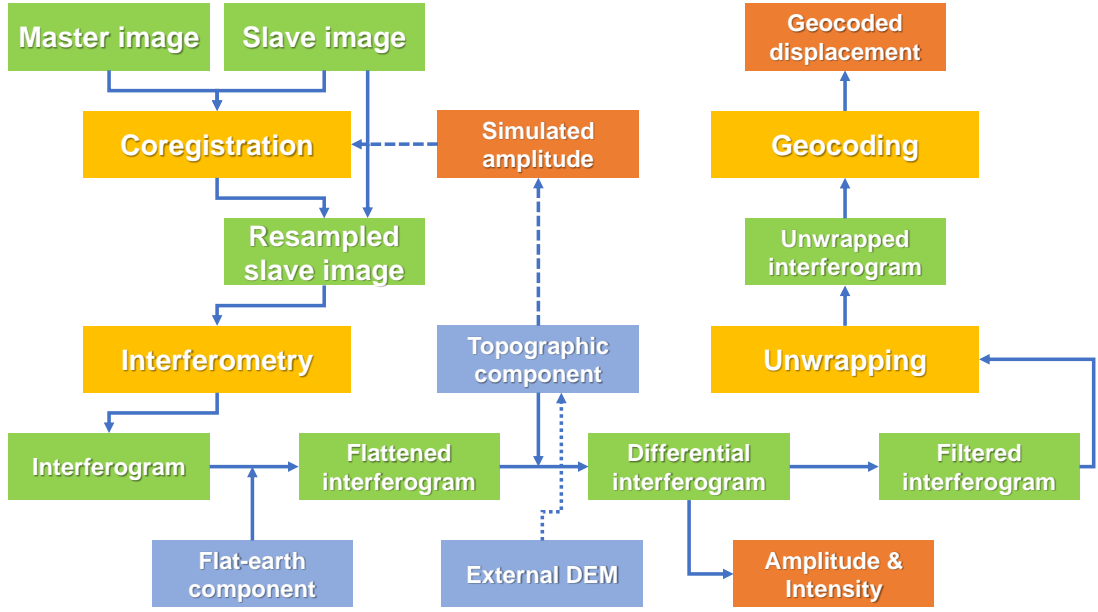


**Figure 2.13:** Simplified workflow of differential InSAR.

demonstrated in Figure 2.14a. Resampling is applying the transformation model to the slave image to align it with the master image, ensuring that corresponding pixels in both images are matched. The aim is to guarantee the accuracy of the interferogram generated from the aligned images.

3. After aligning the master and slave images, the interferogram is generated by multiplying the master image with the resampled slave image using a complex conjugate. The estimated interferometric phase is a summation of coherent components, including surface deformation, flat-Earth, topography, atmosphere, and noise as follows (Rosen et al., 2000; Bürgmann et al., 2000; Bamler and Hartl, 1998):

$$\Delta\phi = \Delta\phi_{def} + \Delta\phi_{flat} + \Delta\phi_{topo} + \Delta\phi_{atm} + \Delta\phi_{noise} \quad (2.3)$$

4. To achieve precise measurements of deformation in an interferogram, it is crucial to eliminate the influences of other components. Among them, the flat-Earth and topographic components are determined by the sensor's geometry and the Earth's shape, which can be accurately computed and subtracted from the data, as revealed in Figure 2.14c. The flat-Earth component's computation relies on the sensor's relative geometry and the Earth model. An exact estimate of this component can be obtained by leveraging the accurate orbital data and the ellipsoidal Earth model, such as the widely-used World Geodetic System 1984 (WGS84) model (Bamler and Hartl, 1998):

$$\Delta\phi_{flat} = -\frac{4\pi}{\lambda} B^{\parallel} \quad (2.4)$$

where  $\lambda$  represents the wavelength of SAR imaging,  $B^{\parallel}$  represents the parallel baseline. The flattened interferogram is derived after the removal of the flat-Earth component. In addition, the interferometric phase is often filtered to minimize noise and increase phase measurement accuracy (Goldstein and Werner, 1998).

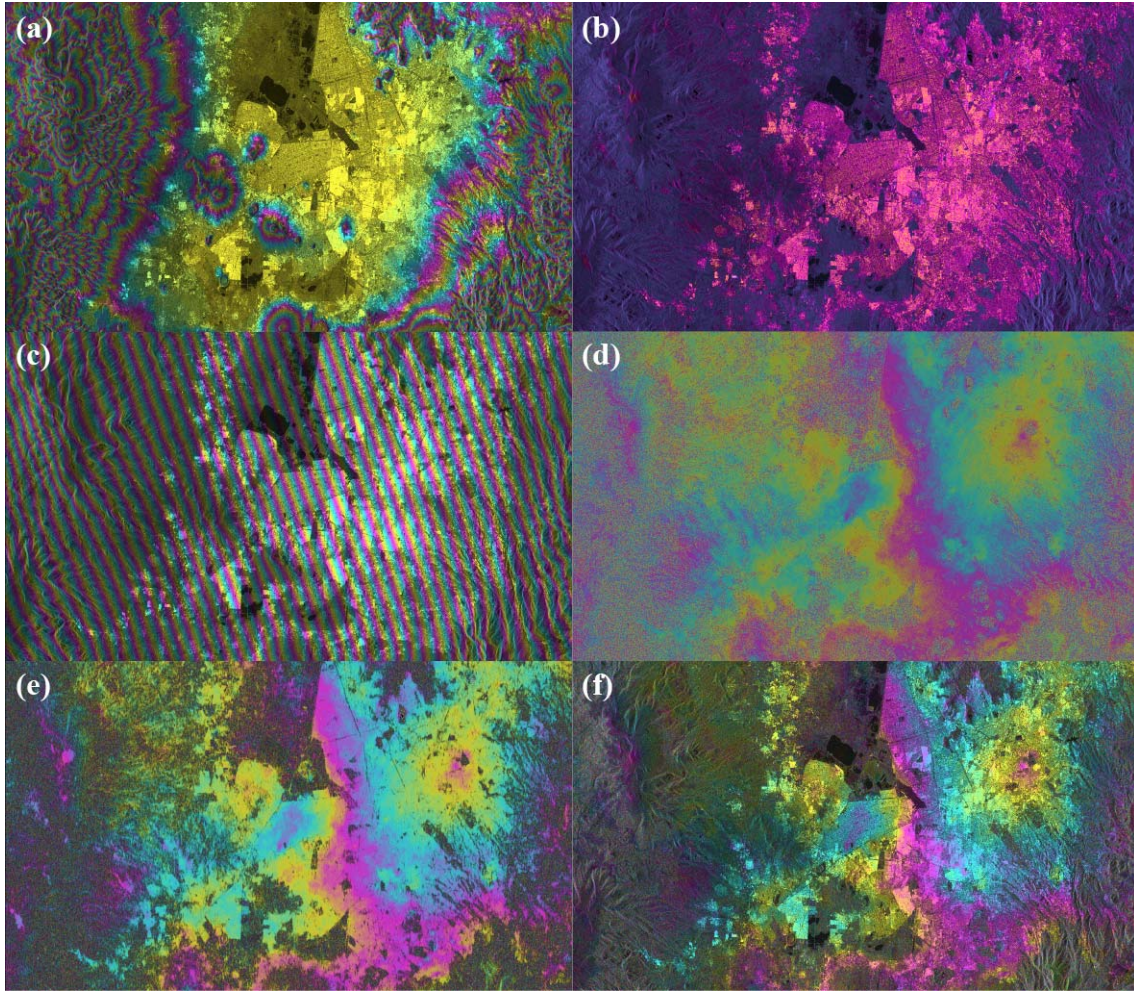


**Figure 2.14:** Examples of intermediate results of InSAR processing, i.e., (a) DEM, (b) coherence map, (c) flat-Earth component, (d) differential interferogram, (e) filtered differential interferogram, and (f) filtered differential interferogram with intensity map.

5. The topographic component in an interferogram arises due to the difference between the actual Earth surface elevation and the ellipsoidal model exploited in the analysis. To rectify this, an external DEM is utilized to estimate the topographic component, which can then be effectively removed from the interferogram (Bamler and Hartl, 1998):

$$\Delta\phi_{topo} = -\frac{4\pi}{\lambda} \frac{B^\perp}{r \sin \theta} \Delta h \quad (2.5)$$

where  $B^\perp$  represents the perpendicular baseline of the interferogram,  $r$  represents the distance between SAR sensor and Earth surface,  $\sin \theta$  represents the incidence angle, and  $\Delta h$  is the surface height from ellipsoid. The differential interferogram is generated after the removal of the topographic component.

6. Although the flat-Earth and topographic components can be precisely estimated and subtracted from interferograms, the atmospheric phase components differ. This is because several physical parameters of the ionosphere and troposphere layers influence

the atmospheric phase delay. Obtaining accurate information on these parameters in space and time is intricate. As a result, estimating the atmospheric phase can be a complex process (Hanssen, 2001). The tropospheric component can be either neglected or estimated through the interferometric phase or external atmospheric information.

7. After eliminating the components above from the interferogram and discarding the remaining noise, the observed phase change is typically attributed to surface deformation as follows:

$$\Delta\phi_{def} = -\frac{4\pi}{\lambda}\Delta d \quad (2.6)$$

where  $\Delta d$  represents the surface deformation acquired between the two SAR images. Due to the periodicity of the interferometric phase, only a modulo  $2\pi$  of the phase values can be obtained. Thus, an unwrapping process, as described by Goldstein and Werner (1998), is required to solve the phase ambiguity in the wrapped phase and recover the integer phase cycle from obtaining the absolute phase value.

8. Eventually, the unwrapped interferogram can be geocoded from SAR geometry to WGS84, and the displacement map can be generated.

### 2.5.2.2 Coherence and Decorrelation

The degree of similarity between the radar echoes of master and slave images in InSAR processing is typically assessed as the coherence:

$$\gamma = \frac{|E(s_1 s_2^*)|}{\sqrt{E(s_1 s_1^*) E(s_2 s_2^*)}} \quad (2.7)$$

where  $E$  denotes the mathematical expectation, and symbol  $*$  represents the complex conjugate.

In practice, estimating the mathematical expectations by repeated measurements is impossible. Therefore, coherence is usually estimated using the values within a window around a pixel:

$$\hat{\gamma} = \frac{|\sum_{i=1}^n s_1^i s_2^{i*}|}{\sqrt{\sum_{i=1}^n s_1^i s_1^{i*} \sum_{i=1}^n s_2^i s_2^{i*}}} \quad (2.8)$$

To estimate the coherence, removing the flat-Earth and topographic components is often necessary. This is because coherence estimation assumes that the pixels within the estimation window are statistically stationary (Zebker and Chen, 2005). In order to meet this assumption, all pixels within the coherence window must exhibit the exact scattering mechanisms.

In InSAR processing, decorrelation is a primary source of the noise (Figure 2.15). When the radar echoes interact with the elements within a resolution cell similarly for both master and slave images, the phase is correlated. Two sources of interferometric phase decorrelation assume that the radar system's thermal noise is negligible. The first source is temporal decorrelation, which occurs when there is a significant change in scattering properties, such as coverage of snow and ice or dense vegetation. The second source is spatial decorrelation, which results from the slightly different viewing geometries of the master and slave images (Zebker et al., 1992).



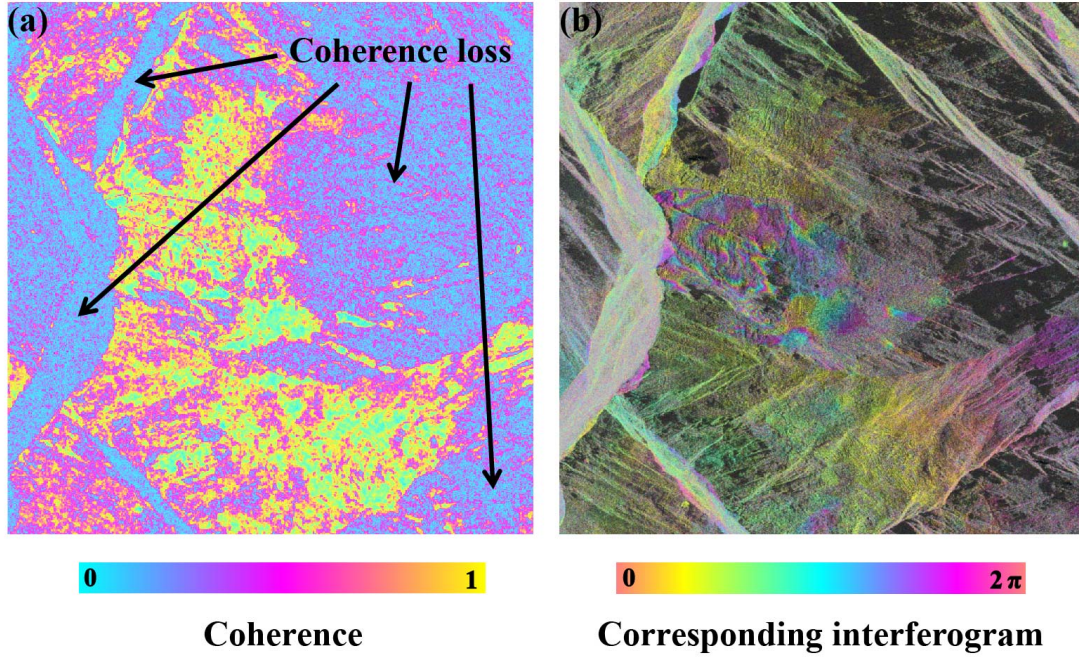


**Figure 2.15:** An example of decorrelation during InSAR processing. (a) The coherence map of two TSX images has a temporal baseline of 11 days and a perpendicular baseline of -5 meters. (b) The corresponding differential interferogram is derived using the same SAR image pair.

### 2.5.2.3 Topographic and Orbital Errors

The remaining DEM and orbital errors also exist. Any inaccuracies in the DEM would result in correlated errors in the interferogram with the perpendicular baseline. This is because the topographic component of the interferogram is directly proportional to the baseline, making it a sensitive indicator of any errors in the underlying DEM:

$$\delta\phi_{topo} = -\frac{4\pi}{\lambda} \frac{B^\perp}{r \sin \theta} \delta h \quad (2.9)$$

where  $\delta\phi_{topo}$  and  $\delta h$  represent the phase and topographic errors.

Generating DEM using SAR images can result in significant topographic errors due to large perpendicular baselines. One approach to correcting this issue is to estimate the remaining DEM error through least squares adjustment by generating interferograms with different perpendicular baselines, provided that multiple images are available. This correction method can help to ensure accurate interferograms (Fattahi and Amelung, 2013). For example, S1, designed with a narrow orbital tube specifically for InSAR applications, typically experiences less DEM error than other sensors when generating DEM using SAR images (Salvi et al., 2012). However, inaccuracies in the satellite's orbital estimation can still result in errors when estimating the flat-Earth component. These errors can present as a linear trend across the interferogram and can be corrected by fitting a linear ramp to the phase change across the interferogram. Historical SAR missions such as ERS and Envisat are particularly susceptible to such errors. In contrast, modern satellites like TSX

and CSK have higher orbital accuracy and usually produce precise estimations of the flat-Earth component (Fattahi and Amelung, 2014).

#### 2.5.2.4 Atmospheric Artifacts

Atmospheric artifacts can also lead to inaccuracies in InSAR processing. Atmospheric artifacts refer to phase delays in the ionospheric and tropospheric layers of the atmosphere. The ionospheric phase shift is commonly caused by changes in the total electron content (TEC) within the ionospheric layer of the atmosphere. The ionospheric phase change can be estimated and mitigated by utilizing internal information within the original SAR data (Gomba et al., 2015; Jung et al., 2012). The degree of delay is directly proportional to the wavelength of the microwave signal and is particularly pronounced in high latitudes and equatorial regions (Meyer, 2010). Thus, ionospheric artifacts are typically less significant in mid-latitudes for shorter wavelengths, such as those in the C- and X-bands, and can often be disregarded. The ionospheric phase change can be estimated and corrected by utilizing internal information within the original SAR data, as mentioned in previous studies (Gomba et al., 2015; Jung et al., 2012).

On the other hand, the occurrence of tropospheric delays in interferometry is mainly due to three different types of variations in tropospheric parameters, i.e., The first type arises from broad-scale lateral variations and increases with relative lateral distance. It is corrected by removing a low-order phase ramp or estimated using global weather models (Jolivet et al., 2011). The second type is caused by vertical variations of water vapor, resulting in topography-dependent atmospheric delays, estimated empirically or using global weather models (Jolivet et al., 2011). The third type is caused by the short-wavelength turbulent troposphere, which is highly variable in space and time, making it challenging to estimate (Bekaert et al., 2015). To reduce this type of tropospheric delay, atmospheric information with the high spatial and temporal resolution is required, such as from densely distributed GNSS networks.

#### 2.5.2.5 Sensitivity of Line-of-sight (LOS) to Slope Motion

InSAR methods only acquire displacements along the LOS direction, while for slope motion, it is often assumed that the surface deformation is along the slope surface. Figure 2.16 demonstrate the relationship between the actual displacement rates  $V_{slope}$  and the LOS displacement rates from ascending data  $V_A$  and descending data  $V_D$ , respectively (Dai et al., 2022):

- If the terrain slope faces almost towards the south or the north, the measured LOS displacements from ascending and descending SAR data tend to be nearly equal (Figure 2.16a).
- If the terrain slope is oriented towards the east, the measured LOS displacement obtained from the ascending data will generally be more significant than that from the descending data (Figure 2.16b).
- If the terrain slope is oriented towards the west, the measured LOS displacement obtained from the descending data will generally be more significant than that from the ascending data (Figure 2.16c).

## 2 Theoretical Background

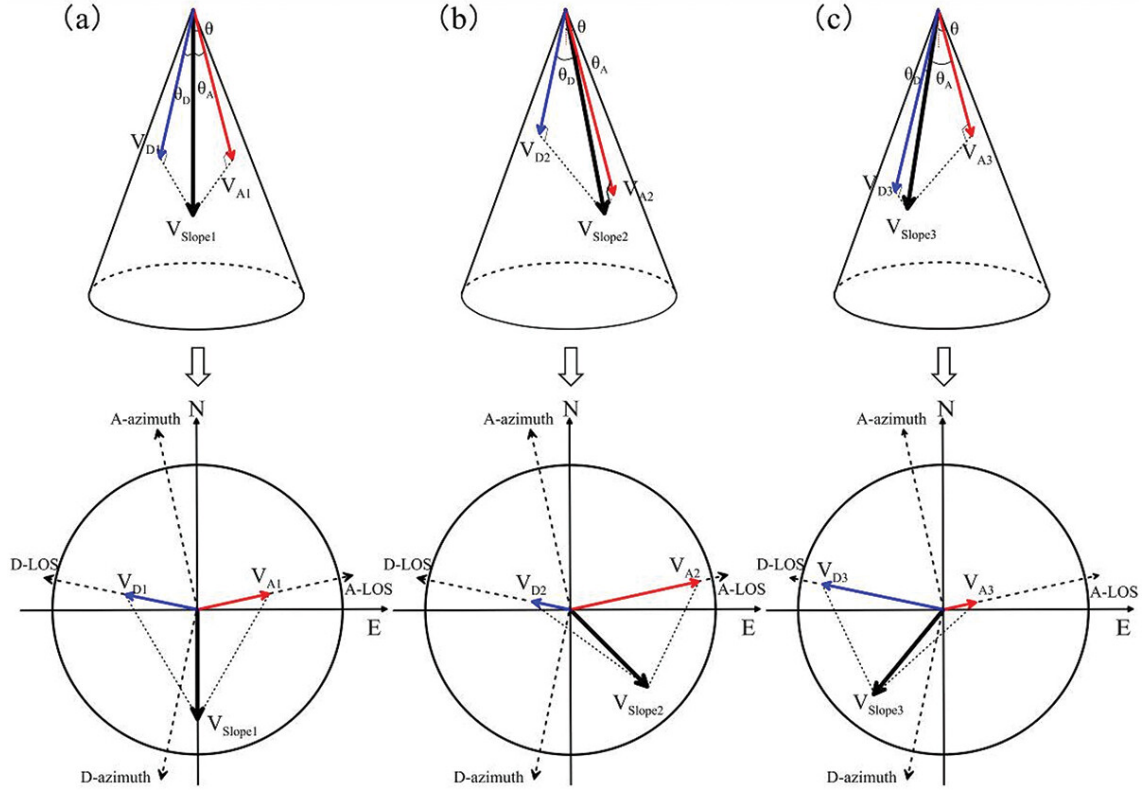


**Figure 2.16:** Diagrams from the side view and the plan view illustrating the effects of variation in aspect on the LOS projection component (Source: Dai et al. (2022)).

Figure 2.17 reveals the geometric relationship between an ascending LOS direction and a specific slope aspect, and the LOS displacement can be expressed as (Cascini et al., 2010):

$$\vec{u} = \begin{bmatrix} \vec{u}_E \\ \vec{u}_N \\ \vec{u}_Z \end{bmatrix} = \begin{bmatrix} \cos \alpha_s \sin \theta \\ \sin \alpha_s \sin \theta \\ -\cos \theta \end{bmatrix} \quad (2.10)$$

where  $\vec{u}$  refers to the unit vector of LOS displacement,  $\alpha_s$  and  $\theta$  denote the angle between satellite heading direction and incidence angle, and  $|\vec{u}| = 1$ .

Moreover, the real deformation along the slope could be expressed as (Cigna et al., 2014):

$$\vec{r} = \begin{bmatrix} \vec{r}_E \\ \vec{r}_N \\ \vec{r}_Z \end{bmatrix} = \begin{bmatrix} \sin \alpha \cos \varphi \\ \cos \alpha \cos \varphi \\ -\sin \varphi \end{bmatrix} \quad (2.11)$$

where  $\alpha$  and  $\varphi$  denote the slope aspect and slope angle,  $\vec{r}$  refers to the unit vector of the real displacement along the slope, and  $|\vec{r}| = 1$ .

The two unit vectors have the relationship as follows:

$$\cos \beta = \frac{\vec{r} \cdot \vec{u}}{|\vec{r}| \cdot |\vec{u}|} = \cos \alpha_s \sin \theta \sin \alpha \cos \varphi + \sin \alpha_s \sin \theta \cos \alpha \cos \varphi + \cos \theta \sin \varphi \quad (2.12)$$

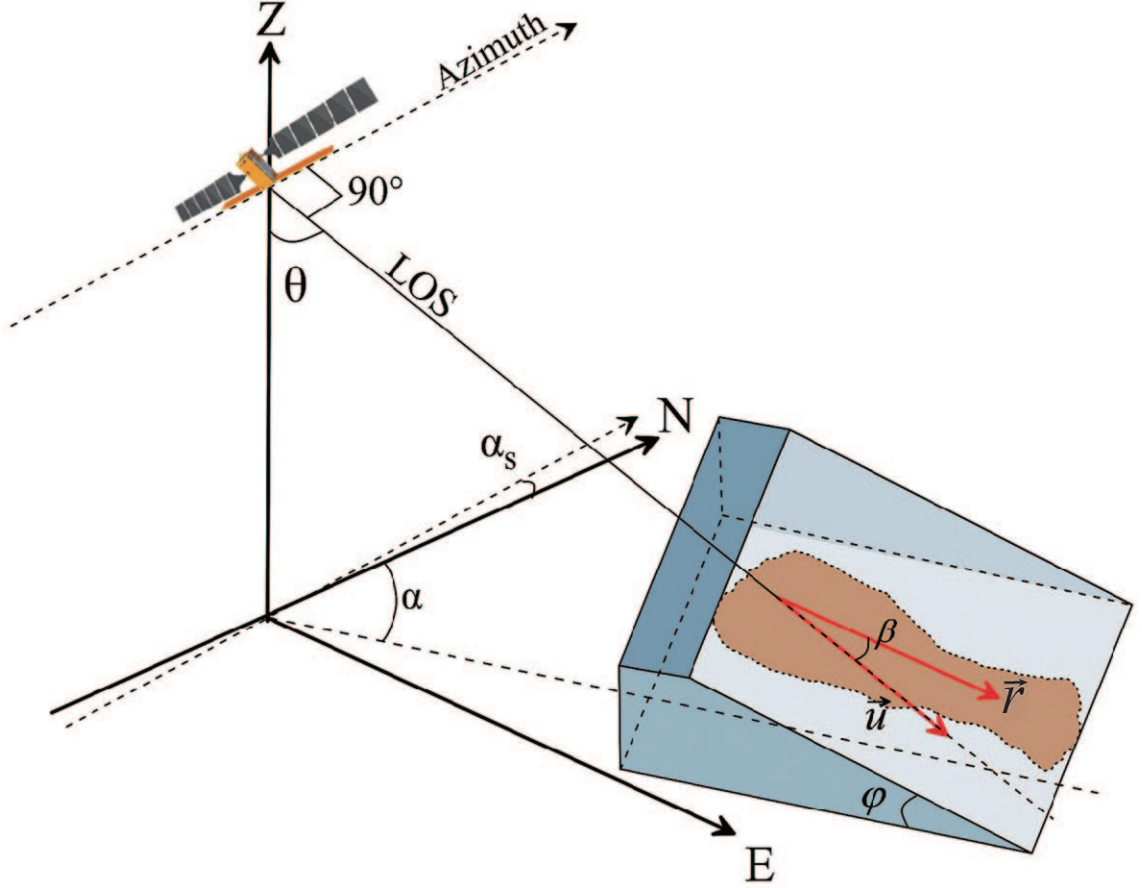


**Figure 2.17:** Geometric relationship between an ascending LOS direction and a specific maximum slope aspect (Source: adapted by Dai et al. (2022)).

where  $\beta$  refers to the angle between two unit vectors. Hence, the LOS and real displacement can be derived as (Dai et al., 2022):

$$V_{LOS} = V_{slope} \times \cos \beta \quad (2.13)$$

Finally, the sensitivity  $S$  of LOS to slope motions can be derived as (Dai et al., 2022):

$$S = \frac{V_{LOS}}{V_{slope}} \quad (2.14)$$

where  $S$  demonstrates how much a unit change in LOS displacement can be used to measure the actual displacement.

### 2.5.3 Advanced Multi-temporal InSAR (MT-InSAR)

Conventional DInSAR is a robust technique for investigating significant displacements resulting from sudden earthquakes. However, when the displacement is subtle or spans a more extended period, DInSAR struggles to detect the signal due to phase decorrelation and atmospheric disturbance, usually in the range of a few millimeters or centimeters. Hence, the advanced MT-InSAR methods have been introduced to overcome such limitations and extract the time series of displacements. Although these methods differ in theory

and practice, they share the common objective of generating a time series displacement from a series of SAR data using a few key steps. Firstly, an interferogram stack is derived, followed by selecting coherent pixels and connecting their interferometric phases over time to derive the displacement time series. MT-InSAR approaches are divided into two broad categories, i.e., PSI and SBAS methods, each optimized for a specific type of scattering mechanism in SAR imagery.

### 2.5.3.1 Scattering Mechanism

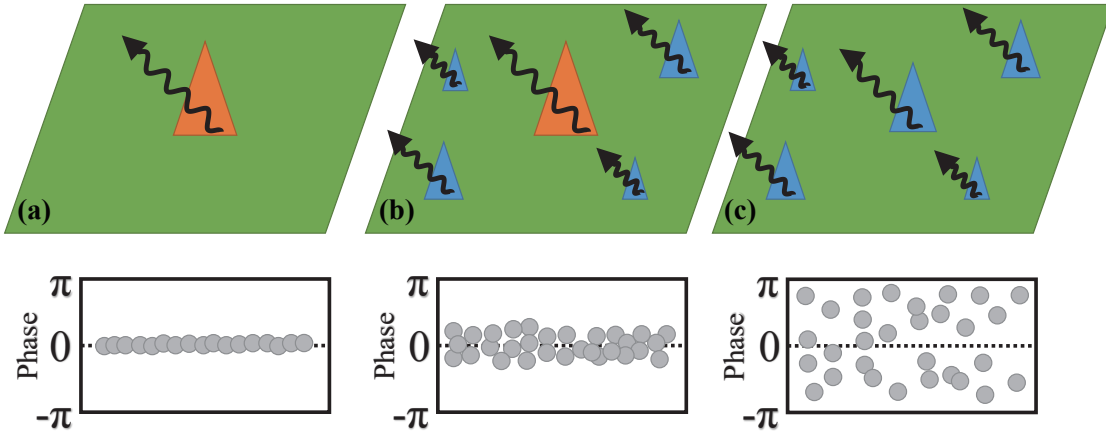


**Figure 2.18:** Scattering mechanisms for (a) an ideal single scatterer element, (b) a persistent scatterer element, and (c) a distributed scatterer. The corresponding temporal phase variations of the scattered waves are simulated and visualized.

In SAR imaging, the phase of a pixel signifies the combined contribution of wavelets from all scattering elements present within that pixel, as depicted in Figure 2.18. Due to the unpredictable movements of these scattering elements, the phase changes across multiple radar measurements. Ideally, a pixel would have a single scattering solid element, such as an artificial corner reflector (CR), for InSAR to be perfectly implemented. This results in minimal phase noise and guarantees the coherence of the pixel phase in any combination of SAR images. Maintaining temporal phase correlation in interferograms with long temporal and perpendicular baselines can be challenging, as a pixel may contain multiple scattering elements. However, PSs can still preserve enough temporal phase correlation in interferograms, even with long baselines, if one of the scattering elements within the pixel dominates the other elements. PS points are typically found in urban areas where buildings act as scattering solid elements. Multi-looking is not applied to the interferograms during the analysis to detect PS points, as multi-looking introduces more scatterers to a resolution cell (Hooper et al., 2012). Although PSs are valuable in remote sensing applications, they are not commonly found in natural environments. Instead, pixels typically consist of multiple scattering elements, known as DSs, whose phase correlation decays rapidly due to random scatterer movements. As a result, DSs can only maintain enough correlation in interferograms with short baselines. To enhance the SNR of DS data, it is customary to employ multi-looking techniques (Parizzi and Brcic, 2010).



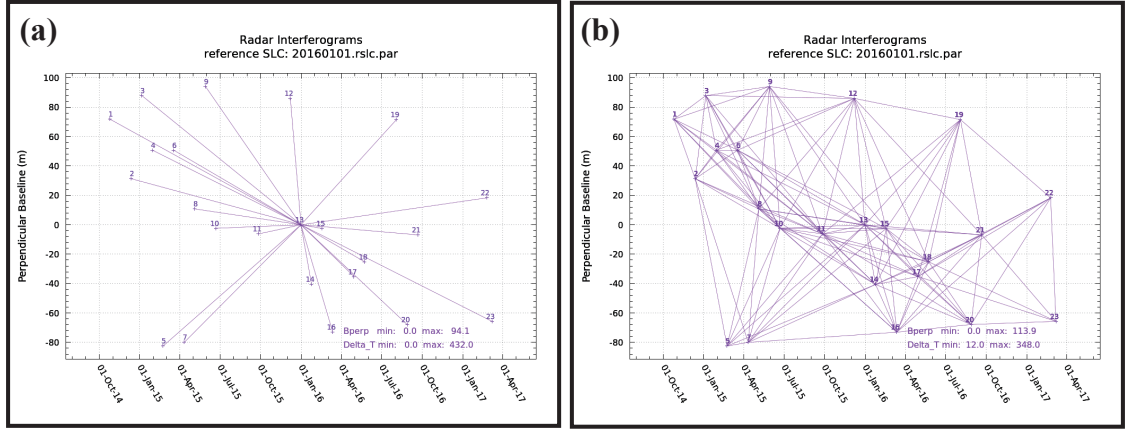


**Figure 2.19:** An example of interferogram network in (a) persistent scatterer interferometry (PSI) and (b) small baseline subsets (SBAS) approaches. The  $x$  and  $y$  axes illustrate the temporal and spatial baselines.

### 2.5.3.2 Interferogram Stacking

The most straightforward technique of MT-InSAR is stacking, which assumes a linear model for displacement and calculates the average displacement rate from a collection of interferograms. To maintain the phase correlation of DSs, the interferograms are generated using image pairs with short temporal and perpendicular baselines. Additionally, the interferograms are multi-looked to improve the SNR. The interferometric phase of a specific pixel in differential interferogram  $i$  can be expressed as (Hooper et al., 2004):

$$\Delta\phi^i = \Delta\phi_{def}^i + \delta\phi_{orb}^i + \delta\phi_{topo}^i + \Delta\phi_{atm}^i + \Delta\phi_{noise}^i \quad (2.15)$$

where  $\delta\phi_{orb}$  and  $\delta\phi_{topo}$  represent the remaining errors in orbital data and topography. For pixel in interferogram with  $m$  samples, the linear rate of displacement  $\hat{v}$  is:

$$\hat{v} = \frac{1}{m} \sum_{i=1}^m \frac{\Delta\phi^i}{B_T^i} \quad (2.16)$$

where  $B_T^i$  represents the temporal baseline of interferogram  $i$  (Wright et al., 2001).

The stacking approach is practical when the phase component of displacement displays a linear trend over time while other phase components remain constant. As a result, averaging eliminates random errors and maintains the linear displacement trend. However, the estimated displacement rate may be biased if this assumption is not met. To improve the reliability of the estimated displacement rate, it is recommended to mitigate errors resulting from atmospheric phase delay, orbital inaccuracies, and any remaining DEM prior to averaging the interferograms (Wang et al., 2009a).

### 2.5.3.3 Persistent Scatterer Interferometry (PSI)

During PSI processing, a collection of single-master interferograms is created, and the pixels displaying the highest signal-to-noise values are selected (Hooper et al., 2007, 2004). These pixels are referred to as PSs, and they typically originate from rocks and manufactured objects. PSs maintain a stable phase even in interferograms with large temporal and

## 2 Theoretical Background

perpendicular baselines. Then, one of the SAR images is chosen as the reference, and all other images are resampled to match the reference image, as illustrated in Figure 2.19a. PSI first identifies PSs by leveraging amplitude dispersion, the ratio of standard deviation to the average amplitude value for a specific pixel in a stack of interferograms as follows (Hooper et al., 2007):

$$D_A = \frac{\sigma_A}{\mu_A} \quad (2.17)$$

where  $D$ ,  $\sigma$ , and  $\mu$  represent the dispersion, standard deviation, and mean amplitude value.

Each PS candidate's temporal phase behavior is then analyzed to estimate its noise level. There are two primary methods for estimating the noise level of a pixel. The first method involves the double phase difference between neighboring PS candidates, which removes spatially correlated atmospheric and orbital errors (Kampes, 2005; Ferretti et al., 2001). This method is most effective in urban areas but relies on a predefined displacement model, which may lead to high noises. The second method estimates the noise level in a stack of interferograms without relying on a predefined displacement model (Hooper et al., 2004). Contributions from deformation, atmosphere, and orbital errors are estimated by spatial filtering, while DEM error is estimated by correlation with perpendicular baselines. This approach provides a higher density of detected PSs in non-urban areas. After selecting the PS pixels, their phases are unwrapped and connected temporally to obtain the displacement time series. Tropospheric artifacts and unwanted components are estimated and removed by spatial and temporal filtering. Finally, the remaining DEM errors are modeled and removed based on the correlation of unwrapped phases with perpendicular baselines.

### 2.5.3.4 Small Baseline Subsets (SBAS)

SBAS method exploits a network of small temporal and spatial baselines as revealed in Figure 2.19b, to minimize the decorrelation between image pairs (Anderssohn et al., 2009; Lanari et al., 2007). The distributed scatterer DSs, defined as the pixel that shares similar statistical behavior with its neighboring pixels, is considered. The pixels with high coherence are usually selected with thresholding in a given percentage of interferograms (Berardino et al., 2002). To improve the reliability of detecting DS pixels, SBAS interferograms are typically multi-looked to increase the SNR of phase values. However, this process can result in a loss of resolution and blurring of coherent pixels within noisy surroundings. To overcome this limitation, a statistical phase analysis can be employed to identify coherent pixels at the original interferogram resolution (Hooper, 2008). Once the reliable pixels have been found, their phases are either independently unwrapped in two dimensions or jointly unwrapped with time acting as the third dimension of each interferogram (Hooper, 2008; Berardino et al., 2002). Finally, to resolve the displacement at each date, the unwrapped displacement of interferograms in the network is inverted.

For instance, suppose  $\Delta d_i$  is the displacement in the  $t$ -th interferogram between two dates. In that case, the following linear system is created for each pixel, with  $m$  equations for each interferogram and  $n$  unknowns for each SAR date:

$$A_{m,n} X_{n,1} = L_{m,1} \quad (2.18)$$

where  $A$  is a matrix filled with 1 and -1 for the image pairs and 0 otherwise,  $L$  represents the displacements of a pixel in all SBAS interferograms,  $X$  denotes the unknown displacement

at each SAR data and is solved by least squares estimation by minimizing the  $L_p$  norm of residuals:

$$\hat{X} = \arg \min \|L - AX\|_p \quad (2.19)$$

The unknown displacement is solved by conventional least squares estimation (Amemiya, 1983):

$$\hat{X} = (A^T A)^{-1} A^T L \quad (2.20)$$

As the last stage of SBAS processing, after estimating the time series of displacement, DEM error is estimated by considering its correlation with the perpendicular baseline and atmospheric artifact is removed from the time series by spatial and temporal filtering.

## 2.5.4 Corner Reflector InSAR (CR-InSAR)

### 2.5.4.1 Overview

Artificial CR is manufactured equipment utilized as auxiliary tools in SAR and InSAR analysis. Their primary function is to generate coherent echoes with stable amplitude and phase information during radar acquisitions (Bovenga et al., 2014). By deploying CRs as artificial coherent scatters, it is possible to increase the number of measurement points in MT-InSAR analysis, particularly in areas such as vegetated, semi-vegetated, or agricultural regions, where there is a risk of severe coherence loss between successive SAR image acquisitions (Garthwaite, 2017; Bovenga et al., 2014; Shan et al., 2013; Fu et al., 2010; Froese et al., 2008; Xia et al., 2004). Furthermore, this approach offers an alternative solution for increasing the accuracy and reliability of SAR and InSAR measurements in challenging environments, which are commonly used to calibrate and validate SAR sensors, both in terms of radiometric and geometric measurements (Gisinger et al., 2020; Doerry, 2014; Marinkovic et al., 2007; Freeman, 1992; Gray et al., 1990).

### 2.5.4.2 Conventional Designs

CRs typically consist of two or three electrically conducting surfaces that can generate strong radar echoes from regions with low effective radar cross-section (RCS). By reflecting incoming electromagnetic waves multiple times, they can accurately backscatter the waves in the same direction as they arrived, leading to solid echoes even from objects with small dimensions.

Conventional trihedral corner reflectors (TCRs) with large dimensions, such as those with an edge of 1 meter, are known for their steady and robust echoes (Figure 2.20a and 2.20b). Therefore, these TCRs have been proposed as an effective instrument for monitoring slope stability in vegetated mountainous areas, as they provide a reliable source of coherent scatters that can be detected by SAR and InSAR systems (Bovenga et al., 2017, 2014; Shan et al., 2013; Froese et al., 2008; Xia et al., 2004, 2002). The variation of shape and size of metal plates would influence the RCS and signal-to-clutter ratio (SCR). For instance, the triangular, squared, and pentagonal TCRs were designed and tested in different studies (Crosetto et al., 2013; Qin et al., 2013; Xia et al., 2004). Figure 2.21 reveals examples of the intensity map of the conventional TCRs in high-resolution TSX data. Those TCRs were settled to monitor the slope kinematics of the Shuping landslide in the previous study by Xia et al. (2004), which are still valid nowadays.

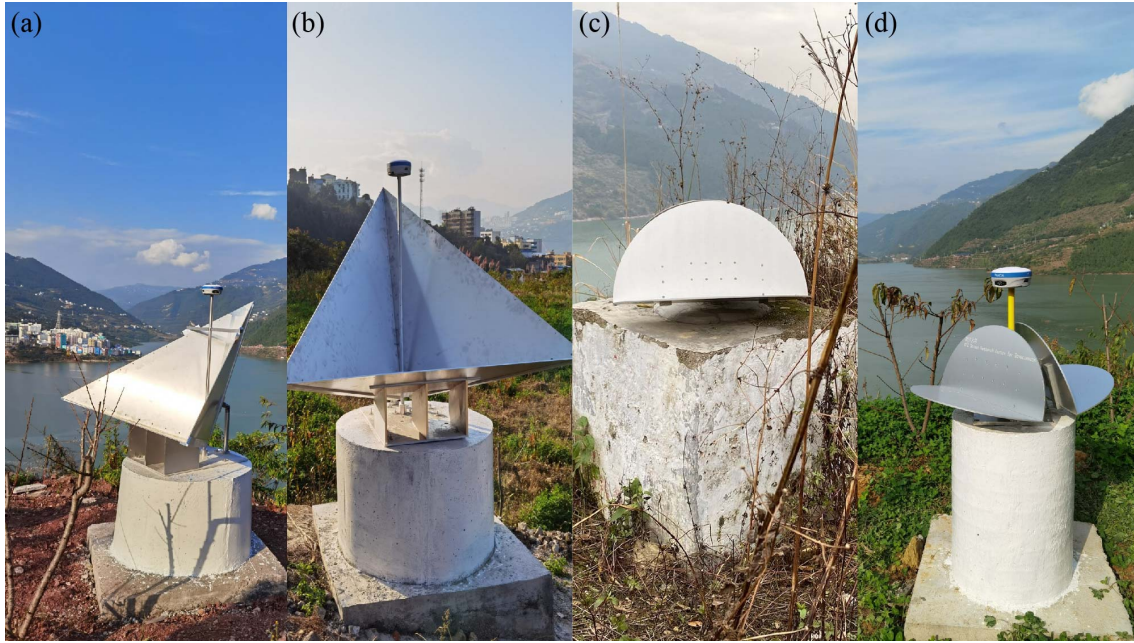


**Figure 2.20:** Examples of the conventional triangular TCRs and our experimental designs for monitoring slope instability.

On the other hand, Dheenathayalan et al. (2017) conducted a study where they tested significantly smaller TCRs designed especially for high-resolution data, with an edge measuring approximately 14.5 cm. Their results showed an average SCR of around 6 dB, with corresponding clutter intensity improvement by around 6 dB. However, the small-scale CRs in their study were only suitable for high-resolution datasets such as TSX or CSK, not for medium or even lower-resolution datasets like S1. Larger CRs would have higher RCS and SCR values but with more challenging deployment and maintenance procedures, as reported by Shan et al. (2013). To address this issue, we introduce our CRs as a compromise solution that can be used for InSAR monitoring using both high-resolution and medium-resolution SAR images. It is a cost-effective option with easy installation and maintenance.

#### 2.5.4.3 Our Experimental Designs

It is essential to highlight that when designing CRs for SAR satellites, no universal solution would work equally well for all operational satellites (Garthwaite, 2017). Therefore, creating a CR specific to the sensor being used or a compromise solution that considers the need for multiple sensors for effective operational monitoring is necessary.

Therefore, we experiment to evaluate the effectiveness of a newly designed dihedral corner reflector (DCR) with compact dimensions (30-40 cm radius), featuring symmetrical geometry that enables its use for both ascending and descending SAR observations. They are composed of two sets of semi-circular metal plates positioned perpendicular to each other, which are installed on a standard pillar, with the same inclination angle of  $10^\circ$  symmetrically, as revealed in Figure 2.20c and 2.20d. These reflectors have broadened the scope of their application to fields that require 3D velocity mapping from SAR data.



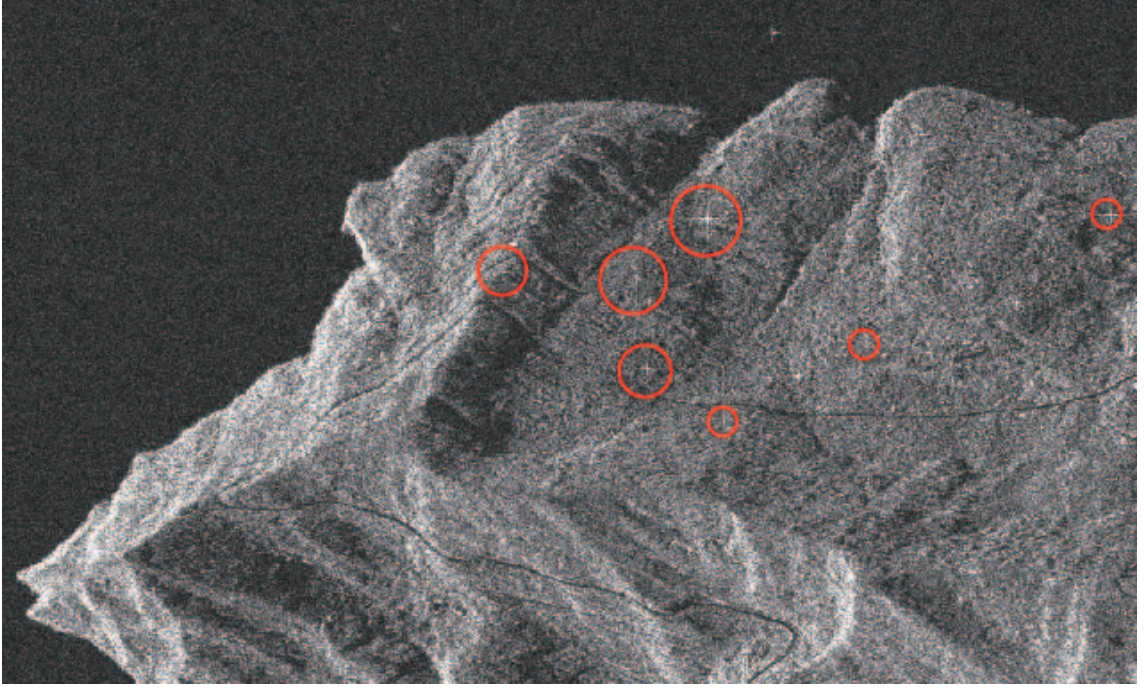


**Figure 2.21:** Examples of the intensity map of the conventional triangular TCRs in high-resolution TSX data.

#### 2.5.4.4 CR-InSAR Processing

CR-InSAR is a specialized InSAR technique for studying CRs (Shan et al., 2013; Froese et al., 2008; Xia et al., 2004). The method primarily relies on the calculation of the double-phase difference of a reference CR across various epochs to extract valuable information as follows:

$$\Delta\phi_{ij} = (\phi_i^s - \phi_j^s) - (\phi_i^m - \phi_j^m) \quad (2.21)$$

where  $\Delta\phi_{ij}$  represents the double phase difference of CRs  $i$  and  $j$ , the superscripts  $m$  and  $s$  are master and slave images.

Then following Equations 2.3 to 2.6 and 2.21, the double phase difference could be expressed as:

$$\Delta\phi_{ij} = -2\pi \cdot K_{ij} - \frac{4\pi}{\lambda} \frac{B^\perp}{r \sin \theta} \Delta h_{ij} - \frac{4\pi}{\lambda} \Delta d_{ij} + \Delta\phi_{atm} \quad (2.22)$$

where  $K$  denotes the phase ambiguity,  $\Delta h$  represents the differences in DEM error, and  $\Delta d$  refers to the displacement parameters based on linear and seasonal functional models. The atmospheric effects, i.e., tropospheric and ionospheric phase components, are neglected by the double-difference of phase observations considering the closing distance of deployed CRs (Froese et al., 2008; Xia et al., 2004).

After obtaining the wrapped phase through double differencing, the next step is to unwrap it to determine the phase ambiguity. To accomplish this, we utilized the least squares ambiguity decorrelation adjustment (LAMBDA) method to estimate the absolute phase and derive the LOS motion (Kampes and Hanssen, 2004).

By introducing pseudo-observations for DEM errors and displacement parameters as a priori knowledge due to the lack of redundancy, the problem can be converted to integer

## 2 Theoretical Background

ambiguity estimation as follows (Kampes and Hanssen, 2004):

$$y = Aa + Bb + n \quad (2.23)$$

where  $y$  represents the observed double phase differences,  $a$  and  $b$  are integer-valued unknown ambiguities and unknowns for the baseline components, respectively.  $A$  and  $B$  are design matrices for ambiguity terms and baseline components, respectively.  $n$  represents noises and errors.

To obtain the integer ambiguity, the solution of Equation 2.23 is estimated from solving the minimization problem (Kampes and Hanssen, 2004):

$$\min ||y - Aa - Bb||_{Q_y}^2 \quad (2.24)$$

where  $Q_y$  is the variance-covariance-matrix of observations, and  $a$  is integer. This minimization problem is a classical integer least squares problem addressed in the previous study (Teunissen, 1993).

## 3 Methodological Contribution

### 3.1 Challenges in Landslide Monitoring Using Spaceborne Remote Sensing

First of all, when studying landslide hazards, one important objective is to forecast a possible timeframe for when a failure is likely to occur. For such purpose, the inverse velocity (INV) algorithm has gained popularity due to its simplicity and effectiveness in early warning as evidenced by numerous recent studies (Zhou et al., 2020; Carlà et al., 2017). In practice, however, one of the primary obstacles faced when implementing INV is the presence of various types of artificial or systematic disturbances. InSAR time series often exhibit a range of regular or irregular fluctuations that arise from systematic errors and anthropogenic factors. These disturbances can be measurement inaccuracies, instrument malfunctions, and periodic variations caused by precipitation, groundwater fluctuations, and anthropogenic actions. Such disturbances may result in outlier data points and unusual behaviors concerning the INV method, necessitating data smoothing techniques. In past studies, several approaches have been developed to carry out data smoothing of displacement data, including using short-term and long-term moving averages and exponential smoothing functions (Carlà et al., 2017; De Blasio, 2011). However, such filtering can not always be satisfying: if the kernel utilized in the smoothing function is too large, critical features may be lost in the filtered curve, while reducing the size of the kernel does not adequately address the noise present in the displacement data. Therefore, we propose an analytically-based modeling before the INV analysis.

Secondly, coherence loss is a significant limitation when using InSAR techniques, especially for those densely-vegetated areas, which is often found for landslide cases in mountainous regions. To tackle this issue, the ground-based artificial CRs are very good auxiliaries for InSAR measurements in increasing the number of the measurement point. However, no universal solution for designing CRs would work equally well for all operational satellites. In our study, we carried out experiments to assess the performance of our newly designed small DCRs in monitoring post-failure kinematics, which could be utilized in both ascending and descending satellite data. It can also be suitable for both medium-resolution and high-resolution images. Such small DCRs lack the strong echoes found in traditional large triangular CRs. To address challenges like biased GNSS positioning or interference from other scatterers and to identify our DCRs in SAR images correctly, we propose a selection strategy based on variations in pixel power resulting from the installation of CRs. This strategy utilizes different properties and characteristics of the CRs to ensure accurate identification.

Thirdly, when using spaceborne remote sensing techniques to monitor slope instability, the mechanism of landslides can be complex. In many cases, landslides begin as slow-moving events, with speeds ranging from a few millimeters to several meters per year (Lacroix et al., 2020). Due to the variety of landslide types, it is difficult to observe them all using a single spaceborne sensor. Furthermore, each sensor has unique advantages and

disadvantages, e.g., spaceborne optical imaging being beneficial for measuring large-scale displacement. However, accuracy can be impacted by factors such as measurement precision, alignment error between relevant image pairs, and interpolation methods (Debella-Gilo and Kääb, 2011; Delacourt et al., 2004). In addition, acquiring cloud-free images during rainy seasons or in mountainous regions can be challenging. Finally, assessing the physical characteristics of catastrophic landslides, such as velocity and friction, can be extremely difficult due to the temporal gap between suitable imagery when applying optical remote sensing (Lacroix et al., 2020). In contrast, InSAR technology can monitor subtle ground motions, but the displacement measured is limited to one-fourth of the wavelength between adjacent pixels (Singleton et al., 2014; Jiang et al., 2011). InSAR technology is inappropriate for monitoring rapid displacements exceeding the threshold limit, such as glacier motion, seismic deformation near faults, and catastrophic failures. Additionally, SAR sensors are not sensitive to deformation in the N-S direction. GNSS measurements could improve the reliability of horizontal components of InSAR observations, but GNSS data may be unavailable in remote areas. Only a few particular landslide cases in hot-spot areas can be continuously analyzed and monitored with GNSS. Therefore, a methodology that integrates multiple techniques is required to monitor the complicated procedures for landslide disasters.

## 3.2 Proposed Methodology

### 3.2.1 Analytically-based Modeling for Inverse Velocity

In order to obtain accurate fittings that capture the relevant features and minimize the influence of noise, we propose an analytical approach for smoothing the displacement values obtained through MTI processing. Our method utilizes least squares adjustment and L1 regression, assuming that the displacement within the landslide area remains relatively constant after the primary failure. We introduce parameters and thresholds that reflect the limitations of MTI processing precision. This approach effectively removes disturbances and smooths the MTI time series.

In specific, we modeled the fluctuated displacement time series by the following equation:

$$\begin{cases} \arg \min \left\{ \|y - x\|_2^2 + \lambda \|Ax\|_1 \right\} \\ c_1 \leq x_{i+1} - x_i \leq c_2 \end{cases} \quad (3.1)$$

where  $y$  represents the observation,  $x$  is variable,  $A$  comprises the sparse matrix for the tridiagonal representation of the standard second difference operator, and  $\lambda$  is the factor balancing the fitting and sparsity.

Since the obtained MTI measurements are characterized by cm to mm precision, we introduce a relatively generous threshold amounting to  $c_1$  is 0.01 meter. Since we do not want to over-smooth the features caused by the landslide failure in the fitting process, the parameter  $c_2$  is not set in this study.

Values of INV will approach zero corresponding to the increasing time as velocities increase asymptotically closer to the failure. Once the smoothed displacements are generated, INV could be derived and thus, a prediction of the failure could be achieved.

More details will be elaborated in Section 4.4.4.



### 3.2.2 Identification of Small-scale CR-like Objectives

We utilize three distinct weighting factors to develop our selection strategy for identifying CRs in SAR images.

- The first factor is the inverse of the amplitude dispersion index, which indicates the stability of the CRs. Higher values correspond to increased stability.
- The second factor considers the intensity increments of pixels after the installation of the CRs. We expect the CRs to improve lower clutter intensity in SAR images, and this factor helps to identify pixels that exhibit such improvements.
- The third factor is an upper empirical bound based on the ensemble average of pixel intensities in sequential images following the deployment of the CRs. This factor sets a threshold to prevent the selection of pixels with stable and strong signals that may originate from sources other than CRs, such as broken roads or buildings on the landslide slope.

After deriving and normalizing all three weighting factors, we use a conditional probability model to calculate the probability of each pixel within the search window being a CR:

$$P_w = P(w_A) \cdot P(w_I|w_A) \cdot P(w_E|w_A, w_I) \quad (3.2)$$

Based on our established parameters, pixels with higher probabilities within the search window are more likely to exhibit features similar to the tested CRs. In our experiment, this selection strategy successfully identified and located the tested CRs in both TSX and S1 images. Our proposed method can also serve as a general strategy for identifying similar targets with CR-like echoes in other cases. To apply this method to other types of CRs, we need only adjust the time interval for estimation and the empirical value for calculation based on the specific properties of each CR.

Additional information on this topic can be found in Section 5.3.2.

### 3.2.3 Modeling 4D Slope Instability Dynamics

In order to monitor and interpret the life cycle of landslides and their failure mechanisms from multiple perspectives, a combination of satellite remote sensing observations, in-situ measurements, and geophysical approaches can be implemented. This thesis proposes a framework that integrates spaceborne optical imaging and InSAR techniques with feature extractions using time series decomposition and a mathematical relaxation model. Figure 3.1 outlines the data-processing workflow and significant steps in this framework.

This approach allows us to assess complete post-failure slope 4D spatiotemporal patterns. By combining multiple remote sensing techniques with feature extraction and relaxation modeling, we can overcome the limitations of individual sensors and gain insights into the complete 4D spatiotemporal characteristics of post-failure landslide deformation. This approach provides a comprehensive understanding of the evolution of landslides, enabling us to monitor and interpret their kinematics more effectively.

The deformation components between optical and SAR observations in the common E-W direction are modeled, indicating the same temporal evolution. The multi-sensor

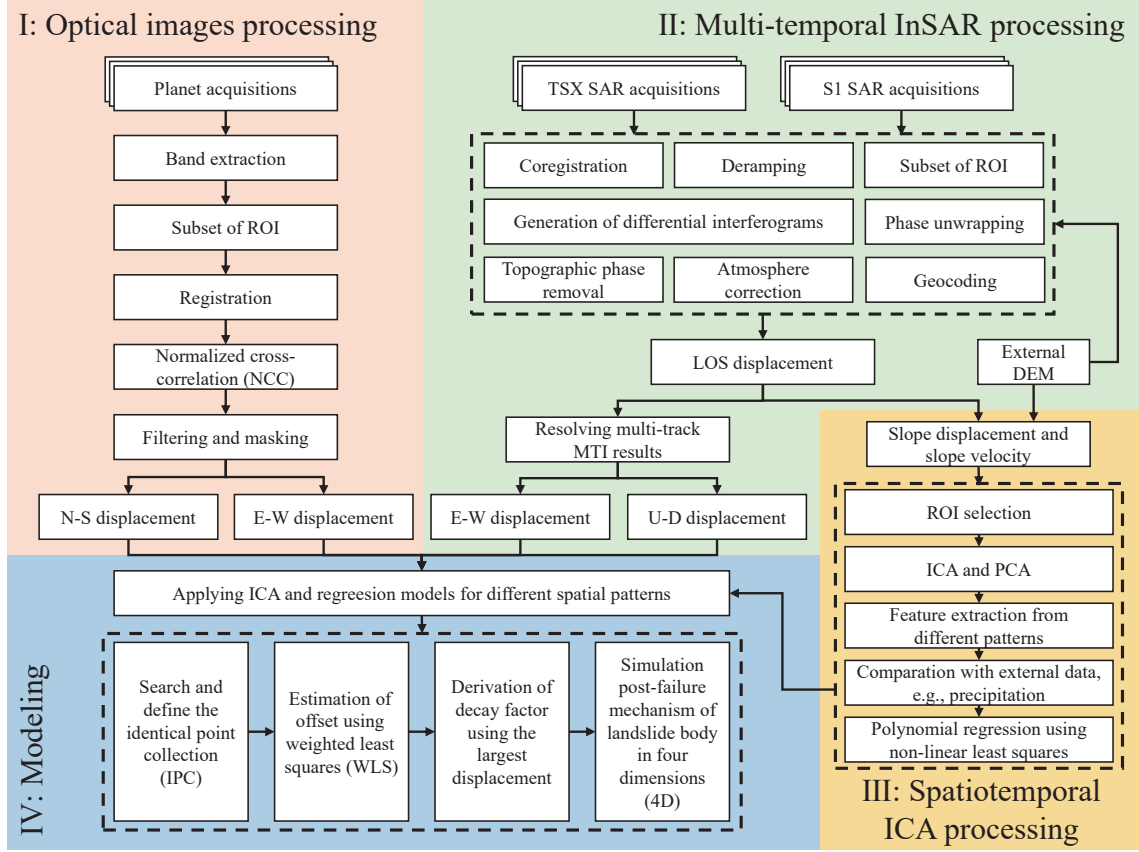


**Figure 3.1:** Flowchart of data processing and the framework of modeling 4D post-failure slope instability dynamics.

remote sensing observations are resolved as follows:

$$\begin{bmatrix} d_{LOS1} \\ d_{LOS2} \\ d_{LOS3} \\ d_{EW-OP} \\ d_{NS-OP} \end{bmatrix} = \begin{bmatrix} \cos\theta_1 & -\sin\theta_1\cos\alpha_1 & \sin\theta_1\sin\alpha_1 \\ \cos\theta_2 & -\sin\theta_2\cos\alpha_2 & \sin\theta_2\sin\alpha_2 \\ \cos\theta_3 & -\sin\theta_3\cos\alpha_3 & \sin\theta_3\sin\alpha_3 \\ 0 & 1 & 0 \\ 0 & 0 & 1 \end{bmatrix} \cdot \begin{bmatrix} d_U \\ d_E \\ d_N \end{bmatrix} \quad (3.3)$$

where  $d$  represents displacement,  $LOS^{1,2,3}$  are S1 ascending data, S1 descending data, and TSX descending data, respectively.  $\theta$  and  $\alpha$  are inclination angle and heading angle, respectively.

Then, we could conduct ICA modeling different magnitudes of relaxation decaying for the E-W and N-S displacements from the optical images after the primary failure. Similarly, the E-W and U-D displacements for the period of MTI results were resolved with different polynomial regressions following ICA analysis. The process of ICA is achieved assuming that each independent component follows a non-Gaussian probability distribution. The mixed signals and independent components have the following relationship:

$$O_{t \times n} = D_{t \times l} \cdot S_{l \times n} \quad (3.4)$$

where  $O$  is the remote sensing observations,  $D$  represents the mixing matrix, and  $S$  is the decomposed source matrix. The subscripts  $t$  is the number of observations,  $n$  represents pixels in each acquisition, and  $l$  is the number of ICs.

Finally, we continue to integrate the multi-sensor remote sensing data by modeling a mathematical exponential decay to represent the stress relaxation mechanisms of the landslide body after failure. The exponential model helps to link the multi-sensor observations in the temporal domain. The modeling equation has been applied as follows:

$$d_k(t_k) = a_k \cdot e^{t_k/\tau} + c_k \quad (3.5)$$

where  $d(t)$  is the displacement at the time since failure  $t$ , and  $k=x,y,z$ , where  $x,y,z$  represent the E-W, N-S and vertical directions, respectively.  $a$  is amplitude associated with decay,  $c$  is an offset, and  $\tau$  is the decay factor ( $\tau < 0$ ), representing the decelerating phases.

More details on this framework can be found in Section 6.5.



## 4 Pre- and Co-failure: Slope Instability Monitoring Using Spaceborne Remote Sensing

*This chapter was published as:*

**Zhuge Xia**, Mahdi Motagh, Tao Li, and Sigrid Roessner. “The June 2020 Aniangzhai landslide in Sichuan Province, Southwest China: Slope instability analysis from radar and optical satellite remote sensing data.” *Landslides* 19(2), 313–329.

*Author contribution statement:*

**Zhuge Xia** did most of the work, including conceptualization, methodology development, validation, formal analysis, investigation, writing, and visualization. Mahdi Motagh contributed to the discussion and writing. Tao Li and Sigrid Roessner helped in the discussion.

## 4.1 Abstract

A large, deep-seated ancient landslide was partially reactivated on 17 June 2020 close to the Aniangzhai village of Danba County in Sichuan Province of Southwest China. It was initiated by undercutting of the toe of this landslide resulting from increased discharge of the Xiaojinchuan River caused by the failure of a landslide dam, which had been created by the debris flow originating from the Meilong valley. As a result, 12 townships in the downstream area were endangered leading to the evacuation of more than 20,000 people. This study investigates the Aniangzhai landslide area by optical and radar satellite remote sensing techniques. A horizontal displacement map produced using cross-correlation of high-resolution optical images from Planet shows a maximum horizontal motion of approximately 15 meters for the slope failure between the two acquisitions. The undercutting effects on the toe of the landslide are clearly revealed by exploiting optical data and field surveys, indicating the direct influence of the overflow from the landslide dam and water release from a nearby hydropower station on the toe erosion. Pre-disaster instability analysis using a stack of SAR data from Sentinel-1 between 2014 and 2020 suggests that the Aniangzhai landslide has long been active before the failure, with the largest annual LOS deformation rate more than 50 mm/yr. The 3-year wet period that followed a relative drought year in 2016 resulted in a 14% higher average velocity in 2018–2020, in comparison to the rate in 2014–2017. A detailed analysis of slope surface kinematics in different parts of the landslide indicates that temporal changes in precipitation are mainly correlated with kinematics of motion at the head part of the failure body, where an accelerated creep is observed since spring 2020 before the large failure. Overall, this study provides an example of how full exploitation of optical and radar satellite remote sensing data can be used for a comprehensive analysis of destabilization and reactivation of an ancient landslide in response to a complex cascading event chain in the transition zone between the Qinghai-Tibetan Plateau and the Sichuan Basin.

## 4.2 Introduction

Landslides are widespread geological hazards in mountainous regions worldwide. Once a landslide mass loses its stability, it could induce strong destructiveness. Landslide processes are complex and often comprise different process types. Some of them move fast (Quecedo et al., 2004), but several other landslides also take place slowly and steadily at the beginning, and then accelerate suddenly terminating in catastrophic avalanche-type or collapse-like movement styles (De Blasio, 2011). Landslides have occurred more frequently due to increased urbanization, continued deforestation, and increased extreme weather events (Lee et al., 2017; Biasutti et al., 2016; Schuster, 1996). To monitor landslide disasters and build effective early warning systems (EWSs), the adopted technical means should meet at least the following requirements: adequate regional coverage and temporal sampling capacity, sufficient measuring accuracy related to the velocity of the monitored processes, and good cost performance. Ground-based methods, such as continuous GNSS for landslide monitoring, are difficult to set up and implement in mountainous and remote areas (Akbarimehr et al., 2013). Instead, optical and radar satellite remote sensing plays a promising role in driving innovation in large-scale detection, monitoring, and assessment of landslide hazards and can be quite useful to incorporate in the framework of multidisciplinary disaster risk reduction (DRR).

Cross-correlation of optical images can be used to assess the kinematics of large slope failures (Yang et al., 2020; Travelletti et al., 2012). Furthermore, automated and semi-automated approaches using time series of multi-sensor optical images have already been developed to create multi-temporal inventories by identifying landslide areas based on changes in vegetation cover (Yang et al., 2019; Behling et al., 2016). Optical remote sensing data have become more commonly available in recent years and are easily understood and handled by non-experts (Yang et al., 2020). However, clear sky images may not be readily available prior to and during a given landslide event. Moreover, the displacement accuracies retrieved from cross-correlation analyses are highly dependent on the resolution of the optical remote sensing acquisitions and the satellite's precise orbit position and orientation posture (Debella-Gilo and Kääb, 2011). Hence, optical remote sensing has limited use in reliably supporting near real-time hazard assessments and EWSs.

Synthetic Aperture Radar (SAR) offers new opportunities to support the systematic detection and monitoring of landslides over extensive regions and for the development of regional-scale landslide warning systems (Motagh et al., 2013; Bianchini et al., 2013; Herrera et al., 2013; Colesanti and Wasowski, 2006). With synoptic imaging capabilities, under inclement weather conditions and independent of sunlight conditions, SAR techniques provide invaluable information on landslide locations, boundaries and changes to vegetation within landslide bodies, based on the exploitation of radar amplitude and phase information. Advanced Multi-temporal InSAR (MT-InSAR) methods, e.g., Persistent Scatterer Interferometry (PSI) and Small Baseline Subsets (SBAS), can be exploited to evaluate subtle changes in landslide creep rates in response to external triggering factors; these changes can indicate impending failures (Hu et al., 2020; Handwerger et al., 2019; Teshebaeva et al., 2015). The new surge in available SAR data via Sentinel-1 (S1) satellites has provided golden opportunities to use SAR sensors as operational instruments for landslide hazard assessments (Solari et al., 2019) and temporal predictions of large failures (Mantovani et al., 2019). In particular, S1 data have higher spatial resolution and global dual-polarization coverage with improved revisit times of 6–12 days over the data from previous C-band SAR missions such as ERS and Envisat. As S1 data are available at no cost, there has also been growing interest from scholars for objective change detections, landslide hazard assessments, and potential techniques for multidisciplinary DRR (Dai et al., 2020; Dini et al., 2020; Intrieri et al., 2018; Dai et al., 2016; Barra et al., 2016; Feng et al., 2015).

On 17 June 2020, close to Aniangzhai village of Danba County in Sichuan Province of Southwest China, a massive landslide of  $\sim 6$  million  $\text{m}^3$  (Yan et al., 2021) was partially reactivated. The main triggering factors were the undercutting effects and erosion on the toe of the landslide body from the overflow of a dammed lake (height of nearly 8–10 meters), which was created by debris flows coming from the northern Meilong valley comprising a complex cascading event chain. Firstly, the heavy rainfall in summer 2020 induced debris flows in the Meilong valley. With the help of Sentinel-2 (S2) optical images, we observe that the debris flow generated from the valley regions north of the reservoir flowed towards the south. Then, the washed-out stones and soils formed a barrier dam just under the ancient Aniangzhai landslide body and blocked the Xiaojinchuan River, leading to an increase in the water level (seeing supporting material: Figure 4.13). Thereafter, the overflow of the barrier dam, influenced by the discharge of the surplus water from the nearby hydropower station to reduce the flood pressure, undercut the toe of the landslide, resulting in partial reactivation of this ancient landslide body. Soon after the lower part of

the landslide area collapsed gradually. In this case, this specific cascading event chain of “rainfall - debris flows - dammed lake - outburst floods - erosion - landslide” was formed and threatened a dozen villages downstream, resulting in an evacuation of more than 20,000 people to abandon and leave their home towns (Yan et al., 2021).

In this study, we report investigations on ground deformation of the Aniangzhai landslide before and during June 2020 failure using optical and radar satellite remote sensing data. Sub-pixel cross-correlation of high-resolution optical images from Planet is utilized to obtain information on the main landslide failure, e.g., horizontal movement and moving direction. Then, S1 SAR data are analyzed using the MT-InSAR techniques to assess the slope instability between 2014 until the time of failure. The results are then analyzed against changes in meteorological conditions to assess the long-term and transient behavior of the Aniangzhai landslide. We also evaluate a method for anticipating the time of failure based on MT-InSAR results using a modified inverse-velocity method. Finally, we introduce some findings based on the abnormal behaviors of the Normalized Difference Vegetation Index (NDVI) and interferometric coherence over the landslide mass before the failure.

### 4.3 Environmental and Geomorphological Settings

Danba County is located on the southeastern edge of the Qinghai-Tibet Plateau, and Aniangzhai village is located in the center of Danba County. The geomorphological structure of the region comprises high mountains and narrow valleys with an average elevation of approximately 1800 m above sea level (a.s.l.). The June 2020 Aniangzhai landslide is a case of a partial reactivation of an ancient and larger slope failure (Zhao et al., 2021). The original ground surface of the Aniangzhai landslide has an elevation of approximately 2000~2500 m a.s.l. The topographic profile and possible thickness of the landslide body were investigated in a recent study exploiting UAVs (Zhao et al., 2021), suggesting a maximum thickness of approximately 60 meters. Based on our field investigation and Zhao et al. (2021), the vertical component of motion was significant at the head part of the failure; while the landslide slipped down as a whole in the middle-lower part. Therefore, we assume that the Aniangzhai landslide has a rotational-translational mechanism, with rotational component being more significant in the upper part and translational component becoming predominant in the middle-lower part. Moreover, this region is located in the upper reaches of the Yangtze River, which is full of water resources. The foot of the Aniangzhai landslide area reaches the Xiaojinchuan River. There is also a dam nearby, which is very close to the failure region upstream (Figure 4.1). We compared the river courses in June over the last 3 years before the 2020 failure (seeing supporting materials: Figure 4.14). The river courses demonstrate similar extents and appearances in 2018 and 2019, regulated by the reservoir upstream. In contrast, the river course during the 2020 failure event shows major inundation due to surplus water from the reservoir. The annual mean temperature for this region is approximately 14°C. However, due to elevation changes, the differences between the top of the mountain and the valley could be greater than 24°C. Because of the plateau monsoon climate and complicated geomorphology, lots of natural disasters are taken place frequently in this region, especially landslide hazards.

Figure 4.2 illustrates a Skysat optical image and several photos from the fieldwork, in which different zones of the landslide area are highlighted. The high-resolution optical image from Skysat was acquired on 25 November 2020 with an accuracy of half-meter



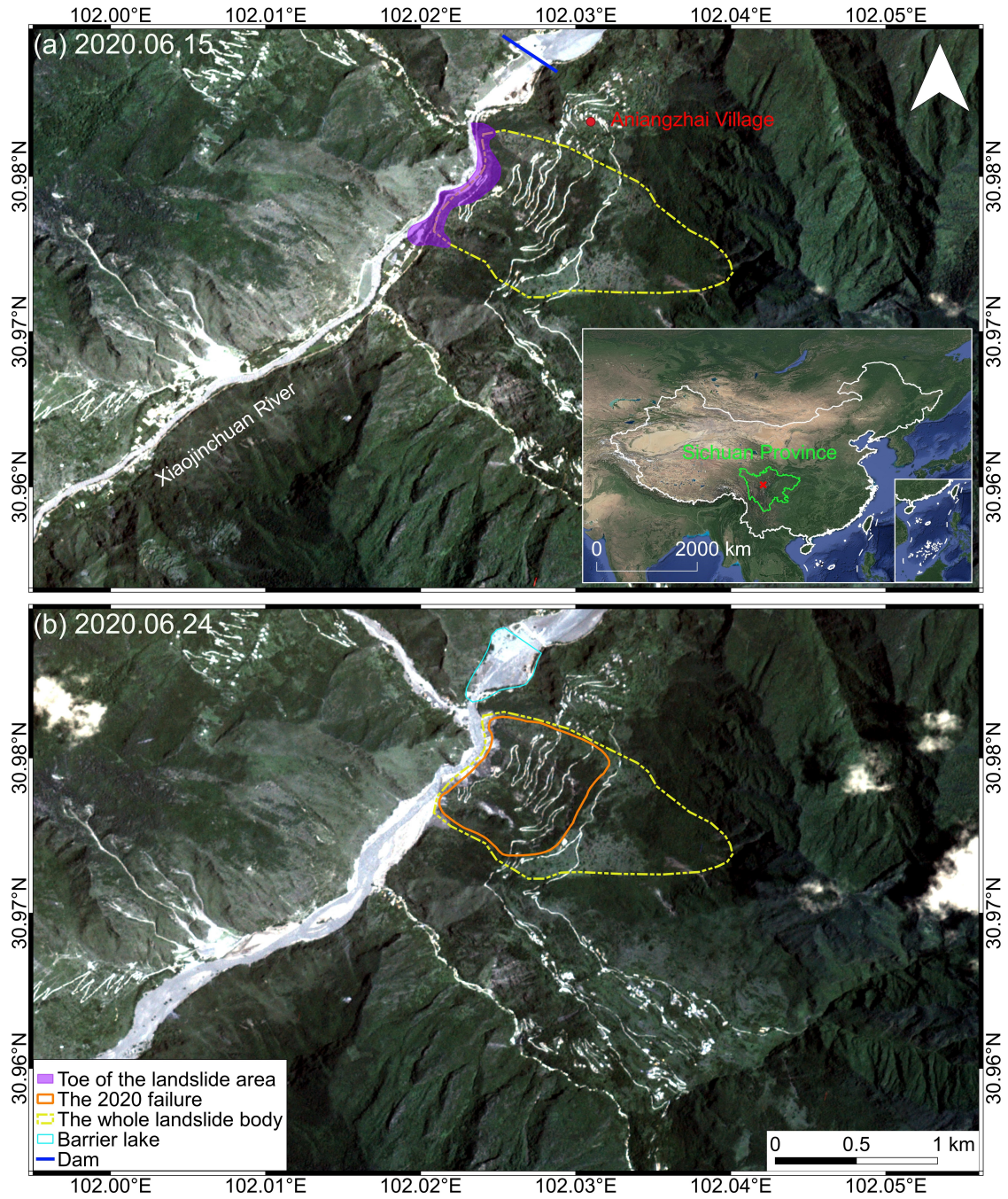


**Figure 4.1:** Location of the study area. Backgrounds are Planet high-resolution remote sensing optical images (RGB bands), which are acquired (a) before the failure on 15 June 2020, and (b) after the failure on 24 June 2020.

(Figure 4.2f). The landslide area lays on the hillside north of the country town, and it was previously described as an ancient rockfall area. The red line in Figure 4.2f, indicates the center part of the failure, which had the largest deformation in this event; the orange line indicates the medium motion of approximately 1~5 meters, whilst the yellow line reveals the extent of the whole landslide body. It is obvious to see the main scarp on the head





**Figure 4.2:** Display of the landslide failure and different zones of the landslide body, as well as examples of damages in the event. (a) Ravaged roads on the edge of the central failure. (b) The northern lateral flank of the landslide. (c) Damaged extra high voltage (EHV) transmission tower. (d) Front view of ravaged roads. (e) The toe of the landslide body. (f) Skysat optical image acquired on 25 November 2020, with the boundaries of three different zones of the landslide, i.e. the red, orange and yellow lines represent the areas with the fast, medium and slow movements in this event, respectively. (g) Cracked house. (h) The southern flank of the center part, which had the fastest displacement rates during this failure. (i) The main scarp of the failure in the southeast direction.

of the failure area, as well as the erosion on the toe of the landslide. As demonstrated in Figure 4.2e, the vegetation on the toe was washed away and a steep valley was formed in the front of the landslide body due to enormous mass loss. And this directly triggered the reactivation of the ancient landslide body. The deformation then started in the upper part, and the whole block was moving downwards.

Figures 4.2b, h and i show the boundaries of the landslide failure. Figure 4.2b reveals the northern lateral flank of the landslide, where cracks, approximately 1~1.5 meters wide, caused by block motion are clearly visible. Figure 4.2h displays the southern flank of the central failure, which had the fastest displacement rates during the 2020 failure. Figure 4.2i shows the main scarp of the failure in the southeast direction. Other pictures reveal examples of damages that occurred in this disaster. Figures 4.2a and d show the ravaged roads, which were broken and had a drop of a few meters. Figures 4.2c and g display a damaged extra high voltage (EHV) transmission tower and a cracked house in this event.

## 4.4 Data and Methodology

### 4.4.1 Remote Sensing Optical Images

We use two high-resolution optical satellite images acquired by Planet Lab (Team, 2017) satellite constellation to assess the horizontal kinematics of the failure, i.e. extent, direction and magnitude. The satellite data is acquired right before and after the event, i.e. on 15 June 2020 and 24 June 2020, respectively (Figure 4.1). The used Planet Lab satellite imagery has a resolution of about 3 meters. Indeed, the horizontal displacements are quite obvious when these two images are superimposed on each other. The Planet Lab images comprise three multi-spectral bands covering the visible part of the spectrum (RGB). The red band is used in this study with the best root-mean-square error in image registration among these three bands. The two Planet images are cropped to the same subset covering the landslide area forming the input to the cross-correlation analysis using the COSI-Corr software package to estimate the horizontal displacements (Leprince et al., 2007). The cross-correlation is estimated with steps of  $2 \times 2$ , which provides the east-west (E-W) and north-south (N-S) horizontal displacements calculated by every two steps. Then a median filter is applied. In the end, the magnitude of displacement in each pixel is calculated as the norm of vectors from the results in two directions.

### 4.4.2 MT-InSAR Analysis Using Sentinel-1 SAR Data

We apply the C-Band SAR images acquired by S1 satellite for MT-InSAR analysis in this study (Copernicus, 2020), specific information of the acquisition can be found in supporting materials (Table 4.4). In detail, the InSAR processing is carried out immediately after the failure with 89 descending images of S1 Interferometric Wide (IW) swath mode from October 2014 to July 2020. Among them, a few images in 2014–2015 cover the study area partially and they are stitching together for the exploitation. The spatial resolution is approximately  $5\text{m} \times 20\text{m}$  with a 250 km swath. There are both ascending and descending datasets available. As seen from optical images, the main direction of the slope is towards the north-west, which causes foreshortening effect in ascending data. Thus, the descending data are selected for our analysis in this case. Due to the temporal gap of the original dataset in 2017–2018, the MT-InSAR processing is carried out in two temporal frames, i.e. 2014–2017 and 2018–2020.

During the processing, the time series of SAR images are well-coregistered and then cropped to the identified subset of the landslide area. The subset covers an area of approximately 26 square kilometers ( $4.7 \times 5.6$  km). The 2000 SRTM DEM (30m) is utilized for geocoding and estimating the topographic phase component in InSAR processing (Farr et al., 2007). The processing chain of S1 has already been mentioned in many previous

**Table 4.1:** Parameters investigated for analyzing slope instability before failure using Google Earth Engine (GEE), parameters of SAR images from S1A are listed together for comparison as well.

Exploited dataset		Temporal resolution	Spatial resolution	Duration of exploited dataset
SAR images	Sentinel-1A	12 days	5m $\times$ 20m	Oct 2014 to June 2020
Rainfall	CHIRPS	daily	0.05° ( $\sim$ 5km)	Jan 2000 to June 2020
NDVI	MODIS	daily	500m	Jan 2014 to May 2021
NDVI	Landsat-8	16 days	30m	Jan 2014 to May 2021
NDVI	Sentinel-2	5 days	10m	Dec 2018 to May 2021

studies (Haghshenas Haghighi and Motagh, 2017; Fattahi et al., 2016; Grandin et al., 2016; Yagüe-Martínez et al., 2016). The traditional InSAR has limitations for landslide monitoring. The main limitations are the widespread loss of coherence between consecutive image acquisitions and atmospheric disturbances (Wasowski and Bovenga, 2014; Zebker et al., 1992). Thus, we apply the advanced MT-InSAR techniques to mitigate the problem and retrieve the information of displacement, i.e. PSI and SBAS methods. The GAMMA and StaMPS software packages are used for the implementation of interferometric and MT-InSAR analysis (Wegmüller et al., 2016; Hooper et al., 2012, 2007), with atmospheric correction obtained using the Generic Atmospheric Correction Online Service (GACOS) product (Morishita et al., 2020; Wang et al., 2019). In PSI processing, a stack of single-master interferograms is generated and the pixels with the highest signal-to-noise values are selected (Hooper et al., 2007, 2004). Such pixels are regarded as Persistent Scatterers (PS), mostly come from rocks and man-made features. As for the SBAS method, the algorithm exploits a network of small temporal and spatial baselines to minimize the decorrelation between image pairs (Andersson et al., 2009; Lanari et al., 2007). The distributed scatterer (DS), which is defined as the pixel that shares similar statistical behavior with its neighbouring pixels, is taken into account. MT-InSAR baseline networks and selecting criteria can be found in supporting materials (Figure 4.15). With the help of MT-InSAR techniques, we could obtain comparable results between PSI and SBAS methods for analyzing slope instability. In addition, MT-InSAR time series are further exploited using inverse-velocity (INV) theory to predict the time of failure.

#### 4.4.3 Auxiliary Data

To better understand the dynamics of the Aniangzhai landslide in relation to potential influencing factors, some auxiliaries are exploited (Table 4.1). The first auxiliary includes precipitation retrieved from the Climate Hazards Group InfraRed Precipitation with Station data (CHIRPS). Spanning all longitudes, CHIRPS incorporates 0.05° resolution ( $\sim$ 5km) satellite imagery between 50°S-50°N and in-situ station data to create gridded rainfall time series. The precision of the rainfall datasets is sufficient for applications and exploitation at the regional scale. In our study area, available CHIRPS data cover a time span of 20 years between 2000 and 2020, and the precipitation is calculated for Danba County.

The second auxiliary includes multiple optical remote sensing collections to obtain NDVI values. The NDVI value is calculated as follows:

$$\text{NDVI} = \frac{\text{NIR}-\text{RED}}{\text{NIR}+\text{RED}} \quad (4.1)$$

where RED is the red portion of the electromagnetic spectrum and NIR is near-infrared light. In this study, NDVI time series from three different satellite datasets are exploited and compared. Details can be found in Table 4.1. The MODerate-resolution Imaging Spectroradiometer (MODIS) Reflectance product MCD43A4 provides daily reflectance data adjusted using a bidirectional reflectance distribution function (BRDF). Data of both Terra and Aqua satellites are used in the generation of this product, providing the highest probability for quality assurance input data (DAAC, 2021). For comparison and validation, two other collections of optical remote sensing satellites are applied, i.e., the Landsat-8 collection (16-day temporal resolution and 30-meter spatial resolution), and S2 data (5-day temporal resolution and 10-meter spatial resolution). To be noticed is that the S2 dataset for this study area is only available since late 2018.

The precipitation and NDVI analyses were conducted with the help of the Google Earth Engine (GEE). We developed our own scripts to generate the monthly-mean and yearly precipitation during 2000–2020 for Danba County for further exploration in this study; whilst NDVI is calculated or obtained for the slope affected by the landslide from the mentioned three satellite collections during different periods (Table 4.1). The NDVI values are further compared with the interferometric coherence. The purpose of the comparison is to see whether some features could be obtained for early warning without complex MT-InSAR processing (Jacquemart and Tiampo, 2021).

#### 4.4.4 Inverse-velocity Theory for Anticipating the Time of Failure

When landslides, rockfalls and similar hazards are investigated, one of the major interests is to predict a potential time range when a failure might be likely to happen. For this goal, already several approaches have been developed, among them, the INV method which is considered to be a simple but effective method for EWS being used in many studies during recent years (Zhou et al., 2020; Carlà et al., 2017).

In order to apply INV, the first step is to calculate the velocity of LOS displacement from the time series of displacement. The calculation of landslide velocity is always a complicated problem. On the one hand, the strength parameters for different landslide types should be considered in the calculation. On the other hand, the friction coefficient and friction resistance will change with different stages of activities and the volumes of the landslide (De Blasio, 2011). The key challenge is that in reality the observations of displacement could be influenced by man-made or systematic noises. Such noises include measurement errors, random instrument noises and noises from periodic changing factors such as rainfall, groundwater, human activities, etc. These noises could lead to outliers and abnormal behaviors for INV, which makes data smoothing necessary. In previous studies, some approaches are exploited to generate the smoothing of the displacement, such as short-term and long-term moving averages and exponential smoothing functions (Carlà et al., 2017; De Blasio, 2011). In this study, we have applied these different approaches, but the outcomes have not been satisfying. The reason for this is, if the kernel of the smoothing function is too large, the filtered curve would possibly lose some important features, whilst the noise in displacement could not be improved using a smaller kernel.

In order to obtain ideal fittings which capture the relevant features and to mitigate the influence from noises, we propose a method to smooth the displacement values obtained by MT-InSAR processing. The method uses least squares and L1 regression under the assumption that after the main failure has happened, the further displacement occurring within the landslide area remains more or less constant. In this context, we introduce the parameter  $c$  to represent the limitations of the measurements, whereas  $c_1$  and  $c_2$  represent the minimum and maximum detectable displacements, respectively. In specific, if the magnitude of displacement is larger than  $c_1$ , then the slope movement is considered to occur in form of sliding. Since the obtained MT-InSAR measurements are characterized by cm to mm precision (Haghighi and Motagh, 2019; Motagh et al., 2017; Wang et al., 2012; Osmanoglu et al., 2011), we introduce a relatively generous threshold amounting to  $c_1$  is 0.01 meter. Since we do not want to over-smooth the features caused by the landslide failure in the fitting process, the parameter  $c_2$  is not set in this study. In the result, we calculate the smoothed displacement by the following equation:

$$\begin{cases} \arg \min \left\{ \|y - x\|_2^2 + \lambda \|Ax\|_1 \right\} \\ c_1 \leq x_{i+1} - x_i \leq c_2 \end{cases} \quad (4.2)$$

where  $y$  represents the observation,  $x$  is variable and  $A$  comprises the sparse matrix for the tridiagonal representation of the standard second difference operator, and  $\lambda$  is the factor balancing the fitting and sparsity. To solve (4.2), a package for solving convex optimization problems (Grant and Boyd, 2008, 2014) was used, to derive  $x$  that minimizes expression (4.2) being subject to the constraints while using identical parameters. Values of INV will approach zero corresponding to the increasing time as velocities increase asymptotically closer to the failure. Once the smoothed displacements are generated, INV could be derived and thus, a prediction of the failure could be achieved.

## 4.5 Results

### 4.5.1 Horizontal Displacement Based on High-resolution Optical Images

Figure 4.3 illustrates the horizontal displacement calculated from Planet optical images for a short period of time comprising the situation right before and after the failure, i.e. 1 day before the failure and 8 days after the failure. The applied two Planet images are shown as background in Figure 4.3. The main component of the horizontal displacement occurs in the E-W direction with a maximum displacement of approximately 13.2 meters towards the west. In the N-S direction, the displacement is oriented towards the north with a maximum displacement of approximately 6.9 meters. Overall, the absolute horizontal displacement is estimated as the norm of vectors from displacements in N-S and E-W directions, and the maximum magnitude reaches approximately 14.7 meters in the N-W direction. The result also demonstrates that some localized deformations exist out of the main body of the failure, mainly in the northwest and southwest corners of the area shown on the image in Figure 4.3. The moving directions of those localized deformations are different compared to the ones obtained for the main failure. This subset area is shown with significant motion comparing to the surrounding areas. From Figure 4.3, we can see that the maximum horizontal displacement rate could reach  $\sim 1.6\text{m/day}$ , which is too large to be applied using InSAR monitoring (Crosetto et al., 2016).



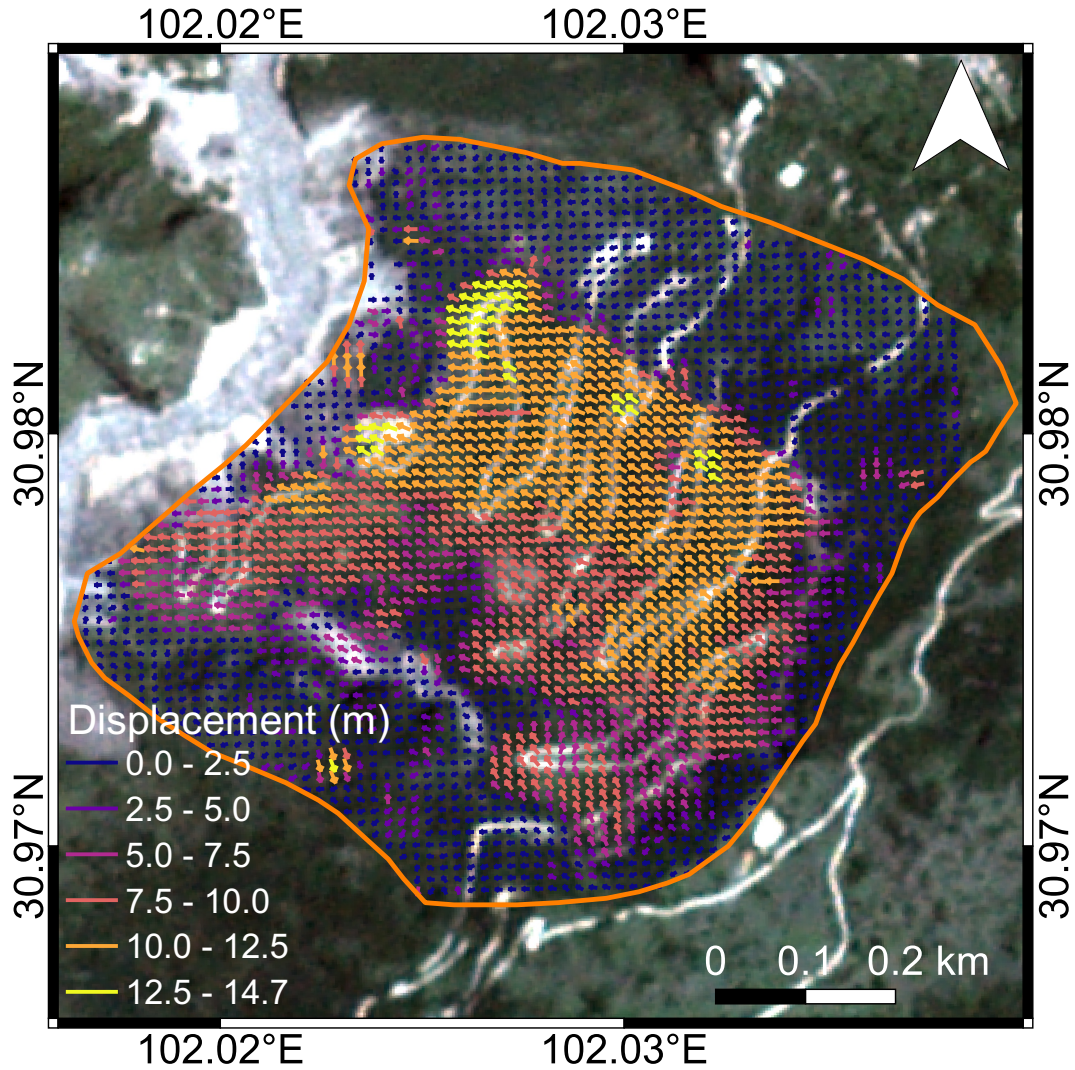


**Figure 4.3:** 2D results of horizontal displacement (Duration: 15 June 2020 and 24 June 2020) generated using Planet optical images. The lengths and directions of the arrows represent the magnitudes and the moving directions of motion. The orange line represents the failure area (same as in Figure 4.2).

#### 4.5.2 MT-InSAR Analysis

Figure 4.4 shows a comparison of the results of MT-InSAR processing for the two different periods using both PSI and SBAS methods. The displacement rates have been derived in line-of-sight (LOS) direction, whereas positive values represent motion towards the satellite, whilst the negative values represent motion away from the satellite. The reference point, representing a stable area during the whole time period is selected outside of the landslide region in the northern hill slope. From the MT-InSAR analysis, it is deduced that the area of the June 2020 failure had already experienced movements prior to the actual failure, especially in the center part of the landslide body.

As seen in Figure 4.4, the creeping movement could already be revealed within the landslide body for the time period of 2014–2017. In this period, the maximum displacement

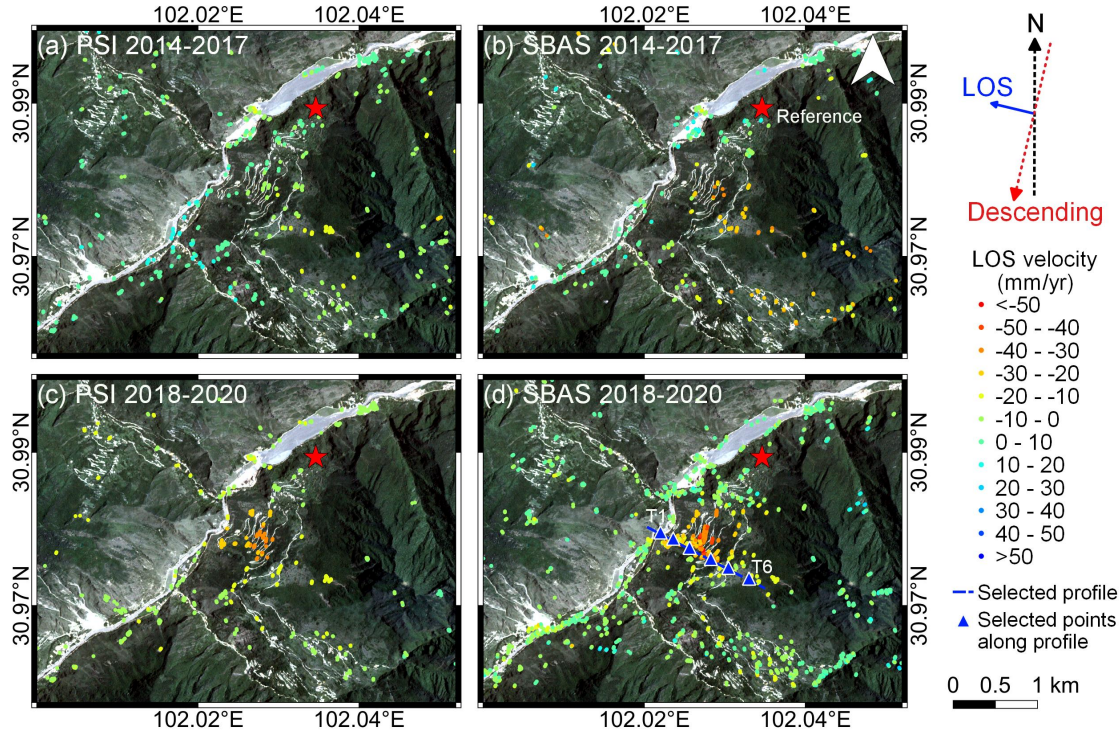


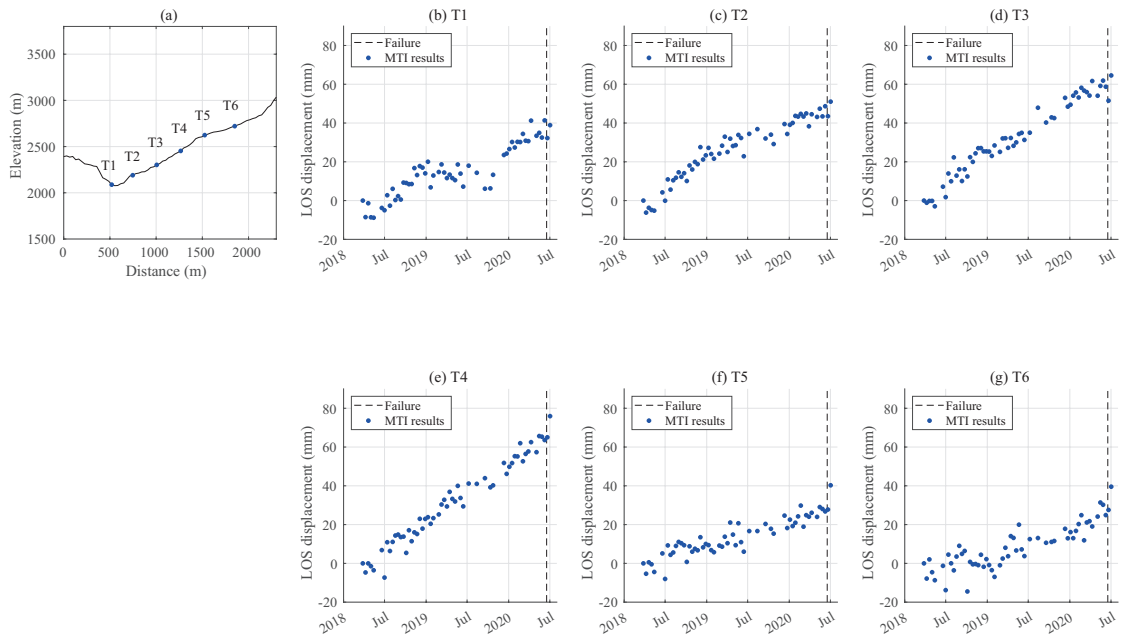
**Figure 4.4:** Comparison of MT-InSAR results for (a) PSI in period of 2014–2017, (b) SBAS in 2014–2017, (c) PSI in 2018–2020 and (d) SBAS in 2018–2020; the blue line and triangles in (d) show the location of the selected topographic profile and points analyzed in Figure 4.5. Image background is comprised of the Planet optical image acquired on 15 June 2020.

**Table 4.2:** Relevant statistics of MT-InSAR results for the ancient slope failure reactivated in 2020 (Figure 4.1). Parameters for the PSI and SBAS results (Figure 4.4) of the two periods are listed respectively.

Statistics (Unit:)	Number of PS/DS (-)	Max. disp. (mm)	Max. velocity (mm/yr)	Mean velocity (mm/yr)
PSI 2014–2017	180	-55.7	-23.8	-12.9
SBAS 2014–2017	133	-88.4	-37.8	-14.7
PSI 2018–2020	167	-91.6	-40.3	-15.6
SBAS 2018–2020	342	-124.1	-54.6	-17.9

rate in LOS direction amounts to approximately -24 and -38 mm/yr, for the PSI and SBAS methods, respectively. For the 2018–2020 period up to the failure, the displacement rates within the area of the June 2020 failure have significantly increased compared to the 2014–2017 period, reaching the maximum of approximately -40 and -55 mm/yr for the PSI and SBAS results, respectively, in the center of the landslide body. Moreover, the areas outside of the landslide failure turn out to be stable in general. The relevant statistics for the PSI and SBAS results for the ancient slope failure reactivated in 2020 can be found in Table 4.2.





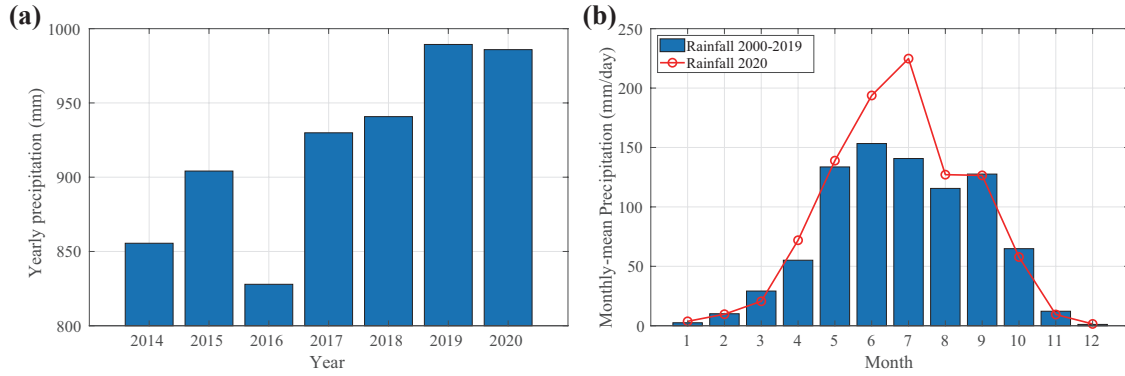
**Figure 4.5:** Plotting of (absolute) LOS displacements along a topographic profile for the SBAS results in 2018–2020. The location of the profile is shown in Figure 4.4d. (a) The selected topographic profile. (b)–(g) show the MT-InSAR results of points along the selected profile from northwest to southeast.

Figure 4.5 shows a comparison of displacement time series along a selected topographic profile (marked by blue in Figure 4.4d) for the SBAS results in 2018–2020. Point T1 is situated on the channel floor and points T2–T4 are located on the partial failure part; while T5 and T6 are situated on the upper part of the ancient landslide and outside of the failure body. The displacements rates of selected points in the top (T5 and T6) and bottom (T1 and T2) zones are smaller compared to the displacements rates in the central failure zones (T3 and T4). Meanwhile, the central failure zones have a relatively larger slope inclination compared to the top and bottom zones. The above results are further elaborated in the Discussion.

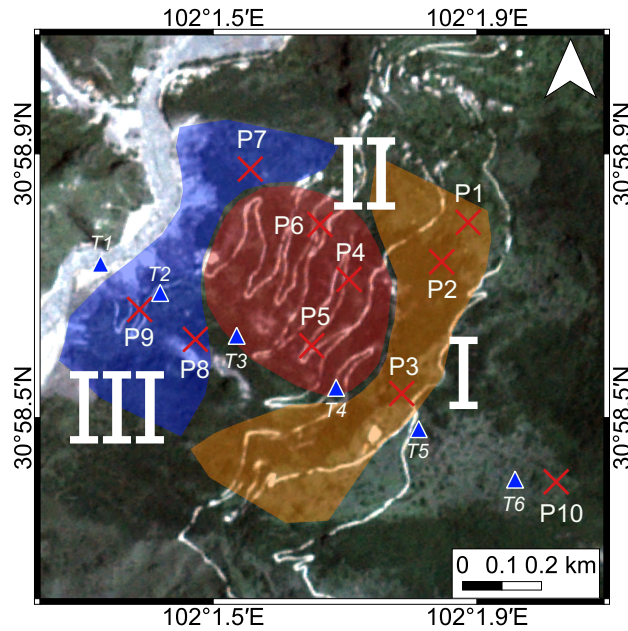
### 4.5.3 Influence of Precipitation on the Kinematics of the Landslide

Figure 4.6a demonstrates the annual precipitation amounting to 855.5 mm in 2014, then increasing by 5.7% in 2015, but decreasing by 9.0% in 2016. In contrast, for the period of 2017–2019, we observe a constant increase by 12.3%, 1.1% and 5.2% respectively compared to the previous year. Figure 4.6b shows that from April to June 2020, rainfall is 30.5%, 4.0% and 26.4% higher than the long-term average for the last 20 years, respectively.

To better quantify the role of the 2020 heavy precipitation in influencing the kinematics of the landslide, we focused on the 2018–2020 period and analyzed the time series of LOS displacements at different parts of the landslide. Figure 4.7 illustrates the locations of ten points selected arbitrarily over the whole landslide body: points P1–P3 from the head of the failure part (Zone I); points P4–P6 from the central failure body (Zone II); points P7–P9 from the foot of the landslide (Zone III); and point P10 from the landslide body, but outside of the 2020 failure.



**Figure 4.6:** (a) Annual precipitation within Danba County for period of 2014 to 2020. (b) Comparison of monthly-mean precipitation for period of the last 20 years with precipitation in 2020.



**Figure 4.7:** Location of arbitrarily selected points (P1–P10) over the landslide body. The region is classified according to the behavior of these points from spring 2020 until the failure; P1–P9 are within the failure region while P10 from the landslide body is located outside of the 2020 failure. T1–T6 are the selected points along topographic profile as shown in Figure 4.4d. The background image is from Planet optical image.

The results of MT-InSAR time series for the selected points are displayed in Figure 4.8; the dot lines show the time series retrieved from the SBAS processing, while the blue lines represent the fitting curves obtained based on the smoothing methodology described in Section 4.4.4. As seen in Figure 4.8, points P1–P3, which are located in Zone I, show accelerations and decelerations throughout the entire time series with a clear accelerating trend as of spring season in 2020. In contrast to points P1–P3, the displacement rates at points P7–P9 are relatively lower; they exhibit periods of acceleration in the step-wise pattern and a constant velocity at the end of the time series. Points P4–P6 in the center region show the highest displacement rates among all the selected points with fewer

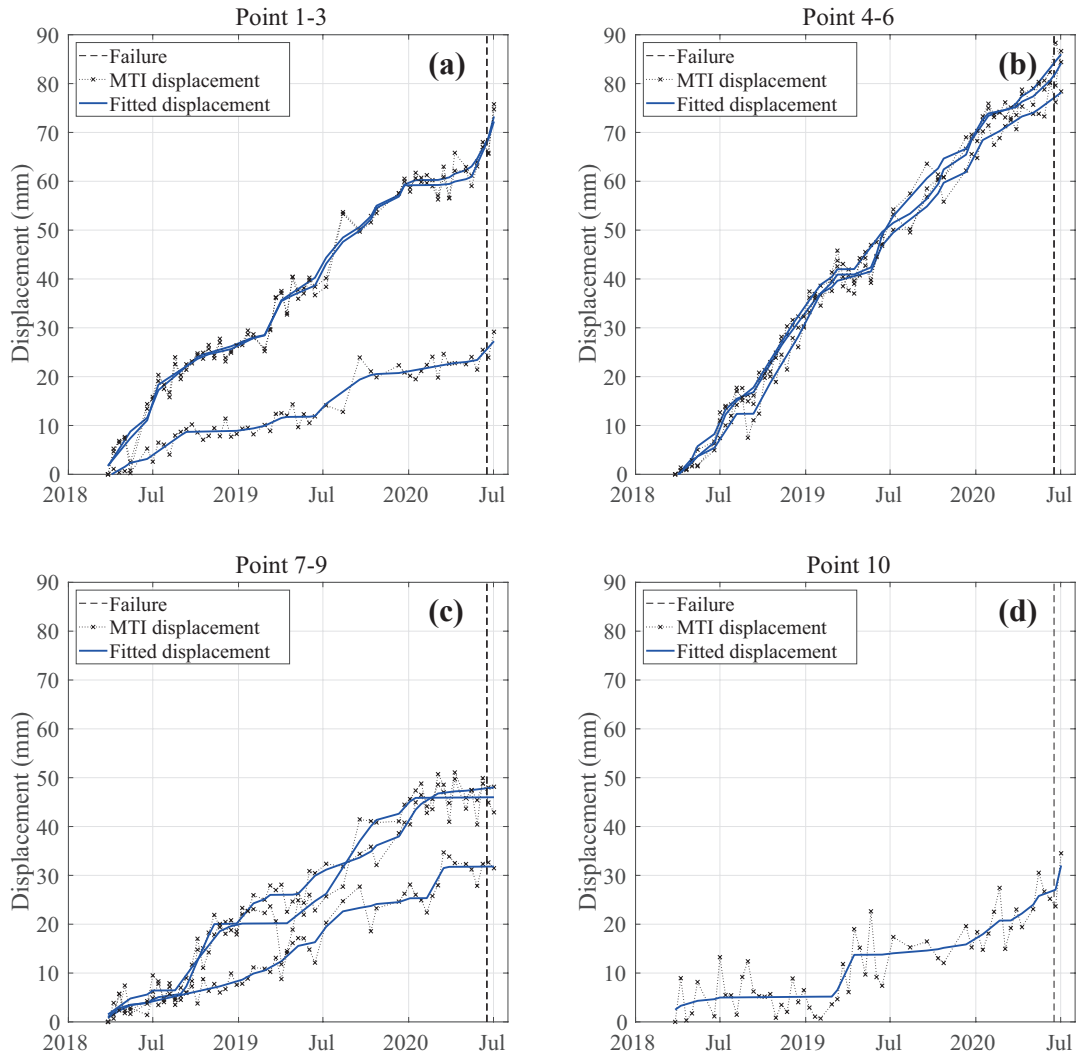


**Figure 4.8:** LOS displacements for period of 2018–2020 for SBAS result and the corresponding fittings of points (a) P1–P3, (b) P4–P6, (c) P7–P9 and (d) P10. The locations of points have shown in Figure 4.7.

variations in overall velocity compared to other parts of the landslide, although some periods of slowing-downs and accelerations occur in the same period as in case of points P1–P3 (e.g., in June 2019). Point P10, located outside of the 2020 failure, reveals a steady movement at the beginning, punctuated by a short episode of acceleration in March–April 2019 and another obvious acceleration since spring 2020.

Figure 4.9 reveals the comparison of the LOS velocity of points P1–P3 on the image of Figure 4.9a and the corresponding precipitation in the period of 2018–2020. These three points are selected for INV processing due to the strong correlation of the simultaneous speeding up of their displacement rates in response to the increasing cumulative precipitation in the rainfall season. Obviously, there are three rainfall seasons in Figure 4.9b, corresponding to the rainy months of May to September. We calculate the increments of

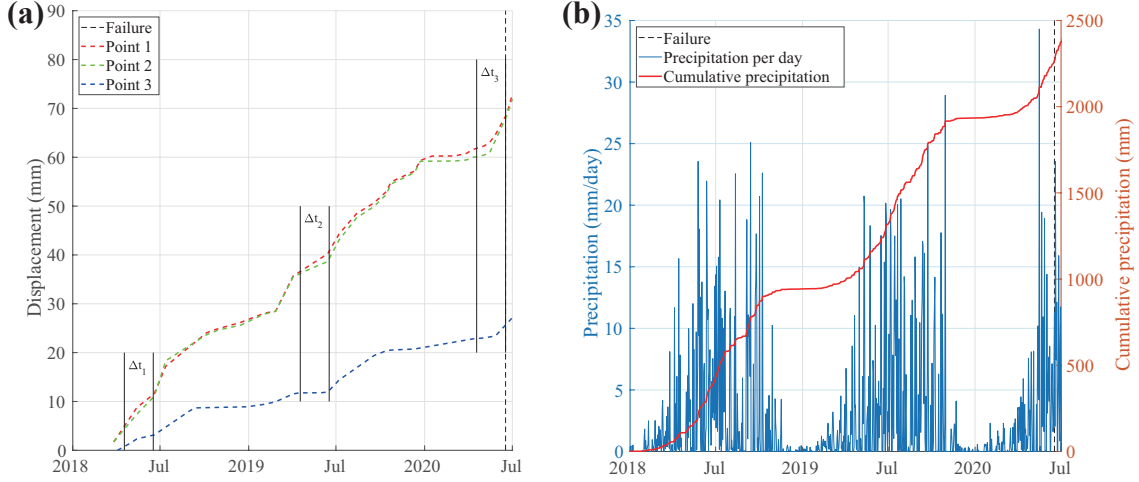


**Figure 4.9:** Comparing of landslide kinematics with the corresponding precipitation in points P1–P3. (a) Fitted LOS displacements of points P1–P3 from 2018 to 2020. The marked periods are mid-April to mid-June in the three rainy seasons before the failure. Relevant statistics of increments are listed in Table 4.3. (b) The daily and cumulative precipitation from 2018 to 2020.

**Table 4.3:** Increments of precipitation and the corresponding increments of LOS displacement of points P1–P3 from mid-April to mid-June in 2018–2020.

Increment	$\Delta t_1$	$\Delta t_2$	$\Delta t_3$
Rainfall (mm)	247.79	217.03	264.49
Displacement in P1 (mm)	6.49	4.14	6.58
Displacement in P2 (mm)	6.49	3.02	7.86
Displacement in P3 (mm)	2.33	0.50	2.78

the precipitation in different years and then compare this with the amount of changes in the corresponding LOS displacements of the selected points in the same duration. The results are displayed in Table 4.3. Here we observe that for the first time period of mid-April to mid-June in 2018, where rainfall reaches 248 mm, approximately 6.5, 6.5 and 2.3 mm increases in displacement values are observed at points P1–P3, respectively. Interestingly, compared to the period  $t_1$ , the increments of displacement in  $t_2$  of these points decline corresponding to the reduced rainfall, i.e., when the rainfall in  $t_2$  drops by approximately 12%, the variations of displacement of points P1–P3 also drop by approximately 36%, 53% and 79%, respectively. However, for the third time span  $t_3$ , we can see that since the rainfall raises by 22% compared to  $t_2$ , the displacement increments of points P1–P3 also increase by 59%, 160% and 456% than the values in  $t_2$ .

#### 4.5.4 INV Results for Anticipating the Time of Failure

Figure 4.10 demonstrates the results of INV analyses. In Section 4.4.4, we described anticipating the time of failure using the modified INV theory. The period considered in the INV analyses is from April 2020 to mid-June 2020, which is affected by the heavy precipitation before the failure, and is the same for all the selected points. It is worth

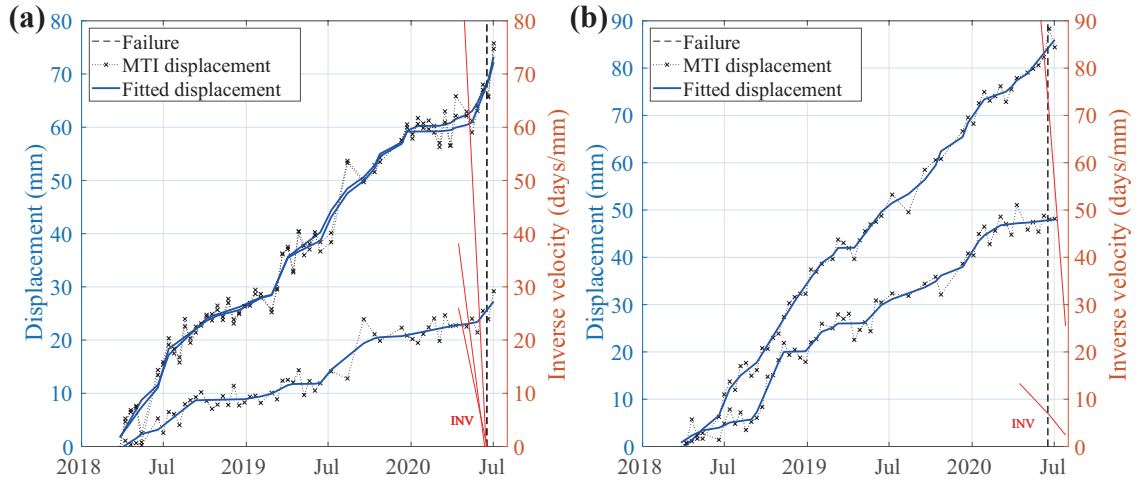


**Figure 4.10:** (a) Results of INV analysis for points (a) P1–P3 and (b) P5 and P7. Red lines display the results of INV, whereas the black dashed lines show the actual failure time.

noting that, the areas with accelerating LOS displacement before failure are needed to be evaluated for INV analysis (Manconi and Giordan, 2016). Otherwise, the method leads to underestimation or overestimation of the failure time. This has been shown in Figure 4.10b for points P5 and P7, which are located in an area, where no acceleration was found before the failure. Applying the INV method to these two points resulted in overestimated prediction times, i.e., approximately 20 and 66 days after failure. The results presented in Section 4.4.4 shows that among the whole landslide body, only the top of the failure area indicated accelerated creep since spring 2020 in response to the heavy rainfall (Zone I in Figure 4.7). By performing INV analysis for the points in this area, we observe that the INV can predict the time of failure properly (Figure 4.10a).

#### 4.5.5 Comparison of NDVI and Coherence Values

Figure 4.11a shows the negative correlation between coherence and NDVI (MODIS) in 2014–2020. Regardless of the temporal gap in SAR data availability, the changes in coherence and NDVI show quite an obvious opposite trend. NDVI indicates whether or not the target region being observed is covered by vegetation, while coherence is used to describe changes in backscattering properties and similarities between radar echoes (Wang et al., 2009b). The high NDVI values occur in summer, when the area is covered by more vegetation and thus the coherence becomes low. In contrast, less vegetation and thus, less volume scattering in winter results in higher coherence values for that season. An interesting result from Figure 4.11a is that coherence drops to its lowest values ( $\sim 0.22$ ) over the past six years before the landslide failure. There are another two minimum values for June 2015 and July 2016 in the coherence plot. However, these minima are caused by long temporal baselines between SAR image pairs during these periods.

Figure 4.11b shows the comparison of NDVI values from three different satellite collections pronounced in Section 4.4.3. Due to the limited temporal resolution, NDVI values generated from Landsat-8 could not reveal promising results for detailed monitoring of vegetation dynamics. In contrast, NDVI time series generated from MODIS and S2 show

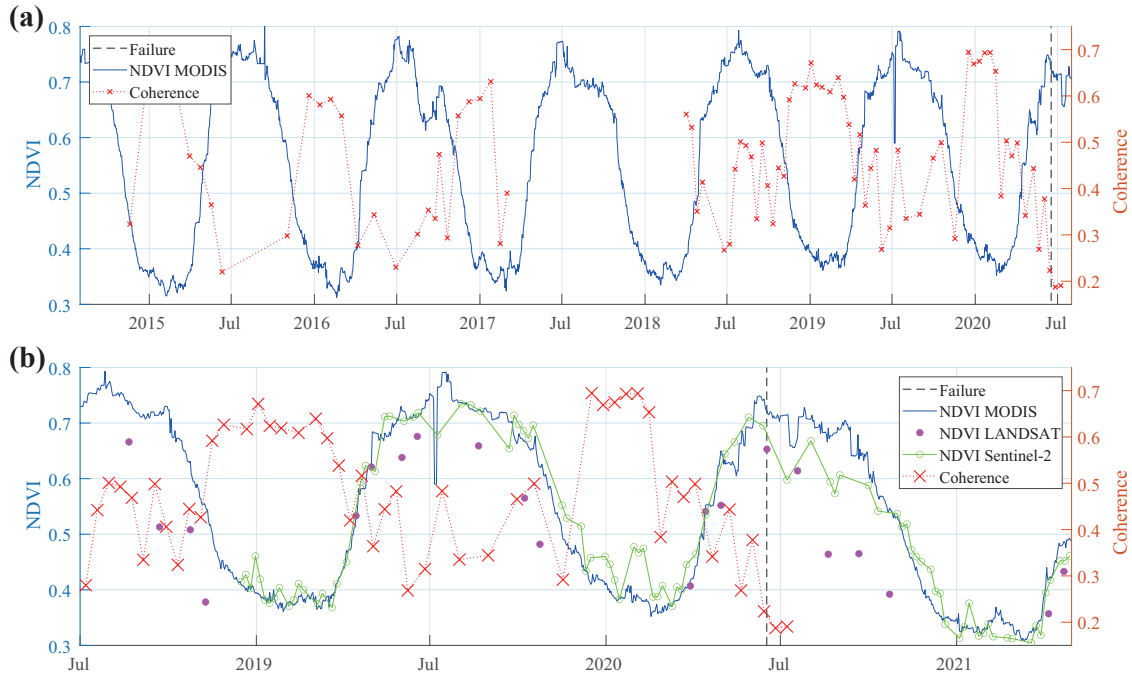


**Figure 4.11:** (a) Comparison of NDVI (MODIS) and interferometric coherence of the 2014–2020 period. The S1 dataset for this region has a temporal gap in 2017–2018. (b) Comparison of NDVI time series from three different satellite collections of the period from July 2018 to May 2021. The NDVI and coherence values are calculated for the same slope area affected by the failure.

good temporal correlation and agreement. Moreover, the two NDVI time series show some declines before the failure, i.e., MODIS-derived NDVI shows two declines of approximately 50 and 10 days before the failure; whilst the one derived from S2 indicates a drop of approximately 20 days before the failure. Reasons for these drops are elaborated in more detail in the Discussion.

## 4.6 Discussion

This study has shown the great potential of applying high-resolution optical and radar satellite remote sensing data and related techniques for the quantitative multi-temporal assessment of surface kinematics related to the 2020 Aniangzhai landslide failure in the mountainous region of Danba County. Generally, optical and radar remote sensing are two methods with their own advantages and weaknesses that can be used to monitor different stages or types of landslides, e.g., from initial slow creep motion to accelerated stage. These methods are complementary to each other and are exploited together in this study.

Based on the optical remote sensing data, the dynamics of the presented cascading events leading to Aniangzhai landslide failure could be clearly observed in their consecutive steps, allowing a comprehensive understanding of the resulting disaster chain. The failure with large displacement as shown in Figure 4.3 is beyond the detective capability of the InSAR technique (Crosetto et al., 2016). Our optical results are similar to the deformation vector distribution of reactivated deposits obtained by Zhao et al. (2021).

However, Zhao et al. (2021) presented the results from tens of monitoring points from 22 June to 12 July, while in our study we derived the horizontal deformation of the whole failure area using optical remote sensing data between 15 June and 24 June. They also concluded that the Aniangzhai landslide slipped down as a whole; as the movement did not change the microtopography, rather the relative positions of points. Our fieldwork supports this observation, e.g., the houses on the failure body were only cracked but not collapsed (Figure 4.2). The flooded areas, as well as the sediments of debris flows, are well demonstrated in the Planet and S2 images, indicating the direct cause and the sources of this event. The main direction of horizontal displacement from Planet optical images also provides a guidance for choosing the 6-year descending dataset in MT-InSAR analysis with a better observation geometry. Moreover, the results obtained from optical images of the June 2020 failure indicate larger deformation on the lower part of the slide compared to its middle and head parts in the large failure zone (Figure 4.3). The explanation for this result could be that the foot of the landslide is closer to the river and is influenced by both water release from the upstream dam and barrier lake to relieve flood pressure. All these factors make the slope more vulnerable to undercutting and erosion, resulting in the large failure on the lower part of the slide. As for the undercutting effects and erosion on the toe of the landslide body, debris flows from the Meilong valley caused by higher rainfall in summer 2020 played a vital role. This is consistent with the conclusions as revealed in Yan et al. (2021). They suggest that the continuous rainfall in 2020 increased groundwater content and reduced the stability of loose sediments in Meilong valley. Then the debris flows formed in Meilong valley washed away loose sediments and bedrocks in the Xiaojinchuan River, a barrier dam was formed just under the Aniangzhai landslide toes and eventually the overflowed current from the barrier dam washed and eroded the foot of the ancient landslide body.

By applying radar remote sensing and MT-InSAR techniques, temporal and spatial variability in the kinematics of the Aniangzhai landslide from 2014 until the 2020 failure could be comprehensively investigated (Figure 4.8 and Table 4.2). Mean LOS deformation rates during pre-disaster stage clearly identifies instability of the landslide, with the largest deformation rates higher than 50 mm/yr in Zone II. The deformation rates, however, change spatially in the entire slope with points located on larger slope angles, i.e., T3 and T4 in Figure 4.5, showing higher LOS displacement rates compared to the other points. Zhao et al. (2021) identified the Aniangzhai slope as showing characteristics of a landslide with a constant deformation state that requires certain prevention measures before entering into next phase of catastrophic failure. Our multi-temporal interferometric results confirm this observation by Zhao et al. (2021) and further show that the long-term displacement rates before the June 2020 failure were not constant; rather, they changed over time. Influenced by above-average precipitation in summer and the 3-year wet period that followed a relative drought year in 2016, we observe that the landslide moved in 2018–2020 approximately 14% faster than in 2014–2017.

To better investigate the role of precipitation in influencing the kinematics of landslides, the statistics on the 2018–2020 period from mid-April to mid-June are analyzed (Table 4.3). This clearly shows how temporal changes in precipitation are correlated with the kinematics of motion of points in Zone I (Figure 4.7). Several InSAR studies have shown that ancient landslides reveal instabilities or even precursors in the form of accelerated creep before the failure (Ao et al., 2020; Handwerger et al., 2019; Teshebaeva et al., 2015), but the source of acceleration could be different. In some cases, e.g., Teshebaeva et al.



(2015), small creeps and accelerations have been correlated well with the increasing seismicity. We have checked the Chinese Earthquake Catalog and searched for earthquakes around Aniangzhai with a radius of 20 km over the last 1 year before the failure. Results, however, show no big earthquake ( $>2.0$ ) occurred in the region; the nearest seismic activity during this period was around 25 km away from Aniangzhai in the southwest direction on 9 January 2020 (M 1.8 and a depth of 10 km). Therefore, we exclude tectonic forces as the source of the accelerated creep in Zone I.

It is worth noting that deep-seated landslides such as Aniangzhai cannot directly react to rainfall, since the changing of groundwater conditions towards activation of the sliding plane requires some time until the surface runoff has been infiltrated to a certain depth (Vallet et al., 2016; Iverson, 2000). In the normal non-flooding seasons, toe erosion of the landslide should be a constantly ongoing process as well, leading to a backward propagation of deformation in the upslope direction until the time of failure (Leroueil and Locat, 2020; Teshebaeva et al., 2015). In this process, rainfall does not play a direct role, but as an indirect one usually occurring with a lag in time (Haghshenas Haghighi and Motagh, 2016; Vallet et al., 2016; Teshebaeva et al., 2015; Iverson, 2000). In our case, however, results show that the lag time is very short as the acceleration occurs almost at approximately the same time when the precipitation increases. More, in-depth geophysical analysis will be needed to investigate the reason behind this short time lag between rainfall and motions in Zone I of this deep-seated landslide. Besides, our results of precipitation analysis also reveal that the formation of debris flows in the Meilong valley could trace back to April 2020 (Figure 4.6 and Figure 4.9), when rainfall was approximately 30% higher than the mean values of the last 20 years. This is consistent with Chen et al. (2005), that the formation of debris flow in this area, i.e. Danba County requires a longer preparatory phase of increased precipitation before a larger rainstorm eventually triggers the onset of the debris flow. All these observations suggest that the ancient Aniangzhai landslide was already active, which eventually failed partially following the undercutting effect in 2020.

The MT-InSAR analysis also provides a good basis for investigating evolution and kinematics of motion in different parts of the Aniangzhai landslide. The smoothing method developed in Section 4.4.4 helped us to properly smooth the data in order to detect the long-term and transient deformation without losing significant information from the data. These results have important implications for developing an early warning system for the Aniangzhai landslide and highlight that InSAR techniques can be used as an operational monitoring system in Aniangzhai to track progressive deformation and potential release areas in near real time in order to mitigate hazards associated with landslide failure (Ao et al., 2020; Carlà et al., 2019, 2018; Hu et al., 2018a). Future works should focus on comparing the performance of moderate resolution S1 images with higher-resolution SAR images from missions like TerrasAR-X or CosmoSky-Med to better investigate the potential and existing limitations in S1 data for landslide analysis (Liu et al., 2020; Hosseini et al., 2018; Milillo et al., 2014; Bovenga et al., 2012).

NDVI analysis using MODIS and S2 data reveals some interesting patterns, which may have the potential for early landslide warnings in the Aniangzhai landslide. As expected, the NDVI values increase while the coherence decreases due to the corresponding increases in the volume scattering. This behavior has been illustrated well in Figure 4.11a, where a negative seasonal correlation is clearly observed between the coherence and NDVI values. Despite having different spatial resolutions, time series of NDVI from MODIS and S2 show good consistency with each other (Figure 4.11b). Two interesting drops are observed in



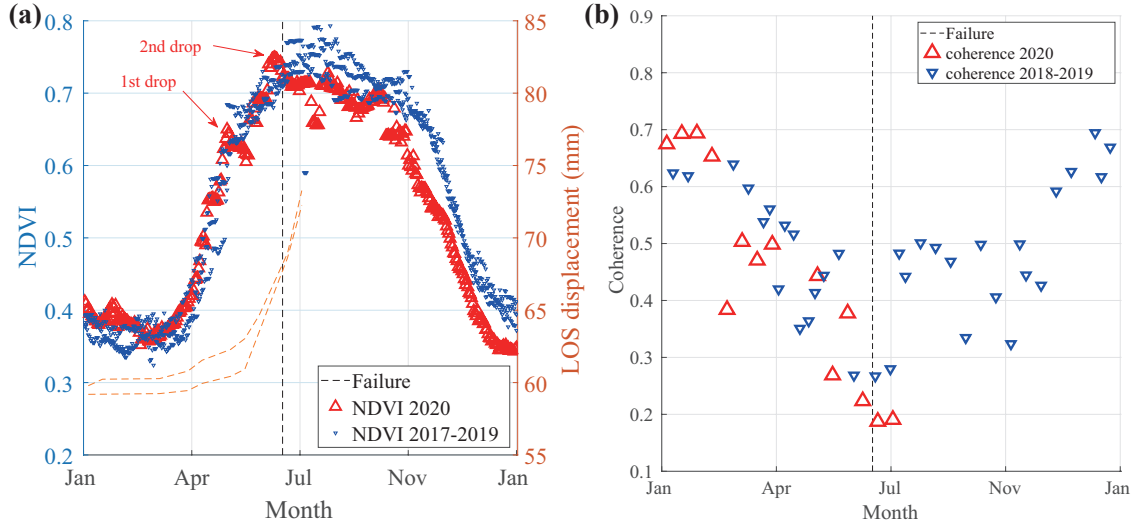


**Figure 4.12:** (a) Comparison of NDVI (MODIS) in 2017–2019 and in 2020, and orange lines are examples of LOS velocities in 2020 for points selected arbitrarily within the head of the failure region. (b) Comparison of coherence for time period of 2018–2019 and in 2020.

NDVI retrieved from MODIS data before the 2020 failure; one in May, and the other in June 2020, i.e., 50 and 10 days before the large failure. For the S2 data, a single drop is observed, i.e., 20 days before the failure. To investigate whether these signals are related to the behavior of the Aniangzhai landslide or whether they occur seasonally and independent of the slope motion, we plotted the NDVI values (MODIS) in 2020 against its historical values of the 2017–2019 period in Figure 4.12a. Examples of LOS displacements in 2020 from points selected arbitrarily from Zone I are also shown in Figure 4.12a for comparison.

It is difficult to fully disentangle the causes of the drops in NDVI values, as such drops are influenced by many factors including soil moisture, surface erosion, plant degradation and slope deformation (Jacquemart and Tiampo, 2021; Liu et al., 2015; Farrar et al., 1994; Nicholson and Farrar, 1994). One explanation could be that the drops are related to errors in data production. As mentioned in Section 4.4.3, the MODIS dataset is generated with adjustment through BDRF, which might contribute to interpolation errors. Alternatively, the drops could be related to changes in vegetation structure before the failure as it occurs at approximately the same time, when a distinct acceleration in landslide active deformation is seen; no similar behaviours were observed in the historical values. Unfortunately, the S2 data do not have a dense temporal coverage for the first drop to be used as the validation. However, based on the above discussion and our results, we do not exclude the interpretation that the increase in rate of active deformation or the occurrence of small landslides before the main failure, as observed in seismic data (Yan et al., 2021), could have altered the scattering properties and vegetation structure in the landslide region, in turn leading to lower NDVI values. Similar observations of shallow soil erosion and vegetation damage near fault zones and river networks have been reported elsewhere (Geitner et al., 2021; Jacquemart and Tiampo, 2021; Gan et al., 2019). As for the post-failure behaviors of NDVI time series, significant changes are expected compared to the pre-failure situation (Figures 4.11 and 4.12a). Similar observations of post-event behaviors can be found

in Behling et al. (2016). The structure of vegetation over the slope area could be greatly influenced by the large failure, and would last for a certain period in the future.

In a similar manner as above, we also investigated the changes in the time series of coherence values for the Aniangzhai landslide. A recent study indicated the linear relationship between NDVI and coherence (Bai et al., 2020). As longer temporal baselines could lead to lower coherence values, only SAR images with a 12-day temporal baseline were used here. However, as shown in Figure 4.12b, the coherence-based results are not very promising. A possible reason is that coherence is usually already low during summer in this region, since this time of the year is characterized by maximal vegetation growth. Therefore, it seems difficult to accurately discern a further drop in the time series due to low coherence and high uncertainty. Nevertheless, we can still observe a relatively stronger declining trend for coherence in 2020 compared to the previous years, which might be related to active deformation and changes in volume scattering of the landslide. Unfortunately, there are no available S1B data for this study area. Otherwise, we could study the coherence from 6-day image pairs to determine whether the drop in coherence caused by slope destabilization would be more accessible. It can be assumed that, if performed in winter, coherence analysis might have resulted in a better performance for ongoing slope activation with less vegetation compared to the analysis in this study.

The stretch to an EWS is hypothetical at this stage, and additional case studies are needed to further analyze the key factors in changing NDVI and coherence values. We suggest that the consideration of both parameters might lead to possible observations of signs of slope activation. With more experiments in the future, these results might contribute to a potential EWS for landslide hazards.

## 4.7 Conclusion

This paper focused on exploiting multi-sensor remote sensing technology to investigate the June 2020 Aniangzhai slope failure and the active deformation prior to the event since late 2014. Cross-correlation analysis of high-resolution optical data from Planet provides detailed information about the spatial pattern of slope kinematics. Moreover, the undercutting effects on the toe of the landslide body, which played a vital role in the toe erosion and reactivation of this ancient landslide body, are also clearly visible in the optical data. The toe erosion was triggered by overflow of a dammed lake, created due to heavy rainfall and the resulting debris flows coming from the Meilong valley to the Xiaojinchuan River, and was influenced also by the discharge of the surplus water from a nearby hydropower station to reduce the flood pressure. Complementary analyses using multi-temporal SAR satellite remote sensing shows that the Aniangzhai landslide was not dormant. Rather, it was already active before the failure, with a maximum LOS displacement rate of around 38 mm/yr in 2014–2017, reaching approximately 55 mm/yr in 2018–2020. Our findings indicate that not the whole landslide body was subject to accelerating creep before the June 2020 failure; rather, only the points situated on the upper parts of the landslide failure sustained pronounced acceleration of the creep starting in spring 2020. As a result, the time series of displacements derived from these points could be utilized to forecast the potential window of failure. Moreover, we observed the sign in which an acceleration of creep on the head part of the failure region and a decrease in NDVI values took place almost at the same time, opposite to the prevailing trends in this area. We discussed the likely causes to interpret this phenomenon and suggested

that this sign may be regarded as a parameter to be integrated into an EWS. With more case studies in the future, the methods proposed in this paper can be utilized under the framework of multidisciplinary DRR for a comprehensive analysis of the cascading event chain influencing the instability of the ancient landslides.

## 4.8 Acknowledgements

The authors acknowledged the Copernicus programme gratefully for the free access to Sentinel-1 and Sentinel-2 data. Landsat 8 and MODIS MCD43A4 collections are courtesy of the U.S. Geological Survey (USGS). Many thanks to Dr. Mahmud Haghshenas Haghighi for supporting us in the COSI-Corr analysis and Dr. Jie Liu for supporting the fieldwork. We also thank two anonymous reviewers for their very constructive comments, which greatly improved the quality of the original manuscript. Z.X. is supported by China Scholarship Council (CSC) Grant #201908080048. This project was supported by the National Natural Science Foundation of China (NSFC) (No.42074031), “Seed Fund Program for Sino-foreign Joint Scientific Research Platform of Wuhan University” (No. KYPT-PY-11), and Helmholtz Imaging Platform (project: MultiSat4SLOWS).

## 4.9 Supplementary Materials

This supporting material includes four three text sections, three figures and one table. First, we show a comparison between the normal river state and the one with debris flows in 2020 failure (based on the S2 data). Moreover, the previous river courses and the one in the 2020 failure, which was flooded in the event, are compared from Planet optical images in this study. Besides, we describe the exploited descending S1 SAR acquisitions and the baseline graphs of interferograms.

### 4.9.1 Comparison of River Courses

By exploiting S2 datasets, the debris flows triggered by the heavy precipitation could be observed quite obviously. Due to the limitation of optical remote sensing and the geological settings in this area, the cloud-free images are hardly to find, especially in the rainy season (May to July). For comparison, we choose these two images from 13 August 2019 and 27 August 2020, respectively. The first one shows the normal state of the river; whilst the latter image clearly shows the debris flows triggered in this event, regarding as the direct cause to the construction of the barrier lake under the Aniangzhai ancient landslide body. As seen in Figure 4.13b, the debris flows were comprised of several failures from the valley region north to the reservoir.

From the Planet optical images, we investigate the river courses of Xiaojinchuan River in previous years. As seen from Figure 4.14, different from the course in the event of the 2020 failure, the previous river courses in June 2018 and June 2019 demonstrated the similar narrow extends and appearances, which indicated the normal states of the river course. In comparison with Figure 4.14d, we can obviously see the floods, the barrier lake and the flooded areas in this event on 24 June 2020.

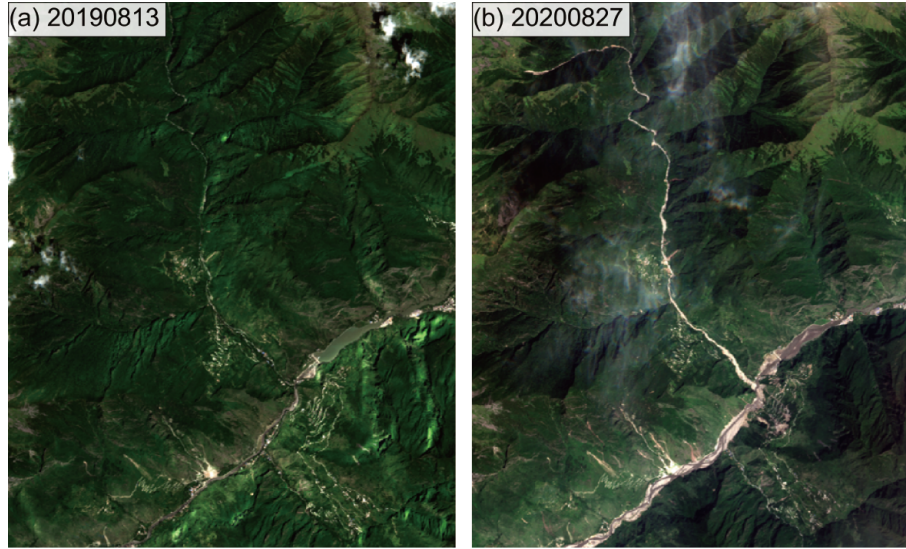


**Figure 4.13:** Comparison of the river courses between (a) the normal one in the previous year on 13 August 2019 and (b) the debris flows on 27 August 2020. The images are S2 acquisitions.

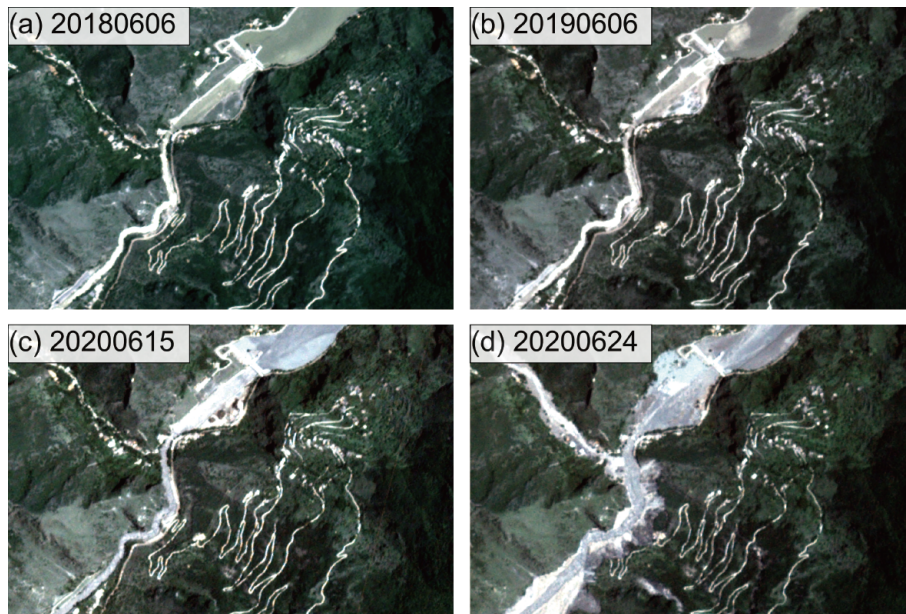


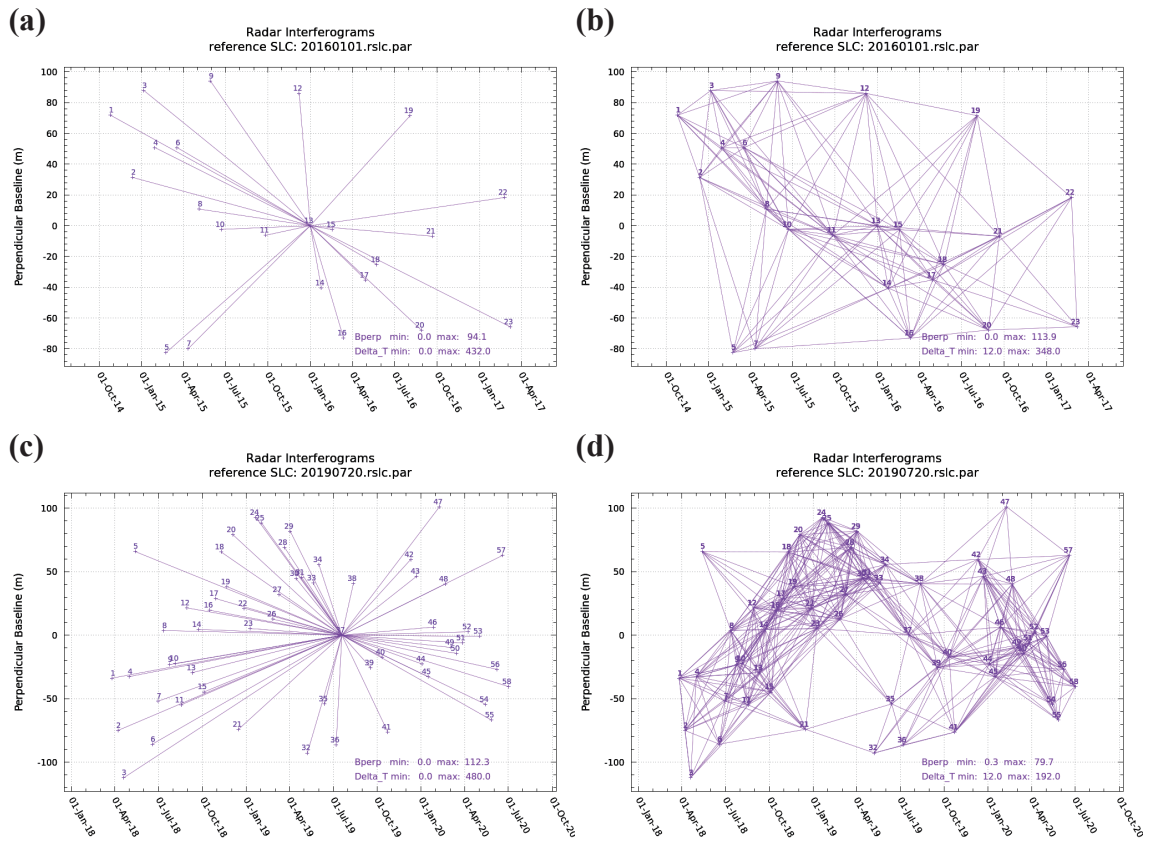
**Figure 4.14:** Comparison of the river courses for the rainy season in the previous years, on (a) 06 June 2018, (b) 06 June 2019, (c) 06 June 2020, to the river course of the accident (d) 24 June 2020. The planet remote sensing optical images are exploited.

#### 4.9.2 Detailed Parameters of Exploited SAR Data

For the exploited S1 data, both ascending and descending images are available. However, since the landslide body has the foreshortening effect in ascending orbit, the descending data is exploited in this study. The utilized images range from October 2014 until June 2020. The detailed parameters can be found in Table 4.4. There are totally 89 images. However, a few images in the period of 2014 to 2015 cover the study area partially and

**Table 4.4:** Summary of parameters of the exploited descending S1 SAR acquisitions in this study.

Parameter	Value	Unit
Duration	2014–2020	—
Orbit	descending	—
Number of images	89	—
Heading angle	192.8	degree
Incidence angle	36.9	degree
Pixel size in azimuth	13.9	m
Pixel size in slant range	2.3	m
Wavelength	5.6	cm

**Figure 4.15:** Baseline networks in MT-InSAR processing of (a) PSI for the first time span in 2014–2017; (b) SBAS for the first time span in 2014–2017; (c) PSI for the second time span in 2018–2020; (d) SBAS for the second time span in 2018–2020.

they are stitching together for the exploitation. In the end, 80 images are applied in this study for the MT-InSAR processing.

### 4.9.3 Comparison of Baseline Graphs

For the baseline graphs in the MT-InSAR processing, the images on 01 January 2016 and 20 July 2019 are selected as the master and supermaster images in the PSI and SBAS

processing for the two time series of SAR images, respectively. Because of the lower sampling frequency in the first period, we set the thresholds for temporal and spatial baselines as 350 days and 120 metres to build the SBAS network. As for the second time span, the consecutive images have a continuous 12-day interval. Hence, we set the thresholds as 200 days and 80 metres. In specific, the corresponding baseline graphs are shown in Figure 4.15.

## 5 Post-failure: Slope Instability Monitoring Using Artificial Corner Reflectors

*This chapter was published as:*

**Zhuge Xia**, Mahdi Motagh, and Tao Li. “Performance analysis of dihedral corner reflectors for slope movements: a case study from Aniangzhai landslide in China.” *IEEE Geoscience and Remote Sensing Letters* 19 (2022): 1-5.

*Author contribution statement:*

**Zhuge Xia** did most of the work, including conceptualization, methodology development, validation, formal analysis, writing, and visualization. Mahdi Motagh contributed to the discussion and writing. Tao Li contributed to the discussion and the fieldwork to install the corner reflectors.



## 5.1 Abstract

Using SAR and InSAR technology, artificial corner reflectors (CR) are popular coherent targets for monitoring ground instability with sub-centimeter accuracy in non-urban areas. In this letter, we investigate the performance of a newly designed small dihedral corner reflector (DCR) for monitoring post-failure creep at the Aniangzhai landslide in Danba County, China. The new double geometry CRs consist of two sets of semi-circular metal plates, each 30–40 cm in radius and perpendicular to each other. Six such CRs are installed for Corner Reflector Interferometric SAR (CR-InSAR) analysis using both TerraSAR-X (TSX) High-resolution Spotlight (HS) data and medium-resolution Sentinel-1 (S1) SAR images. The CRs are first identified in SAR images using a probability model by taking into three factors. These are (1) inverse of amplitude dispersion, (2) intensity increment after the installation, (3) an upper empirical bound derived from the ensemble average of pixel intensities in post-deployment SAR images. Experimental results show that the CRs improve the background intensity in TSX images by around 30 dB, with signal-to-clutter ratio (SCR) exceeding 25 dB. Furthermore, the radar cross-section (RCS) of CRs in both TSX and S1 images remains relatively stable, ranging from 15 dB to 23 dB, making them suitable for CR-InSAR analysis using double-difference phase observations.

## 5.2 Introduction

Artificial corner reflectors (CRs) are manufactured auxiliaries for synthetic aperture radar (SAR) and interferometric SAR (InSAR) analysis, as they introduce coherent scatters with stable amplitude and phase information during radar acquisitions (Bovenga et al., 2014). Deploying CRs as artificial coherent scatters is an alternative to increase the number of measurement points in multi-temporal InSAR analysis, especially when there is a risk of severe coherence loss between successive SAR image acquisitions in vegetated, semi-vegetated, or agricultural regions (Xia et al., 2004). Due to their steady and robust echoes, traditional trihedral corner reflectors (TCRs) with large dimensions, e.g., with an edge of 1 meter, have been proposed as an effective instrument for monitoring slope stability in vegetated mountainous areas (Bovenga et al., 2014; Shan et al., 2013; Froese et al., 2008; Xia et al., 2004).

The increase in the availability of high-resolution X-band SAR imagery by German TerraSAR-X (TSX) and the Italian COSMO-Skymed (CSK) satellites has made the use of CRs more appealing, as such SAR systems could benefit from smaller CRs which can be installed in challenging environments with the advantage of having low cost, easy installation, and simple maintenance (Dheenathayalan et al., 2017). However, there is a limitation in using smaller CRs in that a reduction in power occurs due to the reduced size of reflectors that would limit their applicability for medium-resolution SAR images from missions like Sentinel-1 (S1) and ALOS-2 (Dheenathayalan et al., 2017; Garthwaite, 2017). It is worth noting that with regard to the design of CRs, no single design that could perform equally well for all of the currently operational SAR satellites (Garthwaite, 2017). Thus, a sensor-specific CR or a compromise solution for several sensors needs to be taken for operational monitoring.

In this study, we present the results of our experiment for using a newly designed dihedral corner reflector (DCR) for monitoring post-failure creep at Aniangzhai landslides in China. The CRs have small dimensions (each 30–40 cm in radius), and are constructed



with symmetrical geometry (Figure 5.1), making them suitable for both ascending and descending SAR observations and broadening their application to those fields requiring the generation of 3D velocity maps from SAR data. Previous studies have shown that the primary deformation of the Aniangzhai landslide is along the northwest direction (Xia et al., 2022b), which makes the landslide more sensitive to SAR observations from a descending track. Therefore, here we mainly focused on descending SAR images that have more sensitivity to slope motion in the study area. However, results from S1 ascending data are also presented for comparison purposes. Six CRs were deployed at different positions of landslides in November 2020 (Figure 5.1a). Then through a research proposal with the German Aerospace Agency, we tasked High-resolution Spotlight (HS) data acquisition from a descending orbit between July 2020 and February 2022. We also analyzed S1 ascending and descending data for a similar period to evaluate the performance of CRs for C-band SAR systems. In total, we exploited 51 TSX and 90 S1 images of the Aniangzhai landslide for this experiment.

This paper is organized as follows. Following this introduction, the design of the experiments and the selection strategy using a conditional probability model for CRs for different SAR sensors are introduced. Two important indices to evaluate the CRs, i.e., radar cross-section (RCS) and signal-to-clutter ratio (SCR), and the method of Corner Reflector Interferometric SAR (CR-InSAR), are elaborated as well. Finally, the results of tested DCRs are demonstrated, compared, and discussed in detail, followed by an overall conclusion of this study.

## 5.3 Experiments and Methodology

### 5.3.1 Experimental Design

CRs are usually composed of two or three electrically conducting surfaces to produce powerful radar echoes from areas with low effective RCS. Multiple reflections might precisely backscatter incoming electromagnetic waves in the same direction from which they come. As a result, even objects with small dimensions can produce mighty echoes. When CRs point directly along the boresight of a SAR antenna, the RCS of CRs could reach its maximum. Figure 5.1d shows the schematic design and location of our CRs in the study area. They are composed of two sets of semi-circular metal plates positioned perpendicular to each other, so that they can be used for both ascending and descending high-resolution satellite imagery. These two sets are installed on a standard pillar, with the same inclination angle of  $10^\circ$  symmetrically. Among the six CRs, CR03 and CR04 have a radius of 40 cm, while the rest have a relatively smaller radius of 30 cm. The initial locations of the six CRs for the installation are measured with Global Positioning System (GPS).

### 5.3.2 Selection Strategy for CRs

In order to overcome difficulties such as biased GPS position or unpredictable interference with other scatterers (Figure 5.1c), we propose a general selection strategy for identifying CRs in SAR images based on different properties and variations of power in pixels brought by the installation of CRs. The selection strategy is based on three different weighting factors. The first one is the inverse of amplitude dispersion index  $w_A$ , which represents the phase stability of CRs, with higher values being suggestive of more stability (Ferretti et al., 2001). The second weighting factor  $w_I$  is the intensity increments of pixels after the

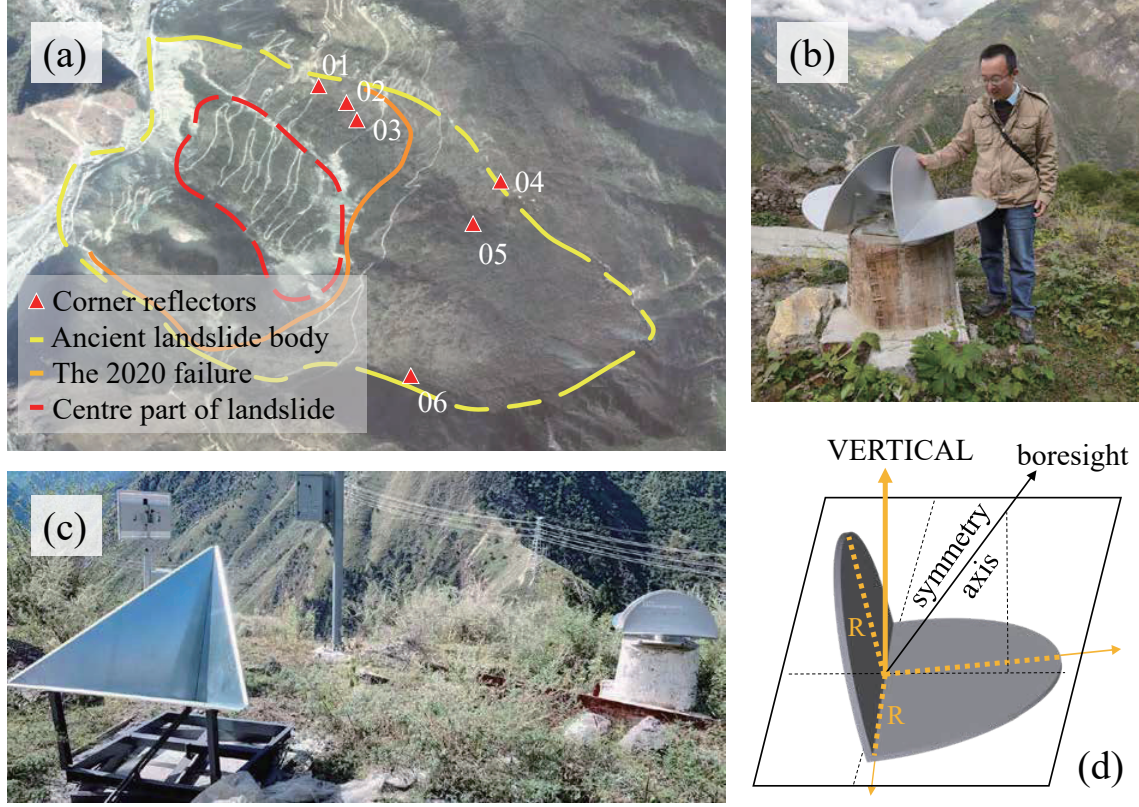


**Figure 5.1:** (a) Study area and locations of tested CRs, specified by numbers 1–6. The background image is from a Skysat high-resolution optical image acquired in November 2020. The boundaries of different zones of the landslide body are presented (Xia et al., 2022b). (b) Field photo from a tested CR over Aniangzhai landslide. (c) Position relationship between CR03 and the newly arranged TCR as an unexpected interference. (d) The general schematic of constructed CRs.

installation, as theoretically we would expect the CRs to improve the lower clutter intensity in SAR images. The third weighting factor  $w_E$  is an upper empirical bound derived from the ensemble average of pixel intensities in sequential images after the deployment. This factor restricts selections of pixels other than CRs with stable and stronger signals that could come from, e.g., broken roads, buildings, and similar constructions on the landslide slope. Finally, after the derivation and normalization of all three weightings, a conditional probability model for every pixel is derived within the search window using

$$P_w = P(w_A) \cdot P(w_I|w_A) \cdot P(w_E|w_A, w_I) \quad (5.1)$$

According to the existing parameters, pixels with a more significant probability inside the search window are more likely to exhibit features similar to the tested CRs. In our experiment, this selection strategy helped properly identify and locate the tested CRs in both TSX and S1 images. Indeed, the method proposed here could also be exploited as a general strategy for other cases to identify similar targets with CR-like echoes. For example, when applied on other types of CRs, the only parameters that need to be changed in the above formulation are the time interval to estimate  $w_I$  and the empirical value for calculating  $w_E$  based on the properties of individual CRs.

### 5.3.3 Radar Cross-section (RCS)

The projected area of a metal sphere scattering the same amount of energy in the same direction as the target is known as RCS (Knott et al., 2004), and its unit is often written in logarithmic form, i.e.,  $dBm^2$  or  $dBsm$ . RCS indicates the measure of the target's detectability (Shan et al., 2013), defined theoretically as

$$RCS = \frac{4\pi \cdot (A_e)^2}{\lambda^2} \quad (5.2)$$

where  $A_e$  is the projected area of the effective cross-section of CR, and  $\lambda$  is the wavelength, i.e., approximately 3.1 and 5.5 cm for TSX and S1 satellites, respectively. The maximum RCS of our tested CR with this specific design of geometry could be computed as

$$RCS_{max} = \frac{4\pi \cdot (\frac{\sqrt{2}}{2}\pi \cdot R^2)^2}{\lambda^2} = \frac{2\pi^3 \cdot R^4}{\lambda^2} \quad (5.3)$$

where  $R$  is the radius of the semi-circular metal plates. According to the equation (5.3), the maximum theoretical RCS of our CRs in TSX images is approximately 32.2 dB for the CRs with a 40 cm radius, and about 27.2 dB for 30 cm radius. As for S1 data, the CRs with a 40-cm and 30-cm radii have the maximum theoretical RCS values of around 27.2 dB and 22.2 dB, respectively.

Alternatively, RCS could also be measured directly from SAR images using the peak method in the spatial domain (Ulander, 1991)

$$RCS_{measure} = E_{CR} \cdot A_{cell} \quad (5.4)$$

where  $E_{CR}$  is the intensity of CR, and  $A_{cell}$  is cell resolution. The measured RCS should be lower than the theoretical value due to the misalignment of the antenna.

### 5.3.4 Signal-to-clutter Ratio (SCR)

SCR is another commonly used metric for target visibility in SAR images (Freeman, 1992). The targets such as CRs are needed to be much higher than the scattering level of the background. The SCR is defined as (Freeman, 1992)

$$SCR = \frac{RCS_T}{\langle RCS_C \rangle} \quad (5.5)$$

where  $RCS_T$  represents the target RCS, and  $\langle RCS_C \rangle$  is the ensemble average of clutter RCS neighboring the point target. For the conventional TCRs with strong power and cross-like signals in the SAR image, the clutter RCS is usually estimated with the average clutter intensity within the four clutter quadrants. However, in our study, the tested CRs were not strong enough to generate such cross-like signals due to small dimensions and differences in spatial resolution. Instead, only several concentrated pixels could be dominated and obtained. Thus, we derive the clutter RCS using an ensemble average within the search window neighboring tested CRs.

### 5.3.5 CR-InSAR Processing

Following identifying CRs, we exploit the CR-InSAR method for deformation analysis of the Aniangzhai landslide. CR-InSAR is a specific InSAR method applied for CRs (Shan et al., 2013; Froese et al., 2008; Xia et al., 2004). It mainly exploits the information from double phase difference compared to a reference CR in different epochs

$$\Delta\phi_{ij} = (\phi_i^s - \phi_j^s) - (\phi_i^m - \phi_j^m) \quad (5.6)$$

where  $\Delta\phi_{ij}$  represents the double phase difference of CRs  $i$  and  $j$ , the superscripts  $m$  and  $s$  are master and slave images. Then the wrapped phase obtained by double differencing needs to be unwrapped to estimate phase ambiguity. Here we used the least squares ambiguity decorrelation adjustment (LAMBDA) method to estimate the absolute phase (Kampes and Hanssen, 2004), and derive line-of-sight (LOS) motion based on linear and seasonal functional models. The atmospheric effects, i.e., tropospheric and ionospheric phase components, are neglected by the double-difference of phase observations considering the closing distance of deployed CRs (Froese et al., 2008; Xia et al., 2004).

## 5.4 Results and Discussion

With the help of new methodology, we were able to identify our newly designed diheral CRs correctly in both high resolution TSX HS and medium resolution S1 data (see supporting material Figure 5.3). The traditional ways to identify the conventional TCRs would be visual checking assisted by GPS coordinates as they would create intense echoes due to their large dimensions. However, this process does not work for our type of CR due to their small dimension and low energy. Moreover, due to the resampling of the CRs, the precise coordinate of CRs may not be the highest CR intensity peak. Our proposed strategy to identify small CRs has the following advantages: (1) It enables to identify CRs containing several concentrated pixels in SAR images, especially when CRs are located at the border of pixels. (2) It mitigates and reduces the influence of unpredictable interference from other scatterers with even stronger echoes in both high- and medium-resolution SAR images. (3) It can be adopted when the signals of tested CRs are not as strong as the conventional TCRs. (4) It can be utilized when the signals are influenced by low sensitivity and layover effect caused by satellite observation geometry. However, this selection strategy also has limitations in that it needs a priori information, e.g., the deployment time of CRs. With more a priori knowledge, a more reliable the estimation of the weighting factors could be obtained, leading to more accurate identification of CRs.

As revealed in Figure 5.2, after selections of CRs in SAR images, we could obtain results of all the evaluation factors on the tested CRs. It is worth mentioning that TSX and S1 datasets are delivered in different types, i.e., the short complex and float complex format, respectively. Therefore, for a better comparison of two SAR data, the format of TSX images is first converted to the same as S1 data; then the calibrated intensity time series for two data are checked to ensure that the tested CRs exhibit identifiable scattering in SAR images. In order to illustrate the spatial distribution characteristics of radar intensity in this area, the radar intensity maps for the tested CRs are also displayed after their deployment (see Figures 5.4 to 5.6 in supporting material).

Figures 5.2a-5.2c show the time series of calibrated intensity on tested CRs in TSX and S1 data. In TSX images, the background intensities of the tested CRs are enhanced

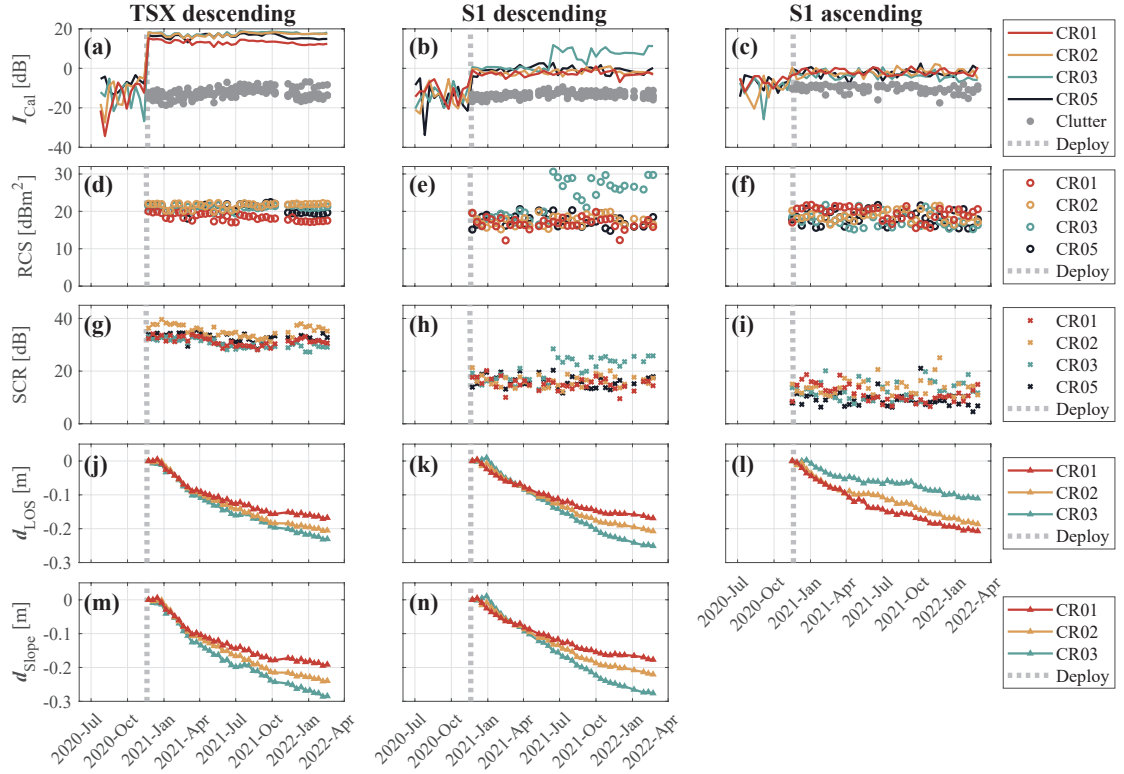


**Figure 5.2:** Results of the tested CRs. (a)-(c) Time series of calibrated radar intensity. (d)-(f) Time series of the measured RCS values. (g)-(i) Time series of the measured SCR values. (j)-(l) LOS displacements estimated using CR-InSAR method. (m)-(n) Converted slope displacements on CRs. The left, middle and right columns are TSX descending, S1 descending, and S1 ascending datasets, respectively. The light gray dashed lines represent the deployment of the CRs.

from approximately -15 dB to 15 dB after the deployment. For S1 images, however, this improvement is lower, i.e., by around 10 and 5 dB for the descending and ascending images, respectively. We also found that two CRs were missing by analyzing the results. CR04 could be observed initially after the deployment, but as of 2021, its intensity had decreased rapidly and was no longer visible in the search window. CR06 was completely missing in our analysis. Through the field investigation in late 2021, we found that the major reason for missing signals could be the skewed viewing orientations caused by man-made impediments, which were fixed during later fieldwork.

In general, we can say that the tested CRs work better in TSX images than in S1 images in improving the background clutter. This is mainly due to the great difference in spatial resolution between TSX and S1 SAR images, with the resolution of  $0.9 \times 1.2m$  and  $2.3 \times 14.0m$ , respectively. Moreover, except for CR03 in S1 images, the intensity time series of CRs remains stable until the end of both SAR data. The calibrated intensity of CR03 shows a significant increase after June 2021 in S1 data. Checked by the fieldwork, we found that another group had set a new TCR with an edge of one meter very close to our CR03 (Figure 5.1c, around 2~3 meters), which also appears in SAR data since June 2021. As a result, the intensity of CR03 interfered by this new TCR in S1 descending images, leading to an unusual signal rising (Figure 5.2b). On the contrary, this interference

was not dominant in TSX HS images due to their higher spatial resolution, enabling us to easily separate echoes from CR03 and its neighbouring CR (Figure 5.2a), a task which was impossible to accomplish in medium-resolution S1 descending images. Besides, this TCR is descending-orbit orientated, so the results of S1 ascending data are not affected by the new TCR in the evaluation (Figure 5.2c).

Figures 5.2d-5.2f demonstrate the time series of measured RCS on tested CRs in TSX and S1 images. Generally, we observe that the derived RCS values remain more or less stable for both TSX and S1 images, ranging from 15–23 dB; whilst the RCS of CRs in TSX images is approximately 5–10 dB higher than the values in S1 images. Compared to the theoretical RCS, it is not surprising that the derived RCS from SAR images could not reach the maximum analytical values expected, as the CRs are not optimally deployed for specific satellite orbits. Moreover, the CRs are not directed towards the boresight, too. Similar to the intensity analysis, the same rising feature of RCS for CR03 could be observed after June 2021 due to the influence of another TCR nearby.

Figures 5.2g-5.2i reveal the time series of derived SCR for tested CRs in TSX and S1 images. Overall, SCR in TSX images exceeds 25 dB, suggesting the great potential for recognition between CRs and background clutter when using TSX images. On the contrary, SCR in S1 is lower, mainly around 15 dB and 10 dB in descending and ascending data. Although it is not as good as in TSX, the RCS of CRs in S1 images is still apparent compared to the clutter. This suggests that the tested CRs could be distinguished compared to the dark background coming from dense vegetation in this area. Taking into account SCR, the effective phase errors for TSX and S1 images are about 0.04 and 0.13 radians, respectively (see supporting material); while the effective displacement errors in the LOS direction are about 0.1 and 0.6 mm in X-band and C-band, respectively. Another interesting feature revealed in Figure 5.2g is the drop of SCR values in TSX images since April and its increase in winter. This feature could possibly be linked to the increase in precipitation and growth in vegetation in the summer season that causes the drops of the SCR values (Kozu et al., 2001).

Figures 5.2j-5.2l reveal results from CR-InSAR analysis of CRs using TSX and S1 datasets with CR05 on the upper slope above the failure part of the landslide being selected as the reference CR. For the LOS displacements, the amounts of deformation from ascending and descending are different. For a better comparison, we further converted LOS displacements into slope displacements of the two descending SAR data. The movement of the landslide block may be controlled by a sliding surface that is approximately parallel to the surface of the slope (Xia et al., 2022b). Therefore, the average slope and aspect of the middle and lower parts of the landslide are exploited to calculate the scaling factors. Figures 5.2m and 5.2n demonstrate the converted slope displacements from TSX and S1 descending datasets. Please note that the Aniangzhai landslide slope is facing to the west, which causes a layover effect in ascending orbit SAR data (Haghshenas Haghighi and Motagh, 2016). Moreover, it is not feasible to convert the S1 ascending data to slope direction, as this observation geometry has very low sensitivity to the landslide slope motion (Haghshenas Haghighi and Motagh, 2016; Motagh et al., 2013); during the process of calculation, the scaling factors for transformation from LOS direction to slope direction are within the interval of 0.19~0.23, causing great artificial exaggeration and extreme values. Hence, the results derived from ascending orbit data are not as promising as the results from descending orbit.

As seen in Figures 5.2m and 5.2n, for both TSX and S1 descending data, CR01–03 suggest similar kinematics of motion from the beginning until October 2021. After conversion into slope direction, the differences in magnitude of slope displacements between TSX and S1 data are found to be reduced compared to the differences in LOS displacements, i.e. from a few cm to 1 cm, especially for CR03. Until the end of October 2021, cumulative slope displacements of CR01–03 in TSX images are 17.8, 21.5, and 24.3 cm, respectively; in S1 images the displacements are 16.3, 19.4, and 24.0 cm, respectively. As of October 2021 we observe a distinct slowing-down of slope motion in both SAR images. The slowing down could be linked to the upslope loading from deposition of new material into the vacancies in landslide toe and foot areas (Xia et al., 2022b; Lacroix et al., 2020).

In a previous study, Dheenathayalan et al. (2017) successfully tested trihedral CRs with even smaller dimensions than ours containing an edge of around 14.5 cm, with their SCR of around 6 dB on average and improving the clutter intensity by around 6 dB. The small-scale CRs in Dheenathayalan et al. (2017) are specialized only to be used for high-resolution datasets such as TSX or CSK, and not for lower resolution datasets such as S1. Larger CRs would undoubtedly result in higher RCS and SCR values. However, the deployment and maintenance procedures would also be more difficult (Shan et al., 2013). Our dihedral CR could act as a compromise solution among different CRs, which can be used for InSAR monitoring using both TSX and S1 SAR data at a relatively low cost with easy installation and maintenance.

## 5.5 Conclusion

This study confirms that small DCRs designed within the framework of this experiment can reliably be used for deformation monitoring using CR-InSAR technique. An experimental study to assess post-failure creep at Aniangzhai landslide in China using both TSX HS and S1 images showed that the background intensity in TSX images was enhanced by around 30 dB after CR installation, with SCR exceeding 25 dB. In comparison, the background intensity in S1 images was improved by only about 5–10 dB, with SCR of around 10–15 dB. In both TSX HS and S1 SAR images, the RCS of CRs remained rather consistent, ranging from 15 dB to 23 dB, making them appropriate for CR-InSAR analysis using the double-difference phase method. High-resolution SAR images have irreplaceable advantages in SAR and InSAR analysis due to the significant improvement in spatial resolution and shorter revisit times. Although our CRs were initially designed for X-band SAR systems, they illustrated sufficient SCR to be applied in S1 images for interferometric analysis, making them complementary to other traditional survey methods such as GPS or leveling. They can be installed quickly and easily at a relatively low cost in landslide regions, where ground-based measurements are lacking, for near real-time deformation monitoring and supplementing landslide hazard warning systems.

## 5.6 Acknowledgments

The authors acknowledged the German Space Agency (DLR) gratefully for providing the TerraSAR-X data (proposal id. motagh.GEO1916), and the Copernicus program for the free access to Sentinel-1 data. This work was supported in part by the National Natural Science Foundation of China under Grant 42074031 and in part by GFZ. The work of Zhuge Xia was supported by the China Scholarship Council (CSC) under Grant #201908080048.

## 5.7 Supplementary Materials

This supporting material includes four text sections and five figures. Here, the formula for calculating effective displacement and phase errors from SCR is demonstrated. And we describe and elaborate on the proposed selection strategy for our CRs based on a conditional probability model applied in TSX and S1 datasets. Four different examples of intensity near CRs are displayed correspondingly. Moreover, the radar intensity maps for the tested CRs CR01–03 and CR05 are demonstrated in all exploited SAR images after their deployment in November 2020. Besides, we present one site photo of the interference from the triangle CR.

### 5.7.1 Calculation of SCR

The effective displacement error and phase error could be derived from SCR as (Ketelaar, 2009):

$$d_{err} = \frac{\lambda}{4\pi} \cdot \phi_{err} \approx \frac{\lambda}{4\pi} \cdot \frac{1}{2 \cdot SCR} \quad (5.7)$$

where  $d_{err}$  is the effective displacement error,  $\phi_{err}$  is the effective phase error,  $\lambda$  is the wavelength,  $SCR$  is the signal-to-clutter ratio.

### 5.7.2 Selection Strategy

In this study, the proposed selection strategy works appropriately for identifying our tested CRs in all exploited satellite datasets, though our CRs have small dimensions and low energies than the conventional triangular CRs. Generally, we calculate the probability for each pixel in SAR with the different setting conditions. Then, the highest one within the search window based on the GPS coordinates is identified to be the CR's position. The advantages of the proposed selection strategy are demonstrated with four examples in Figure 5.3 as follows:

- As shown in Figure 5.3a, several concentrated pixels instead of a single pixel could be dominated for CRs in high-resolution SAR images, especially when CRs are located at the border of pixels. In this case, the probabilities of all pixels are calculated. The location of CR shall be identified as the pixel containing the highest probability using the proposed strategy.
- As shown in Figure 5.3b, in TSX images, unpredictable interference could occur with other scatterers with even stronger echoes. In this case, our proposed strategy could help identify the correct position of CR, avoiding interference from another CR settled by another group.
- As shown in Figure 5.3c, as for S1 descending images, our CRs could not be easily recognizable due to the small dimensions in medium-resolution SAR images. There would be clutter pixels with similar or even stronger echoes than the CRs. In this case, our proposed strategy could help identify the correct position of CR in S1 images.
- As shown in Figure 5.3d, in S1 ascending images, our CRs could not be easily recognizable due to the layover effect and low sensitivity caused by satellite observation



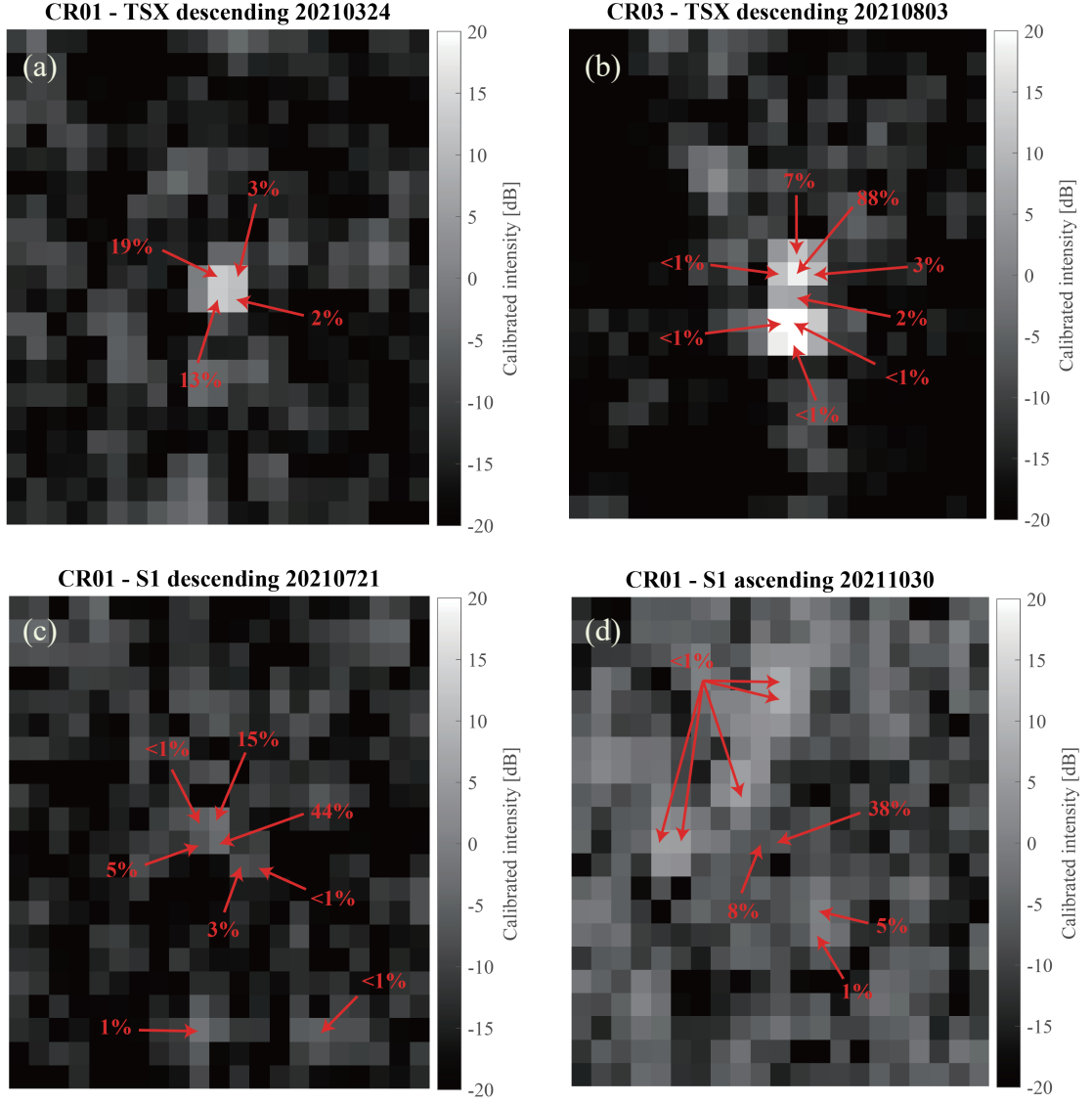


**Figure 5.3:** Examples of demonstrating the proposed selection strategy using a conditional probability model for (a) CR01 in TSX descending image on 24 March 2021; (b) CR03 in TSX descending image on 03 August 2021; (c) CR01 in S1 descending image on 21 July 2021; (d) CR01 in S1 ascending image on 30 October 2021. The rest pixels without markers have the probability of zero.

geometry. In this case, our proposed strategy is working to identify the correct position of CR.

### 5.7.3 Radar Intensity Map

The radar intensity maps for the tested CRs CR01–03 and CR05 are displayed in Figures 5.4 to 5.6 for all datasets after their deployment. The purpose is to illustrate the spatial distribution characteristics of radar intensity in this area, especially the intensity map of CR03 after July 2021. The interference from the newly arranged triangular CR could

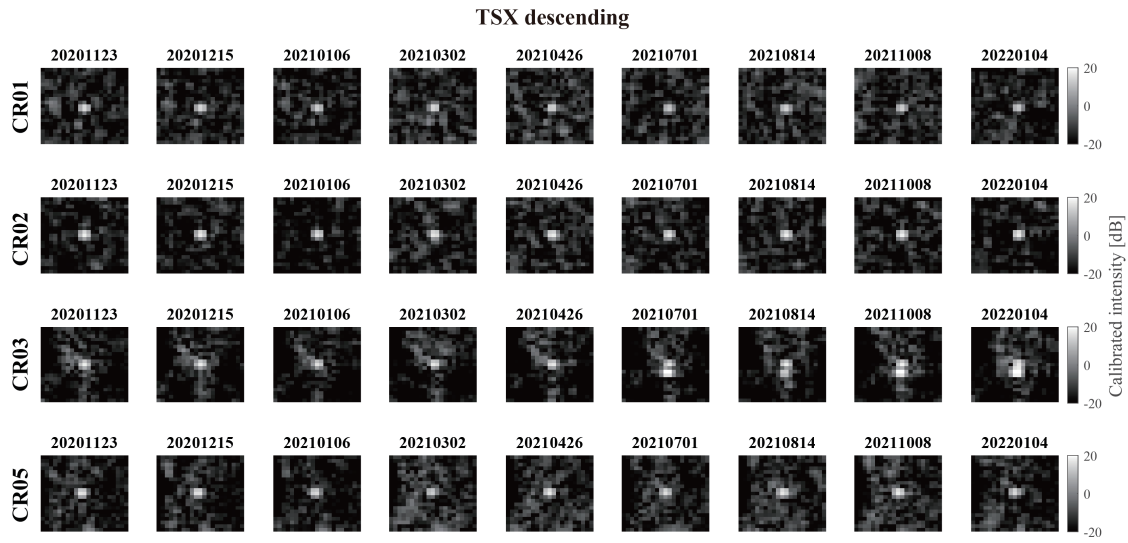


**Figure 5.4:** Radar intensity map for the tested DCRs CR01–03 and CR05 after the deployment in TSX descending dataset.

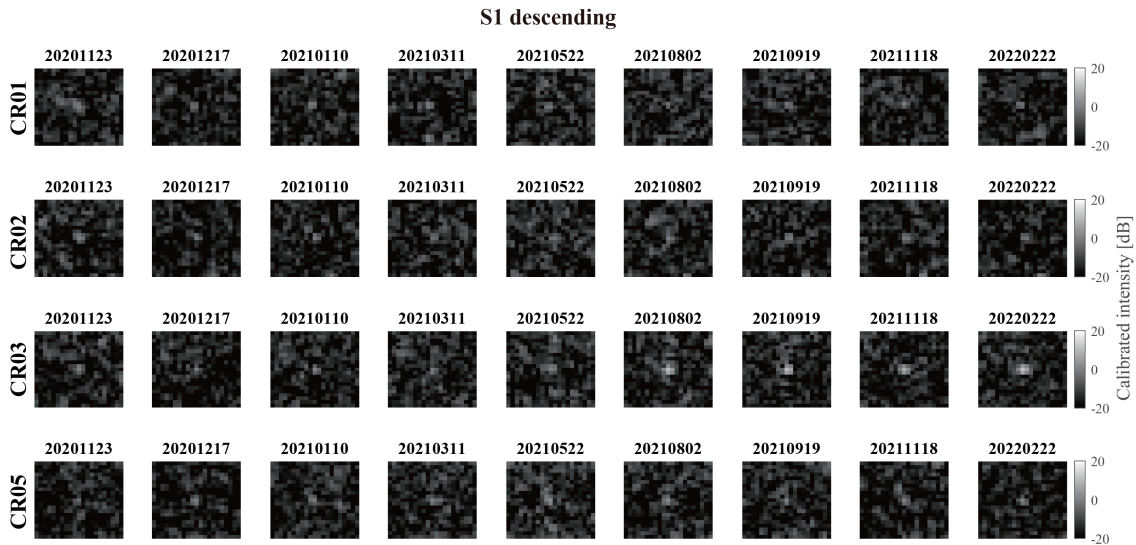


**Figure 5.5:** Radar intensity map for the tested DCRs CR01–03 and CR05 after the deployment in S1 descending dataset.

be clearly seen in the TSX images (Figure 5.4). In addition, the influence of the layover effects brought by the observation geometry could be clearly observed in the ascending intensity time series (Figure 5.6).

#### 5.7.4 Site Photo of Interference Reflector

Figure 5.7 shows a site photo of the interference TCR near our tested CR03. The triangle TCR can accumulate water, which could cause its RCS to be unstable. The following photos can be used as an example to illustrate this.

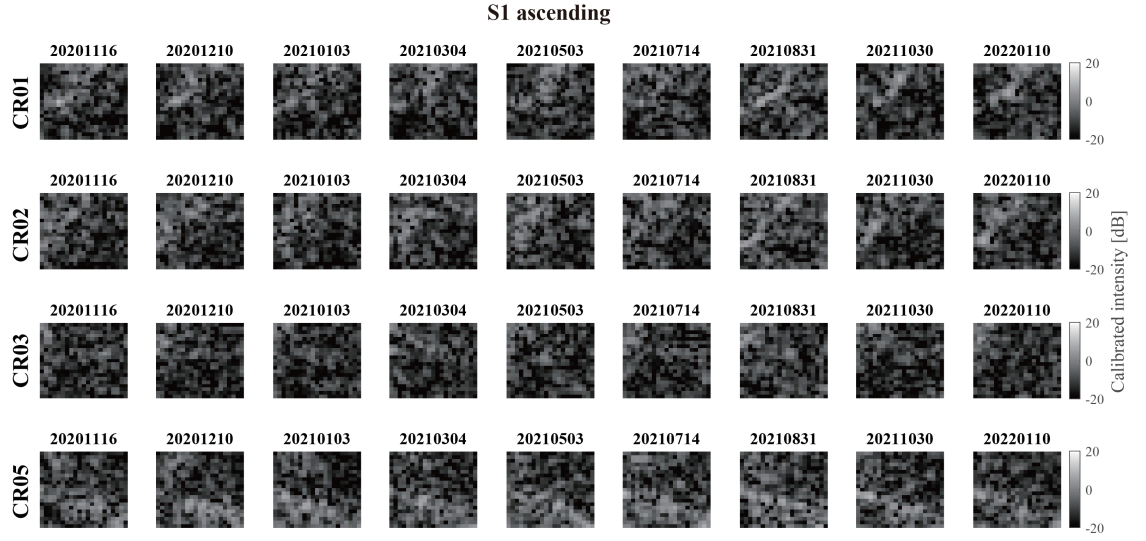


**Figure 5.6:** Radar intensity map for the tested DCRs CR01–03 and CR05 after the deployment in S1 ascending dataset.



**Figure 5.7:** Site photos of the interference TCR near our tested CR03.



## 6 Post-failure: Characterizing 4D Slope Instability Dynamics

*This chapter was published as:*

**Zhuge Xia**, Mahdi Motagh, Tao Li, Mimi Peng, and Sigrid Roessner. “A methodology to characterize 4D post-failure slope instability dynamics using remote sensing measurements: A case study of the Aniangzhai landslide in Sichuan, Southwest China.” *ISPRS Journal of Photogrammetry and Remote Sensing* 196 (2023): 402-414.

*Author contribution statement:*

**Zhuge Xia** did most of the work, including conceptualization, methodology development, validation, formal analysis, writing, and visualization. Mahdi Motagh contributed to the discussion and writing. Tao Li, Mimi Peng, and Sigrid Roessner contributed to the discussion.

### 6.1 Abstract

A massive landslide often causes long-lasting instability dynamics that need to be analyzed in detail for risk management and mitigation. Multiple satellite remote sensing observations, in-situ measurements, and geophysical approaches have been jointly implemented to monitor and interpret the life cycle of landslides and their failure mechanisms from various perspectives. In this work, we propose a framework where satellite optical and synthetic aperture radar (SAR) remote sensing techniques are combined with feature extractions using independent component analysis (ICA) and a mathematical relaxation model to assess the complete four-dimensional (4D) spatiotemporal patterns of post-failure slope evolution. The large, deep-seated Aniangzhai landslide in Southwest China that occurred on 17 June 2020 is comprehensively analyzed and characterized for its post-failure mechanism. Time series of Planet high-resolution optical images are first explored to derive the large horizontal motions for the first six months after the failure. Spatiotemporal dynamics of line-of-sight (LOS) displacement in the landslide body are then derived between November 2020 and February 2022 by combining 40 TerraSAR-X (TSX) High-resolution Spotlight (HS) images and 76 medium-resolution Sentinel-1 (S1) SAR datasets using Multi-temporal InSAR (MT-InSAR) method. The InSAR-derived results are subsequently analyzed with ICA to find common deformation components of points between optical and MT-InSAR results, indicating the same temporal evolution in the deformation pattern. Finally, the complete 4D deformation field for the whole post-failure period is modeled using a decaying exponential model representing stress relaxation after the failure by integrating multiple remote sensing datasets. Cross-correlation analysis of Planet imagery shows a decaying exponential pattern of post-failure displacements with an approximately 94% reduction in the deformation rate after six months with respect to the co-failure event. MT-InSAR analysis suggests a maximum LOS displacement rate of approximately 30 cm/year over the main failure body from November 2020 to February 2022; while the high-resolution TSX datasets show irreplaceable advantages in choosing the number of measurement points in MT-InSAR analysis with the number of measurement points being five times larger than those obtained by S1 datasets. The ICA analysis reveals three main types of kinematic patterns in the temporal evolution of post-failure deformation in MT-InSAR results, the dominant one being an exponential declining pattern similar to the results from Planet observations. Integrated 4D deformation modeling suggests that the most significant post-failure displacement mainly occurred toward the west, amounting to 28 meters during the entire post-failure acquisitions from June 2020 until February 2022. Additionally, maximum displacements of 17 meters and 19 meters occurred in this period toward the north and downward, respectively.

### 6.2 Introduction

Landslides are a common geological hazard in mountainous areas worldwide, causing fatalities in urban settlements, damage to infrastructure and agriculture, and substantial economic losses. The mechanism of landslides is often complicated, with most of the landslides being slow-moving at the beginning, at speeds ranging from a few millimeters to several meters each year (Lacroix et al., 2020). Then, due to specific triggers such as earthquakes, violent storms, or scouring from debris flows, creeping landslides can rapidly accelerate, leading to shear stress resisting shear strength, and eventually generating a

catastrophic avalanche-like movement (De Blasio, 2011). In remote mountainous regions with steep slopes, ground-based systems for landslide monitoring, such as GNSS, are challenging to implement (Xia et al., 2022b). In order to effectively compensate for this deficiency, satellite remote sensing techniques could be applied as an alternative to detect, monitor, and evaluate landslide hazards at regional scales. However, satellite optical and SAR remote sensing have unique advantages and weaknesses.

Due to its simplicity and reliability, the sub-pixel offset tracking technique using the normalized cross-correlation (NCC) algorithms has been widely implemented in optical remote sensing for horizontal displacement monitoring (Paul et al., 2015; Debella-Gilo and Kääb, 2011; Delacourt et al., 2004). For example, large-scale horizontal deformations can be derived from optical image time series for glacier movement, where the maximum velocity could exceed a hundred meters per year (Paul et al., 2015). Horizontal displacement of unstable slopes could also be obtained using the NCC to evaluate the kinematic properties of landslides (Delacourt et al., 2004). However, measurement precision, alignment error between relevant image pairs, and different interpolation factors can significantly impact the accuracy of the deformation maps produced through the NCC method (Debella-Gilo and Kääb, 2011; Delacourt et al., 2004), so this processing is only available when the magnitude of deformation is more than one-tenth of the pixel size (Hu et al., 2018b; Debella-Gilo and Kääb, 2011). It is also challenging to acquire cloud-free images during catastrophic failures as landslides more frequently occur in mountainous regions and during the rainy seasons. Additionally, assessing the physical characteristics (e.g., velocity, friction, and other physical parameters) of catastrophic landslides is extremely difficult due to their destructive capability and the temporal gap between suitable imagery when applying optical remote sensing (Lacroix et al., 2020).

SAR interferometry (InSAR) technology is another alternative for systematically identifying and monitoring geological hazards on a regional and even continental scale (Festa et al., 2022; Garg et al., 2022; Hu et al., 2022; Zhou et al., 2022b; Tomás et al., 2019; Motagh et al., 2017; Herrera et al., 2013), which could be implemented in inclement weather and be unaffected by sunlight conditions. In InSAR technology, many different methods can be adopted to precisely identify ground motion. For instance, advanced Multi-temporal InSAR (MT-InSAR) techniques such as persistent scatterer interferometry (PSI) and small baseline subset (SBAS) can be used to estimate landslide creep rates and time series with centimeter to millimeter level precision (Zhou et al., 2022a; Handwerger et al., 2019; Teshebaeva et al., 2015; Motagh et al., 2013). Over the last decades, an increasing number of academics have shown interest in monitoring slope instability dynamics using InSAR due to the significant increase in the number of images from the C-band Sentinel-1 (S1) satellite since its launch in 2014 (Festa et al., 2022; Dai et al., 2020; Tomás et al., 2019; Di Martire et al., 2018; Intrieri et al., 2018; Barra et al., 2016; Feng et al., 2015). Meanwhile, the development of the X-band high-resolution TSX mission also makes MT-InSAR techniques more promising in low coherence areas due to the increased spatial resolution and higher density of measurement points, as shown by numerous studies (Xia et al., 2022a; Di Martire et al., 2018; Singleton et al., 2014; Bovenga et al., 2014; Motagh et al., 2013). However, the application of InSAR technology has limitations due to decorrelation between radar images or unwrapping errors caused by rapid motions with significant gradients. The limitation of measured displacement is one-fourth of the wavelength between adjacent pixels (Singleton et al., 2014; Jiang et al., 2011). Therefore, using InSAR technology for rapid displacements, such as glacier motion, seismic deformation near faults, and

catastrophic failure exceeding the threshold limit is inappropriate (Singleton et al., 2014). Furthermore, SAR sensors are not sensitive to the deformation in the North-South (N-S) direction. GNSS measurements could be applied to improve the reliability of horizontal components of InSAR observations (Hu et al., 2018b). However, GNSS data are often unavailable in remote areas, especially for studying inaccessible landslides. Only a small number of particular landslide cases in hot-spot areas could be continuously analyzed and monitored with GNSS.

Taking the Aniangzhai landslide event in Sichuan Province of Southwest China as a case study, we investigate and characterize the post-failure mechanism of 17 June 2020. This ancient landslide near the Aniangzhai village was partially reactivated under a complex cascading event. Triggered by heavy rainfall in summer, the debris flows came from the northern gully to the Xiaojinchuan River, which flowed directly under the ancient landslide body and eroded the slope toe (Zhao et al., 2021; Zhu et al., 2021); then a big failure was triggered, and more than 20,000 people and 12 townships downstream were impacted (Xia et al., 2022b; Yan et al., 2021; Zhao et al., 2021). After the event, Zhao et al. (2021) conducted an emergency response and exploited UAVs to study the topographic change and the causality of the failure; whilst Yan et al. (2021) analyzed the seismic data and extracted different signals for landslide, debris flows, and floods, to obtain further interpretations for different stages of the hazard chain. Subsequent studies for this event confirmed that an apparent precursory motion already existed before the 2020 failure over the ancient landslide body, ranging from -50 to -80 mm/year (Kuang et al., 2022; Xia et al., 2022b; Zhu et al., 2021).

In this paper, we complement and design a framework to characterize the complete 4D post-failure deformation dynamics of the Aniangzhai landslide by integrating high-resolution optical and SAR satellite remote sensing data with feature extraction techniques and a mathematical relaxation model. Horizontal and line-of-sight (LOS) displacements for different periods are first derived using Planet and SAR data, respectively. Then three ascending and descending SAR datasets from TSX and S1 are combined to retrieve the displacements in East-West (E-W) and Up-Down (U-D) directions from LOS observations by ignoring the N-S displacement. In the following, optical and InSAR observations are then analyzed using independent component analysis (ICA) to extract the common spatiotemporal features of post-failure displacement between different sensors. Finally, the entire post-failure mechanism is retrieved from optical and radar data using an exponential decay model representing stress relaxation after the failure.

### 6.3 Geographical Setting of the Study Area

Danba County is situated on the southeastern side of the Qinghai-Tibet Plateau, and the Aniangzhai village is centered in this county. This region consists of steep mountains and narrow valleys. The landslide area is located at an altitude of around 2000~2500 m a.s.l., with the thickness of around 60 meters being evaluated by a local study exploiting UAV (Zhao et al., 2021). Figure 6.1 illustrates the post-failure status of the Aniangzhai landslide and the different zones of the landslide body. During the complex hazard chain in June 2020, the soil, stones and vegetation on the toe of the landslide were washed away by the debris flows; then a deep valley was formed in front of the landslide body, and this debuttressing directly triggered the reactivation of the ancient landslide body. Figures 6.1c and 6.1d show the boundaries of the landslide failure and reveal the southern and northern



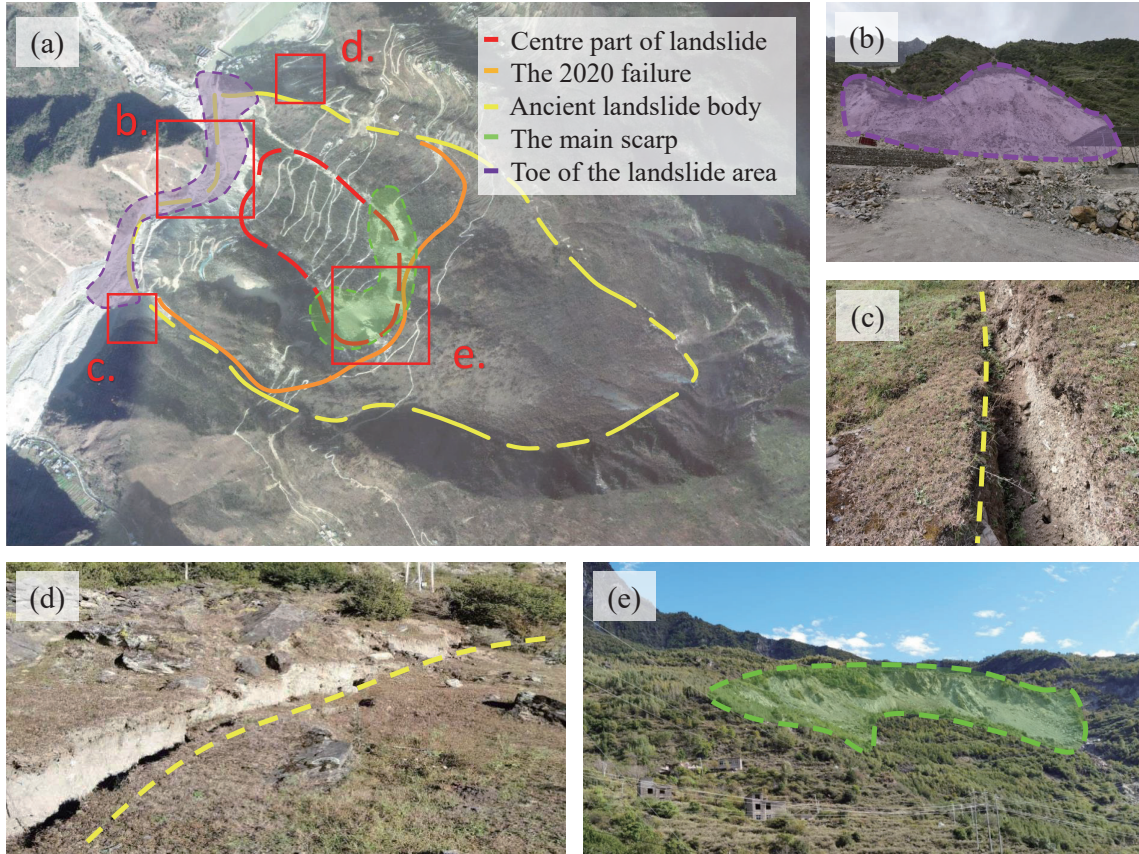


**Figure 6.1:** The Aniangzhai landslide and ground pictures of its different zones: (a) geographical setting of the study area, (b) the toe, (c) the southern lateral flank, (d) the northern lateral flank, and (e) the main scarp (adapted by Xia et al. (2022b)). The red line reveals the central zone of the 2020 event, which had the most significant movement during the catastrophic failure; the orange line depicts a medium motion of around 1~5 meters, whereas the yellow line shows the extent of the ancient landslide body. The background image in (a) is from Skysat high-resolution image acquired in November 2020.

lateral flanks of the landslide, respectively. Those cracks are clearly visible caused by block motion, with a width of approximately 1~1.5 meters. Indeed, this structure improves the difficulties in phase unwrapping for MT-InSAR processing.

## 6.4 Methodology

The data-processing workflow and significant steps included in this framework are outlined in Figure 6.2, as well as the methodologies are discussed in detail in this section.

### 6.4.1 Optical Images Processing

We process and evaluate post-failure horizontal kinematics of the landslide body after the June 2020 failure, e.g., extent, direction, and magnitude of the motion, using a sequence of high-resolution optical satellite images taken by the Planet Lab satellite constellation

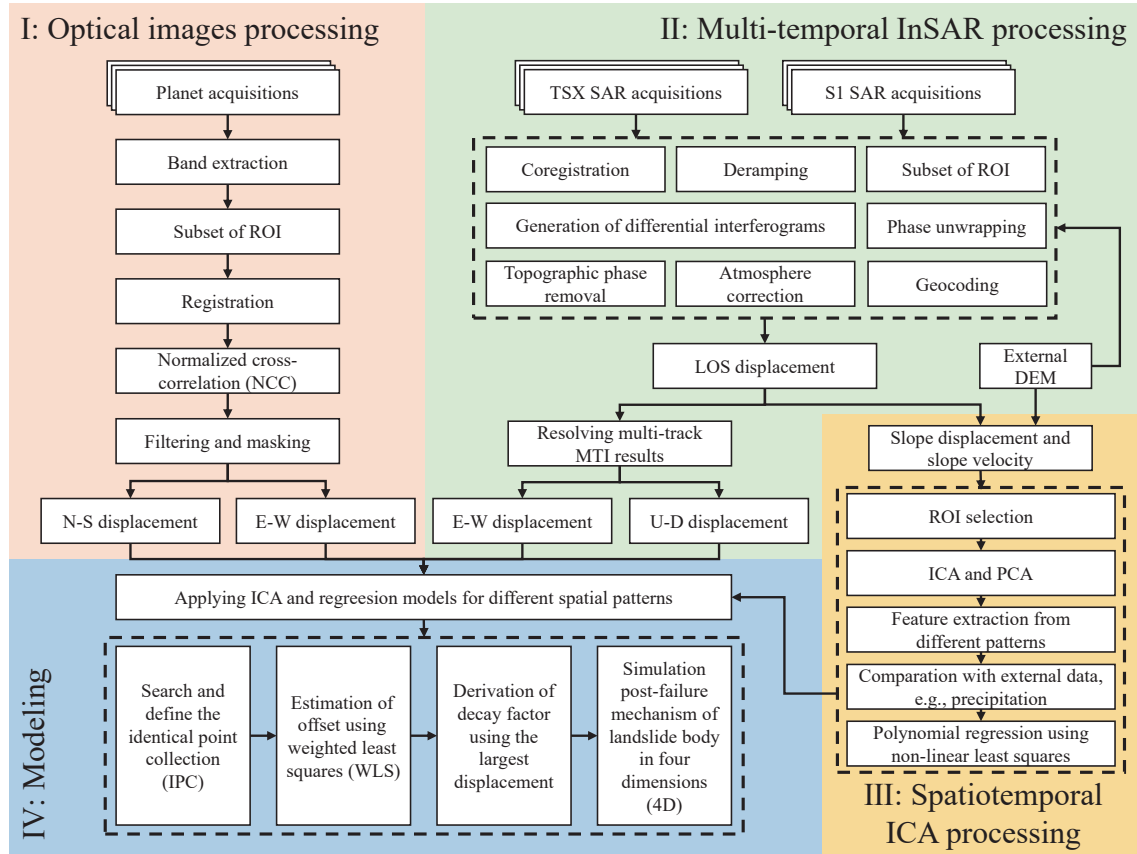


**Figure 6.2:** Flowchart of data processing and the framework. (The missing abbreviations: ROI is the area of interest; E-W is the East-West direction; N-S is the North-South direction; U-D is the up-down direction; PCA is the principal component analysis.)

(Team, 2017). The applied Planet satellite imagery has a resolution of 3 meters, which is acquired from June 2020 to January 2021. The steps to generate the time series of horizontal deformation from Planet images are as follows: (i) the red band is split out of the multi-spectral Planet imagery, since it has the lowest root-mean-square error (RMSE) in image registration among those three RGB bands; (ii) all the Planet acquisitions are cropped and registered to the same subset spanning the landslide region, constituting the input to the NCC analysis using the COSI-Corr software package (Leprince et al., 2007) for the computation of the E-W and N-S horizontal displacements for every two steps of pixels; (iii) a median filter is then applied, and the irrelevant areas outside of the failure body, as well as the outliers whereas the signal-to-noise ratio (SNR) is below 0.9, are masked out; SNR belongs to the interval  $[0,1]$ , and the higher, the better; (iv) the magnitude and direction of displacements are finally derived for each pixel.

### 6.4.2 Multi-temporal InSAR Processing

This study exploits X-band TSX SAR images and the C-band S1 SAR images for MT-InSAR processing. The detailed features of the data are shown in Table 6.1. Based on the already existing knowledge from previous studies that the displacement is towards the North-West direction, the descending TSX images from the German Aerospace Agency

**Table 6.1:** Relevant features of the deployed SAR data for MT-InSAR processing. HS represents the High-resolution Spotlight mode, while IW refers to the Interferometric Wide (IW) swath mode.  $\sigma_T$  and  $\sigma_S$  represent the temporal resolution and spatial resolution, respectively. The unit of  $\sigma_T$  is day, and the unit of  $\sigma_S$  is meter $\times$ meter in range and azimuth directions.

SAR Data	Mode	Duration	Image	$\sigma_T$	$\sigma_S$
TSX descending	HS	2020.11–2022.02	40	11	$0.91 \times 1.25$
S1 descending	IW	2020.11–2022.02	40	12	$2.33 \times 13.96$
S1 ascending	IW	2020.11–2022.02	36	12	$2.33 \times 13.93$

(DLR) are exploited due to their higher sensitivity (Haghshenas Haghighi and Motagh, 2016). The TSX data in spotlight mode has a resolution of around  $0.9 \times 1.2\text{m}$  in range and azimuth direction, respectively. The restrictions imposed by decorrelation and unwrapping errors due to rapid motions prohibit the use of the images from July 2020 to October 2020 for the MT-InSAR processing, despite the fact that we acquired the TSX immediately after the failure. In fact, only a few scatters could be obtained when we initially tried to analyze the entire collection of TSX data since the failure. Therefore, for the MT-InSAR processing, we only used 40 TSX images from November 2020 to February 2022. Meanwhile, we analyze 40 S1 descending and 36 S1 ascending C-band SAR images during the same period for the MT-InSAR processing (Copernicus, 2020). The S1 images have a resolution of around  $2.3 \times 14.0\text{m}$  in range and azimuth direction, respectively.

The MT-InSAR processing chain has been discussed in a number of previous studies (Haghshenas Haghighi and Motagh, 2017; Fattahi et al., 2016; Grandin et al., 2016). In InSAR processing, time series of SAR images are well-coregistered and then cropped to the selected subset of the area of interest (ROI). For landslide monitoring, the traditional InSAR has limitations, which is the extensive coherence loss between successive image collections and atmospheric disturbances (Wasowski and Bovenga, 2014; Zebker et al., 1992). Hence, advanced MT-InSAR techniques are used to deal with the problem and derive displacement in the LOS direction. In this study, we apply the SBAS technique to process all SAR data, exploiting a network of small spatial and temporal baselines to reduce the decorrelation (Anderssohn et al., 2009; Lanari et al., 2007). In SBAS processing, the distributed scatter is taken into consideration, which is defined as a pixel having similar statistical behavior to its neighbors. The GAMMA and StaMPS software packages are used to implement the interferometric and MT-InSAR analysis (Wegmüller et al., 2016; Hooper et al., 2012, 2007).

After multiple MT-InSAR results are derived from various SAR datasets, we resolve the horizontal and vertical deformation with the weighted least squares (WLS) method following the equation (Fuhrmann and Garthwaite, 2019; Hu et al., 2014):

$$\begin{bmatrix} d_{LOS1} \\ d_{LOS2} \\ d_{LOS3} \end{bmatrix} = \begin{bmatrix} \cos\theta_1 & -\sin\theta_1\cos\alpha_1 & \sin\theta_1\sin\alpha_1 \\ \cos\theta_2 & -\sin\theta_2\cos\alpha_2 & \sin\theta_2\sin\alpha_2 \\ \cos\theta_3 & -\sin\theta_3\cos\alpha_3 & \sin\theta_3\sin\alpha_3 \end{bmatrix} \cdot \begin{bmatrix} d_{U1} \\ d_{E1} \\ d_{N1} \end{bmatrix} \quad (6.1)$$

where  $d$  represents displacement,  $LOS^{1,2,3}$  are S1 ascending data, S1 descending data, and TSX descending data, respectively.  $\theta$  and  $\alpha$  are inclination angle and heading angle, respectively. We use a diagonal matrix  $W_1$  to weight the least squares, containing different

spatial resolutions for different sensors, i.e.,  $W_1 = \text{diag}[\sigma_{LOS1}^2 \sigma_{LOS2}^2 \sigma_{LOS3}^2]^{-1}$ . The spatial resolutions  $\sigma_{TSX}$  and  $\sigma_{S1}$  are around 1.5m and 14.2m, respectively.

The three unknowns are theoretically solvable using the three observations, i.e., deformation in E-W, N-S, and U-D directions. However, the SAR sensor is not sensitive to the deformation of the N-S direction since the satellite heading angle is near that direction, possibly leading to artificial exaggeration. Hence, the N-S component is often ignored in resolving three-dimensional velocity in the studies (Ren et al., 2022; Fuhrmann and Garthwaite, 2019). Here, we adopt the same strategy to only resolve the deformation in the E-W and U-D directions using three tracks by omitting the N-S component; as for our case study of the Aniangzhai landslide, the E-W displacements dominate the horizontal displacement. It is equivalent to having one track InSAR observation as a redundant observation in the least squares adjustment.

### 6.4.3 Spatiotemporal Independent Component Analysis (ICA) of Displacement

In this section, we introduce the feature extraction of landslide kinematics from different spatiotemporal patterns over the entire Aniangzhai landslide body by performing ICA decomposition (the yellow curve in Figure 6.1). Since the obtained observations often contain different components in experiments, time series decomposition is a frequently utilized strategy for data processing to isolate the mixed signals from noises. In this study, we mainly use the ICA based on the fixed-point algorithms for ICA (FastICA) approach (Hyvärinen and Oja, 2000). ICA is a leading method for finding hidden factors or components in multivariate multidimensional statistics, which decomposes time series into independent components (ICs) in statistics (Delac et al., 2005; Draper et al., 2003; Hyvärinen and Oja, 2000).

The process of ICA is achieved assuming that each independent component follows a non-Gaussian probability distribution. The mixed signals and independent components have the following relationship:

$$O_{t \times n} = D_{t \times l} \cdot S_{l \times n} \quad (6.2)$$

where  $O$  is the remote sensing observations,  $D$  represents the mixing matrix, and  $S$  is the decomposed source matrix. The subscripts  $t$  is the number of the observations,  $n$  represents pixels in each acquisition, and  $l$  is the number of ICs.

As a pre-processing step for ICA, centralization and whitening should be implemented to make the initially solved mixing matrix degenerate into an orthogonal array, reducing the correlation between features and the workload. As an alternative, this procedure can also be implemented with principal component analysis (PCA), a method for extracting uncorrelated signals from heterogeneous data. With PCA, we reduce the dimensionality and noise from the remote sensing observations, maintain the features with the largest contribution to the variance, and retrieve the principal components (Peng et al., 2022; Delac et al., 2005; Draper et al., 2003). Eventually, with the help of the fixed-point iterative algorithm in FastICA, the source, mixing, and unmixing matrices can be derived by maximizing spatially non-Gaussian sources (Hyvärinen and Oja, 2000).

The optical and InSAR displacements are individually processed with the ICA algorithm. For the horizontal deformation derived using optical observations, its temporal kinematics can be simply extracted and simulated with ICA using a mathematical relaxation model. The kinematics are comprised of different magnitudes of temporal decay

since the large failure, in a manner of exponential or logarithmic forms, which we have tested both of them in this study. For the InSAR observations, the chosen TSX observations are exploited due to availability and the highest density of scatters, i.e., five times higher than in the S1 dataset. In order to reduce the geometric discrepancy introduced by the different satellite sensors, we converted the displacement time series from the LOS direction to the slope direction (Herrera et al., 2013).

Furthermore, to mathematically describe the dominated motion kinematics for different spatial patterns of InSAR observations, polynomial kernel ridge regression is adopted to simulate the motion characteristics from different ICs (Exterkate, 2013), representing those expanded features extracted from different spatiotemporal patterns as follows:

$$y(x) = \sum_{i=1}^n \alpha_i \cdot k(x_i, x) + \beta_i \quad (6.3)$$

with

$$k(x_i, x) = (x_i x + 1)^q \quad (6.4)$$

where  $x$  and  $y(x)$  represent the InSAR observations and the output of the nonlinear system at each pixel  $i$ ,  $\alpha$  is the weight coefficients, and  $\beta$  is the constant offsets,  $q$  is the order of polynomial function. To avoid over-fitting, we only apply low-order polynomial regression, i.e., second to 4th-order polynomials containing the best RMSEs, which are then used for integrating optical and InSAR observations in the next section.

#### 6.4.4 Multi-sensor Integration Modeling

In this section, we propose a methodology to integrate multi-sensor satellite remote sensing datasets using a decaying exponential model in order to overcome the limitations of a single sensor and derive a complete 4D map of landslide deformation characteristics. For example, when using NCC to process optical images, the measurement precision is limited by the accuracy of the applied images, and the vertical information is unavailable. On the other hand, when applying the MT-InSAR method, only the deformation in the LOS direction can be obtained using data with a single satellite track, and the sensor is not sensitive to the deformation in the N-S directions as well. Here, the identical points distributed in all remote sensing datasets are defined as identical point collection (IPC).

As mentioned in the previous section, we could conduct ICA modeling different magnitudes of relaxation decaying for the E-W and N-S displacements from the optical images for the first six months after the failure. Similarly, the E-W and U-D displacements for the period of MT-InSAR results were resolved with different polynomial regressions following ICA analysis. Here, the common deformation components between optical and SAR observations in the common E-W direction are modeled, indicating the same temporal evolution, and the corresponding offsets are estimated as follows:

$$\begin{bmatrix} d_{LOS1} \\ d_{LOS2} \\ d_{LOS3} \\ d_{EW-OP} \\ d_{NS-OP} \end{bmatrix} = \begin{bmatrix} \cos\theta_1 & -\sin\theta_1\cos\alpha_1 & \sin\theta_1\sin\alpha_1 \\ \cos\theta_2 & -\sin\theta_2\cos\alpha_2 & \sin\theta_2\sin\alpha_2 \\ \cos\theta_3 & -\sin\theta_3\cos\alpha_3 & \sin\theta_3\sin\alpha_3 \\ 0 & 1 & 0 \\ 0 & 0 & 1 \end{bmatrix} \cdot \begin{bmatrix} d_{U2} \\ d_{E2} \\ d_{N2} \end{bmatrix} \quad (6.5)$$

with

$$\Delta d_{E,i} = \frac{1}{m} \sum_{i=1}^m \sqrt{(d_{E2,i} - d_{E1,i})^2} \quad (6.6)$$

**Table 6.2:** Relevant statistics of NCC results from Planet images. The maximum and mean displacements  $d_{max}$  and  $d_{mean}$ , as well as the maximum and mean velocities  $v_{max}$  and  $v_{mean}$  are derived and displayed for the sequential time spans. The co-failure results (June 17 to June 24) is from our previous studies (Xia et al., 2022b). The unit for displacement is meter, and the unit for velocity is meter/day.

Duration	Time lag (day)	$d_{max}$	$d_{mean}$	$v_{max}$	$v_{mean}$
20200617–20200624	$t_0 = 8$	14.72	3.82	1.84	0.48
20200624–20200726	$t_1 = 33$	14.30	7.78	0.43	0.24
20200726–20200930	$t_2 = 67$	8.95	2.67	0.13	0.04
20200930–20210111	$t_3 = 104$	11.70	2.62	0.11	0.03

where  $\Delta d_{E,i}$  represents the displacement offset in the common E-W direction at each pixel  $i$ , being derived from the ensemble average of all offsets for common pixels in temporal evolution.  $m$  is the number of common observations at each pixel following ICA analysis. The rest parameters are the same as in equation (6.1). We considered the weighting matrix  $W_2$  here for the least squares adjustment, which is  $W_2 = \text{diag}[\sigma_{LOS1}^2 \sigma_{LOS2}^2 \sigma_{LOS3}^2 \sigma_{OP}^2 \sigma_{OP}^2]^{-1}$ . The spatial resolution of TSX and S1 has been previously mentioned, and  $\sigma_{OP}$  is approximately 4.2 meters. Similarly, the offsets in the U-D directions could be derived as the generation of E-W offsets. However, as the N-S components are ignored in the previous derivations in multi-track InSAR processing, only the measurements from optical observations are available and taken into the subsequent modeling procedures by setting the initial displacement in the N-S direction to zero.

After that, we continue to integrate the multi-sensor remote sensing data by modeling a mathematical exponential decay to represent the stress relaxation mechanisms of the landslide body after failure. The modeling equation has been applied as follows:

$$d_k(t_k) = a_k \cdot e^{t_k/\tau} + c_k \quad (6.7)$$

where  $d(t)$  is the displacement at the time since failure  $t$ , and  $k=x,y,z$ , where  $x,y,z$  represent the E-W, N-S and vertical directions, respectively.  $a$  is amplitude associated with decay,  $c$  is an offset, and  $\tau$  is the decay factor ( $\tau < 0$ ), representing the decelerating phases. The decay factor is derived using the largest displacement in the E-W direction. We assume that the post-failure dynamics are homogeneous under the natural state and the decay factor remains the same for decaying kinematics of all time series over the landslide body. The logarithmic form of the model is also tested and will be elaborated more in the discussion.

## 6.5 Results

### 6.5.1 Horizontal Deformation Based on Planet Images

Figure 6.3 illustrates the time series of horizontal displacements derived from Planet optical images after the catastrophic failure in June 2020. The results show quite a large displacement for 1.5 months after the failure, with the maximum deformation of around 14.3 meters towards the N-W direction. After that, the rate of horizontal deformation decreases with time (see Table 6.2 for statistical details).



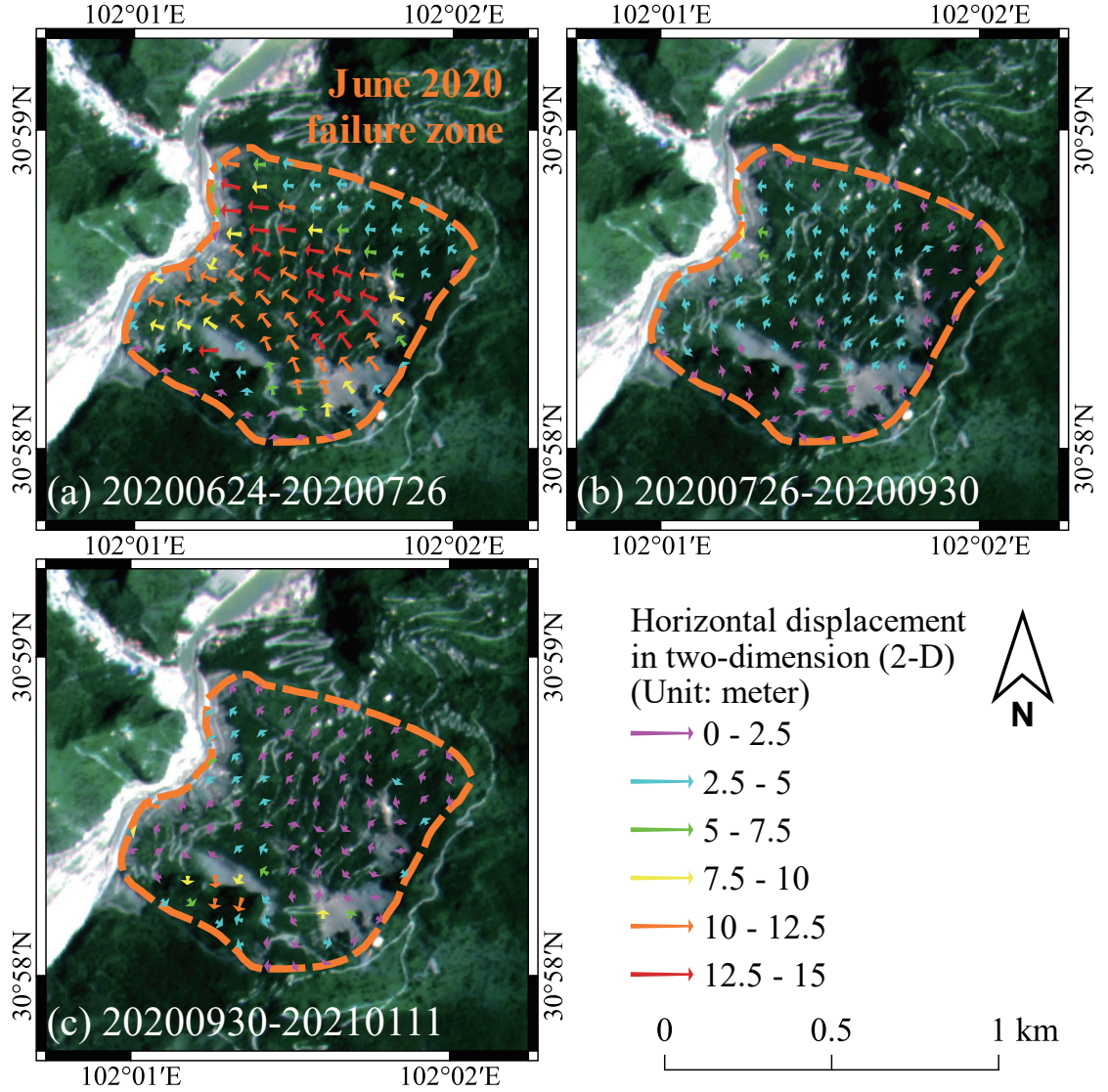


**Figure 6.3:** 2D results of horizontal displacement derived using Planet images. The results are within the time spans (a) from 24 June 2020 to 26 July 2020, (b) from 26 July 2020 to 30 September 2020, and (c) from 30 September 2020 to 11 January 2021. The arrows demonstrate the magnitude and direction of the motions for different patterns using a step of 15 pixels in both W-E and N-S directions. The boundaries of the landslide body are presented in Figure 6.1d.

Table 6.2 reveals that both  $v_{max}$  and  $v_{mean}$  of the failure body were reducing after failure in an exponential form during the period of observations. The co-failure results in Table 6.2, i.e., from 17 June to 24 June, are from our previous study and are used here for comparison (Xia et al., 2022b). The four time intervals  $t_0 \sim t_3$  that we choose for NCC calculation are increasing with time, to be suitable for catching the incrementally decreasing displacements of the failure part. Between phases of  $t_0 \sim t_1$ ,  $t_1 \sim t_2$  and  $t_2 \sim t_3$ , the decaying ratios in  $v_{max}$  are approximately 76%, 70% and 15%, respectively; while the decay ratios in  $v_{mean}$  are about 50%, 83% and 25%, respectively. In total, the

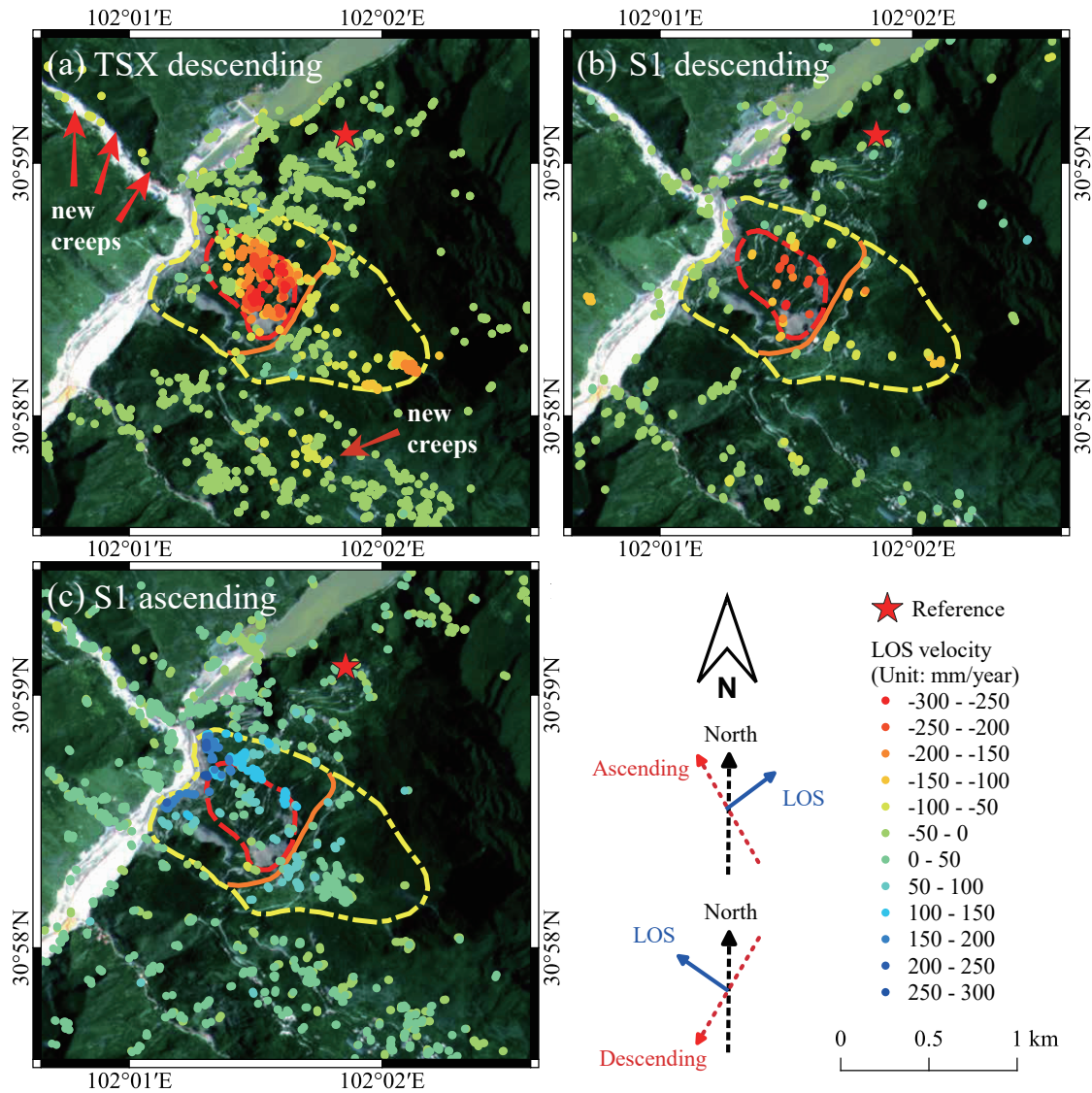


**Figure 6.4:** MT-InSAR results with displacement rates in LOS direction using (a) descending TSX data, (b) descending S1 data, and (c) ascending S1 data. The time period of observations for the MT-InSAR processing is from November 2020 to February 2022. The boundaries of different zones of the landslide body are the same as the ones in Figure 6.1d. Image background is from Planet image acquired in August 2021.

$v_{max}$  and  $v_{mean}$  have been reduced by around 94.02% and 93.75% with respect to the co-failure displacement rates during the entire optical acquisition.

### 6.5.2 MT-InSAR Results

Figure 6.4 demonstrates the MT-InSAR displacement rates in the LOS direction for TSX and S1 data from November 2020 to February 2022, with positive values indicating motion towards the satellite and negative values indicating motion away from it. Outside of the landslide zone in the northern hillslope, a reference point is selected to represent a stable location throughout the entire data acquisition.



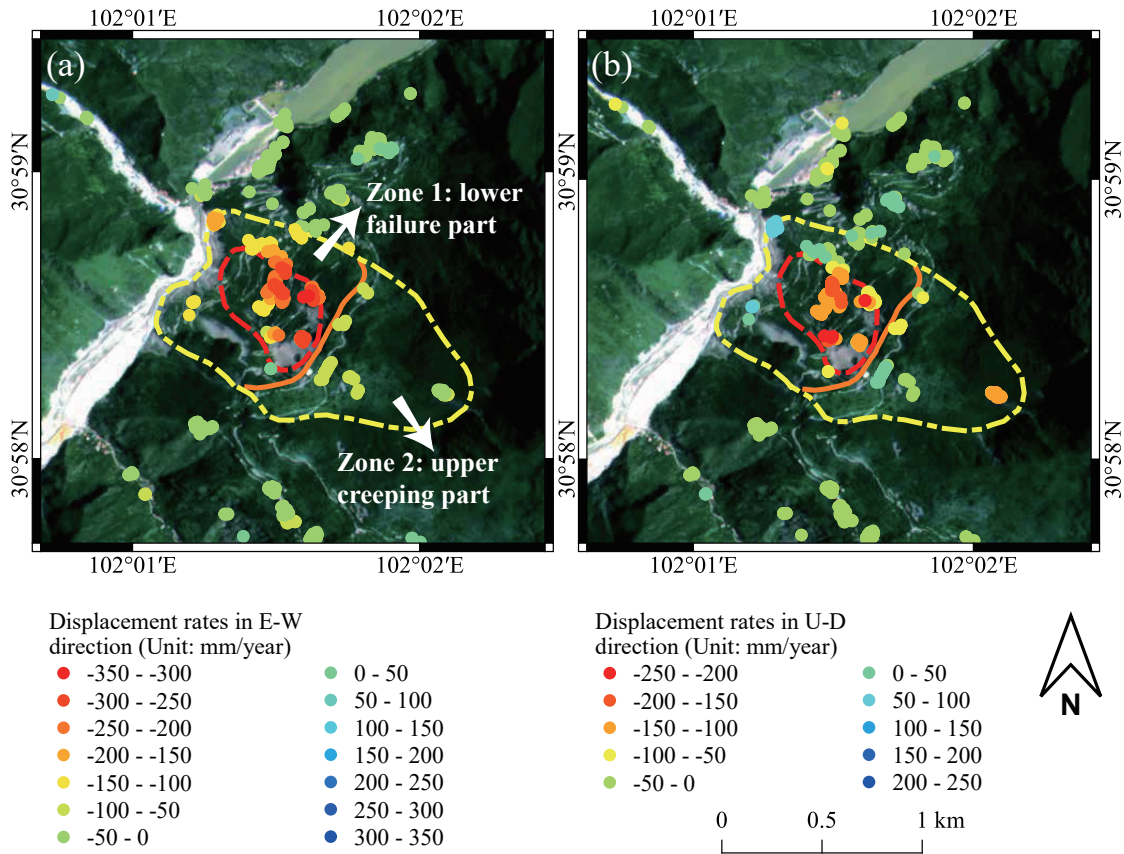


**Figure 6.5:** Resolved horizontal and vertical displacements in (a) East-West (E-W) and (b) Up-Down (U-D) directions from multi-track MT-InSAR observations. The boundaries of different zones of the landslide body are presented in Figure 6.1d. Image background is from a Planet image acquired in August 2021.

As seen in Figure 6.4a and Figure 6.4b, the central failure part has the largest displacement rates with a maximum velocity in the LOS direction reaching approximately -300 mm/year for both descending TSX and S1 data. Interestingly, the upper part outside the ancient landslide body also shows deformation, with a LOS velocity amounting to -200 to -100 mm/year. Moreover, another creeping landslide outside the ancient landslide could be seen in the southern hillslope and along the river channel with displacement rates of approximately -100 to -50 mm/year. Although the MT-InSAR results from S1 data, demonstrate similar distributions and features as the TSX results (Figures 6.4a and 6.4b), the number of measurement points is significantly lower compared to TSX data, i.e., more than five times smaller. This is not surprising considering the significant difference in spatial resolution of the two exploited datasets. Figure 6.4c shows the MT-InSAR results using ascending S1 data. The ascending satellite observation geometry is less sensitive than the descending data for this landslide case with N-W motions. Accordingly, the revealed maximum displacement rates could also reach a magnitude of about 300 mm/year. However, for the descending datasets, the most significant deformation could be observed in the central failure part of the landslide (red curve), while for the ascending datasets, the toe area of the landslide body could be observed with the largest deformation.

By integrating ascending and descending S1 data with descending TSX data using least squares inversion (see Section 6.4.2), we resolved the horizontal and vertical displacements in E-W and U-D directions by ignoring the N-S component, and Figure 6.5 shows the results. For the E-W displacement, positive values indicate motion towards the East, while negative values indicate motion towards the West. For the vertical displacement, positive values indicate motion upwards while negative values indicate motion downwards.

Interestingly, Figure 6.5 reveals two opposite characteristics of the kinematics over the ancient landslide body. For the failure part in the downslope (Zone 1), the horizontal deformation dominates the motion as the largest displacement in the E-W direction amounts to -350 mm/year, much larger than the vertical motion with a displacement rate of about -200 mm/year. On the contrary, the head part of the landslide (Zone 2) reveals larger vertical displacements than horizontal motions, amounting to -150 to -100 mm/year. The new landslides in the southern hillslope contain more horizontal displacements than vertical, horizontal motions after the June 2020 failure.

### 6.5.3 Feature Extraction Using ICA

In order to investigate the spatiotemporal patterns of landslide kinematics, we further conducted the ICA decomposition to the optical and InSAR time series. For the optical measurements, exponential decay is the dominant decomposed feature, from which different deformation magnitudes could be simply expressed. Taking the advantages of the high density in the included measurement points over the landslide body (Figure 6.4), the descending TSX data is exploited with the LOS velocities converted along slope direction as mentioned in Section 6.4.3 for better interpretation. It is worth noting that artificial exaggeration and extreme values could be obtained when the conversion factor approaches zero. For example, in the studies of Kalia (2018) and Herrera et al. (2013), anomalous solution occurs when the conversion factor ranges in  $[-0.3, 0.3]$ . Hence, we filtered out scatters with the conversion factor within the same interval, leading to approximately 2% of total scatters being excluded from MT-InSAR results.

Figure 6.6 demonstrates the ICA results applied to the TSX time series in order to extract deformation features over the entire ancient landslide body from November 2020 to February 2022. Figure 6.6a shows the locations of derived scatters with the most significant independent components, i.e., the most significant features from the observations; while Figure 6.6b reveals the solved mixing matrix for the first three ICs. Figure 6.6c shows the corresponding mean and cumulative daily precipitation covering this period. We use the daily rainfall dataset from the Climate Hazards Group InfraRed Precipitation with Station data (CHIRPS). CHIRPS creates gridded rainfall time series that cover all longitudes using  $0.05^\circ$  resolution ( $\sim 5\text{km}$ ) satellite images, as well as in-situ station data. Its accuracy is sufficient for regional applications and exploitation.

By performing ICA, we can see that IC1 reveals the feature of a general exponential trend of decline for the entire period, similar to the result from Planet data, dominating the pixels mainly, which are concentrated in the central failure part (Zone 1). In comparison, IC2 reveals a feature dominating the upper part with creeping motions (Zone 2), which remains stable from the beginning until April 2020, then speeds up since April 2020 due to the rising amount of precipitation, and slows down again correlated with the dry season since November 2021. The third component, IC3, which dominates the toe and foot part of the landslide, reveals the same feature as IC2 before October 2021. Thereafter, however, IC3 moves reversely and remains relatively stable compared to IC2. Overall,

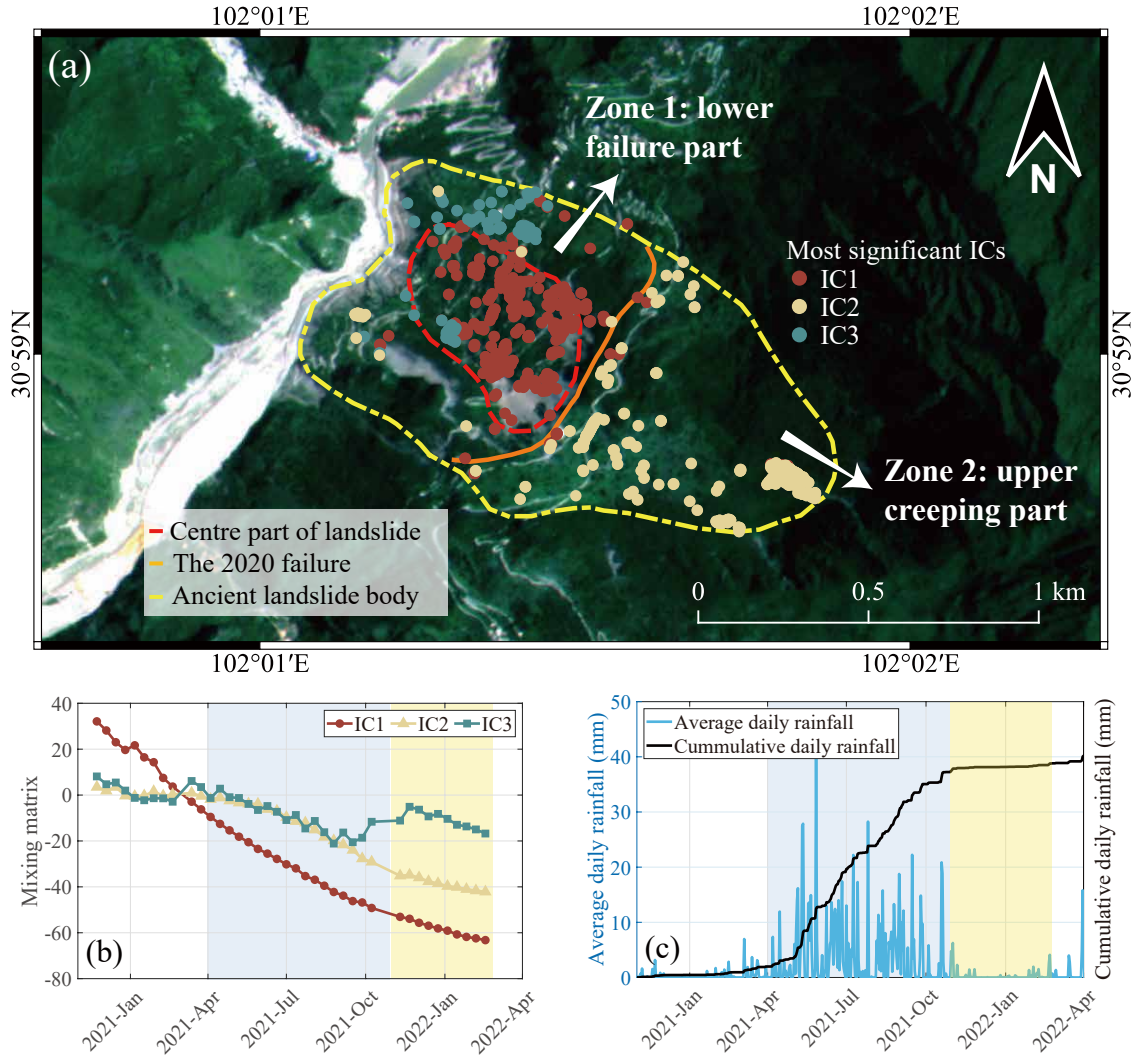
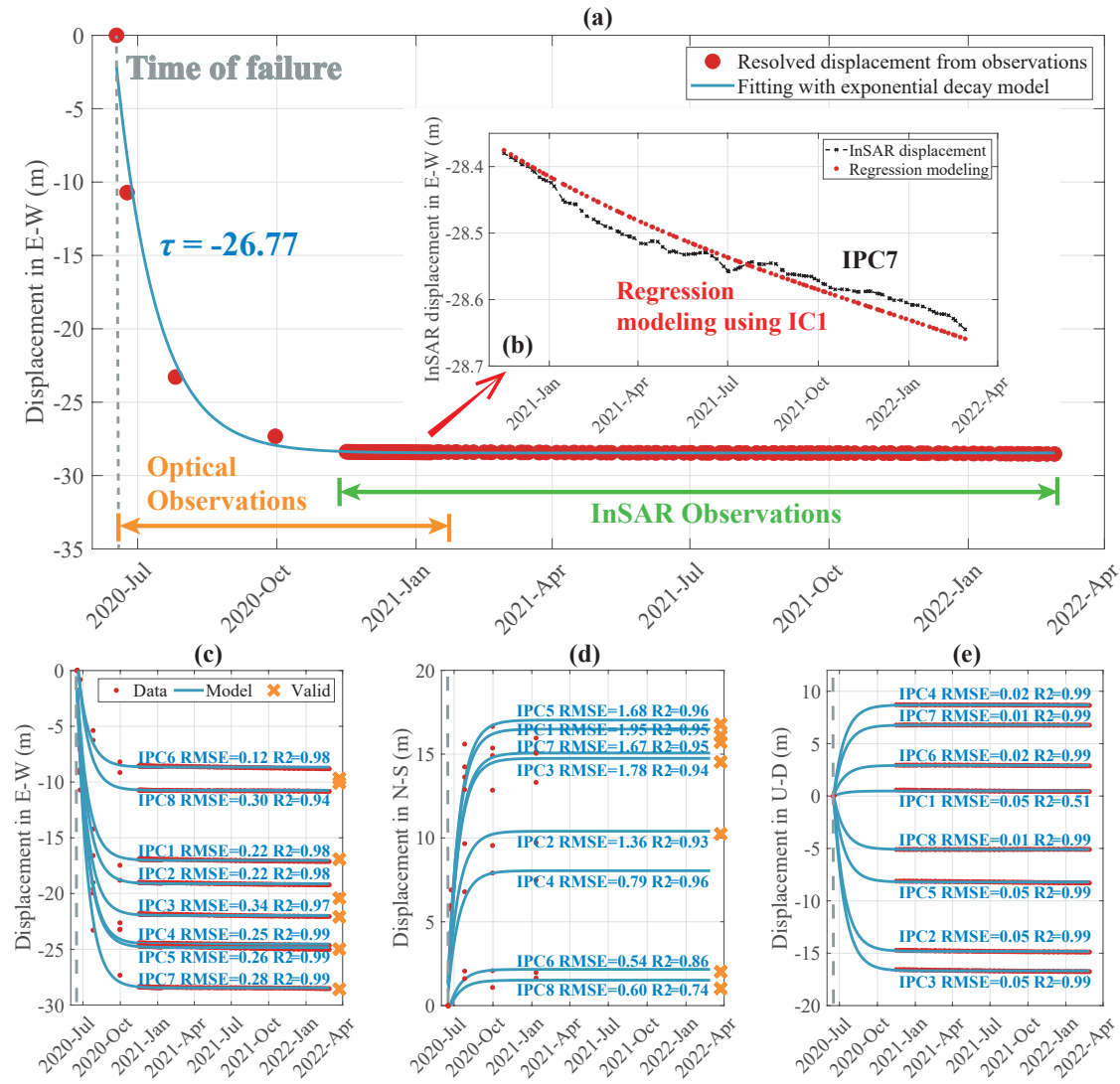


**Figure 6.6:** Results of independent component analysis (ICA) applied to TSX observations over the area of the ancient landslide body. (a) Locations of derived scatters with the most significant independent components. Image background is from a Planet image acquired in August 2021. (b) The mixing matrix from independent component analysis. (c) The corresponding daily and cumulative precipitation. The corresponding blue and yellow windows in (b) and (c) represent the rainy period and dry period afterwards.

ICA decomposition helps to extract and classify the time series of kinematics for different spatiotemporal patterns over the landslide body.

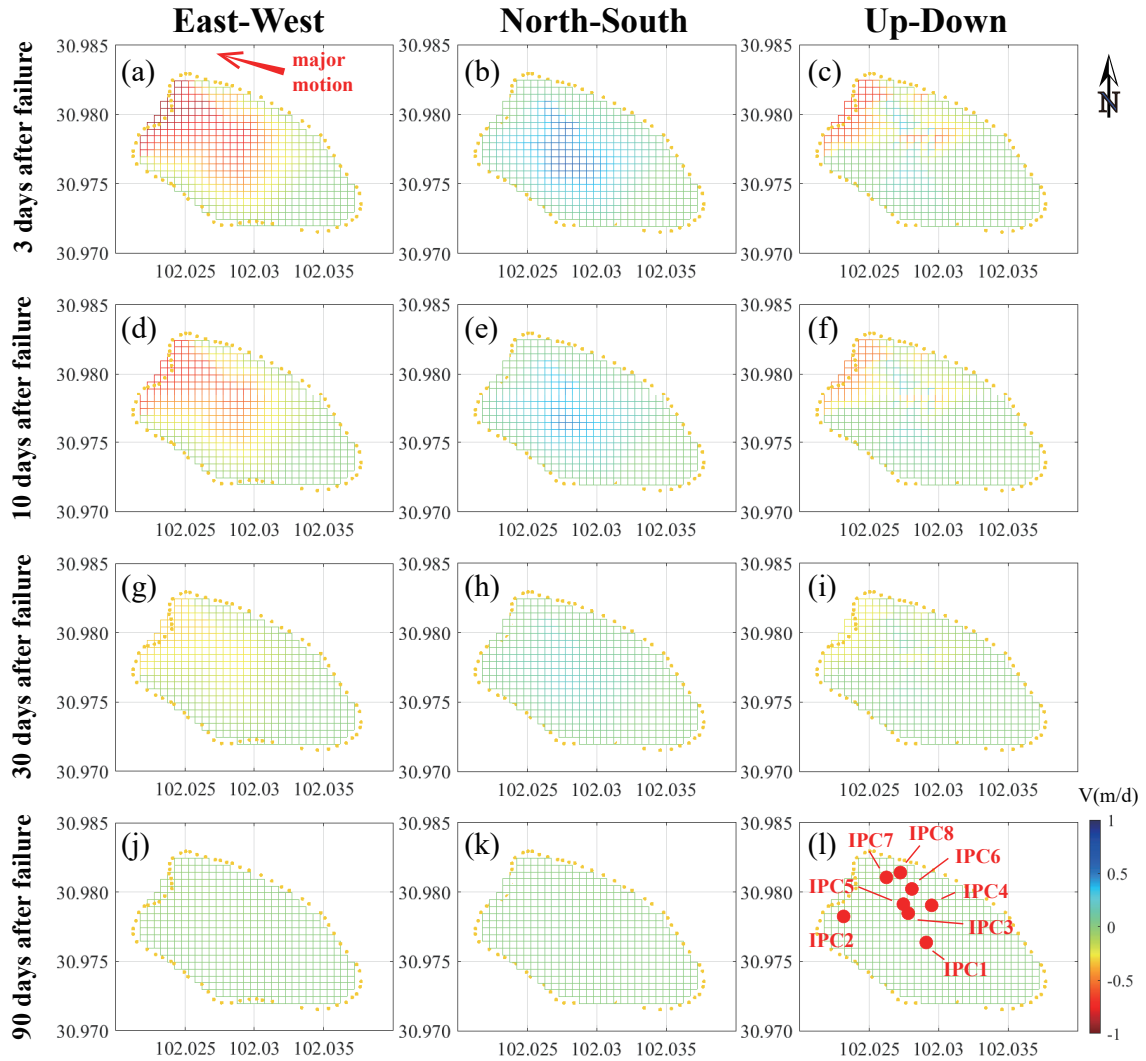
#### 6.5.4 4D Deformation Modeling

Figure 6.7 shows the results of the integration of optical and InSAR measurements using an exponential decay model representing the stress relaxation after the failure. The decay factor  $\tau$  is estimated using the largest displacement in the E-W direction, i.e., the IPC7, assumed to be the same for all the time series for landslide kinematics. Eight samples are chosen randomly and displayed as examples in Figure 6.7, and their locations are shown



**Figure 6.7:** (a) Example of deriving decay factor in the exponential modeling using the largest displacement in E-W direction integrating both optical and InSAR measurements. (b) Example of InSAR observations in E-W direction for ICP7 using regression with IC1 model. Examples of derived 4D displacements using an exponential decay model in (c) E-W direction, (d) N-S direction, and (e) U-D direction. The corresponding locations of the IPCs are shown in Figure 6.8l.

in Figure 6.8l. For the validation of the modeling, since we do not obtain in-situ data, we exploited two Planet images to derive the horizontal displacements covering the entire remote sensing collection, i.e., the first one on 15 June 2020 before the failure, the latter one on 24 March 2022. We apply the NCC algorithms to derive the horizontal displacement, and the validation can only be performed in E-W and N-S directions. Figures 6.7c and d reveal the validation results. To be noticed is that the overall displacement of IPC4 for validation is discarded due to lower SNR values ( $<0.9$ ). Nevertheless, the rest validations show good correspondence with the modeled displacements.



**Figure 6.8:** Examples of 4D post-failure modeling from IPCs in E-W, N-S and vertical directions for various time frames of 3 days, 10 days, 30 days and 90 days after the catastrophic failure on 17 June 2020. Yellow curve shows the boundary of ancient landslide body (see Figure 6.1a).

Figure 6.8 reveals examples applying the integrated model for recovering displacement rates in 3 days, 10 days, 30 days, and 90 days after the failure. The modeling is derived in E-W, N-S, and U-D directions, and applied to the re-gridded pixels over the landslide body. We set here the areas outside of the northern and southern flanks, and on the head part, which did not fail during the 2020 event, to be stable; and the areas between them to be active with the largest deformation existing near the river channel, which is proved by our studies and fieldworks as shown in Figure 6.1. To evaluate the quality of the modeling in three dimensions, we examine the RMSEs of the derived model. The RMSEs are 0.12~0.54, 0.32~2.07, and 0~0.08 meters in the W-E, N-S, and U-D directions, respectively. Aside from RMSEs, we also check the coefficient of determination  $R^2$ , which is the measure of the proportion of the variation in a strain that can be interpreted by the independent variable, which is used to judge the explanatory power of the regression



model (Steel et al., 1960). In our study,  $R^2$  are 92%~99%, 68%~99%, and 50%~99% in modeling the W-E, N-S, and U-D displacement, respectively.

### 6.6 Discussion

In this paper, we developed a framework to demonstrate how the high-resolution optical and SAR satellite remote sensing data can be applied and integrated with the exponential relaxation model to assess complicated post-failure slope stability related to the 2020 Aniangzhai landslide failure in Southwest China. A comprehensive analysis of the entire landslide dynamics after failure cannot be performed using only a single sensor, since the sensor has its own unique strengths and weaknesses. However, a combination of SAR and optical data can be exploited to detect various procedures or types of landslides. For example, in this study, we used optical imagery to monitor the rapid phase of the Aniangzhai landslide after failure, and applied InSAR techniques to investigate the creeping movement from November 2020 to February 2022. To integrate multi-sensor observations, we apply exponential decay modeling with least squares adjustment to simulate and recover the complete 4D time series for the kinematics of the entire ancient landslide.

#### 6.6.1 Early Post-failure Deformation from Planet

The dynamics of the slope stability after the Aniangzhai landslide failure are clearly demonstrated in their sequential phases using optical remote sensing time series. Our previous study revealed that the maximum horizontal displacement rate during the failure could reach approximately 1.8 meters per day (Table 6.1). In contrast, the displacement rate decreased significantly by approximately 76% and 94% at 1.5 and 6 months after the failure, respectively. Though, the horizontal displacements over the failure part could still be distinctly observed until the end of July 2020, amounting to approximately 14.3 meters toward the N-W direction. Thereafter, we observed a reduction in the maximum and mean velocities. For comparison, Kuang et al. (2022) also derived horizontal displacement using offset tracking techniques after the failure, with a maximum horizontal displacement of approximately 16 meters. By comparing our study with their distributed deformation vectors, the results are clearly consistent with each other, although the horizontal deformation is slightly lower in our study. The difference could be due to various post-processing and parameter strategies in the data processing. We also observed a squeezing phenomenon from the northern and southern flanks toward the central failure zone, which was observed during our fieldwork.

Generally, the Planet results show that the deformation failure part becomes stepwise stabilized after the June 2020 failure, indicating that the increased shear stress has been reduced and relaxed with time after a failure. The increase in shear stress is mainly due to the debuttreasing and the mass loss at the toe due to rapid river incision during the cascading event (Zhao et al., 2021; Lacroix et al., 2020). After the catastrophic failure, the slowing-down in landslide kinematics implies the restabilization of the landslide body, mainly due to the decreased shear stress and increased shear strength. Possible reasons behind this could be the reload by the downward-moving materials from the upslope, the compaction effects of new materials under gravitational force, the improvement of soil cohesion, and the recovery of support to the landslide body (Lacroix et al., 2020; Catane et al., 2019).

In addition, the derived optical results reveal that until the end of September 2020, larger deformation could still be observed near the northern ridges close to the channel of the failure part, which is similar to our previous co-failure results (Xia et al., 2022b). Explanations for this phenomenon may be that the toe of the landslide was closer to the river and was more severely influenced during the 2020 cascading event, by both the upstream dam and the release of water from the barrier lake to relieve flood pressure during the failure. After September 2020, although the general trend of the failure area deformation stabilized, small zones of displacement could still be found with noticeable deformation close to the southwestern bedrock.

### 6.6.2 Post-failure Kinematics from MT-InSAR

Applying SAR remote sensing and MT-InSAR technology, we can study the evolution of creeping kinematics of the Aniangzhai landslide body after failure. Overall, the activation and instability dynamics of the ancient Aniangzhai landslide body are obviously revealed by comparing the pre-failure and post-failure LOS deformation rates. With the help of fieldwork investigation, we see two main regions for the ancient Aniangzhai landslide body: the main area that failed during the June 2020 event (Zone 1), and the other part in the above that did not fail (Zone 2). The geographical divider can be recognized as the orange curve in Figure 6.5 above the main scarp of the failure part. For the failure part, the precursory LOS displacement rates could only range from -50 to -80 mm per year (Kuang et al., 2022; Xia et al., 2022b), while its post-failure velocities could reach approximately -300 mm annually. In comparison, the upper part had a sort of pre-failure displacement rate of around -40~0 mm/year, which now amounts to over -150 mm/year.

Interestingly, the retrieved horizontal and vertical deformation also reveal different kinematics for those two parts. The horizontal displacements for the lower failure part exceed the vertical displacements and dominate the post-failure kinematics during the SAR observations. In contrast, the upper part was more dominated by vertical displacements. These two different features could be observed on the landslide body at the same time. These results indicate that the lower failure part continues to move similarly to the June 2020 failure, i.e., toward the river channel, while the upper active part mainly proceeds with vertical motions. Through field investigations, we can confirm that the upper active landslide is shallow in depth, and much steeper slopes ( $>45^\circ$ ) could be observed there. Hence, the vertical displacement could be explained as vertical creeping motions rather than gravity compaction. It is relatively common that the movement rates within the lower parts of the landslide body are higher since its initial movement is induced from its bottom by the constant undercutting of its toe area during the 2020 event. The movement retrogressively transfers into the landslide's upper parts, causing subsequent deformation of lesser intensity.

It is essential to mention that, during our field expeditions, we see a lot of anti-slide piles have been deployed by authorities along the river channel after the failure, and the reinforcement of the bottom has been ongoing to increase the surface resistance and prevent further downslope sliding for the lower failure part. However, our MT-InSAR results found a significant acceleration of the upper part after June 2020, where such equipment and measurements are not observed or taken above the main scarp. Therefore, for prevention, similar measurements are suggested to be implemented over the main scarp of failure in case it turns from creeping landslides to catastrophic failure in the future.

A comparison of MT-InSAR results derived from TSX and S1 indicates the irreplaceable advantages of exploiting high-resolution TSX imagery for slope stability monitoring in this study. Due to the significant spatial resolution and better observation geometry, the acquired scatters over the sliding slope are much denser when using TSX data than when exploiting S1 data (Figure 6.4), which is capable of capturing more details and features of different patterns in landslide dynamics. Furthermore, for the new creeping landslides in the southern hillslope and along channels, it is reasonable to assume that they were triggered due to the complex cascading event in June 2020, since the creeping motions were not detected in the previous studies (Xia et al., 2022b). In general, MT-InSAR techniques with proper post-processing strategies could be used as an essential complement to remote monitoring systems similar to those in mountainous areas such as Aniangzhai for monitoring progressive deformation and detecting possible release zones to control and reduce the hazards posed by landslides (Carlà et al., 2019).

### 6.6.3 ICA-based Spatiotemporal Features of Deformation

The ICA decomposition could offer another opportunity to characterize complicated landslide kinematics. The rapid motions observed by optical data reveal different magnitudes of exponential decay. As for the InSAR observations, most features of the ancient Aniangzhai landslide body are represented by three independent components; then, they are analyzed qualitatively rather than quantitatively due to the dimensionless quantity of ICs. IC1 mainly reveals that the kinematic changes at the landslide's central failure parts are not correlated with precipitation. IC2 and IC3 illustrate stability before April 2021, and then accelerations from April 2021, corresponding to the increased precipitation during the rainy season. This is due to the water infiltration and saturation, which can decrease the shear strength (Lacroix et al., 2020). In the winter season, with a reduced amount of precipitation, IC2 is inverted to have the dynamics to slow down accordingly. In contrast, however, IC3 seems to move in the opposite direction and remains stable after October 2021 (Figure 6.6b). A possible explanation could be that since IC3 refers to the lower part of the landslide; with the deployed anti-slide piles increasing the resistance, the downslope mass accumulates and reloads from upslope materials. The gravitational compaction and increased friction help decrease shear stress and restabilize the mass on the slip surface in this area. This explanation also coincided with the optical and MT-InSAR results we obtained, in which buttressing at the toe of the landslide could be observed, and the landslide was incrementally slowing down with time. In addition, as proven by our field investigation, we can find that the lower failure part (Zone 1) and the upper creeping part (Zone 2) contain different motion characteristics, consistent with the different features of IC1 and IC2 extracted using ICA decomposition (Figure 6.6).

### 6.6.4 Resolving 4D Post-failure Kinematics

The tool we applied to integrate optical and SAR remote sensing is an exponential decay model representing the stress relaxation after failure as suggested by optical observations. Experimental investigations have shown that post-failure relaxation mechanisms of landslide body follow an exponential or logarithmic decay (Cui et al., 2021; Wang et al., 2008; Rice et al., 2001). Similar models have also been used to model post-seismic deformation following earthquakes (Kreemer et al., 2006; Savage and Prescott, 1978). Indeed, we have also tried the decaying logarithmic model. However, when deriving the model parameters



along the common E-W directions, the logarithmic model, with an  $R^2$  of about 67%~89%, does not perform as well as the exponential model, with an  $R^2$  of about 92%~99%. Hence, we eventually adopted the exponential decay model in this study for sensor integration and modeling of the 4D deformation field.

For the multi-sensor integration, the regridding of multiple remote sensing results is required since a number of observations are discarded, i.e., InSAR scatters from different orbits are not identical due to different SAR observation geometries, as well as the shadow and overlay effects; optical results could also face anomaly issues or low SNR values during NCC processing, making the results unconvincing. Hence, we regridded and calculated the pixel size based on new results from the exponential modeling to facilitate this situation. We assume that the selected common points in the new grid share the same or similar behaviors and magnitude in motion kinematics. It is worth noting that if the grid spacing is too small, the number of points in each grid will also be low; in contrast, the number of points in each collection will increase when the grid space rises, but by doing so, it is difficult to distinguish the features of different patterns from landslides. With testing, we set  $0.0005^\circ$  (approximately 50 meters) as the size of a regridded pixel in this study.

For modeling 4D displacements, the results in the U-D direction show the lowest RMSEs, followed by the E-W and N-S direction results. This is expected considering the different precision between optical and InSAR monitoring, as well as the limited number of optical observations. Indeed, the RMSE in N-S could be improved by using densely distributed optical images in the temporal domain. However, this is not an easy task considering the limited quantity of cloud-free acquisitions. As for the coefficient of determination,  $R^2$  responds to what percentage of the fluctuations in the dependent variable  $y$  can be described by the fluctuations in the independent variable  $x$ . A coefficient of determination greater than 0.3 is generally considered meaningful (Abdi, 2007; Asuero et al., 2006). The coefficient of determination in the E-W direction is the best, followed by the N-S and vertical directions, respectively, which have almost reached 50%. This is also reasonable when the equation has a slight change in the dependent variable  $y$  and mainly the independent variable  $x$  is changing, i.e., when the equation and the  $x$ -axis are nearly parallel, the regression model has a small  $R^2$  at this time (Hastie et al., 2009). Overall, the modeling in the N-S directions is not as good as in the other two directions; however, the modeling of all three directions is considered satisfactory in this study.

It should be stressed that our method for 4D modeling has some limitations and advantages. The major limitation is that many observations will be discarded in the selection process of the IPCs due to different observation geometries of sensors, as sensors with lower resolution do not contain densely distributed scatters. On the contrary, the gaps in optical and SAR remote sensing could be resolved to derive the complete 4D deformation pattern, which is impossible to achieve using only optical or SAR data. Therefore, even without GNSS measurements, the InSAR measurements, initially representing the relative displacement, are converted into absolute displacement by integrating with optical data and using least squares adjustments. Furthermore, the exponential decay model used to connect the observations of different sensors at different times could be easily improved in the future, either by a better alternative physical model or a statistical model. For example, a Kalman filtering approach could be incorporated with the stress relaxation mechanism due to its capability to suppress the measured noises and predict the prospective state and mechanism of landslides (Meinhold and Singpurwalla, 1983).

## 6.7 Conclusion

This paper presents a methodology to characterize the complete 4D post-failure deformation of the 17 June 2020 Aniangzhai landslide using various remote sensing sensors. The 3-meter high-resolution optical data from Planet provide detailed information on the early ( $\sim 6$  months) spatial patterns of slope kinematics, demonstrating how the post-failure velocities decay with time. Further slope deformation analysis using SAR data indicates that the Aniangzhai landslide is active with a maximum LOS rate of approximately 30 cm/year from November 2020 until February 2022. New creeping landslides are also found on the southern hillslope and along river channels, thanks to high-resolution SAR datasets.

Integrating multi-sensor remote sensing techniques using a feature extraction technique and a relaxation model helps overcome the limitation of every single sensor, providing insights into the complete 4D spatiotemporal characteristics of post-failure landslide deformation. For the Aniangzhai landslide, maximum deformation from June 2020 until February 2022 was estimated toward the west, amounting to approximately 28 meters, followed by 17 and 19 meters displacements toward the north and downwards, respectively. The temporal evolution of displacement illustrates a declining characteristic, which can be modeled using an exponential relaxation model, representing stress relaxation after the failure. Such a predictive capability can be used to forecast landslide displacements effectively and to help reduce landslide risk. Although we used high-resolution remote sensing imagery from Planet and TerraSAR-X in this study, the methodology can be similarly applied to the freely available medium-resolution Sentinel-1 SAR and Sentinel-2 optical remote sensing images covering various landslide life cycles. However, the measurement accuracy could be compromised due to the lower resolution of Sentinel data.

## 6.8 Acknowledgments

The authors acknowledge two anonymous reviewers and Prof. Zhong Lu for their constructive suggestions and discussions. The authors also acknowledge the German Space Agency (DLR) gratefully for providing the TerraSAR-X datasets (motagh\_GEO1916) and the Copernicus program for free access to Sentinel-1 data. Z.X. is supported by China Scholarship Council (CSC) Grant #201908080048. This work was partially sponsored by the National Natural Science Foundation of China Grant No. 42074031, and partly supported by Helmholtz within the framework of HIP project MultiSaT4SLOWS.

## 7 Summary and Future Perspectives

### 7.1 Summary

This thesis involves investigating the pre-, co- and post-failure of the catastrophic Aniangzhai landslide in Danba County, China, which evolves from slow-moving at displacement rates of a millimeter per year to devastating failure. The spatiotemporal features of various displacements with long-term and transient behaviors were analyzed using high-resolution and moderate-resolution satellite sensors, such as Planet, Skysat, TSX, S1, S2, and Landsat. On the other hand, artificial corner reflectors were employed as auxiliaries to support spaceborne remote sensors in monitoring slope instabilities over densely vegetated and mountainous regions. The integration of multiple sensors offers new opportunities to overcome the limitations of a single satellite sensor.

Chapter 4 of this study utilizes multi-sensor remote sensing technology to investigate the Aniangzhai slope failure in June 2020 and the active deformation leading up to the event since late 2014. High-resolution optical data from Planet is analyzed using cross-correlation to obtain detailed information about the spatial pattern of slope kinematics. Additionally, the undercutting effects on the toe of the landslide body, which played a vital role in the toe erosion and reactivation of this ancient landslide body, are visible in the optical data. Complementary analyses using multi-temporal SAR satellite remote sensing indicate that the Aniangzhai landslide was not dormant, with a maximum LOS displacement rate of around 38 mm/yr in 2014–2017, reaching approximately 55 mm/yr in 2018–2020. Furthermore, this study shows that only the points on the upper parts of the landslide failure sustained pronounced acceleration of the creep starting in spring 2020, which can be utilized to forecast the potential failure window. Furthermore, a sign of the acceleration of creep on the head part of the failure region and a decrease in NDVI values took place almost simultaneously, opposite to the prevailing trends in this area. This phenomenon might be integrated into an EWS.

Chapter 5 confirms the reliability of small dihedral corner reflectors for deformation monitoring using the InSAR technique. An experimental study of post-failure creep at the Aniangzhai landslide in China using TSX and S1 images showed that the background intensity in TSX images improved by around 30 dB after CR installation, with SCR exceeding 25 dB. In comparison, S1 images showed an improvement of only about 5–10 dB, with an SCR of around 10–15 dB. The RCS of CRs remained relatively consistent in both TSX HS and S1 SAR images, ranging from 15 dB to 23 dB, making them suitable for CR-InSAR analysis using the double-difference phase method. These CRs can be easily installed at a relatively low cost in landslide regions where ground-based measurements are lacking, providing near real-time deformation monitoring and supplementing landslide hazard warning systems. Furthermore, they complement other traditional survey methods such as GPS or leveling and can be applied in S1 images for interferometric analysis, despite being initially designed for high-resolution SAR systems. This study also verified

that high-resolution SAR images have significant advantages in SAR and InSAR analysis due to their improved spatial resolution and shorter revisit times.

Chapter 6 introduces a methodology for characterizing the complete 4D post-failure deformation of the Aniangzhai landslide using various remote sensing sensors. The study utilizes high-resolution optical data from Planet and multiple SAR data to analyze the spatiotemporal characteristics of post-failure landslide deformation. The results show that the Aniangzhai landslide is still active, and new creeping landslides have been detected. A feature extraction technique and a relaxation model are integrated to provide insights into post-failure landslide deformation's complete 4D spatiotemporal characteristics. The methodology can be applied to medium-resolution S1 SAR and S2 optical remote sensing images, but measurement accuracy may be compromised. In general, the proposed methodology and framework can be used to forecast landslide displacements and reduce landslide risk effectively.

After conducting extensive research and analysis, the findings of this thesis provide insightful answers to the research questions posed in the first chapter, which are summarized as follows:

1. **Question:** What is the most important role of spaceborne remote sensing technology in identifying, monitoring, predicting and managing landslide hazards? What are the advantages of spaceborne remote sensing compared to other geodetic methodologies?

**Answer:** The most critical role of spaceborne remote sensing techniques is to provide time series of slope surface kinematics remotely at a local or regional scale. The complexity of landslide prediction makes it challenging to understand slope instability comprehensively, with only a limited number of instances where accurate insights are obtained. However, the obtained surface kinematics using remote sensing can offer valuable assistance in defining warnings and thresholds for alerts and reconstructing physical models close to reality as the foundation for comprehending slope stability and designing mitigation measures. In addition, continuous landslide remote sensing is necessary to create a long-term archive of data and analysis results, providing a more profound and credible comprehension of the physical processes involved in landslides.

Compared to other geodetic methodologies, such as airborne remote sensing or ground measurements, the advantages of spaceborne remote sensing involve a large coverage area, consistent and frequent data acquisition and quality, and cost-effective and rapid response for remote regions.

2. **Question:** What is the performance of spaceborne remote sensing techniques in monitoring slope instability caused by different triggering factors and procedures? How can these triggers be integrated into landslide analysis for the causality, mechanism and anticipation during the complex cascading event?

**Answer:** Spaceborne remote sensing techniques have shown promising performance in monitoring local and regional scale slope instability caused by various triggering factors and procedures. These techniques can provide information on the terrain, land cover, ground displacements with subtle changes, and variation in the landscape that may indicate the presence or evolution of slope instability. On the other hand, many different triggering factors may affect landslide procedures, such as precipitation, river water fluctuation, pore pressure and erosion. Some of these factors

are easily observed and analyzed together with the surface kinematics obtained by spaceborne remote sensing; other factors may not be possible to be obtained directly. Instead, physical modeling is required based on remote sensing observation for further joint analysis.

Various methods have been developed to integrate these triggering factors into landslide analysis to identify and quantify their influence on slope instability. For example, geospatial models can simulate the interactions between different factors, such as rainfall, slope angle, and soil properties, to better understand the causal mechanisms of slope instability. Additionally, time series decomposition and feature extraction methods, such as PCA, ICA, Fourier transform, and wavelet analysis, can support the analysis of spatiotemporal remote sensing data and identify the most critical factors contributing to slope instability. The recently extended deep learning algorithms can also contribute to that. Anticipation of complex cascading events can be achieved using real-time remote sensing data and modeling techniques. For example, landslide susceptibility maps can be updated in real-time using continuous monitoring data to provide early warnings and anticipate the occurrence of cascading events. Integrating spaceborne remote sensing data and analysis techniques into landslide analysis can improve our understanding of slope instability and enable the development of effective mitigation strategies.

3. **Question:** What is the difference between spaceborne optical and SAR remote sensing sensors in monitoring local and regional scale slope instability? What are their advantages and limitations? To what extent can they be integrated to address and highlight the deformation at different scales?

**Answer:** Spaceborne optical sensors capture images using visible and infrared wavelengths, while SAR sensors transmit and receive microwave signals to create images. The horizontal deformation of surface kinematics can be derived using spaceborne optical imaging, while single SAR techniques can measure displacement in LOS directions.

As a result, optical sensors are better suited for capturing detailed surface features and large ground deformation. In contrast, SAR sensors are better for detecting subtle changes in terrain and subsurface deformations. In addition, optical sensors can be affected by cloud cover and weather conditions, while SAR sensors can penetrate clouds and operate in all weather conditions.

The two types of sensors can be integrated to provide complementary information and improve the accuracy of deformation monitoring at different scales. Using integration methodology like our proposed framework, the mathematical and geophysical modeling could fully exploit each sensor's unique advantages. Integration may require specialized software and expertise, and the cost of processing and analyzing data from both sensors may be higher than just one type of sensor.

4. **Question:** How and to what extent can landslide monitoring be improved using auxiliaries like artificial corner reflectors? What is the better strategy for designing the reflectors and selection in imagery?

**Answer:** Artificial CRs can improve landslide monitoring by providing stable and precise coherent pixels for both optical and SAR remote sensing. Scholars can more accurately track deformation over time by placing CRs in areas of interest. For

example, when measuring densely vegetated, semi-vegetated, or agricultural areas, it is possible to design and deploy a network of CRs. The kinematics obtained from the surface of CR-network using spaceborne remote sensing could be accomplished instead of measuring the challenging coherence loss area for landslide cases.

Regarding design, CRs should be made of durable and stable materials, such as metal, and placed in a location unlikely to be disturbed by natural processes or human activities. It should be acknowledged that no single reflector design can provide optimal performance across all operational satellites. Therefore, to ensure effective monitoring, it is necessary to either use sensor-specific CR designs or adopt a compromise solution that can accommodate multiple sensors. Thus, our new CRs are good examples that can be applied for both ascending and descending orbits, while they can also be applied for both medium- and high-resolution images. Of course, the cost element is a vital aspect of CR design.

When selecting imagery, choosing a sensor with a suitable wavelength and resolution for the application is essential. Additionally, the sensor should be able to acquire data consistently and regularly to enable effective monitoring. In this thesis, our proposed selection strategy with the probability model helped identify and locate the tested CRs that exhibited weaker echoes than the traditional reflectors across various images. Moreover, this approach proposed here could be utilized as a universal strategy for detecting analogous targets with echoes resembling those of CRs in other scenarios.

### 7.2 Future Perspectives

In this dissertation, the case study of a large, deep-seated landslide during a complex cascading event was conducted, in which heavy precipitation, debris flows, dammed lake, and erosion effects coupled and triggered the reactivation of the ancient landslide body. When there are rivers and dams near unstable slopes, we can see that the landslide dynamics and its intrinsic physical mechanisms are often more complicated, and the reaction of slope instability to induced factors is more difficult to interpret. However, observing such complex geological hazard chains is often crucial, and in this regard, spaceborne remote sensing plays an essential role in landslide detection, monitoring, analysis and prediction. These satellite-based methods have revolutionized the study and investigation of landslide hazards compared to conventional ground methods, providing critical information on the dynamics and risks associated with these geological disasters.

Looking to the future, we can see that there are still several opportunities for advancing the field of satellite-based landslide remote sensing:

1. Recent advancements in advanced sensors and platforms have significantly expanded the potential of spaceborne landslide remote sensing. For instance, cooperated by the National Aeronautics and Space Administration (NASA) and the Indian Space Research Organisation (ISRO), the NASA-ISRO SAR (NISAR) mission is a joint project to develop and launch a dual-frequency SAR on an Earth observation satellite. It will use a deployable antenna to operate on both L-band and S-band (Rosen et al., 2017). It is noted that L- and S-band have a better penetration capability than C- or X-band, making NISAR suitable for landslide monitoring. On the other hand, all data collected from NISAR will be freely available for 1–2 days commonly

or within hours for emergencies like disasters (Rosen and Kumar, 2021). Such short sampling frequency can significantly improve the spaceborne capability to emergency response for geological hazards such as catastrophic failure or debris flows. Therefore, spaceborne landslide remote sensing has the potential to be integrated into an EWS and a multidisciplinary DRR framework for prompt response to landslide disasters. On the one hand, the densely sampled images can be beneficial for conducting a comprehensive analysis of the cascading events that impact the stability of landslides. They can also offer new opportunities in landslide anticipating and prediction, e.g., the INV method can be significantly improved based on real-time updated images.

Another example is the recent experiments conducted by Xu et al. (2023), where an airborne P-band SAR sensor is tested and verified to have superior performance in landslide monitoring compared to conventional C-, X- or L-band due to its better capability of penetration. With the development of satellite sensor technology, we may see a SAR mission carrying P-band sensors in the future, which could be a critical improvement for landslide hazard analysis and risk assessment.

2. Another exciting area of research is the integration of multiple remote sensing techniques for landslide monitoring, as we conducted in this thesis. More importantly, the inversion of the deeper physical mechanisms of landslides involved could be performed. For the time being, combining SAR, optical, GNSS or CRs can provide a complete understanding of landslide surface kinematics and help validate and refine landslide detection algorithms, since each sensor has unique advantages and weaknesses in monitoring complicated landslide dynamics. What needs to be counted here is the in-depth analysis and inversion of the intrinsic stability of landslides beneath surface movements based on spaceborne remote sensing techniques.

Future perspectives can include numerical modeling approaches based on the surface kinematics derived using remote sensing observations, such as viscoplastic flow and pore pressure diffusion model (Hu et al., 2020) or modeling evolution of solid volume fraction (Xu et al., 2021). Since landslides comprise many different types of motion, the required numerical modeling approaches can also be various.

Future perspectives can also include using physically- or statistical-based modeling to integrate various sensors, which can consider different features of motion characteristics behind the slope instability. For instance, a Kalman filtering approach could be integrated with the stress relaxation mechanism, given its ability to filter out measurement noises and predict potential states and mechanisms for landslide study.

3. Moreover, decorrelation is still a significant limitation in InSAR applications for landslide investigation, since most occur in mountainous regions. Although advanced MT-InSAR methods have been developed, much room remains for improvement. For instance, from the algorithm aspect, specific new methodologies are proposed to solve the decorrelation issues, e.g., Mirzaee et al. (2022) proposed a “phase linking” approach which could solve the seasonal decorrelation over snowfall areas using Delaunay networks for phase unwrapping.

On the other hand, auxiliaries such as artificial CRs can be explicitly applied to the decorrelation problem when studying landslide cases in densely vegetated, semi-



vegetated and agricultural areas. CRs are beneficial, cost-effective and long-lasting auxiliaries in spaceborne remote sensing. They can provide coherent targets for InSAR monitoring and be applied for NCC analysis in optical and SAR images. For example, for a large area with dense vegetation or low coherence, deploying a network of CRs to help derive the ground kinematics is possible. In this thesis, we evaluate the performance of our newly designed small DCRs and display preliminary results. However, more efforts are still needed to comprehensively understand and compare the role of different CRs in various landslide cases, as well as better ways to design, deploy and analyze different CRs. For such purposes, we have deployed our new and conventional TCRs on a large, deep-seated, slowing-moving landslide body and tasked C-band, X-band and L-band datasets and GNSS data. Future perspectives also involve developing a more compromise design of CRs for various satellite-based sensors in landslide monitoring.

4. At last, with the development of artificial intelligence and neural networks, another key area of focus is the development of automated or semi-automated algorithms for landslide identification and mapping in the spatiotemporal domain, in order to produce inventory maps for landslide hazards at a regional or even larger scale. In this regard, machine learning and deep learning can be applied to analyze SAR and optical data, allowing for the rapid identification and classification of landslides based on different bands and various terrain features using satellite-based remote sensing techniques. This will significantly enhance the ability to respond to landslide hazards and facilitate decision-making for disaster management. The image processing for landslide remote sensing has already significantly been enhanced based on machine learning (Novellino et al., 2021; Ji et al., 2020). However, combining machine learning and the physics of slope instability is still challenging work at the moment, and plenty of scholars are endeavoring to solve this issue.

# List of Figures

2.1	Terminology of landslide glossary (Source: adapted by Cooper et al. (2007)).	8
2.2	The diagram features three rings, each representing different types of landslides, which comes from statistical analysis of 383 landslide-related articles (Source: Reichenbach et al. (2018)). The left ring depicts eight classes of landslide movements, while the center ring displays four classes of landslide materials. The right ring shows two classes of estimated landslide depth, as described in the studied literature database. In all three rings, NC denotes non-classified.	9
2.3	Landslide types according to different movements (Source: adapted by Hungr et al. (2014) and Cruden and Varnes (1996)).	10
2.4	Examples of landslide types revealed by photos according to different movements, i.e., (a) fall, (b) topple, (c) slide, (d) spread, and (e) flow (Source: adapted by Regmi et al. (2014), Hungr et al. (2014), and Michoud et al. (2012)).	10
2.5	The count and distribution of fatal landslides that were not triggered by seismic activity between 2004 and 2016, categorized by different countries (Source: adapted by Froude and Petley (2018)).	12
2.6	(a) Example for one of the largest slow-moving landslides in China, i.e., the Huangtupo landslide, with annual displacement rates of around 10–20 mm/year. (b) Examples of the potential damages for the slow-moving Huangtupo landslides. Note that north arrows approximately indicate the downhill direction. (Source: adapted by Wang et al. (2018) and Tomás et al. (2014).)	14
2.7	Schematic of pixel offset tracking techniques using the normalized cross-correlation algorithms showing the investigated pixel for the reference and search images (Source: adapted by Debella-Gilo and Kääb (2011)). The corresponding coordinate system is pixel coordinate.	18
2.8	Schematic of spaceborne SAR imagery.	20
2.9	Different modes of spaceborne SAR missions for image acquisition.	21
2.10	Simplified example of distortions in satellite SAR imagery.	22
2.11	Overview of the major spaceborne SAR missions, the duration at the end of each mission (unit: days) indicates the repeat cycle of the satellites.	23
2.12	Displacement of InSAR geometry in the plane normal to the flight. $B_{\perp}$ and $B_{\parallel}$	24
2.13	Simplified workflow of differential InSAR.	25
2.14	Examples of intermediate results of InSAR processing, i.e., (a) DEM, (b) coherence map, (c) flat-Earth component, (d) differential interferogram, (e) filtered differential interferogram, and (f) filtered differential interferogram with intensity map.	26

## List of Figures

2.15	An example of decorrelation during InSAR processing. (a) The coherence map of two TSX images has a temporal baseline of 11 days and a perpendicular baseline of -5 meters. (b) The corresponding differential interferogram is derived using the same SAR image pair. . . . .	28
2.16	Diagrams from the side view and the plan view illustrating the effects of variation in aspect on the LOS projection component (Source: Dai et al. (2022)). . . . .	30
2.17	Geometric relationship between an ascending LOS direction and a specific maximum slope aspect (Source: adapted by Dai et al. (2022)). . . . .	31
2.18	Scattering mechanisms for (a) an ideal single scatterer element, (b) a persistent scatterer element, and (c) a distributed scatterer. The corresponding temporal phase variations of the scattered waves are simulated and visualized.	32
2.19	An example of interferogram network in (a) persistent scatterer interferometry (PSI) and (b) small baseline subsets (SBAS) approaches. The $x$ and $y$ axes illustrate the temporal and spatial baselines. . . . .	33
2.20	Examples of the conventional triangular TCRs and our experimental designs for monitoring slope instability. . . . .	36
2.21	Examples of the intensity map of the conventional triangular TCRs in high-resolution TSX data. . . . .	37
3.1	Flowchart of data processing and the framework of modeling 4D post-failure slope instability dynamics. . . . .	42
4.1	Location of the study area. Backgrounds are Planet high-resolution remote sensing optical images (RGB bands), which are acquired (a) before the failure on 15 June 2020, and (b) after the failure on 24 June 2020. . . . .	49
4.2	Display of the landslide failure and different zones of the landslide body, as well as examples of damages in the event. (a) Ravaged roads on the edge of the central failure. (b) The northern lateral flank of the landslide. (c) Damaged extra high voltage (EHV) transmission tower. (d) Front view of ravaged roads. (e) The toe of the landslide body. (f) Skysat optical image acquired on 25 November 2020, with the boundaries of three different zones of the landslide, i.e. the red, orange and yellow lines represent the areas with the fast, medium and slow movements in this event, respectively. (g) Cracked house. (h) The southern flank of the center part, which had the fastest displacement rates during this failure. (i) The main scarp of the failure in the southeast direction. . . . .	50
4.3	2D results of horizontal displacement (Duration: 15 June 2020 and 24 June 2020) generated using Planet optical images. The lengths and directions of the arrows represent the magnitudes and the moving directions of motion. The orange line represents the failure area (same as in Figure 4.2). . . . .	55
4.4	Comparison of MT-InSAR results for (a) PSI in period of 2014–2017, (b) SBAS in 2014–2017, (c) PSI in 2018–2020 and (d) SBAS in 2018–2020; the blue line and triangles in (d) show the location of the selected topographic profile and points analyzed in Figure 4.5. Image background is comprised of the Planet optical image acquired on 15 June 2020. . . . .	56

4.5	Plotting of (absolute) LOS displacements along a topographic profile for the SBAS results in 2018–2020. The location of the profile is shown in Figure 4.4d. (a) The selected topographic profile. (b)–(g) show the MT-InSAR results of points along the selected profile from northwest to southeast. . . .	57
4.6	(a) Annual precipitation within Danba County for period of 2014 to 2020. (b) Comparison of monthly-mean precipitation for period of the last 20 years with precipitation in 2020. . . . .	58
4.7	Location of arbitrarily selected points (P1–P10) over the landslide body. The region is classified according to the behavior of these points from spring 2020 until the failure; P1–P9 are within the failure region while P10 from the landslide body is located outside of the 2020 failure. T1–T6 are the selected points along topographic profile as shown in Figure 4.4d. The background image is from Planet optical image. . . . .	58
4.8	LOS displacements for period of 2018–2020 for SBAS result and the corresponding fittings of points (a) P1–P3, (b) P4–P6, (c) P7–P9 and (d) P10. The locations of points have shown in Figure 4.7. . . . .	59
4.9	Comparing of landslide kinematics with the corresponding precipitation in points P1–P3. (a) Fitted LOS displacements of points P1–P3 from 2018 to 2020. The marked periods are mid-April to mid-June in the three rainy seasons before the failure. Relevant statistics of increments are listed in Table 4.3. (b) The daily and cumulative precipitation from 2018 to 2020. . .	60
4.10	(a) Results of INV analysis for points (a) P1–P3 and (b) P5 and P7. Red lines display the results of INV, whereas the black dashed lines show the actual failure time. . . . .	61
4.11	(a) Comparison of NDVI (MODIS) and interferometric coherence of the 2014–2020 period. The S1 dataset for this region has a temporal gap in 2017–2018. (b) Comparison of NDVI time series from three different satellite collections of the period from July 2018 to May 2021. The NDVI and coherence values are calculated for the same slope area affected by the failure. . .	62
4.12	(a) Comparison of NDVI (MODIS) in 2017–2019 and in 2020, and orange lines are examples of LOS velocities in 2020 for points selected arbitrarily within the head of the failure region. (b) Comparison of coherence for time period of 2018–2019 and in 2020. . . . .	65
4.13	Comparison of the river courses between (a) the normal one in the previous year on 13 August 2019 and (b) the debris flows on 27 August 2020. The images are S2 acquisitions. . . . .	68
4.14	Comparison of the river courses for the rainy season in the previous years, on (a) 06 June 2018, (b) 06 June 2019, (c) 06 June 2020, to the river course of the accident (d) 24 June 2020. The planet remote sensing optical images are exploited. . . . .	68
4.15	Baseline networks in MT-InSAR processing of (a) PSI for the first time span in 2014–2017; (b) SBAS for the first time span in 2014–2017; (c) PSI for the second time span in 2018–2020; (d) SBAS for the second time span in 2018–2020. . . . .	69

## List of Figures

5.1	(a) Study area and locations of tested CRs, specified by numbers 1–6. The background image is from a Skysat high-resolution optical image acquired in November 2020. The boundaries of different zones of the landslide body are presented (Xia et al., 2022b). (b) Field photo from a tested CR over Aniangzhai landslide. (c) Position relationship between CR03 and the newly arranged TCR as an unexpected interference. (d) The general schematic of constructed CRs. . . . .	74
5.2	Results of the tested CRs. (a)-(c) Time series of calibrated radar intensity. (d)-(f) Time series of the measured RCS values. (g)-(i) Time series of the measured SCR values. (j)-(l) LOS displacements estimated using CR-InSAR method. (m)-(n) Converted slope displacements on CRs. The left, middle and right columns are TSX descending, S1 descending, and S1 ascending datasets, respectively. The light gray dashed lines represent the deployment of the CRs. . . . .	77
5.3	Examples of demonstrating the proposed selection strategy using a conditional probability model for (a) CR01 in TSX descending image on 24 March 2021; (b) CR03 in TSX descending image on 03 August 2021; (c) CR01 in S1 descending image on 21 July 2021; (d) CR01 in S1 ascending image on 30 October 2021. The rest pixels without markers have the probability of zero. . . . .	81
5.4	Radar intensity map for the tested DCRs CR01–03 and CR05 after the deployment in TSX descending dataset. . . . .	82
5.5	Radar intensity map for the tested DCRs CR01–03 and CR05 after the deployment in S1 descending dataset. . . . .	82
5.6	Radar intensity map for the tested DCRs CR01–03 and CR05 after the deployment in S1 ascending dataset. . . . .	83
5.7	Site photos of the interference TCR near our tested CR03. . . . .	83
6.1	The Aniangzhai landslide and ground pictures of its different zones: (a) geographical setting of the study area, (b) the toe, (c) the southern lateral flank, (d) the northern lateral flank, and (e) the main scarp (adapted by Xia et al. (2022b)). The red line reveals the central zone of the 2020 event, which had the most significant movement during the catastrophic failure; the orange line depicts a medium motion of around 1~5 meters, whereas the yellow line shows the extent of the ancient landslide body. The background image in (a) is from Skysat high-resolution image acquired in November 2020. . . . .	89
6.2	Flowchart of data processing and the framework. (The missing abbreviations: ROI is the area of interest; E-W is the East-West direction; N-S is the North-South direction; U-D is the up-down direction; PCA is the principal component analysis.) . . . . .	90
6.3	2D results of horizontal displacement derived using Planet images. The results are within the time spans (a) from 24 June 2020 to 26 July 2020, (b) from 26 July 2020 to 30 September 2020, and (c) from 30 September 2020 to 11 January 2021. The arrows demonstrate the magnitude and direction of the motions for different patterns using a step of 15 pixels in both W-E and N-S directions. The boundaries of the landslide body are presented in Figure 6.1d. . . . .	95

6.4	MT-InSAR results with displacement rates in LOS direction using (a) descending TSX data, (b) descending S1 data, and (c) ascending S1 data. The time period of observations for the MT-InSAR processing is from November 2020 to February 2022. The boundaries of different zones of the landslide body are the same as the ones in Figure 6.1d. Image background is from Planet image acquired in August 2021. . . . .	96
6.5	Resolved horizontal and vertical displacements in (a) East-West (E-W) and (b) Up-Down (U-D) directions from multi-track MT-InSAR observations. The boundaries of different zones of the landslide body are presented in Figure 6.1d. Image background is from a Planet image acquired in August 2021. . . . .	97
6.6	Results of independent component analysis (ICA) applied to TSX observations over the area of the ancient landslide body. (a) Locations of derived scatters with the most significant independent components. Image background is from a Planet image acquired in August 2021. (b) The mixing matrix from independent component analysis. (c) The corresponding daily and cumulative precipitation. The corresponding blue and yellow windows in (b) and (c) represent the rainy period and dry period afterwards. . . . .	99
6.7	(a) Example of deriving decay factor in the exponential modeling using the largest displacement in E-W direction integrating both optical and InSAR measurements. (b) Example of InSAR observations in E-W direction for ICP7 using regression with IC1 model. Examples of derived 4D displacements using an exponential decay model in (c) E-W direction, (d) N-S direction, and (e) U-D direction. The corresponding locations of the IPCs are shown in Figure 6.8l. . . . .	100
6.8	Examples of 4D post-failure modeling from IPCs in E-W, N-S and vertical directions for various time frames of 3 days, 10 days, 30 days and 90 days after the catastrophic failure on 17 June 2020. Yellow curve shows the boundary of ancient landslide body (see Figure 6.1a). . . . .	101



# List of Tables

4.1	Parameters investigated for analyzing slope instability before failure using Google Earth Engine (GEE), parameters of SAR images from S1A are listed together for comparison as well. . . . .	52
4.2	Relevant statistics of MT-InSAR results for the ancient slope failure re-activated in 2020 (Figure 4.1). Parameters for the PSI and SBAS results (Figure 4.4) of the two periods are listed respectively. . . . .	56
4.3	Increments of precipitation and the corresponding increments of LOS displacement of points P1–P3 from mid-April to mid-June in 2018–2020. . . .	60
4.4	Summary of parameters of the exploited descending S1 SAR acquisitions in this study. . . . .	69
6.1	Relevant features of the deployed SAR data for MT-InSAR processing. HS represents the High-resolution Spotlight mode, while IW refers to the Interferometric Wide (IW) swath mode. $\sigma_T$ and $\sigma_S$ represent the temporal resolution and spatial resolution, respectively. The unit of $\sigma_T$ is day, and the unit of $\sigma_S$ is meter $\times$ meter in range and azimuth directions. . . . .	91
6.2	Relevant statistics of NCC results from Planet images. The maximum and mean displacements $d_{max}$ and $d_{mean}$ , as well as the maximum and mean velocities $v_{max}$ and $v_{mean}$ are derived and displayed for the sequential time spans. The co-failure results (June 17 to June 24) is from our previous studies (Xia et al., 2022b). The unit for displacement is meter, and the unit for velocity is meter/day. . . . .	94





# Bibliography

- Abdi H (2007) Multiple correlation coefficient. *Encyclopedia of Measurement and Statistics* 648:651
- Akbarimehr M, Motagh M, Haghshenas-Haghighi M (2013) Slope stability assessment of the sarcheshmeh landslide, northeast iran, investigated using insar and gps observations. *Remote Sensing* 5(8):3681–3700
- Amatya P, Kirschbaum D, Stanley T (2019) Use of very high-resolution optical data for landslide mapping and susceptibility analysis along the karnali highway, nepal. *Remote Sensing* 11(19):2284
- Amelung F, Galloway DL, Bell JW, Zebker HA, Laczniaak RJ (1999) Sensing the ups and downs of las vegas: Insar reveals structural control of land subsidence and aquifer-system deformation. *Geology* 27(6):483–486
- Amemiya T (1983) Non-linear regression models. *Handbook of Econometrics* 1:333–389
- Anderssohn J, Motagh M, Walter TR, Rosenau M, Kaufmann H, Oncken O (2009) Surface deformation time series and source modeling for a volcanic complex system based on satellite wide swath and image mode interferometry: The lazufre system, central andes. *Remote Sensing of Environment* 113(10):2062–2075
- Ao M, Zhang L, Dong Y, Su L, Shi X, Balz T, Liao M (2020) Characterizing the evolution life cycle of the sunkoshi landslide in nepal with multi-source sar data. *Scientific Reports* 10(1):1–12
- Asuero AG, Sayago A, González A (2006) The correlation coefficient: An overview. *Critical Reviews in Analytical Chemistry* 36(1):41–59
- Bai Z, Fang S, Gao J, Zhang Y, Jin G, Wang S, Zhu Y, Xu J (2020) could vegetation index be derive from synthetic aperture radar?—the linear relationship between interferometric coherence and ndvi. *Scientific Reports* 10(1):1–9
- Bamler R, Hartl P (1998) Synthetic aperture radar interferometry. *Inverse Problems* 14(4):R1
- Barra A, Monserrat O, Mazzanti P, Esposito C, Crosetto M, Scarascia Mugnozza G (2016) First insights on the potential of sentinel-1 for landslides detection. *Geomatics, Natural Hazards and Risk* 7(6):1874–1883
- Behling R, Roessner S, Golovko D, Kleinschmit B (2016) Derivation of long-term spatiotemporal landslide activity—a multi-sensor time series approach. *Remote Sensing of Environment* 186:88–104
- Bekaert D, Walters R, Wright T, Hooper A, Parker D (2015) Statistical comparison of insar tropospheric correction techniques. *Remote Sensing of Environment* 170:40–47
- Berardino P, Fornaro G, Lanari R, Sansosti E (2002) A new algorithm for surface deformation monitoring based on small baseline differential sar interferograms. *IEEE Transactions on Geoscience and Remote Sensing* 40(11):2375–2383
- Bianchini S, Herrera G, Mateos RM, Notti D, Garcia I, Mora O, Moretti S (2013) Landslide activity maps generation by means of persistent scatterer interferometry. *Remote Sensing* 5(12):6198–6222

## *Bibliography*

- Biasutti M, Seager R, Kirschbaum DB (2016) Landslides in west coast metropolitan areas: The role of extreme weather events. *Weather and Climate Extremes* 14:67–79
- Bovenga F, Wasowski J, Nitti D, Nutricato R, Chiaradia M (2012) Using cosmo/skymed x-band and envisat c-band sar interferometry for landslides analysis. *Remote Sensing of Environment* 119:272–285
- Bovenga F, Refice A, Pasquariello G, Nitti DO, Nutricato R (2014) Corner reflectors and multi-temporal sar interferometry for landslide monitoring. In: *SAR Image Analysis, Modeling, and Techniques XIV*, International Society for Optics and Photonics, vol 9243, p 92430I
- Bovenga F, Pasquariello G, Pellicani R, Refice A, Spilotro G (2017) Landslide monitoring for risk mitigation by using corner reflector and satellite sar interferometry: The large landslide of carlantino (italy). *Catena* 151:49–62
- Bürgmann R, Rosen PA, Fielding EJ (2000) Synthetic aperture radar interferometry to measure earth's surface topography and its deformation. *Annual Review of Earth and Planetary Sciences* 28(1):169–209
- Carlà T, Intrieri E, Di Traglia F, Nolesini T, Gigli G, Casagli N (2017) Guidelines on the use of inverse velocity method as a tool for setting alarm thresholds and forecasting landslides and structure collapses. *Landslides* 14(2):517–534
- Carlà T, Macciotta R, Hendry M, Martin D, Edwards T, Evans T, Farina P, Intrieri E, Casagli N (2018) Displacement of a landslide retaining wall and application of an enhanced failure forecasting approach. *Landslides* 15(3):489–505
- Carlà T, Intrieri E, Raspini F, Bardi F, Farina P, Ferretti A, Colombo D, Novali F, Casagli N (2019) Perspectives on the prediction of catastrophic slope failures from satellite insar. *Scientific Reports* 9(1):1–9
- Casagli N, Frodella W, Morelli S, Tofani V, Ciampalini A, Intrieri E, Raspini F, Rossi G, Tanteri L, Lu P (2017) Spaceborne, uav and ground-based remote sensing techniques for landslide mapping, monitoring and early warning. *Geoenvironmental Disasters* 4:1–23
- Cascini L, Fornaro G, Peduto D (2010) Advanced low-and full-resolution dinsar map generation for slow-moving landslide analysis at different scales. *Engineering Geology* 112(1-4):29–42
- Catane SG, Veracruz NAS, Flora JRR, Go CMM, Enrera RE, Santos ERU (2019) Mechanism of a low-angle translational block slide: evidence from the september 2018 naga landslide, philippines. *Landslides* 16(9):1709–1719
- Causes L (2001) *Landslide types and processes*. US Geological Survey: Reston, VA, USA
- Chen NS, Li TC, Gao YC (2005) A great disastrous debris flow on 11 july 2003 in shuikazi valley, danba county, western sichuan, china. *Landslides* 2(1):71–74
- Chen Y, He X, Xu C, Huang Y, Zhang P, Luo Z, Zhan T (2022) Development characteristics and causes of a fatal landslide occurred in shuicheng, guizhou province, china. *ISPRS International Journal of Geo-Information* 11(2):119
- Cigna F, Lasaponara R, Masini N, Milillo P, Tapete D (2014) Persistent scatterer interferometry processing of cosmo-skymed stripmap himage time series to depict deformation of the historic centre of rome, italy. *Remote Sensing* 6(12):12593–12618
- Coe JA, McKenna JP, Godt JW, Baum RL (2009) Basal-topographic control of stationary ponds on a continuously moving landslide. *Earth Surface Processes and Landforms* 34(2):264–279

- Colesanti C, Wasowski J (2006) Investigating landslides with space-borne synthetic aperture radar (sar) interferometry. *Engineering Geology* 88(3-4):173–199
- Cooper RG, et al. (2007) Mass movements in Great Britain. Joint Nature Conservation Committee
- Copernicus (2020) Copernicus Sentinel data [2014-2020]. Retrieved from ASF DAAC, processed by ESA. Accessed 30 June 2020.
- Crosetto M, Gili J, Monserrat O, Cuevas-González M, Corominas J, Serral D (2013) Interferometric sar monitoring of the vallcebre landslide (spain) using corner reflectors. *Natural Hazards and Earth System Sciences* 13(4):923–933
- Crosetto M, Monserrat O, Cuevas-González M, Devanthéry N, Crippa B (2016) Persistent scatterer interferometry: A review. *ISPRS Journal of Photogrammetry and Remote Sensing* 115:78–89
- Cruden D, Varnes D (1996) Landslide types and processes in: Turner ka, schuster rl (eds) landslides-investigation and mitigation. national research council transportation research board special report 247
- Cui D, Wang S, Chen Q, Wu W (2021) Experimental investigation on loading-relaxation behaviors of shear-zone soil. *International Journal of Geomechanics* 21(4):06021003
- DAAC L (2021) Mcd43a4 - modis/t+a brdf/albedo nadir brdf-adjusted reflectance (nbar) daily l3 global - 500m. <https://ladsweb.modaps.eosdis.nasa.gov/missions-and-measurements/products/MCD43A4/> Accessed May 2021
- Dai K, Li Z, Tomás R, Liu G, Yu B, Wang X, Cheng H, Chen J, Stockamp J (2016) Monitoring activity at the daguangbao mega-landslide (china) using sentinel-1 tops time series interferometry. *Remote Sensing of Environment* 186:501–513
- Dai K, Li Z, Xu Q, Burgmann R, Milledge DG, Tomas R, Fan X, Zhao C, Liu X, Peng J, et al. (2020) Entering the era of earth observation-based landslide warning systems: a novel and exciting framework. *IEEE Geoscience and Remote Sensing Magazine* 8(1):136–153
- Dai K, Deng J, Xu Q, Li Z, Shi X, Hancock C, Wen N, Zhang L, Zhuo G (2022) Interpretation and sensitivity analysis of the insar line of sight displacements in landslide measurements. *GIScience & Remote Sensing* 59(1):1226–1242
- De Blasio FV (2011) Introduction to the physics of landslides: lecture notes on the dynamics of mass wasting. Springer Science & Business Media
- Debella-Gilo M, Kääb A (2011) Sub-pixel precision image matching for measuring surface displacements on mass movements using normalized cross-correlation. *Remote Sensing of Environment* 115(1):130–142
- Delac K, Grgic M, Grgic S (2005) Independent comparative study of pca, ica, and lda on the feret data set. *International Journal of Imaging Systems and Technology* 15(5):252–260
- Delacourt C, Allemand P, Casson B, Vadon H (2004) Velocity field of the “la clapière” landslide measured by the correlation of aerial and quickbird satellite images. *Geophysical Research Letters* 31(15)
- Delacourt C, Allemand P, Berthier E, Raucoules D, Casson B, Grandjean P, Pambrun C, Varel E (2007) Remote-sensing techniques for analysing landslide kinematics: a review. *Bulletin de la Société Géologique de France* 178(2):89–100
- Delacourt C, Raucoules D, Le Mouélic S, Carnec C, Feurer D, Allemand P, Cruchet M (2009) Observation of a large landslide on la reunion island using differential sar interferometry (jers and radarsat) and correlation of optical (spot5 and aerial) images. *Sensors* 9(1):616–630

## Bibliography

- Dheenathayalan P, Cuenca MC, Hoogeboom P, Hanssen RF (2017) Small reflectors for ground motion monitoring with insar. *IEEE Transactions on Geoscience and Remote Sensing* 55(12):6703–6712
- Di Martire D, Confuorto P, Frezza A, Ramondini M, Lòpez AV, Del Rosso MP, Sebastianelli A, Ullo SL (2018) X-and c-band sar data to monitoring ground deformations and slow-moving landslides for the 2016 manta and portoviejo earthquake (manabi, ecuador). In: 2018 IEEE International Conference on Environmental Engineering (EE), IEEE, pp 1–6
- Dille A, Kervyn F, Handwerger AL, d'Oreye N, Derauw D, Bibentyo TM, Samsonov S, Malet JP, Kervyn M, Dewitte O (2021) When image correlation is needed: Unravelling the complex dynamics of a slow-moving landslide in the tropics with dense radar and optical time series. *Remote Sensing of Environment* 258:112402
- Dini B, Manconi A, Loew S, Chopel J (2020) The punatsangchhu-i dam landslide illuminated by insar multitemporal analyses. *Scientific Reports* 10(1):1–10
- Doerry AW (2014) Reflectors for sar performance testing. Tech. rep., Sandia National Lab.(SNL-NM), Albuquerque, NM (United States)
- Draper BA, Baek K, Bartlett MS, Beveridge JR (2003) Recognizing faces with pca and ica. *Computer Vision and Image Understanding* 91(1-2):115–137
- Duman TY, Çan T, Emre Ö, Keçer M, Doğan A, Ateş Ş, Durmaz S (2005) Landslide inventory of northwestern anatolia, turkey. *Engineering Geology* 77(1-2):99–114
- Eineder M, Adam N, Bamler R, Yague-Martinez N, Breit H (2009) Spaceborne spotlight sar interferometry with terrasars-x. *IEEE Transactions on Geoscience and Remote Sensing* 47(5):1524–1535
- Exterkate P (2013) Model selection in kernel ridge regression. *Computational Statistics & Data Analysis* 68:1–16
- Fan X, Xu Q, Scaringi G, Dai L, Li W, Dong X, Zhu X, Pei X, Dai K, Havenith HB (2017) Failure mechanism and kinematics of the deadly june 24th 2017 xinmo landslide, maoxian, sichuan, china. *Landslides* 14:2129–2146
- Farr TG, Rosen PA, Caro E, Crippen R, Duren R, Hensley S, Kobrick M, Paller M, Rodriguez E, Roth L, et al. (2007) The shuttle radar topography mission. *Reviews of Geophysics* 45(2)
- Farrar T, Nicholson S, Lare A (1994) The influence of soil type on the relationships between ndvi, rainfall, and soil moisture in semiarid botswana. ii. ndvi response to soil oisture. *Remote Sensing of Environment* 50(2):121–133
- Fattahi H, Amelung F (2013) Dem error correction in insar time series. *IEEE Transactions on Geoscience and Remote Sensing* 51(7):4249–4259
- Fattahi H, Amelung F (2014) Insar uncertainty due to orbital errors. *Geophysical Journal International* 199(1):549–560
- Fattahi H, Agram P, Simons M (2016) A network-based enhanced spectral diversity approach for tops time-series analysis. *IEEE Transactions on Geoscience and Remote Sensing* 55(2):777–786
- Federico A, Popescu M, Elia G, Fidelibus C, Internò G, Murianni A (2012) Prediction of time to slope failure: a general framework. *Environmental Earth Sciences* 66:245–256
- Feng G, Li Z, Shan X, Zhang L, Zhang G, Zhu J (2015) Geodetic model of the 2015 april 25 m w 7.8 gorkha nepal earthquake and m w 7.3 aftershock estimated from insar and gps data. *Geophysical Journal International* 203(2):896–900

- Ferretti A, Prati C, Rocca F (2001) Permanent scatterers in sar interferometry. *IEEE Transactions on Geoscience and Remote Sensing* 39(1):8–20
- Festa D, Bonano M, Casagli N, Confuorto P, De Luca C, Del Soldato M, Lanari R, Lu P, Manunta M, Manzo M, et al. (2022) Nation-wide mapping and classification of ground deformation phenomena through the spatial clustering of p-sbas insar measurements: Italy case study. *ISPRS Journal of Photogrammetry and Remote Sensing* 189:1–22
- Freeman A (1992) Sar calibration: An overview. *IEEE Transactions on Geoscience and Remote Sensing* 30(6):1107–1121
- Fritz A, Kattenborn T, Koch B (2013) Uav-based photogrammetric point clouds–tree stem mapping in open stands in comparison to terrestrial laser scanner point clouds. *The International Archives of the Photogrammetry, Remote Sensing and Spatial Information Sciences* 40:141–146
- Frodella W, Gigli G, Morelli S, Lombardi L, Casagli N (2017) Landslide mapping and characterization through infrared thermography (irt): suggestions for a methodological approach from some case studies. *Remote Sensing* 9(12):1281
- Froese C, Poncos V, Skirrow R, Mansour M, Martin D (2008) Characterizing complex deep seated landslide deformation using corner reflector insar (cr-insar): Little smoky landslide, alberta. In: *Proc. 4th Can. Conf. Geohazards*, pp 1–4
- Froude MJ, Petley DN (2018) Global fatal landslide occurrence from 2004 to 2016. *Natural Hazards and Earth System Sciences* 18(8):2161–2181
- Fu W, Guo H, Tian Q, Guo X (2010) Landslide monitoring by corner reflectors differential interferometry sar. *International Journal of Remote Sensing* 31(24):6387–6400
- Fuhrmann T, Garthwaite MC (2019) Resolving three-dimensional surface motion with insar: Constraints from multi-geometry data fusion. *Remote Sensing* 11(3):241
- Gabriel AK, Goldstein RM, Zebker HA (1989) Mapping small elevation changes over large areas: Differential radar interferometry. *Journal of Geophysical Research: Solid Earth* 94(B7):9183–9191
- Gan Br, Yang Xg, Zhang W, Zhou Jw (2019) Temporal and spatial evolution of vegetation coverage in the mianyuan river basin influenced by strong earthquake disturbance. *Scientific Reports* 9(1):1–14
- Garg S, Motagh M, Indu J, Karanam V (2022) Tracking hidden crisis in india’s capital from space: implications of unsustainable groundwater use. *Scientific Reports* 12(1):1–17
- Gariano SL, Guzzetti F (2016) Landslides in a changing climate. *Earth-Science Reviews* 162:227–252
- Garthwaite MC (2017) On the design of radar corner reflectors for deformation monitoring in multi-frequency insar. *Remote Sensing* 9(7):648
- Geitner C, Mayr A, Rutzinger M, Löbmann MT, Tonin R, Zerbe S, Wellstein C, Markart G, Kohl B (2021) Shallow erosion on grassland slopes in the european alps–geomorphological classification, spatio-temporal analysis, and understanding snow and vegetation impacts. *Geomorphology* 373:107446
- Genevois R, Ghirotti M (2005) The 1963 vaiont landslide. *Giornale di Geologia Applicata* 1(1):41–52

## Bibliography

- Gisinger C, Schubert A, Breit H, Garthwaite M, Balss U, Willberg M, Small D, Eineder M, Miranda N (2020) In-depth verification of sentinel-1 and terrasar-x geolocation accuracy using the australian corner reflector array. *IEEE Transactions on Geoscience and Remote Sensing* 59(2):1154–1181
- Goldstein RM, Werner CL (1998) Radar interferogram filtering for geophysical applications. *Geophysical Research Letters* 25(21):4035–4038
- Gomba G, Parizzi A, De Zan F, Eineder M, Bamler R (2015) Toward operational compensation of ionospheric effects in sar interferograms: The split-spectrum method. *IEEE Transactions on Geoscience and Remote Sensing* 54(3):1446–1461
- Grandin R, Klein E, Métois M, Vigny C (2016) Three-dimensional displacement field of the 2015 mw8. 3 illapel earthquake (chile) from across-and along-track sentinel-1 tops interferometry. *Geophysical Research Letters* 43(6):2552–2561
- Grant M, Boyd S (2008) Graph implementations for nonsmooth convex programs. In: Blondel V, Boyd S, Kimura H (eds) *Recent Advances in Learning and Control, Lecture Notes in Control and Information Sciences*, Springer-Verlag Limited, pp 95–110, [http://stanford.edu/~boyd/graph\\_dcp.html](http://stanford.edu/~boyd/graph_dcp.html)
- Grant M, Boyd S (2014) CVX: Matlab software for disciplined convex programming, version 2.1. <http://cvxr.com/cvx>
- Gray AL, Vachon PW, Livingstone CE, Lukowski TI (1990) Synthetic aperture radar calibration using reference reflectors. *IEEE Transactions on Geoscience and Remote Sensing* 28(3):374–383
- Guzzetti F, Mondini AC, Cardinali M, Fiorucci F, Santangelo M, Chang KT (2012) Landslide inventory maps: New tools for an old problem. *Earth-Science Reviews* 112(1-2):42–66
- Habumugisha JM, Chen N, Rahman M, Islam MM, Ahmad H, Elbeltagi A, Sharma G, Liza SN, Dewan A (2022) Landslide susceptibility mapping with deep learning algorithms. *Sustainability* 14(3):1734
- Haghighi MH, Motagh M (2019) Ground surface response to continuous compaction of aquifer system in tehran, iran: Results from a long-term multi-sensor insar analysis. *Remote Sensing of Environment* 221:534–550
- Haghshenas Haghighi M, Motagh M (2016) Assessment of ground surface displacement in taihape landslide, new zealand, with c-and x-band sar interferometry. *New Zealand Journal of Geology and Geophysics* 59(1):136–146
- Haghshenas Haghighi M, Motagh M (2017) Sentinel-1 insar over germany: Large-scale interferometry, atmospheric effects, and ground deformation mapping. *ZfV: Zeitschrift für Geodäsie, Geoinformation und Landmanagement* 2017(4):245–256
- Hall A, Lamb D, Holzapfel B, Louis J (2002) Optical remote sensing applications in viticulture-a review. *Australian Journal of Grape and Wine Research* 8(1):36–47
- Hancock PJ (2002) Human impacts on the stream-groundwater exchange zone. *Environmental Management* 29(6):763–781
- Handwerger AL, Huang MH, Fielding EJ, Booth AM, Bürgmann R (2019) A shift from drought to extreme rainfall drives a stable landslide to catastrophic failure. *Scientific Reports* 9(1):1–12
- Hanssen RF (2001) *Radar interferometry: data interpretation and error analysis*, vol 2. Springer Science & Business Media

- Hanssen RF (2005) Satellite radar interferometry for deformation monitoring: a priori assessment of feasibility and accuracy. *International Journal of Applied Earth Observation and Geoinformation* 6(3-4):253–260
- Hastie T, Tibshirani R, Friedman JH, Friedman JH (2009) The elements of statistical learning: data mining, inference, and prediction, vol 2. Springer
- Hendron Jr A, Patton FD (1985) The vaiont slide. a geotechnical analysis based on new geologic observations of the failure surface. volume 1. main text. Tech. rep., ARMY ENGINEER WATERWAYS EXPERIMENT STATION VICKSBURG MS GEOTECHNICAL LAB
- Herrera G, Gutiérrez F, García-Davalillo J, Guerrero J, Notti D, Galve J, Fernández-Merodo J, Cooksley G (2013) Multi-sensor advanced dinsar monitoring of very slow landslides: The tena valley case study (central spanish pyrenees). *Remote Sensing of Environment* 128:31–43
- Highland L, Bobrowsky PT, et al. (2008) The landslide handbook: a guide to understanding landslides. US Geological Survey Reston, VA, USA
- Hooper A (2008) A multi-temporal insar method incorporating both persistent scatterer and small baseline approaches. *Geophysical Research Letters* 35(16)
- Hooper A, Zebker H, Segall P, Kampes B (2004) A new method for measuring deformation on volcanoes and other natural terrains using insar persistent scatterers. *Geophysical Research Letters* 31(23)
- Hooper A, Segall P, Zebker H (2007) Persistent scatterer interferometric synthetic aperture radar for crustal deformation analysis, with application to volcán alcedo, galápagos. *Journal of Geophysical Research: Solid Earth* 112(B7)
- Hooper A, Bekaert D, Spaans K, Arkan M (2012) Recent advances in sar interferometry time series analysis for measuring crustal deformation. *Tectonophysics* 514:1–13
- Hosseini F, Pichierri M, Eppler J, Rabus B (2018) Staring spotlight terrasars-x sar interferometry for identification and monitoring of small-scale landslide deformation. *Remote Sensing* 10(6):844
- Hu J, Li Z, Ding X, Zhu J, Zhang L, Sun Q (2014) Resolving three-dimensional surface displacements from insar measurements: A review. *Earth-Science Reviews* 133:1–17
- Hu J, Motagh M, Guo J, Haghighi MH, Li T, Qin F, Wu W (2022) Inferring subsidence characteristics in wuhan (china) through multitemporal insar and hydrogeological analysis. *Engineering Geology* 297:106530
- Hu K, Wu C, Tang J, Pasuto A, Li Y, Yan S (2018a) New understandings of the june 24th 2017 xinmo landslide, maoxian, sichuan, china. *Landslides* 15(12):2465–2474
- Hu X, Wang T, Liao M (2013) Measuring coseismic displacements with point-like targets offset tracking. *IEEE Geoscience and Remote Sensing Letters* 11(1):283–287
- Hu X, Lu Z, Pierson TC, Kramer R, George DL (2018b) Combining insar and gps to determine transient movement and thickness of a seasonally active low-gradient translational landslide. *Geophysical Research Letters* 45(3):1453–1462
- Hu X, Bürgmann R, Lu Z, Handwerger AL, Wang T, Miao R (2019) Mobility, thickness, and hydraulic diffusivity of the slow-moving monroe landslide in california revealed by l-band satellite radar interferometry. *Journal of Geophysical Research: Solid Earth* 124(7):7504–7518
- Hu X, Bürgmann R, Schulz WH, Fielding EJ (2020) Four-dimensional surface motions of the slumgullion landslide and quantification of hydrometeorological forcing. *Nature Communications* 11(1):1–9



## *Bibliography*

- Hungr O, Leroueil S, Picarelli L (2014) The varnes classification of landslide types, an update. *Landslides* 11:167–194
- Hyvärinen A, Oja E (2000) Independent component analysis: algorithms and applications. *Neural Networks* 13(4-5):411–430
- Inglada J, Arias M, Tardy B, Hagolle O, Valero S, Morin D, Dedieu G, Sepulcre G, Bontemps S, Defourny P, et al. (2015) Assessment of an operational system for crop type map production using high temporal and spatial resolution satellite optical imagery. *Remote Sensing* 7(9):12356–12379
- Intrieri E, Raspini F, Fumagalli A, Lu P, Del Conte S, Farina P, Allievi J, Ferretti A, Casagli N (2018) The maoxian landslide as seen from space: detecting precursors of failure with sentinel-1 data. *Landslides* 15(1):123–133
- Iverson RM (2000) Landslide triggering by rain infiltration. *Water Resources Research* 36(7):1897–1910
- Jacquemart M, Tiampo K (2021) Leveraging time series analysis of radar coherence and normalized difference vegetation index ratios to characterize pre-failure activity of the mud creek landslide, california. *Natural Hazards and Earth System Sciences* 21(2):629–642
- Ji S, Yu D, Shen C, Li W, Xu Q (2020) Landslide detection from an open satellite imagery and digital elevation model dataset using attention boosted convolutional neural networks. *Landslides* 17:1337–1352
- Jiang M, Li Z, Ding X, Zhu J, Feng G (2011) Modeling minimum and maximum detectable deformation gradients of interferometric sar measurements. *International Journal of Applied Earth Observation and Geoinformation* 13(5):766–777
- Jolivet R, Grandin R, Lasserre C, Doin MP, Peltzer G (2011) Systematic insar tropospheric phase delay corrections from global meteorological reanalysis data. *Geophysical Research Letters* 38(17)
- Joshi N, Baumann M, Ehammer A, Fensholt R, Grogan K, Hostert P, Jepsen MR, Kuemmerle T, Meyfroidt P, Mitchard ET, et al. (2016) A review of the application of optical and radar remote sensing data fusion to land use mapping and monitoring. *Remote Sensing* 8(1):70
- Jung HS, Lee DT, Lu Z, Won JS (2012) Ionospheric correction of sar interferograms by multiple-aperture interferometry. *IEEE Transactions on Geoscience and Remote Sensing* 51(5):3191–3199
- Kääb A (2002) Monitoring high-mountain terrain deformation from repeated air-and spaceborne optical data: examples using digital aerial imagery and aster data. *ISPRS Journal of Photogrammetry and remote sensing* 57(1-2):39–52
- Kalia AC (2018) Classification of landslide activity on a regional scale using persistent scatterer interferometry at the moselle valley (germany). *Remote Sensing* 10(12):1880
- Kampes B (2005) Displacement parameter estimation using permanent scatterer interferometry [ph. d. thesis]. Dutch: Delft University of Technology
- Kampes BM, Hanssen RF (2004) Ambiguity resolution for permanent scatterer interferometry. *IEEE Transactions on Geoscience and Remote Sensing* 42(11):2446–2453
- Kenner R, Bühler Y, Delaloye R, Ginzler C, Phillips M (2014) Monitoring of high alpine mass movements combining laser scanning with digital airborne photogrammetry. *Geomorphology* 206:492–504

- Ketelaar VG (2009) Satellite radar interferometry: Subsidence monitoring techniques, vol 14. Springer Science & Business Media
- Knott EF, Schaeffer JF, Tulley MT (2004) Radar cross section. SciTech Publishing
- Kozu T, Kawanishi T, Kuroiwa H, Kojima M, Oikawa K, Kumagai H, Okamoto K, Okumura M, Nakatsuka H, Nishikawa K (2001) Development of precipitation radar onboard the tropical rainfall measuring mission (trmm) satellite. *IEEE Transactions on Geoscience and Remote Sensing* 39(1):102–116
- Kreemer C, Blewitt G, Maerten F (2006) Co-and postseismic deformation of the 28 march 2005 nias mw 8.7 earthquake from continuous gps data. *Geophysical Research Letters* 33(7)
- Krzeminska D, Bogaard T, Malet JP, Van Beek L (2013) A model of hydrological and mechanical feedbacks of preferential fissure flow in a slow-moving landslide. *Hydrology and Earth System Sciences* 17(3):947–959
- Kuang J, Ng AHM, Ge L (2022) Displacement characterization and spatial-temporal evolution of the 2020 aniangzhai landslide in danba county using time-series insar and multi-temporal optical dataset. *Remote Sensing* 14(1):68
- Lacasse S, Nadim F, Lacasse S, Nadim F (2009) Landslide risk assessment and mitigation strategy. *Landslides–Disaster Risk Reduction* pp 31–61
- Lacroix P, Handwerker AL, Bièvre G (2020) Life and death of slow-moving landslides. *Nature Reviews Earth & Environment* 1(8):404–419
- Lanari R, Zoffoli S, Sansosti E, Fornaro G, Serafino F (2001) New approach for hybrid strip-map/spotlight sar data focusing. *IEE Proceedings-Radar, Sonar and Navigation* 148(6):363–372
- Lanari R, Casu F, Manzo M, Zeni G, Berardino P, Manunta M, Pepe A (2007) An overview of the small baseline subset algorithm: A dinsar technique for surface deformation analysis. *Deformation and Gravity Change: Indicators of Isostasy, Tectonics, Volcanism, and Climate Change* pp 637–661
- Lee CT, et al. (2017) Landslide trends under extreme climate events. *Terr Atmos Ocean Sci* 28:33–42
- Leprince S, Barbot S, Ayoub F, Avouac JP (2007) Automatic and precise orthorectification, coregistration, and subpixel correlation of satellite images, application to ground deformation measurements. *IEEE Transactions on Geoscience and Remote Sensing* 45(6):1529–1558
- Leprince S, Berthier E, Ayoub F, Delacourt C, Avouac JP (2008) Monitoring earth surface dynamics with optical imagery. *Eos, Transactions American Geophysical Union* 89(1):1–2
- Leroueil S, Locat J (2020) Slope movements—geotechnical characterization, risk assessment and mitigation. In: *Geotechnical Hazards*, CRC Press, pp 95–106
- Lissak C, Bartsch A, De Michele M, Gomez C, Maquaire O, Raucoules D, Roulland T (2020) Remote sensing for assessing landslides and associated hazards. *Surveys in Geophysics* 41:1391–1435
- Liu X, Zhao C, Zhang Q, Yang C, Zhu W (2020) Heifangtai loess landslide type and failure mode analysis with ascending and descending spot-mode terrasars-x datasets. *Landslides* 17(1):205–215
- Liu Y, Li Y, Li S, Motesharrei S (2015) Spatial and temporal patterns of global ndvi trends: correlations with climate and human factors. *Remote Sensing* 7(10):13233–13250

## *Bibliography*

- Lucieer A, Jong SMd, Turner D (2014) Mapping landslide displacements using structure from motion (sfm) and image correlation of multi-temporal uav photography. *Progress in Physical Geography* 38(1):97–116
- Mackey BH, Roering JJ (2011) Sediment yield, spatial characteristics, and the long-term evolution of active earthflows determined from airborne lidar and historical aerial photographs, eel river, california. *Bulletin* 123(7-8):1560–1576
- Mahdianpari M, Salehi B, Rezaee M, Mohammadimanesh F, Zhang Y (2018) Very deep convolutional neural networks for complex land cover mapping using multispectral remote sensing imagery. *Remote Sensing* 10(7):1119
- Manconi A, Giordan D (2016) Landslide failure forecast in near-real-time. *Geomatics, Natural Hazards and Risk* 7(2):639–648
- Mansour MF, Morgenstern NR, Martin CD (2011) Expected damage from displacement of slow-moving slides. *Landslides* 8:117–131
- Mantovani F, Soeters R, Van Westen C (1996) Remote sensing techniques for landslide studies and hazard zonation in europe. *Geomorphology* 15(3-4):213–225
- Mantovani M, Bossi G, Marcato G, Schenato L, Tedesco G, Titti G, Pasuto A (2019) New perspectives in landslide displacement detection using sentinel-1 datasets. *Remote Sensing* 11(18):2135
- Marinkovic P, Ketelaar G, van Leijen F, Hanssen R (2007) Insar quality control: Analysis of five years of corner reflector time series. In: *Proceedings of the Fringe 2007 Workshop (ESA SP-649)*, Frascati, Italy, pp 26–30
- Maul GA, Gordon HR (1975) On the use of the earth resources technology satellite (landsat-1) in optical oceanography. *Remote Sensing of Environment* 4:95–128
- Meinhold RJ, Singpurwalla ND (1983) Understanding the kalman filter. *The American Statistician* 37(2):123–127
- Meyer F (2010) A review of ionospheric effects in low-frequency sar—signals, correction methods, and performance requirements. In: *2010 IEEE International Geoscience and Remote Sensing Symposium, IEEE*, pp 29–32
- Michel R, Avouac JP, Taboury J (1999) Measuring ground displacements from sar amplitude images: Application to the landers earthquake. *Geophysical Research Letters* 26(7):875–878
- Michoud C, Derron MH, Horton P, Jaboyedoff M, Baillifard FJ, Loye A, Nicolet P, Pedrazzini A, Queyrel A (2012) Rockfall hazard and risk assessments along roads at a regional scale: example in swiss alps. *Natural Hazards and Earth System Sciences* 12(3):615–629
- Milillo P, Fielding EJ, Shulz WH, Delbridge B, Burgmann R (2014) Cosmo-skymed spotlight interferometry over rural areas: The slumgullion landslide in colorado, usa. *IEEE Journal of Selected Topics in Applied Earth Observations and Remote Sensing* 7(7):2919–2926
- Mirzaee S, Amelung F, Fattahi H (2022) Non-linear phase linking using joined distributed and persistent scatterers. *Computers & Geosciences* p 105291
- Montanarella L (2007) Trends in land degradation in europe. *Climate and land degradation* pp 83–104
- Morishita Y, Lazecky M, Wright TJ, Weiss JR, Elliott JR, Hooper A (2020) Licsbas: An open-source insar time series analysis package integrated with the licsar automated sentinel-1 insar processor. *Remote Sensing* 12(3):424

- Motagh M, Wetzel HU, Roessner S, Kaufmann H (2013) A terrasarsar-x insar study of landslides in southern kyrgyzstan, central asia. *Remote Sensing Letters* 4(7):657–666
- Motagh M, Shamshiri R, Haghighi MH, Wetzel HU, Akbari B, Nahavandchi H, Roessner S, Arabi S (2017) Quantifying groundwater exploitation induced subsidence in the rafsanjan plain, south-eastern iran, using insar time-series and in situ measurements. *Engineering Geology* 218:134–151
- NBSC (2018) National bureau of statistics of china. *China Statistic Year Book* 2018
- Nicholson S, Farrar T (1994) The influence of soil type on the relationships between ndvi, rainfall, and soil moisture in semiarid botswana. i. ndvi response to rainfall. *Remote Sensing of Environment* 50(2):107–120
- Nitti DO, Hanssen RF, Refice A, Bovenga F, Nutricato R (2010) Impact of dem-assisted coregistration on high-resolution sar interferometry. *IEEE Transactions on Geoscience and Remote Sensing* 49(3):1127–1143
- Novellino A, Cesarano M, Cappelletti P, Di Martire D, Di Napoli M, Ramondini M, Sowter A, Calcaterra D (2021) Slow-moving landslide risk assessment combining machine learning and insar techniques. *Catena* 203:105317
- Osmanoğlu B, Dixon TH, Wdowinski S, Cabral-Cano E, Jiang Y (2011) Mexico city subsidence observed with persistent scatterer insar. *International Journal of Applied Earth Observation and Geoinformation* 13(1):1–12
- Palmer J (2017) Creeping earth could hold secret to deadly landslides. *Nature* 548(7668)
- Parizzi A, Brcic R (2010) Adaptive insar stack multilooking exploiting amplitude statistics: A comparison between different techniques and practical results. *IEEE Geoscience and Remote Sensing Letters* 8(3):441–445
- Paul F, Bolch T, Kääb A, Nagler T, Nuth C, Scharrer K, Shepherd A, Strozzi T, Ticconi F, Bhambri R, et al. (2015) The glaciers climate change initiative: Methods for creating glacier area, elevation change and velocity products. *Remote Sensing of Environment* 162:408–426
- Peng M, Lu Z, Zhao C, Motagh M, Bai L, Conway BD, Chen H (2022) Mapping land subsidence and aquifer system properties of the willcox basin, arizona, from insar observations and independent component analysis. *Remote Sensing of Environment* 271:112894
- Petley D (2012) Global patterns of loss of life from landslides. *Geology* 40(10):927–930
- Pradhan B (2010) Remote sensing and gis-based landslide hazard analysis and cross-validation using multivariate logistic regression model on three test areas in malaysia. *Advances in Space Research* 45(10):1244–1256
- Provost F, Michéa D, Malet JP, Boissier E, Pointal E, Stumpf A, Pacini F, Doin MP, Lacroix P, Proy C, et al. (2022) Terrain deformation measurements from optical satellite imagery: The mpic-opt processing services for geohazards monitoring. *Remote Sensing of Environment* 274:112949
- Qin Y, Perissin D, Lei L (2013) The design and experiments on corner reflectors for urban ground deformation monitoring in hong kong. *International Journal of Antennas and Propagation* 2013
- Quecedo M, Pastor M, Herreros M, Fernández Merodo J (2004) Numerical modelling of the propagation of fast landslides using the finite element method. *International Journal for Numerical Methods in Engineering* 59(6):755–794

## *Bibliography*

- Regmi AD, Yoshida K, Nagata H, Pradhan B (2014) Rock toppling assessment at mugling–narayanghat road section: ‘a case study from mauri khola landslide’, nepal. *Catena* 114:67–77
- Reichenbach P, Rossi M, Malamud BD, Mihir M, Guzzetti F (2018) A review of statistically-based landslide susceptibility models. *Earth-science reviews* 180:60–91
- Ren K, Yao X, Li R, Zhou Z, Yao C, Jiang S (2022) 3d displacement and deformation mechanism of deep-seated gravitational slope deformation revealed by insar: a case study in wudongde reservoir, jinsha river. *Landslides* pp 1–17
- Rice JR, Lapusta N, Ranjith K (2001) Rate and state dependent friction and the stability of sliding between elastically deformable solids. *Journal of the Mechanics and Physics of Solids* 49(9):1865–1898
- Rosen P, Hensley S, Shaffer S, Edelstein W, Kim Y, Kumar R, Misra T, Bhan R, Sagi R (2017) The nasa-isro sar (nisar) mission dual-band radar instrument preliminary design. In: 2017 IEEE international geoscience and remote sensing symposium (IGARSS), IEEE, pp 3832–3835
- Rosen PA, Kumar R (2021) nasa-isro sar (nisar) mission status. In: 2021 IEEE Radar Conference (RadarConf21), IEEE, pp 1–6
- Rosen PA, Hensley S, Joughin IR, Li FK, Madsen SN, Rodriguez E, Goldstein RM (2000) Synthetic aperture radar interferometry. *Proceedings of the IEEE* 88(3):333–382
- Rossi C, Gonzalez FR, Fritz T, Yague-Martinez N, Eineder M (2012) Tandem-x calibrated raw dem generation. *ISPRS Journal of Photogrammetry and Remote Sensing* 73:12–20
- Rufino G, Moccia A, Esposito S (1998) Dem generation by means of ers tandem data. *IEEE Transactions on Geoscience and Remote Sensing* 36(6):1905–1912
- Salvi S, Stramondo S, Funning G, Ferretti A, Sarti F, Mouratidis A (2012) The sentinel-1 mission for the improvement of the scientific understanding and the operational monitoring of the seismic cycle. *Remote sensing of environment* 120:164–174
- Savage J, Prescott W (1978) Asthenosphere readjustment and the earthquake cycle. *Journal of Geophysical Research: Solid Earth* 83(B7):3369–3376
- Scaioni M, Longoni L, Melillo V, Papini M (2014) Remote sensing for landslide investigations: An overview of recent achievements and perspectives. *Remote Sensing* 6(10):9600–9652
- Schlögel R, Doubre C, Malet JP, Masson F (2015) Landslide deformation monitoring with alos/pal-sar imagery: A d-insar geomorphological interpretation method. *Geomorphology* 231:314–330
- Schuster RL (1996) Landslides: Investigation and mitigation. chapter 2. Transportation Research Board Special Report 247
- Shahabi H, Hashim M (2015) Landslide susceptibility mapping using gis-based statistical models and remote sensing data in tropical environment. *Scientific reports* 5(1):9899
- Shan XJ, Yin JY, Yu DL, Li CF, Zhao JJ, Zhang GF (2013) Analysis of artificial corner reflector’s radar cross section: a physical optics perspective. *Arabian Journal of Geosciences* 6(8):2755–2765
- Simoni A, Ponza A, Picotti V, Berti M, Dinelli E (2013) Earthflow sediment production and holocene sediment record in a large apennine catchment. *Geomorphology* 188:42–53
- Singleton A, Li Z, Hoey T, Muller JP (2014) Evaluating sub-pixel offset techniques as an alternative to d-insar for monitoring episodic landslide movements in vegetated terrain. *Remote Sensing of Environment* 147:133–144

- Smyth CG, Royle SA (2000) Urban landslide hazards: incidence and causative factors in niterói, rio de janeiro state, brazil. *Applied Geography* 20(2):95–118
- Solari L, Del Soldato M, Montalti R, Bianchini S, Raspini F, Thuegaz P, Bertolo D, Tofani V, Casagli N (2019) A sentinel-1 based hot-spot analysis: landslide mapping in north-western italy. *International Journal of Remote Sensing* 40(20):7898–7921
- Steel RGD, Torrie JH, et al. (1960) Principles and procedures of statistics. Principles and Procedures of Statistics
- Stumpf A, Malet JP, Delacourt C (2017) Correlation of satellite image time-series for the detection and monitoring of slow-moving landslides. *Remote Sensing of Environment* 189:40–55
- Team P (2017) Planet application program interface: In space for life on earth. San Francisco, CA 2017:40
- Teshebaeva K, Roessner S, Echtler H, Motagh M, Wetzel HU, Molodbekov B (2015) Alos/pal-sar insar time-series analysis for detecting very slow-moving landslides in southern kyrgyzstan. *Remote Sensing* 7(7):8973–8994
- Teunissen PJ (1993) Least-squares estimation of the integer gps ambiguities. In: Invited lecture, section IV theory and methodology, IAG general meeting, Beijing, China, pp 1–16
- Tomás R, Li Z, Liu P, Singleton A, Hoey T, Cheng X (2014) Spatiotemporal characteristics of the huangtupo landslide in the three gorges region (china) constrained by radar interferometry. *Geophysical Journal International* 197(1):213–232
- Tomás R, Li Z, Lopez-Sanchez JM, Liu P, Singleton A (2016) Using wavelet tools to analyse seasonal variations from insar time-series data: a case study of the huangtupo landslide. *Landslides* 13(3):437–450
- Tomás R, Pagán JI, Navarro JA, Cano M, Pastor JL, Riquelme A, Cuevas-González M, Crosetto M, Barra A, Monserrat O, et al. (2019) Semi-automatic identification and pre-screening of geological–geotechnical deformational processes using persistent scatterer interferometry datasets. *Remote Sensing* 11(14):1675
- Torres R, Snoeijs P, Geudtner D, Bibby D, Davidson M, Attema E, Potin P, Rommen B, Floury N, Brown M, et al. (2012) Gmes sentinel-1 mission. *Remote Sensing of Environment* 120:9–24
- Travelletti J, Delacourt C, Allemand P, Malet JP, Schmittbuhl J, Toussaint R, Bastard M (2012) Correlation of multi-temporal ground-based optical images for landslide monitoring: Application, potential and limitations. *ISPRS Journal of Photogrammetry and Remote Sensing* 70:39–55
- Twigg J, Mosel I (2017) Emergent groups and spontaneous volunteers in urban disaster response. *Environment and Urbanization* 29(2):443–458
- Ulander I (1991) Accuracy of using point targets for sar calibration. *IEEE Transactions on Aerospace and Electronic Systems* 27(1):139–148
- Vallet A, Charlier J, Fabbri O, Bertrand C, Carry N, Mudry J (2016) Functioning and precipitation-displacement modelling of rainfall-induced deep-seated landslides subject to creep deformation. *Landslides* 13(4):653–670
- Wang H, Wright T, Biggs J (2009a) Interseismic slip rate of the northwestern xianshuihe fault from insar data. *Geophysical Research Letters* 36(3)
- Wang H, Wright TJ, Yu Y, Lin H, Jiang L, Li C, Qiu G (2012) Insar reveals coastal subsidence in the pearl river delta, china. *Geophysical Journal International* 191(3):1119–1128

## *Bibliography*

- Wang J, Su A, Liu Q, Xiang W, Yeh HF, Xiong C, Zou Z, Zhong C, Liu J, Cao S (2018) Three-dimensional analyses of the sliding surface distribution in the huangtupo no. 1 riverside sliding mass in the three gorges reservoir area of china. *Landslides* 15(7):1425–1435
- Wang Q, Yu W, Xu B, Wei G (2019) Assessing the use of gacos products for sbas-insar deformation monitoring: a case in southern california. *Sensors* 19(18):3894
- Wang T, Liao M, Perissin D (2009b) Insar coherence-decomposition analysis. *IEEE Geoscience and Remote Sensing Letters* 7(1):156–160
- Wang Z, Yin K, Jian W, Zhang F (2008) Experimental research on stress relaxation of slip zone soils for anlesi landslide in wanzhou city. *Chinese Journal of Rock Mechanics and Engineering* 27(5):931–937
- Wasowski J, Bovenga F (2014) Investigating landslides and unstable slopes with satellite multi temporal interferometry: Current issues and future perspectives. *Engineering Geology* 174:103–138
- Wegmüller U, Werner C, Strozzi T, Wiesmann A, Frey O, Santoro M (2016) Sentinel-1 support in the gamma software. *Procedia Computer Science* 100:1305–1312
- Wright T, Parsons B, Fielding E (2001) Measurement of interseismic strain accumulation across the north anatolian fault by satellite radar interferometry. *Geophysical Research Letters* 28(10):2117–2120
- Xia Y, Kaufmann H, Guo X (2002) Differential sar interferometry using corner reflectors. In: *IEEE International Geoscience and Remote Sensing Symposium, IEEE*, vol 2, pp 1243–1246
- Xia Y, Kaufmann H, Guo X (2004) Landslide monitoring in the three gorges area using d-insar and corner reflectors. *Photogrammetric Engineering & Remote Sensing* 70(10):1167–1172
- Xia Z, Motagh M, Li T (2022a) Performance analysis of dihedral corner reflectors for slope movements: A case study from aniangzhai landslide in china. *IEEE Geoscience and Remote Sensing Letters* 19:1–5
- Xia Z, Motagh M, Li T, Roessner S (2022b) The june 2020 aniangzhai landslide in sichuan province, southwest china: slope instability analysis from radar and optical satellite remote sensing data. *Landslides* 19(2):313–329
- Xia Z, Motagh M, Li T, Peng M, Roessner S (2023) A methodology to characterize 4d post-failure slope instability dynamics using remote sensing measurements: A case study of the aniangzhai landslide in sichuan, southwest china. *ISPRS Journal of Photogrammetry and Remote Sensing* 196:402–414
- Xiong Z, Feng G, Feng Z, Miao L, Wang Y, Yang D, Luo S (2020) Pre-and post-failure spatial-temporal deformation pattern of the baige landslide retrieved from multiple radar and optical satellite images. *Engineering Geology* 279:105880
- Xu Y, George DL, Kim J, Lu Z, Riley M, Griffin T, de la Fuente J (2021) Landslide monitoring and runout hazard assessment by integrating multi-source remote sensing and numerical models: an application to the gold basin landslide complex, northern washington. *Landslides* 18:1131–1141
- Xu Y, Lu Z, Bürgmann R, Hensley S, Fielding E, Kim J (2023) P-band sar for ground deformation surveying: Advantages and challenges. *Remote Sensing of Environment* 287:113474
- Yagüe-Martínez N, Prats-Iraola P, Gonzalez FR, Brcic R, Shau R, Geudtner D, Eineder M, Bamler R (2016) Interferometric processing of sentinel-1 tops data. *IEEE Transactions on Geoscience and Remote Sensing* 54(4):2220–2234

- Yan Y, Cui Y, Liu D, Tang H, Li Y, Tian X, Zhang L, Hu S (2021) Seismic signal characteristics and interpretation of the 2020 “6.17” danba landslide dam failure hazard chain process. *Landslides* pp 1–18
- Yang W, Wang Y, Sun S, Wang Y, Ma C (2019) Using sentinel-2 time series to detect slope movement before the jinsha river landslide. *Landslides* 16(7):1313–1324
- Yang W, Wang Y, Wang Y, Ma C, Ma Y (2020) Retrospective deformation of the baige landslide using optical remote sensing images. *Landslides* 17(3):659–668
- Yoo JC, Han TH (2009) Fast normalized cross-correlation. *Circuits, Systems and Signal Processing* 28(6):819–843
- Zebker HA, Chen K (2005) Accurate estimation of correlation in insar observations. *IEEE Geoscience and Remote Sensing Letters* 2(2):124–127
- Zebker HA, Goldstein RM (1986) Topographic mapping from interferometric synthetic aperture radar observations. *Journal of Geophysical Research: Solid Earth* 91(B5):4993–4999
- Zebker HA, Villasenor J, et al. (1992) Decorrelation in interferometric radar echoes. *IEEE Transactions on Geoscience and Remote Sensing* 30(5):950–959
- Zhang L, Xiao T, He J, Chen C (2019a) Erosion-based analysis of breaching of baige landslide dams on the jinsha river, china, in 2018. *Landslides* 16:1965–1979
- Zhang Z, He S, Liu W, Liang H, Yan S, Deng Y, Bai X, Chen Z (2019b) Source characteristics and dynamics of the october 2018 baige landslide revealed by broadband seismograms. *Landslides* 16:777–785
- Zhao B, Zhang H, Hongjian L, Li W, Su L, He W, Zeng L, Qin H, Dhital MR (2021) Emergency response to the reactivated aniangzhai landslide resulting from a rainstorm-triggered debris flow, sichuan province, china. *Landslides* 18(3):1115–1130
- Zhao C, Lu Z, Zhang Q, de La Fuente J (2012) Large-area landslide detection and monitoring with alos/palsar imagery data over northern california and southern oregon, usa. *Remote Sensing of Environment* 124:348–359
- Zhou C, Cao Y, Hu X, Yin K, Wang Y, Catani F (2022a) Enhanced dynamic landslide hazard mapping using mt-insar method in the three gorges reservoir area. *Landslides* pp 1–13
- Zhou C, Cao Y, Yin K, Intrieri E, Catani F, Wu L (2022b) Characteristic comparison of seepage-driven and buoyancy-driven landslides in three gorges reservoir area, china. *Engineering Geology* 301:106590
- Zhou S, Kuester T, Bochow M, Bohn N, Brell M, Kaufmann H (2021) A knowledge-based, validated classifier for the identification of aliphatic and aromatic plastics by worldview-3 satellite data. *Remote Sensing of Environment* 264:112598
- Zhou S, Kaufmann H, Bohn N, Bochow M, Kuester T, Segl K (2022c) Identifying distinct plastics in hyperspectral experimental lab-, aircraft-, and satellite data using machine/deep learning methods trained with synthetically mixed spectral data. *Remote Sensing of Environment* 281:113263
- Zhou XP, Liu LJ, Xu C (2020) A modified inverse-velocity method for predicting the failure time of landslides. *Engineering Geology* 268:105521
- Zhu L, He S, Qin H, He W, Zhang H, Zhang Y, Jian J, Li J, Su P (2021) Analyzing the multi-hazard chain induced by a debris flow in xiaojinchuan river, sichuan, china. *Engineering Geology* 293:106280



## *Bibliography*

Zuazo VHD, Pleguezuelo CRR (2009) Soil-erosion and runoff prevention by plant covers: a review. *Sustainable Agriculture* pp 785–811

# Eidesstattliche Erklärung

Hiermit versichere ich an Eides statt, dass ich

1. die Regeln der geltenden Promotionsordnung kenne und eingehalten habe und mit einer Prüfung nach den Bestimmungen der Promotionsordnung einverstanden bin;
2. die Dissertation selbst verfasst habe (Selbstständigkeitserklärung), keine Textabschnitte von Dritten oder eigener Prüfungsarbeit ohne Kennzeichnung übernommen habe und alle von mir benutzten Hilfsmittel und Quellen in meiner Arbeit angegeben habe;
3. Dritten weder unmittelbar noch mittelbar geldwerte Leistungen für Vermittlungstätigkeiten oder für die inhaltliche Ausarbeitung der Dissertation erbracht habe (d.h. die wissenschaftliche Arbeit wurde weder in Teilen noch in Gänze von Dritten gegen Entgelt oder sonstige Gegenleistung erworben oder vermittelt);
4. die Dissertation noch nicht als Prüfungsarbeit für eine staatliche oder andere wissenschaftliche Prüfung eingereicht habe;
5. die gleiche oder in wesentlichen Teilen ähnliche Arbeit nicht bei einer anderen Hochschule als Dissertation eingereicht habe; desgleichen habe ich keine andere Abhandlung als Dissertation eingereicht;
6. damit einverstanden bin, dass die Dissertation auch zum Zwecke der Überprüfung der Einhaltung allgemein geltender wissenschaftlicher Standards genutzt wird, insbesondere auch unter Verwendung elektronischer Datenverarbeitungsprogramme.

Hannover, 2023



# CV – Zhuge Xia

## EDUCATION

---

**Gottfried Wilhelm Leibniz University Hannover**      Hannover, Germany  
Ph.D. in Satellite Remote Sensing      2019–Current

- Supervisor: Prof. Dr. Mahdi Motagh

**University of Stuttgart**      Stuttgart, Germany  
M.Sc. in Geodesy and Geoinformatics      2017–2019

- Thesis: “Assessment of Altimetric River Water Level Time Series Densification Methods”
- Supervisor: Prof. Dr.-Ing. Nico Sneeuw

**Wuhan University & University of Stuttgart**      China & Germany  
B.Sc. in Geomatics Engineering      2011–2017

- Dual-Degree Program
- Thesis: “Analysis of Helicopter-borne Gravity Gradiometry”
- Supervisor: Prof. Dr.-Ing. Nico Sneeuw

## WORK EXPERIENCE

---

**Gottfried Wilhelm Leibniz University Hannover**      Hannover, Germany  
Research Assistant      2023–Current

**German Research Centre for Geosciences (GFZ)**      Potsdam, Germany  
Doctoral Researcher      2019–Current

**University of Stuttgart**      Stuttgart, Germany  
Member at AltGIS Group      2017–2018

## PUBLICATIONS

---

- [1] Z. Xia, M. Motagh, T. Li, M. Peng, and S. Roessner, “A methodology to characterize 4d post-failure slope instability dynamics using remote sensing measurements: A case study of the aniangzhai landslide in sichuan, southwest china”, *ISPRS Journal of Photogrammetry and Remote Sensing*, vol. 196, pp. 402–414, 2023.
- [2] Z. Xia, M. Motagh, and T. Li, “Performance analysis of dihedral corner reflectors for slope movements: A case study from aniangzhai landslide in china”, *IEEE Geoscience and Remote Sensing Letters*, vol. 19, pp. 1–5, 2022.
- [3] Z. Xia, M. Motagh, T. Li, and S. Roessner, “The june 2020 aniangzhai landslide in sichuan province, southwest china: Slope instability analysis from radar and optical satellite remote sensing data”, *Landslides*, pp. 1–17, 2022.

# Wissenschaftliche Arbeiten der Fachrichtung Geodäsie und Geoinformatik der Leibniz Universität Hannover

*(Eine vollständige Liste der Wiss. Arb. ist beim Geodätischen Institut, Nienburger Str. 1, 30167 Hannover erhältlich.)*

Nr. 362	COENEN, Max:	Probabilistic Pose Estimation and 3D Reconstruction of Vehicles from Stereo Images (Diss. 2020)
Nr. 363	GARCIAFERNANDEZ, Nicolas:	Simulation Framework for Collaborative Navigation: Development - Analysis – Optimization (Diss. 2020)
Nr. 364	VOGEL, Sören:	Kalman Filtering with State Constraints Applied to Multi-sensor Systems and Georeferencing (Diss. 2020)
Nr. 365	BOSTELMANN, Jonas:	Systematische Bündelausgleichung großer photogrammetrischer Blöcke einer Zeilenkamera am Beispiel der HRSC-Daten (Diss. 2020)
Nr. 366	OMIDALIZARANDI, Mohammad:	Robust Deformation Monitoring of Bridge Structures Using MEMS Accelerometers and Image-Assisted Total Stations (Diss. 2020)
Nr. 367	ALKHATIB, Hamza:	Fortgeschrittene Methoden und Algorithmen für die computergestützte geodätische Datenanalyse (Habil. 2020)
Nr. 368	DARUGNA, Francesco:	Improving Smartphone-Based GNSS Positioning Using State Space Augmentation Techniques (Diss. 2021)
Nr. 369	CHEN, Lin:	Deep learning for feature based image matching (Diss. 2021)
Nr. 370	DBOUK, Hani:	Alternative Integrity Measures Based on Interval Analysis and Set Theory (Diss. 2021)
Nr. 371	CHENG, Hao:	Deep Learning of User Behavior in Shared Spaces (Diss. 2021)
Nr. 372	MUNDT Reinhard Walter:	Schätzung von Boden- und Gebäudewertanteilen aus Kaufpreisen bebauter Grundstücke (Diss. 2021)
Nr. 373	WANG, Xin:	Robust and Fast Global Image Orientation (Diss. 2021)
Nr. 374	REN, Le:	GPS-based Precise Absolute and Relative Kinematic Orbit Determination of Swarm Satellites under Challenging Ionospheric Conditions (Diss. 2021)
Nr. 375	XU, Wei:	Automatic Calibration of Finite Element Analysis Based on Geometric Boundary Models from Terrestrial Laser Scanning (Diss. 2021)
Nr. 376	FENG, Yu:	Extraction of Flood and Precipitation Observations from opportunistic Volunteered Geographic Information (Diss. 2021)
Nr. 377	YANG, Chun:	A hierarchical deep learning framework for the verification of geospatial databases (Diss. 2021)
Nr. 378	MEHLTRETTER, Max:	Uncertainty Estimation for Dense Stereo Matching using Bayesian Deep Learning (Diss. 2021)
Nr. 379	KAZIMI, Bashir:	Self Supervised Learning for Detection of Archaeological Monuments in LiDAR Data (Diss. 2021)
Nr. 380	PETERS, Torben:	Learning Multi-View 2D to 3D Label Transfer for Semi-Supervised Semantic Segmentation of Point Clouds (Diss. 2022)
Nr. 381	WASSINK, Martin:	Kommunal- und Regionalentwicklung durch Kooperation und Teilung von Verantwortung in ländlichen Räumen - eine multiperspektivische Untersuchung an Beispielen aus dem Raum Steinwald/Fichtelgebirge (Diss. 2022)
Nr. 382	GOLDSCHMIDT, Jürgen:	Die Berücksichtigung künftiger Entwicklungen bei der Verkehrswertermittlung (Diss 2022)
Nr. 383	KRUSE, Christian:	Impact maps from bomb craters detected in aerial wartime images using marked point processes (Diss. 2023)
Nr. 384	ZOURLIDOU, Stefania:	Traffic Regulation Recognition from GPS Data (Diss. 2023)
Nr. 385	SLEDZ, Artuom:	Thermal anomaly detection based on information fusion from optical and infrared images (Diss. 2023)
Nr. 386	WITTICH, Dennis:	Deep Domain Adaptation for the Pixel-wise Classification of Aerial and Satellite Images (Diss. 2023)
Nr. 387	SINGH, Vishwa Vijay:	Lunar Laser Ranging - Improved Modelling and Parameter Estimation (Diss. 2023)
Nr. 388	HARTMANN, Jens:	Hochgenaue 3D-Erfassung von Großstrukturen durch kinematisches terrestrisches Laserscanning (Diss. 2023)
Nr. 389	ZHUGE, Xia:	Characterizing slope instability kinematics by integrating multi-sensor satellite remote sensing observations (Diss. 2023)